METHODS FOR ANALYZING THE INFLUENCE OF MOLECULAR DYNAMICS ON NEURONAL ACTIVITY

DISSERTATION

zur Erlangung des akademischen Grades

Doktoringenieur (Dr.-Ing.)

angenommen durch die Fakultät für Informatik
der Otto-von-Guericke-Universität Magdeburg

von Dipl. Ing.-Inf. Stefan Sokoll

geb. am 17.01.1981　　　　　in Jena

Gutachter

Prof. Dr.-Ing. Klaus Tönnies
Prof. Dr.-Ing. Joachim Denzler
Ph.D. Jean-Baptiste Sibarita

Magdeburg, den 30.10.2015

ABSTRACT

Investigating the functioning of neurons at the molecular level is an important foundation to understand how higher brain functions like perception, behavior, or learning and memory are accomplished. Since molecular processes occur in the nanometer range and have to be studied in living samples, recently developed optical super-resolution techniques have boosted their characterization. However, super-resolution techniques require complex instrumentation, are hardly applicable to organotypic samples and still suffer from relatively low temporal resolution. This thesis provides new analysis tools that aim to overcome these limitations and allow to study how the dynamics and the interplay of molecules modulate synaptic transmission efficiency.

In the first part, a method that facilitates fast three-dimensional (3D) molecular dynamics analyses in organotypic brain slices is presented. It adjusts fast astigmatism-based 3D single-particle tracking (SPT) techniques to depth-dependent optical aberrations induced by the refractive index mismatch (RIM) so that they are applicable to complex samples. In contrast to existing techniques, the method determines the aberration directly from the acquired two-dimensional (2D) image stream by exploiting the inherent particle movement and the redundancy introduced by the astigmatism. The method at least halves the systematic positioning error introduced by the aberrations and allows to correctly derive the neuronal morphology and molecular diffusion parameters in 3D, independently of the imaging depth. It does not require additional experimental effort for the user and imaging can directly be started once interesting regions in the sample have been identified.

The second contribution comprises a method for the detection of spontaneous activity at individual synapses. It employs an optical marker that allows to visualize synaptic vesicle fusion with the cell membrane. Individual synaptic signals are computed and activity represented by peaks in the data is detected using a wavelet-based algorithm. As opposed to standard peak detection algorithms, the information of multiple wavelets is fused to match all relevant features of the complex peak shape. The method is particularly useful at low signal-to-noise ratios (SNRs), where it outperforms standard amplitude thresholding (AT) approaches by more than 100 %. The total workflow is automatized and spontaneous activity, which has yet not been addressed, can be robustly and reproducibly analyzed.

Both methods are extensively evaluated on synthetic and real data and are available to the public as open source software. Their combined application is discussed.

ZUSAMMENFASSUNG

Die Funktionsweise von Neuronen auf molekularer Ebene analysieren zu können ist eine wichtige Grundlage um zu verstehen, auf welche Weise das Gehirn komplexe Aufgaben wie Wahrnehmung, Verhalten oder Lernen und Gedächtnis bewerkstelligt. Da molekulare Prozesse im Nanometerbereich ablaufen und in lebenden Organismen untersucht werden müssen, haben die erst kürzlich entwickelten Methoden der

hochauflösenden Mikroskopie deren Analyse revolutioniert. Allerdings haben diese Verfahren oft hohe technische Anforderungen, sind nur schwer in organotypischen Proben anzuwenden und erreichen nur eine niedrige zeitliche Auflösung. In dieser Dissertation werden Methoden entwickelt, die versuchen diese Nachteile zu kompensieren, um untersuchen zu können wie die Einzeldynamik als auch das Zusammenspiel von Molekülen die synaptische Signalübertragungseffizienz modulieren.

Im ersten Teil der Arbeit wird eine Methode vorgestellt, die schnelle molekulare 3D Bewegung auch in organotypischen Gehirnschnitten analysierbar macht. Sie passt Einzelpartikelverfolgungsmethoden, welche auf der Ausnutzung induzierter Verzerrungen aufbauen und mit hoher zeitlicher Auflösung arbeiten, auf tiefenabhängige optische Abbildungsfehler an. Diese entstehen durch die unterschiedlichen Brechungsindizes des Gehirnschnittes und dem Immersionsmedium des Objektivs. Im Gegensatz zu existierenden Ansätzen wird hierbei der Einfluss des Abbildungsfehler direkt aus den 2D Mikroskopiebildern ermittelt indem die natürliche Bewegung der Moleküle sowie die zusätzliche Information, welche durch die bewusst induzierte Verzerrung entsteht, ausgenutzt werden. Die Methode verringert den systematischen Positionierungsfehler, der durch die optischen Abbildungsfehler entsteht, um mindestens die Hälfte und ermöglicht es damit die neuronale Struktur sowie molekulare Diffusionsparameter in 3D zu ermitteln. Dies geschieht unabhängig von der Aufnahmetiefe im Gewebe. Dabei entsteht keinerlei zusätzlicher experimenteller Aufwand für den Nutzer. Sobald eine interessante Region gefunden wurde, kann die Aufnahme gestartet werden.

Der zweite Beitrag dieser Arbeit besteht aus einer Methode für die Detektion spontaner einzelsynaptischer Aktivität. Hierbei wird ein optischer Marker eingesetzt, der es erlaubt synaptische Vesikelfusion mit der Zellmembran sichtbar zu machen. Die Signale individueller Synapsen werden berechnet und Aktivität, die als Impulse erkennbar ist, unter Verwendung eines die Wavelet-Transformation nutzenden Algorithmus detektiert. Dabei hebt sich der vorgestellte Algorithmus von existierenden Methoden dadurch ab, dass die Information mehrerer Wavelets fusioniert wird um eine robuste Detektion der komplexen Impulsformen auf Grundlage aller seiner Merkmale zu ermöglichen. Dies zahlt sich gerade bei niedrigen Signal-Rausch-Abständen aus, wo die Methode gängige Schwellenwertstrategien um mehr als 100 % an Detektionsleistung übertrifft. Der Analyseprozess ist vollständig automatisiert und erlaubt somit die robuste und reproduzierbare Analyse spontaner Aktivität, die bisher nicht untersucht werden konnte.

Beide vorgestellten Methoden werden ausführlich auf simulierten und experimentellen Mikroskopieaufnahmen evaluiert und sind als Open-Source-Software frei verfügbar. Zuletzt wird deren gemeinsame Anwendung diskutiert.

PUBLICATIONS

Some ideas and figures have appeared previously in the following publications:

S. Sokoll, Y. Prokazov, M. Hanses, B. Biermann, K. Tönnies and M. Heine. Fast Three-Dimensional Single-Particle Tracking in Natural Brain Tissue. *Biophysical Journal*, 109(7), pages 1463–71, 2015.

B. Biermann[a], S. Sokoll[a], J. Klueva, M. Missler, J.S. Wiegert, J.B. Sibarita, and M. Heine. Imaging of molecular surface dynamics in brain slices using single-particle tracking. *Nature Communications*, 5(3024):1–10, 2014.

S. Sokoll, K. Tönnies, and M. Heine. An online calibration method for astigmatism-based 3d particle tracking in complex living tissue. In 10*th IEEE International Symposium on Biomedical Imaging: From Nano to Macro (ISBI)*, pages 181–4, 2013.

S. Sokoll, K. Tönnies, and M. Heine. Detection of spontaneous vesicle release at individual synapses using multiple wavelets in a cwt-based algorithm. In *Medical Image Computing and Computer-Assisted Intervention (MICCAI)*, pages 165–72, 2012.

S. Sokoll, H. Beelitz, M. Heine, and K. Tönnies. Towards automatic reconstruction of axonal structures in volumetric microscopy images depicting only active synapses. In 3*rd International Conference on Image Processing Theory, Tools and Applications (IPTA)*, pages 426–31, 2012.

S. Sokoll, K. Tönnies, and M. Heine. Towards fast 3d nanoparticle localization for studying molecular dynamics in living cells. In *BIOINFORMATICS: International Conference on Bioinformatics Models, Methods and Algorithms*, pages 210–5, 2011.

---

a The authors contributed equally.

ACKNOWLEDGMENTS

I like to thank all people that supported me to write this thesis.

I like to begin with my supervisor Martin Heine, who gave me the opportunity to work on such an interesting interdisciplinary topic. He always backed me up even when problems needed long time to be solved. I especially thank him for the actually friendly relation. A similar picture applies to my doctorate supervisor Klaus Tönnies. I thank him for encouraging me and especially for giving me a piece of one's mind after three years. That was important. I also thank him for his always fundamental criticisms and discussions. Likewise, I like to thank my secondary supervisors Joachim Denzler and Jean-Baptiste Sibarita, Joachim Denzler particularly for appreciating and reviewing such an interdisciplinary subject.

Many thanks also applies to my friends who provided support for the thesis or, equally important, cheered me up while I was writing the thesis. I like to mention a few of them directly. Many thanks goes to my cousin Ruth as well as Anne, Bettina and Fabienne who checked the spelling and grammar of my writing. I guess I particularly stressed Anne's aesthetic sense. I further like to thank Rainer, who helped me with math and especially for being a close friend during the last years. I also thank André and Sebastian for the helpful scientific emergency meetings.

I thank the people of my research group and the Leibniz Institute for Neurobiology (LIN) for the friendly environment. I especially like to thank Heidi for her humor and the many transfections she did for me. I like to thank Romy and Annika for their always kind support in biological questions and Barbara for preparation and transfection of the slice cultures. I like to thank Juan-Carlos and José for making our office a dubious, but funny place. I further thank them for keeping up the humorous Happy Thursdays. This also includes Jan, Jeet, Rodrigo and Arthur. Very important was Yury. I thank him for his support and his stoical patience for all my statistics and physics questions. I also thank my Hiwis Hagen and Magnus, who did great work that really helped me and particular thanks to Magnus for his very helpful feedback on the structure of my thesis.

I do not want to forget to thank Jonas Fölling, who I met at a conference and with whom I had very helpful discussions on confocal imaging. I further like to thank the people that I met during the time of my PhD and who had some time for valuable practical and scientific discussions. This includes Dr. Gerhard Haunert (BFi OPTiLAS), Dr. Andre Zeug (Hannover Medical School), Prof. Norbert Gaffke (OvGU Magdeburg), Prof. Rainer Heintzmann (FSU Jena) and Christoph Cremer (RKU Heidelberg).

Last but not least, I like to thank my family. I thank my parents for always being there for me when I needed them and my sister Ann and my grandma Antonia for never asking me when I will finally submit my thesis. The same is true for my beloved little boy Olli, who brightens every moment we spend together.

CONTENTS

INTRODUCTION

"In what has become known as nanoscopy, scientists visualize the pathways of individual molecules inside living cells. They can see how molecules create synapses between nerve cells in the brain; they can track proteins involved in Parkinson's, Alzheimer's and Huntington's diseases as they aggregate; they follow individual proteins in fertilized eggs as these divide into embryos." [1]

Only recently, such amazing insides into living organisms have been made available by so called super-resolution techniques. They allow to circumvent the physical limitation established by Ernst Abbe, stating that conventional optical microscopes are unable to resolve structures that are less than $\sim 200\ nm$ apart. This in turn now enables the investigation of organisms at the molecular scale (see Fig. 1a), which has so far been reserved to techniques like electron microscopy. The term nanoscopy has been established to emphasize the advancement into the nanoscale using light. Besides the obvious improvement in resolution, the key advantage of super-resolution techniques is their ability to image living organisms. They maintain the viability of the specimen under investigation. In contrast, electron microscopy requires fixation of the samples. Consequently, investigation of the functioning of organisms is now possible with so far unattainable directness, and this has just recently been appreciated by awarding the Nobel Prize to those that pioneered the development of super-resolution techniques.

Although super-resolution techniques have seen ongoing improvement during the last few years, research had predominantly focused on increasing the available resolution. This has indeed lead to images with formerly unachievable insights into neuronal structures (see Fig. 1b), but there are still shortcomings with respect to the intended investigation of how organisms function at the molecular level.

Most prominently, this is the still relatively low temporal resolution that is in the range of seconds and prevents the analysis of fast molecular processes. Lately, this issue have been receiving increasing attention, but the presented technical solutions are generally proprietary and tend to be technically more and more complex.

Next to their instrumental complexity, such techniques rely on specific experimental conditions. As a result, fixed samples or isolated systems like primary cell cultures are still the primary environment under investigation. Analyses in less artificial systems like organotypic brain slices are of high interest, since they are expected to yield biologically more relevant results.

However, present methods for complex tissues are based on manual and often time-consuming experimental procedures. This is likely to result in subjective findings that are hardly reproducible. It further impedes the creation of robust statistics and biologically relevant results since the viability of the samples deteriorates quickly with time.

As a consequence, automatized and routine procedures that at the same time maintain the viability of the samples are nowadays still unavailable for complex biological systems.

---

1 "The Nobel Prize in Chemistry 2014 - Press Release". Nobelprize.org. Nobel Media AB 2014. Web. 12 Nov 2014. http://www.nobelprize.org/nobel_prizes/chemistry/laureates/2014/press.html
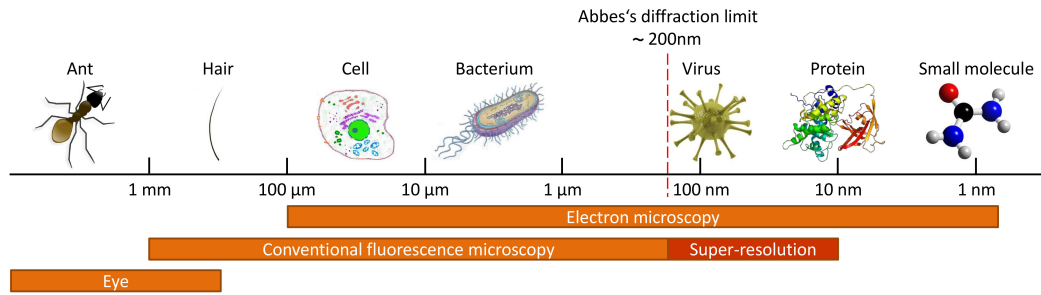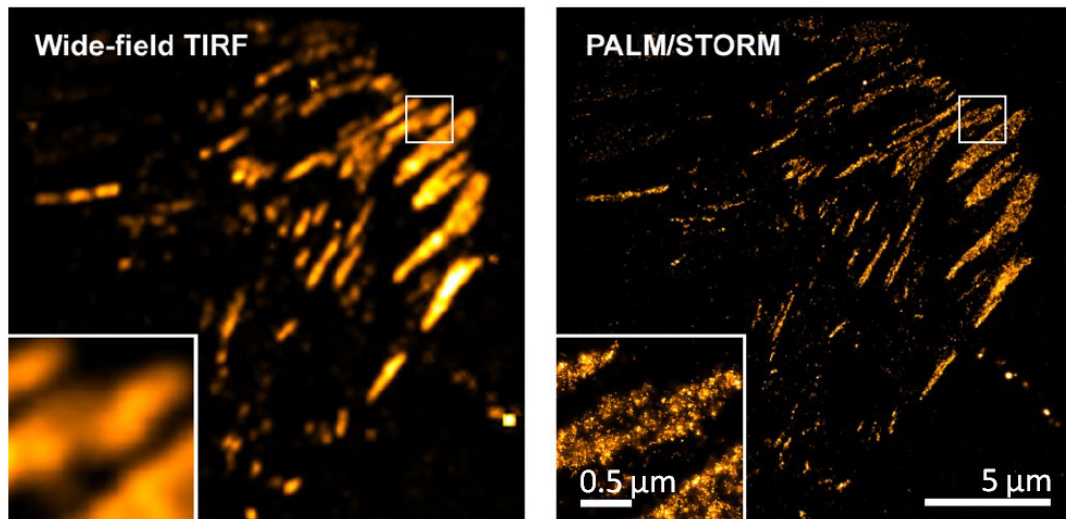
Figure 1: (a) Illustration of the size of several biological structures with respect to Abbes's diffraction limit and available imaging techniques. (b) Conventional fluorescence and the corresponding (c) super-resolution image of labeled adhesion complexes at the surface of a Hep G2 cell. (Adapted from Schermelleh et al. 2010, originally published in The Journal of Cell Biology, doi: 10.1083/jcb.201002018.)

1.1 OBJECTIVES

The present work is embedded in the study of the functioning of neurons at the molecular level and focuses on neuronal signal transmission. Investigation of molecular processes is fundamental for understanding how higher brain functions like perception, behavior, or learning and memory are accomplished. Moreover, their understanding can often directly be used to foster clinical developments such as target specific medication.

In order to support such analyses at the molecular level three main subjects are of utmost importance. They are illustrated in Fig. 2. (1) scientists have to be enabled to determine the motion of individual neuronal molecules. (2) individual synaptic activity has to be detectable to investigate how molecular dynamics modulate signal transmission. And (3), the underlying neuronal structure has to be known for correlation of the measured molecular processes with neuronal compartments.
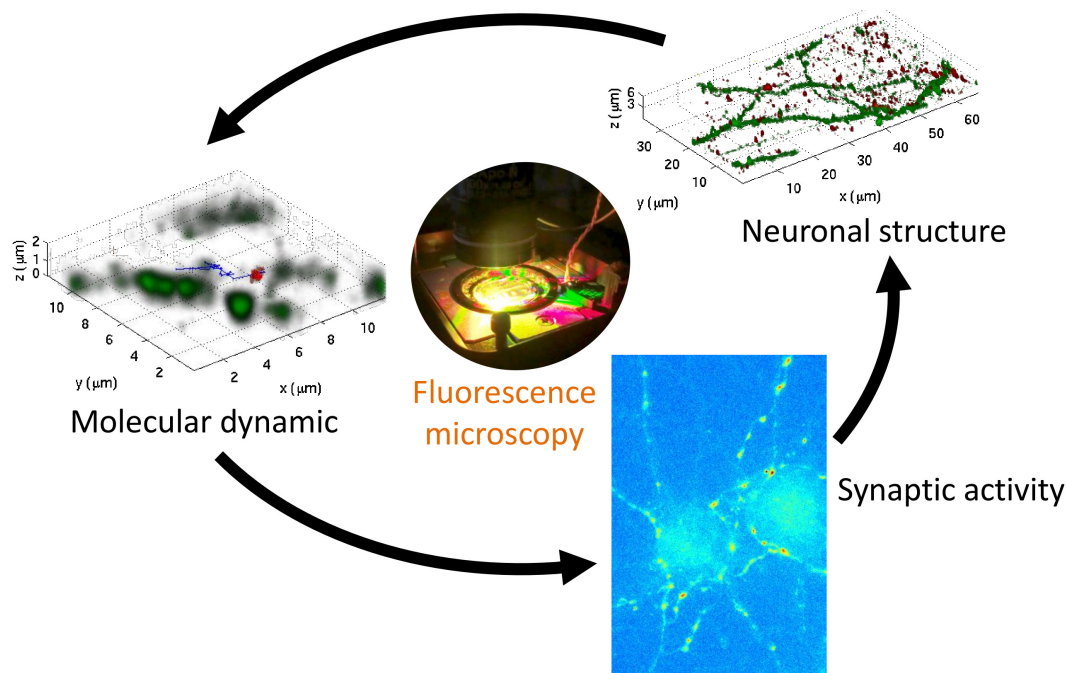
Figure 2: Illustration of the three main subjects that require analysis tools to investigate the functioning of neurons.

The thesis at hand focuses on the first two subjects. Its overall objective is the facilitation of the combined analysis of molecular diffusion parameters and neuronal activity in complex living samples.

Since such analyses take place at the molecular level and require accuracies of only a few nanometers, the technical requirements are similar to those of super-resolution techniques. Consequently, some of their principal ideas have been borrowed, but it was not intended to develop a new super-resolution technique. The focus was set on analyzing fast dynamic processes in nanoscale compartments rather than maximizing the available resolution. Apart from these general objectives, there are further specific demands of the two individual subjects.

At present, analyses of molecular dynamics have mainly been conducted in isolated systems. The obtained results may then lead to misinterpretation of signaling events owing to the limited number of molecular interaction partners (Dustin and Depoil 2011, Chan et al. 1991). Moreover, only the two-dimensional (2D) movement is typically observed for molecular dynamics analyses (Sibarita 2014, Triller and Choquet 2008). It is therefore very important to prove that correct 2D dynamics parameters can be obtained in compact complex samples (Objective 1.1).

Since neuronal compartments are inherently three-dimensional (3D) structures and molecular motion does not solely take place at the focal plane of the microscope, 2D analyses underestimate the true diffusion parameters (Renner et al. 2011) and 3D particle localization is required.

However, 3D analyses in thick complex samples are still a major challenge since the optical properties in the sample vary as functions of the imaging depth. Therefore, features of the point spread function (PSF), which are exploited for computation of 3D molecule positions, do also vary.

Current approaches are unable to automatically adjust to the varying optical conditions. Instead, these effects are either ignored, or time-consuming manual calibration procedures have to be conducted prior to each individual acquisition. The major challenge for a 3D analysis procedure is the automatic adjustment to the depth-dependent optical aberrations of the PSF without additional user interaction (Objective 1.2).

The following side conditions have to be met: molecular positions shall be determined with spatial accuracies of less than 100 nm in order to fulfill tight molecular interaction requirements at molecular compartments (Objective 1.3). The temporal resolution shall be at least 30 Hz, so that subpopulations can be differentiated in nanoscale compartments based on their diffusion (Objective 1.4). The imaging configuration should be relatively simple, so that such analyses may become widely available (Objective 1.5). Finally, the complexity of the experimental procedure should be as low as possible (Objective 1.6). If the technique is routinely applicable and acquisitions can immediately be started, the viability of the specimen can be maintained during the experiment and the results become reproducible.

In order to detect individual neuronal activity, an optical reporter molecule is used. It changes its fluorescence in correlation to the alteration of an intracellular parameter, which indicates activity.

The available computational procedures for the detection of single synaptic events have in common that they require manual interaction. As a result, they are partially subjective: so commonly, neurobiologists evoke single neuronal signals by image-locked electrical stimulation. Small regions with in-focus synapses are then manually selected, and difference images are calculated at the known time of stimulation to analyze intensity responses.

The current situation has shortcomings in two different directions: First, the computational support is very basic, and hence a completely automated approach is required (Objective 2.1). There is to date no automated procedure designed specifically for the detection of individual synaptic activity that goes beyond simple amplitude thresholding (AT). Furthermore, spontaneous activity has yet not been analyzed although this is of utmost importance for the identification of how molecular dynamics modulate synaptic signal transmission. Therefore, the detection of spontaneous activity is a major demand (Objective 2.2).

There are further side challenges that have to be overcome: owing to their representation of stochastic neuronal processes, the shapes of the optical signals are complex and subject to strong variation. The method has to address the fact that it cannot rely on a single pre-defined shape (Objective 2.3). Finally, the detection has to be robust to varying signal strengths and signal-to-noise ratios (SNRs) (Objective 2.4). In order to yield biologically relevant and unbiased results, activity must be detected over a large field of view including synapses independently of their strength of activity or number of involved molecules.

1.2 STRUCTURE

This thesis is structured as follows. Chapter 2 provides the relevant neurobiological knowledge covering the principal functioning of neurons at the molecular level with focus on the principles of neuronal signalling. Furthermore, the variable nature of signal

transmission and its importance for higher brain functions are introduced, providing the neurobiological motivation for the developments of this thesis.

Chapter 3 is dedicated to the fundamentals of optical microscopy. Since the capabilities of optical microscopy are relevant for the development of analysis tools, this technique is introduced in greater detail. The fundamentals of fluorescence microscopy (FM) and what can be expected from this technique are introduced first. Afterwards, standard imaging configurations as well as the recent developments towards super-resolution are explained.

Chapter 4 covers the first main contribution of this thesis. It presents a method that facilitates fast 3D molecular dynamic analyses in brain slices. At first, single-particle tracking (SPT) is introduced as the most suitable technique and the available readout is described. This is followed by a presentation of the related works on 3D SPT. Furthermore, it is proven that the derivation of diffusion parameters is feasible in brain slices. The main part covers the developed workflow for 3D SPT in brain slices. The focus is on the particle localization and the online calibration to the experienced optical aberrations. The proposed methods are evaluated on synthetic and real data. For the online calibration method, it also includes the analysis of intermediate results, robustness tests as well as the assessment of the impact on the readout for molecular dynamics. The chapter concludes with a discussion of the results and the remaining challenges.

Chapter 5 presents the second major contribution. A method for the automatic detection of individual synaptic activity is presented. This chapter is organized in similar manner as the former: first, the optimal optical reporter for that task is selected, its available readout is described, and the related works on peak detection are presented. Next, the proposed wavelet-based method is explained and evaluated. Again, the evaluation is done on synthetic and real data. The results are individually discussed and possible future developments are outlined.

Chapter 6 concludes the contents of this thesis and discusses the individual results with respect to their combined application.

NEUROBIOLOGICAL BACKGROUND

In neuroscience the brain is studied at different levels of abstraction. The first section presents the functional view on the brain. Since the present work is integrated at the molecular level, the second section introduces the neuron and is followed by a detailed description of neuronal signaling at the molecular scale. The final section then provides an insight into the variable nature of signal transmission, which is believed to be an important foundation for higher brain functions.

2.1 THE BRAIN IS ORGANIZED IN FUNCTIONAL UNITS

The brain is the central part of the nervous system. It processes sensory information, mediates behavior, and enables learning and memory. In order to fulfill these tasks the brain can conceptionally be thought of as being organized by means of functional units (Shepherd 1994). These are structural entities with specific functionality. Their structural basis is provided by cells, but their functionality is formed on different levels of organization. According to Shepherd 1994, there are five principle hierarchies whose scale and complexity increases up to the highest level.

At the highest abstraction level the fulfillment of tasks is represented by means of functional pathways. This includes the sensory and central processing as well as the motor system. At the second level each system is build of cells that are organized in networks. This creates local circuits that are necessary to receive, process, and output information between the systems.

The nervous system has two major classes of cells: glial cells and neurons (Kandel et al. 2013). Glial cells support neurons by providing structure, separation, and undertaking vital tasks. They are not directly involved in information processing. In contrast, neurons are the primary signaling units and build the basis of local circuits at the third abstraction level. Each neuron creates a characteristic type of activity and integrates it with the input of other neurons. In order to communicate, neurons use synapses as their contact sites. These synapses arrange to microcircuits at each neuron, which creates specific activity and connectivity patterns that are the foundation for complex information processing.

The next level in the hierarchy is the molecular level. It considers the interplay of signaling molecules in order to render signal transmission at and between neurons possible. The lowest abstraction is the genetic level, where the mechanisms for encoding and expression of molecules are present.

2.2 NEURONS

Neurons are electrically excitable cells that transmit and process information and interact with other neurons. Since the basic principles of operation are similar for all neurons, it is the way they are interconnected that enables the brain to accomplish its complex tasks (Kandel et al. 2013). It is the key principle of brain function that informa-

tion is not determined by the type of signals, but instead by the pathways the signals travel.

This and the next section summarize fundamental knowledge about the physiology of neurons. They are based on the comprehensive textbooks by Kandel et al. 2013, Galizia and Lledo 2013 and Shepherd 1994.

2.2.1 Anatomy and Principal Function

Fig. 3 presents the structural components of a typical neuron. Although neurons vary significantly in form, their major components are the same. Neurons can be morphologically defined by the cell body, the processes that are called neurites, and the synapses.
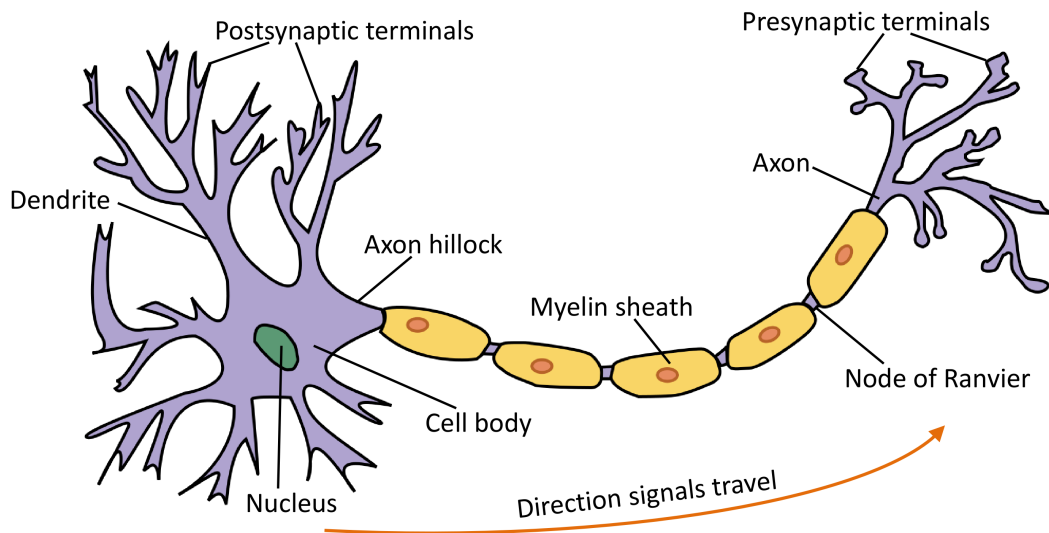
Figure 3: Anatomy of a neuron. (Adapted from `http://commons.wikimedia.org/wiki/File:Derived_Neuron_schema_with_no_labels.svg`.)

The cell body is a blob-like structure and the metabolic center of the cell. It contains organelles like the nucleus, the endoplasmic reticulum, the mitochondria, and the Golgi apparatus. The nucleus contains the deoxyribonucleic acid (DNA) that is the carrier of the genetic information of the cell. It encodes which molecules are to be synthesized. The most important functions of the organelles comprise DNA replication, protein synthesis, and distribution as well as energy supply.

Neurites are tree-like structures that reach out of the cell body in order to connect with other neurons. Their major task is signal transduction from and to other neurons. They exist in two forms: the dendrites and the axon. Dendrites receive and the axon sends signals to other neurons. Dendrites are usually more branchy, and a neuron may have several of them, whereas there is usually only a single axon. The axon emerges from the axon hillock, which morphologically belongs to the cell body and is the origin of the signals of a neuron. The axon is additionally wrapped by the myelin sheath. It electrically isolates the axon and increases the speed and reliability with which signals are conducted. The myelin sheath is periodically interrupted by uninsulated nodes of Ranvier that regenerate the signals.

Synapses are the contact points between neurons that transmit signals. They consist of a pre- and a postsynaptic site. The presynaptic terminals reside at the fine branches at the end of an axon, and postsynaptic terminals are located at dendrites.

The shape of a neuron is provided by the cytoskeleton. It fills the neuron and consists of filamentous structures responsible for cell stability and motility. Furthermore, they organize the transport of molecules within the cell. The neuron is finally bound by the cell membrane, whose major task, next to retaining the interior of the cell, is the actual signal transduction.

2.2.2 *Principle of Operation*

Signaling in neurons is mainly based on electrical properties of the cell membrane. The cell membrane maintains an electrical potential difference between the inside and the outside of cells. This so called membrane potential results from unequal distributions of ions across the membrane. At rest, the potential is ~ -65 mV, seen from the extracellular space. Temporal local changes in polarization that spread along the membrane then serve as the neuronal signaling mechanism.

An important principle of neuronal signaling is that signals typically travel in one direction within a neuron. That is, they spread from the postsynaptic sites along the dendrites, are integrated at the axon hillock, and the resulting signal is forwarded along the axon to the presynaptic terminals (see Fig. 3).

Neuronal signaling starts with signals from other neurons that lead to local potential changes at the involved postsynaptic terminals. These so called synaptic potentials may have reduced or increased potential and degrade back to the resting potential over distance and time. Because they spread, they add up at all positions of the dendrites and the cell body. If the combined potential reaches a certain threshold, this results in a rapid inversion of the membrane potential, which usually happens at the axon hillock.

The resulting action potential (AP) is send to all presynaptic terminals and may in turn trigger synaptic potentials at the connected neurons. Synaptic signal transmission may proceed via direct electrical transmission or chemically by releasing neurotransmitters.

All in all, the neuron operates as an integrative component that adds up the incoming signals of many other neurons. Then it creates a binary decision in form of an AP that in turn represents the input to other neurons.

2.3 NEURONAL SIGNALING

This section provides an inside into neuronal signaling at the molecular level. It covers the signal transduction in the cell membrane and the signal transmission at synapses. Since chemical synapses are the major structure for neuronal communication in the brain and are thought to be crucial for learning and memory, only they will be considered.

2.3.1 *Signal Transduction in the Cell Membrane*

The cell membrane is a 6-8 nm thick lipid bilayer that is almost impermeable to metabolites and ions (see Fig. 4a). Therefore, neurons can maintain different concentrations of ions across the membrane. Na^+, Cl^-, K^+, and organic anions A^- are most significant for the resting potential.

In order to generate membrane potentials, specific transmembrane proteins like ion channels and ion pumps, that span across the bilayer, are of utmost importance. They are able to conduct specific ions through the membrane and therefore annul the impermeability. Channels are passive conductors that allow ions to pass the membrane along a gradient, whereas pumps are active transporters that consume energy to transport ions against a gradient. Both types involve conformational changes that may happen in response to electrical, chemical, or mechanical signals. This switching between conformational states is called gating.

There are two principal gradients: the chemical and the electrical gradient. Although the electrical gradient may be zero across the membrane, there may still be a chemical gradient caused by different concentrations of individual ions. Since both, ion channels and pumps, exist for specific ions, also passive channels can create a potential difference by conducting only a certain type of ions along their chemical gradient. Both types of gradients then compensate at a certain level and a resting potential is maintained. Over time this may lead to an equilibrium without gradients. Therefore, active ion pumps transport ions against their chemical gradient, and the resting potential can be maintained in the long run.
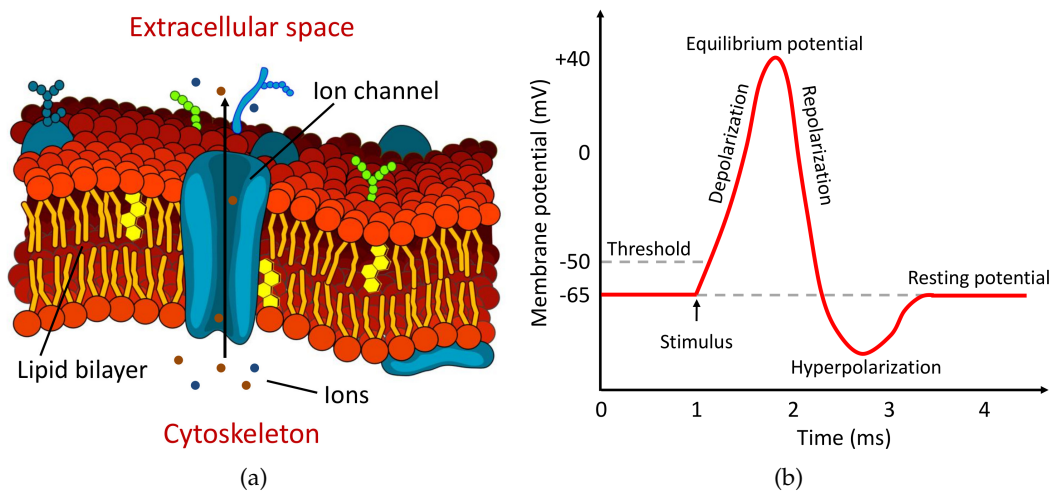
Figure 4: (a) Schematic representation of the cell membrane. (Adapted from `http://commons.wikimedia.org/wiki/File:Kanalprotein_01.png`.) (b) Typical course of an AP.

If the gating of specific ion channels is triggered so that some kind of ions pass the membrane more easily, then the equilibrium may be maintained at another electrical potential. Exactly that happens when signals are received at the postsynaptic terminals. The individual deviations in the resting potential are themselves very small, but their sum may yield very large deviations.

In order to evoke an AP the presence of Na$^+$ channels is crucial. They concentrate preferentially at the axon hillock. If a sufficient number of Na$^+$ channels open, the membrane potential may eventually pass the threshold of ~ -50 mV. This results in a chain reaction where more and more Na$^+$ channels are opened as a result of the change in membrane potential. In consequence, the influx of Na$^+$ exceeds that of other ions, and the membrane depolarizes extremely rapidly to the equilibrium potential of ~ 40 mV (see Fig. 4b).

This equilibrium lasts only for less than 1 ms. The membrane repolarizes quickly, owing to the inactivation of Na$^+$ channels and the delayed activation of K$^+$ channels that act compensating. As a result of the delayed K$^+$ channel response the depolarization is followed by a short period of hyperpolarization. This is also indicated in Fig. 4b. It decreases the likelihood for a second immediate AP. The course of an AP is very stereotyped, and this process is evoked in an all-or-none fashion as soon as the potential threshold is reached.

After initiation of an AP it is further conducted along the axon by opening of adjacent ion channels as a result of the local potential change. This is then followed by depolarization of adjacent parts of the membrane. This way an AP is actively forwarded without loss of strength. Owing to the subsequent hyperpolarization period APs spread only in one direction: from the axon hillock to the presynaptic terminals. AP forwarding thus stands in contrast to the pure passive conduction of synaptic potentials that happen below the potential threshold. They spread in both directions and degrade over distance and time.

2.3.2 *Signal Transmission at Chemical Synapses*

Chemical synapses strongly vary in shape and size and have diameters in the range of several hundred nanometers. They are composed of a pre- and a postsynaptic terminal that are separated by a synaptic cleft of width $\sim 20\text{-}40$ nm. Fig. 5a presents an electron micrograph of an exemplary synapse.

Synaptic transmission is based on two separate processes: neurotransmitter release at the presynaptic terminal and postsynaptic potential creation by neurotransmitter recognition. Chemical synapses convert originally electrical signals into chemical signals and vice versa in order to transmit signals between neurons.

The first half of the transmission process involves the release of neurotransmitters from synaptic vesicles into the synaptic cleft. Neurotransmitters are biochemical messengers that are synthesized in the cell body and the presynaptic terminals. They are encapsulated in vesicles that contain several thousand of them. Vesicles themselves are ovoid structures with a diameter of ~ 40 nm, and each synaptic terminal hosts about 100-200 copies. They are composed of various vesicle proteins. The most important proteins and their average copy numbers are presented in Fig. 5b. In order to release neurotransmitters, vesicles fuse with the cell membrane at the so called active zone that has a diameter of $\sim 200\text{-}500$ nm. These components are also observable in Fig. 5a.

The typical process that finally leads to vesicle fusion with the membrane is illustrated in Fig. 6. The arrival of an AP at the postsynaptic terminal opens Ca^{2+} channels that are concentrated at the active zone. This results in an influx of Ca^{2+} that bind to Ca^{2+} sensors at the vesicle and in turn trigger the formation of a so called SNARE complex. It mediates the fusion of the vesicle membrane with the cell membrane by

(a)   (b)
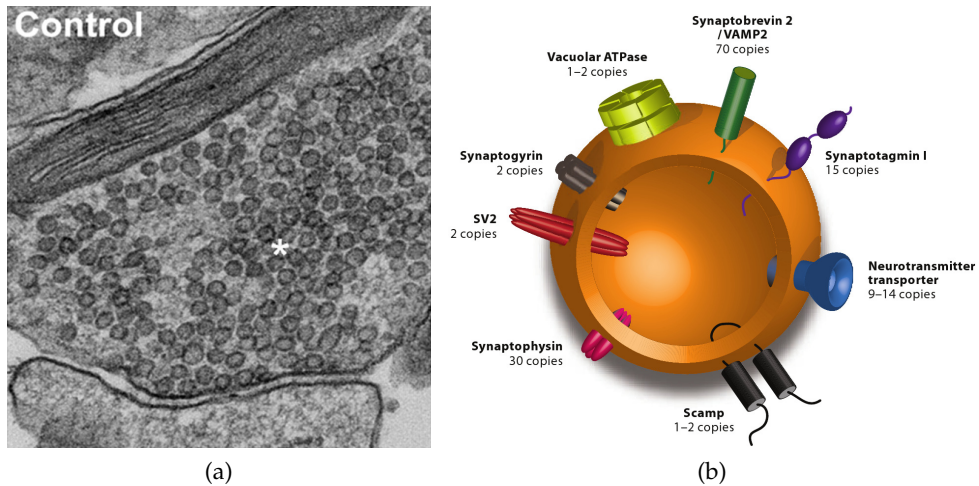
Figure 5: (a) Electron micrograph of a synapse. The synaptic cleft separates the pre- (on top) and the postsynaptic terminal. The presynaptic terminal contains lots of ovoid vesicles. The active zone comprises the region at the synaptic cleft, where vesicles dock to the presynaptic membrane. (Reprinted from Lou et al. 2012, copyright (2012) National Academy of Sciences, USA.) (b) Important vesicle proteins and their average copy numbers. (Reprinted from Dittman and Ryan 2009, originally published in Annual Reviews.)

biochemical interaction of vesicle and membrane proteins. Vesicle fusion is termed exocytosis and turns the inside of vesicles to the outside of the presynaptic terminal, so that the contained neurotransmitters are released into the synaptic cleft. During subsequent endocytosis, vesicles are retrieved from the membrane. Afterwards they are recycled, thus, take up new neurotransmitters in order to be again available for synaptic signal transmission.
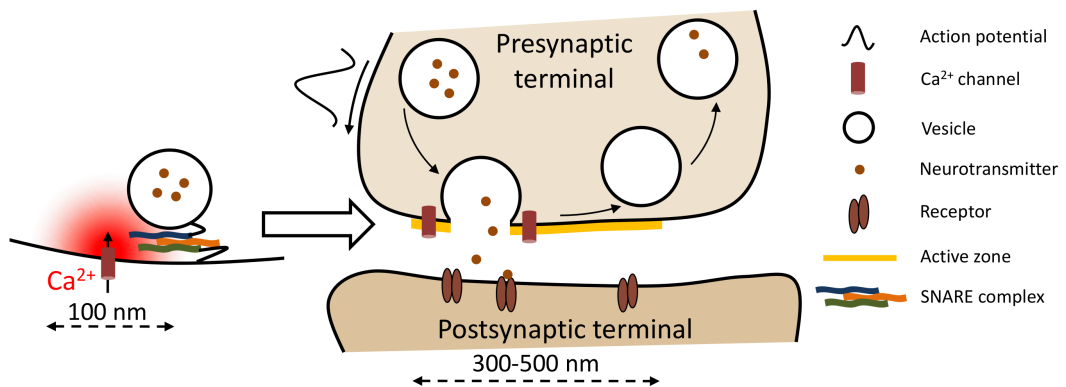
Figure 6: Synaptic signal transmission. The illustration focuses on the first half of the transmission process.

The released neurotransmitters diffuse through the synaptic cleft and may be recognized by postsynaptic receptors that initiate the second half of the signal transmission. These transmembrane receptors are located directly opposite the active zone in a region called postsynaptic density. They gate postsynaptic ion channels either directly or indirectly. Ionotropic receptors have binding sites for neurotransmitters and form their own ion conducting pore, whereas metabotropic receptors use intracellular signalling

molecules in order to gate ion channels biochemically. Direct gating is much faster, but both ways result in the creation of synaptic potentials.

The number of neurotransmitters that are received at the postsynaptic site then defines the strength of the synaptic potential deviation. In contrast, it is primarily the type of postsynaptic ion channels that decides whether the signal acts excitatory (reduced membrane potential) or inhibitory (increased membrane potential). The overall process of synaptic transmission proceeds in less than 1 ms.

2.4 THE VARIABLE NATURE OF SYNAPTIC SIGNAL TRANSMISSION

The principles of synaptic signal transmission were described in the previous sections. However, in reality the involved processes are subject to strong variability. This variability is the subject of the current section.

2.4.1 *Synaptic Plasticity*

Synaptic plasticity is the activity dependent change of synaptic strength (Kandel et al. 2013). This means that depending on the usage of a synapse the strength of the generated postsynaptic potential, that is initiated by an AP, is subject to strong variability. The induced changes in synaptic strength may persist over different time scales (Abbott and Regehr 2004). Changes over milliseconds to minutes are referred to as short-term, but if they last hours or even longer, they are referred to as long-term plasticity. Short-term plasticity is generally considered as being important for computational functions in neuronal networks, whereas long-term plasticity is believed to be an important foundation for memory, learning, and development.

The ability to adjust the synaptic strength at the molecular level can be made clear by consideration of a synapse that was actively used and hence still exhibits high Ca^{2+} concentration. It is then very likely that the next AP results in more vesicles being fused as it would be the case without prior active usage. The buffered Ca^{2+} can be considered as the simplest form of molecular memory since it "reminds" the importance of a certain connection. This supports the understanding of the brain as a device that determines information by the pathways its signals travel.

2.4.2 *Influence of Molecular Dynamics on Synaptic Strength*

The current strength of a synapse is mainly defined by the amount of fused vesicles at the presynaptic terminal as well as the amplitude and timing of the neurotransmitter-induced postsynaptic potential (Ribrault et al. 2011). The underlying molecular conditions that have to be met in order to achieve high transmission efficiency, and whose compliance varies during synaptic plasticity, are manifold.

So it is important for the geometry of the synaptic cleft that the active zone and the postsynaptic density are located close and opposite of each other (Freche et al. 2011). Also, Ca^{2+} channels and vesicles must be in close proximity, so that the Ca^{2+} influx reliably triggers vesicle fusion. The number of Ca^{2+} is expected to directly influence the number of fused vesicles (Bennett et al. 2000). These ions have to diffuse to the vesicles, but are buffered quickly (see Fig. 6). Therefore, the Ca^{2+} concentration is sufficient

only within a distance of tens of nanometers to a Ca^{2+} channel (Burnashev and Rozov 2005, Schneggenburger and Neher 2005). Similarly, the number of arriving neurotransmitters at the postsynaptic side (McAllister and Stevens 2000), and the concentration of postsynaptic neurotransmitter receptors (Heine et al. 2008) considerably influences the efficiency of synaptic transmission.

However, there is no specified procedure to maintain these conditions. All components involved in synaptic transmission are themselves subject to strong variability and operate stochastically. This refers to their timing as well as arrangement. So Ca^{2+} channels and postsynaptic receptors exhibit stochastic opening and closing behavior (Traynelisa and Jaramillo 1998). This means that independently of a signal a variable numbers of channels and receptors are already open. This is caused by their random conformational changes and varying opening times. If a channel is already open, an additional signal will therefore not increase the ion influx.

Similarly, the arrangement is driven by stochastic motion called molecular diffusion. If it results solely from random collisions with other molecules, it is referred to as normal diffusion respectively Brownian motion (Gerrow and Triller 2010). This is the actual motion Ca^{2+} or neurotransmitters undergo when diffusing to their destinations. However, Ca^{2+} channels and receptors that are integrated into the cell membrane are not only subject to Brownian motion. Their diffusion is impeded by interaction with other transmembrane proteins or confined through the membrane skeleton that partitions the entire membrane into 40-300 nm diameter compartments (Kusumi et al. 2012). Consequently, the position of a channel cannot be predicted just according to its inherent diffusion property.

The individual processes of synaptic signal transmission are conducted within small compartments having sizes of only a few tens of nanometers. This is because of the limited size of the active zone and the postsynaptic density. Also, the vesicle to Ca^{2+} channel interaction distance and the compartmentation of the membrane limit the range. Finally, the synapse contains only a few tens of the most important components, like Ca^{2+} channels, docked vesicles, or receptors (Ribrault et al. 2011).

With that said, it is apparent that highly specific timing and arrangement are necessary for successful signal transmission. Moreover, Ribrault et al. 2011 stated that based on their random behavior and their low average quantity, the stochastic properties of molecular events cannot be averaged. This means that the current behavior of a synapse is not predictable. The random properties of molecular events have to be considered in order to understand all contributions to the variability of synaptic transmission.

It is the focus of this thesis to develop tools for the analysis of such highly dynamic processes that modulate synaptic plasticity. Since the underlying neuronal compartments are very small, the tools have to deal with processes at the molecular scale. Furthermore, the viability of living samples has to be maintained. Both prerequisites are principally provided by FM. It is the basic technique for the developments in this thesis and is introduced in detail in the next chapter.

FLUORESCENCE MICROSCOPY

For neuroscience, FM has evolved into today's standard imaging tool. In contrast to electron microscopy that exhibits superior spatial resolution, it offers broad applicability and good compatibility with living cells. In comparison to conventional light microscopy it offers outstanding contrast as well as high specificity and sensitivity.

In the first section of this chapter the principles of FM will be reviewed in order to understand what type of information can be accessed. Also the remaining pitfalls will be addressed. The fundamental resolution limitations will be considered in the second section, because they severely hinder analyses at the molecular scale. Finally, the principles of super-resolution techniques will be introduced because the presented method borrows some of their ideas.

3.1 PRINCIPLES OF FLUORESCENCE MICROSCOPY

This section is mainly based on the fundamental optics book of Hecht 2009, the textbooks of Cox 2007, Lakowicz 2006 and Robenek 1995 as well as the edited books of Kubitscheck 2013b and Pawley 2006c on FM. First, the fundamentals of light as well as the principles of contrast and image formation are reviewed. This is followed by looking at the principal components of FM configurations and is completed with an overview of available fluorophores.

3.1.1 *Fundamentals of Light*

At the very beginning, the fundamental properties and phenomenons of light that are necessary to understand the principles of FM will be briefly reviewed. The underlying physics are for instance described in the comprehensive textbook of Hecht 2009, but are beyond the scope of this thesis.

3.1.1.1 *The Wave-Particle Duality*

To understand the functioning of modern microscopes it is important to realize that light exhibits both wave and particle properties. This is known as the wave-particle duality of light. It states that light cannot solely be described by the wave or the particle concept. It exhibits properties of both concepts depending on the type of measurement. As a consequence, it appears that light spreads in space like a wave undergoing reflection, refraction, or diffraction, and at the same time it behaves like a stream of particles during processes like absorption and emission. An everyday example are digital cameras. The digital image represents the spatial distribution of photons arriving at the sensor, but the shape of this distribution can only be deduced by the propagation of light through the camera optics as a wave.

← Increasing Frequency (f)

| 10^{24} | 10^{22} | 10^{20} | 10^{18} | 10^{16} | 10^{14} | 10^{12} | 10^{10} | 10^{8} | 10^{6} | 10^{4} | 10^{2} | 10^{0} | f(Hz) |

γ rays   X rays   UV   IR   Microwave   FM   AM   Long radio waves

Radio waves

| 10^{-16} | 10^{-14} | 10^{-12} | 10^{-10} | 10^{-8} | 10^{-6} | 10^{-4} | 10^{-2} | 10^{0} | 10^{2} | 10^{4} | 10^{6} | 10^{8} | λ (m) |

Increasing Wavelength (λ) →

Visible spectrum

380   V   450   B   495   G   570   Y   590   O   620   R   750
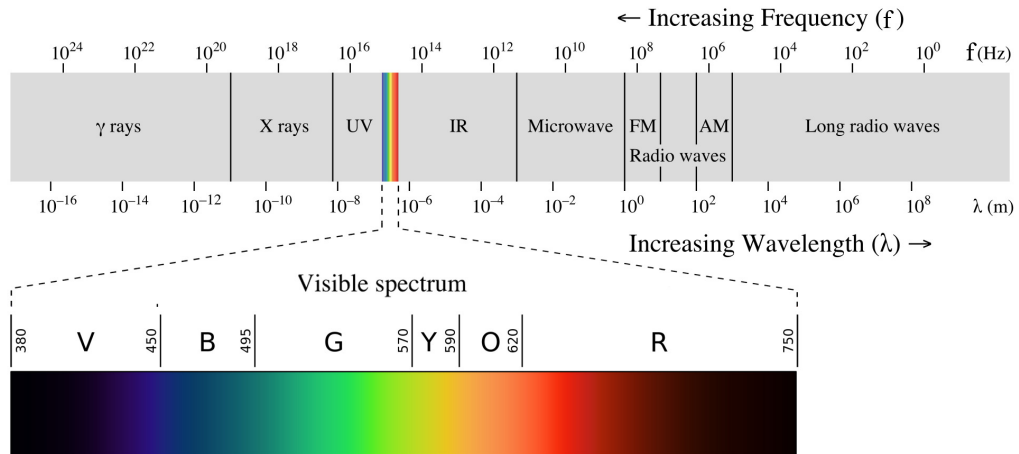
Figure 7: The visible light is part of the electromagnetic spectrum. (Reprinted from http://commons.wikimedia.org/wiki/File:EM_spectrum.svg.)

The particle nature of light is considered first. The elementary particles of light are called photons. According to Hecht 2009, they are uncharged, have no weight, travel with light speed $c \approx 300000\,km/s$ in vacuum, and are assigned with an energy:

$$E = hf. \tag{1}$$

Here, h is Planck's constant, and f denotes the frequency of the light.

Based on the frequency, this is already the link to the description of light as an electromagnetic wave. The visible light is just a small band of wavelengths ranging from 380 to 780 nm of the electromagnetic spectrum (see Fig. 7). To humans they appear as light of different colors, and the sum of all visible wavelengths is perceived as white light.

Each of these waves has a number of properties: the wavelength λ and the frequency f are the spatial respectively the temporal period of a wave. They are interrelated by the the speed c of the propagating wave:

$$c = \lambda f. \tag{2}$$

The phase φ characterizes the fraction of the period relative to the origin, and the intensity i represents the power of light per area. This correlates to the square of the amplitude A of the wave. The polarization $\vec{P}$ is the orientation of the oscillation perpendicular to the propagation of light.

3.1.1.2 *Interaction with Materials*

Now, what happens when light interacts with other materials such as the optical components in a microscope? It is important to know the type of material because some properties are specific. When light passes from vacuum through another material, the speed slows down and the intensity as well as the wavelength decrease (Hecht 2009). The amount to which a certain material decreases the speed of light is described by its

refractive index (RI) n. It is inversely proportional to the speed c_n in the material and defined by:

$$n = \frac{c}{c_n}.$$ (3)

Back in vacuum, the speed and the wavelength of light will be recovered, but the intensity remains decreased as some energy is lost owing to absorption. As an additional result, the phase right after the medium will change in dependence of n.

These changes lead to effects at the interface of two materials that are very important for the image formation process. If incident light contacts the interface to a higher indexed material with a non-zero angle Φ_i, two different effects are observed. First, some portion of light is reflected at the same angle Φ_l, and second, another fraction is propagating through the material at a smaller angle Φ_r (see Fig. 8a). The resulting angles are defined by the laws of reflection and refraction, respectively:

$$\Phi_i = \Phi_l$$ (4)

$$n_1 \sin \Phi_i = n_2 \sin \Phi_r.$$ (5)

Considering Equ. 2 and 3, it is obvious that the angle of refraction depends on the wavelength of light. This phenomenon is called dispersion and is exemplified by the colored rays in Fig. 8b.
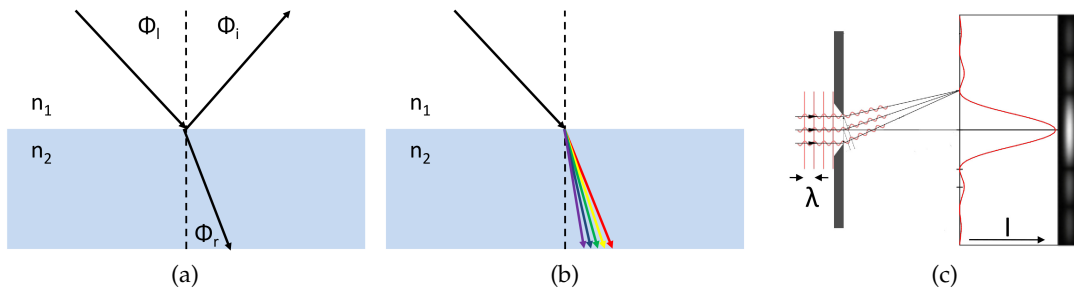
Figure 8: Important effects at the interface during light matter interaction: (a) reflection and refraction, (b) dispersion, and (c) diffraction.

The final phenomenon that needs to be considered is diffraction. It describes the deviation from the linear propagation if light passes an obstacle as light bends behind small obstacles and spreads behind small openings. Fig. 8c presents the resulting diffraction pattern if light passes a single slit of size wider then the wavelength. This pattern can be explained as the result of interfering wave fronts starting at evenly spaced positions within the slit. Next it shall be clarified how light is used in FM to make objects visible.

3.1.2 Fluorescence

In live-cell imaging, light is generally used to detect objects since it is comparatively harmless for the cells. To be detectable, objects have to be distinguishable from their surrounding, so there has to be contrast. In the previous section, important properties of light, and how they alter during interaction with matter were reviewed. These changes are the basis to produce contrast between different objects.

The human eye is sensitive to changes in intensity and wavelength, but cells are transparent and barely absorb light (Kubitscheck 2013a). Instead, they differ in their RIs, which alters the phase. This discrepancy has led to the development of various optical contrasting methods that transform phase contrast to intensity contrast. A comprehensive review is provided by Cox 2007.
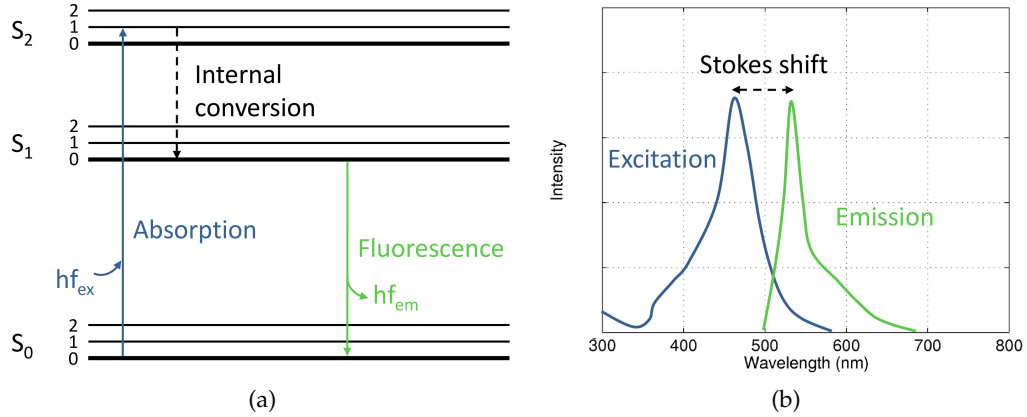
Figure 9: (a) The basic Jablonski diagram illustrates the process that leads to fluorescence. (b) The Stokes shift of an exemplary excitation and emission spectrum.

Today FM has become the most basic contrasting technique. It directly introduces wavelength and intensity contrast by exploiting fluorescence. Fluorescence is the emission of light with a specific wavelength by a molecule after absorption of light with a lower wavelength (Dobrucki 2013). The energetic process that leads to fluorescence is generally described by Jablonski diagrams (Jabłoński 1931). A simplified form is illustrated in Fig. 9a.

Here, the thick lines depict the fundamental electronic energy states S_x of a molecule, and the thin lines represent the vibrational energy levels. The latter can be thought of as the temperature of electrons at each fundamental state (Cox 2007). When a molecule absorbs a photon, its energy hf_{ex} raises an electron to a higher vibrational level at S_1 or S_2 from which it rapidly returns to the lowest vibrational level at S_1. This deexcitation is called internal conversion (IC), and the energy is released as heat. Once the electron has reached the lowest vibrational level at S_1, it drops down to S_0 and releases a photon with the energy hf_{em}. Owing to the IC the emitted energy is always less than the absorbed energy, hence, the emitted photon has a longer wavelength. The resulting difference between the maxima of the excitation and the emission spectra is called Stokes shift and is depicted in Fig. 9b. Another result of the IC is that the emission spectrum is independent of the excitation wavelength. Therefore, it remains specific for a certain molecule (Lakowicz 2006).

Another important characteristic of fluorescence is that since the emission of photons are independent random events, the number of detected photons for a certain period is observed to follow a Poisson distribution (Heintzmann 2013). The probability $P(N)$ to detect N photons with a given expectation μ is:

$$P(N) = \frac{\mu^N}{N!} e^{-\mu}. \tag{6}$$

The detection variability described by this distribution is called photon or shot noise.

Basically, all cells do contain some fluorescent molecules and are therefore weakly fluorescing. This is called autofluorescence (Monici 2005). To distinguish structures of interest from autofluorescence, markers that are strongly fluorescent are employed. For simplicity, they will be referred to as fluorophores in this thesis, and their different types as well as labeling strategies are the subject of Sect. 3.1.5. It is important to recognize that the specific labeling of molecules using fluorophores allows for creation of the required contrast between objects. This fact makes FM such a valuable contrasting technique.

However, fluorescence is not a cure-all. Autofluorescence can decrease the contrast, and most fluorophores bleach over time during constant excitation; a process known as photobleaching (Diaspro et al. 2006). This limited photostability considerably degrades the contrast and limits the recording time for long-term experiments. Further, phototoxicity has to be considered. Although fluorescence is generally compatible with living cells, fluorescent molecules that undergo excitation can react with molecular oxygen causing toxic effects to cell components (Nienhaus and Nienhaus 2013). This may not only alter the cell function under consideration, but also leads to increased autofluorescence after cell death.

3.1.3 *Image Formation*

In the previous sections it was explained how light is generated in the sample and how it interacts with other materials. Now, how do refractive lenses create an image? This can be understood by constructing optical ray diagrams (Heintzmann 2013).

Fig. 10a shows the important rays at the example of a convex lens. They are required to understand the basic optical composition of typical fluorescent microscopes. The most important characteristic of any convex lens is the focal point. By definition, this is the point were all rays, parallel to the optical axis, converge after passing the lens. One differentiates between the front and the back focal point since this is true for parallel rays in both directions. The distance of a focal point to the center of the lens is defined by the focal length f, and the plane perpendicular to the optical axis at a focal point is called the focal plane. All parallel rays that enter the lens at an arbitrary angle are focused on the same spot in the focal plane. Rays passing the center of the lens are not altered in their direction. All of these paths are also retraceable, thus, for instance a ray first passing the focal point and then entering the lens proceeds parallel to the optical axis behind the lens.

Based on these geometrical rules, the image at a single convex lens is constructed by finding the intersection of rays coming from the object (see Fig. 10b). Any object O located at a distance larger than f, but smaller than $2f$ yields a magnified and inverted real image I. Any object located in the focal plane creates an image in infinity.

Based on the operating principle of single lenses, it is straightforward to construct images formed by combinations of lenses. Owing to the context of this thesis, the basic optical setting of FM is considered. The finite optics setup of classic light microscopes is reviewed by Robenek 1995. It consists of an additional convex lens that creates a further magnified virtual image from the real intermediate image so that it can be directly viewed by the human eye.
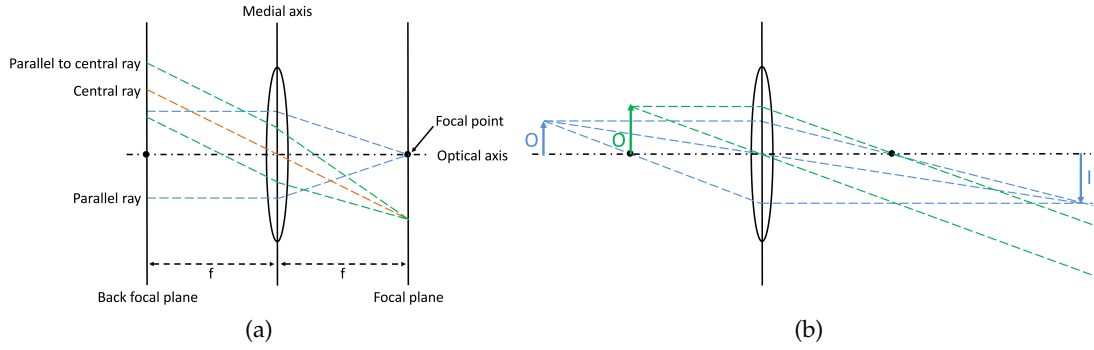
Figure 10: (a) Basic characteristics and rays of a convex lens. (b) Image formation by a convex lens.

For FM, image formation is implemented as an infinity-corrected imaging process (Kubitscheck 2013a). The basic elements are the objective and the tube lens. The corresponding ray diagram is presented in Fig. 11. In contrast to finite optics, an object must be positioned at the focal plane of the objective to form a sharp image at the image plane. The objective first creates an image in infinity, and the tube lens then focuses this image on the image plane forming a real image. The magnification M is then solely defined by the ratio of the focal lengths:

$$M = \frac{f_{tube}}{f_{obj}}. \tag{7}$$

Any off-focus object appears at the image plane with the same size as if it would be in focus, but has a blurred intensity profile.
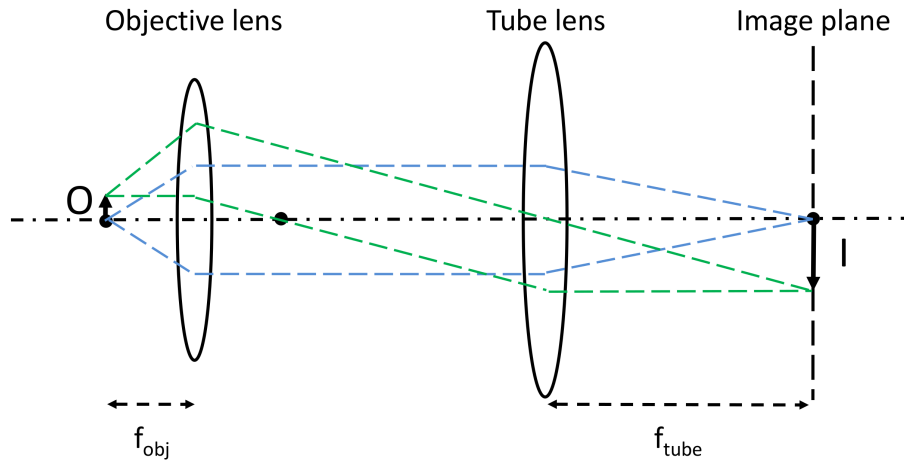
Figure 11: The infinity-corrected imaging process in FM.

This infinity-corrected setup has two important advantages for FM (Keller 2006). As the light path is parallel in the infinity space between the lenses, their distance can be varied to a certain extent. Furthermore, additional planar optical elements can be introduced without affecting the final magnification. This allows to move the objective instead of the stage to focus the image. The optical elements can then for instance be used to combine the excitation and emission light path or to differentiate wavelengths.

By now it was ignored that a lens actually consists of two refractive interfaces, and simply their medial axis was used to draw the diagrams. This simplification to thin lenses allows for getting a basic understanding of how a system is working, but ignores all imperfections that real thick lenses have. The imperfections and the resulting consequences will be covered in Sect. 3.1.4.3 and 3.2.1, respectively. An exhaustive geometrical treatment of thick lenses is provided by Hecht 2009.

After having looked at the fundamental concept of image formation, the next section introduces the principal components and their arrangement in fluorescence microscopes.

3.1.4 Principal Components

Today, epifluorescence microscopes are the most common configuration. Their principle of operation is illustrated in Fig. 12.
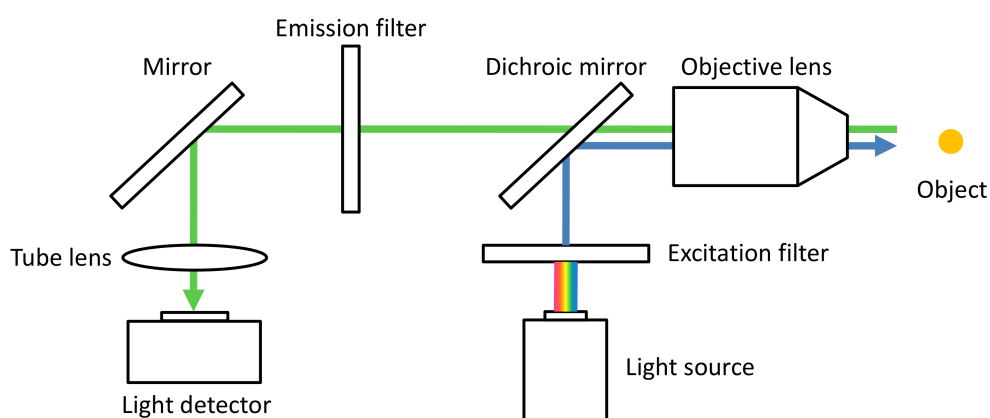
Figure 12: Scheme of the epifluorescence imaging configuration.

As it was explained in the previous section, the objective and the tube lens create an infinity space. In the epifluorescence design, it is used to insert a dichroic mirror. This allows to pass both the excitation and the emission light through the objective and has the great advantage that it is much safer for the person who conducts the experiment not to be exposed to radiation (Dobrucki 2013). The same dichroic is also used to separate excitation and emission light before image acquisition.

Microscopes that directly implement this epifluorescence configuration are commonly known as wide-field (WF) microscopes. Their field of view is homogeneously illuminated by focusing the excitation light beam into the back focal plane of the objective. Today, WF microscopes are routinely used for live-cell imaging owing to their straightforward implementation and their flexibility for accessing molecular dynamic in cell cultures. In the following, the principal components are introduced.

3.1.4.1 Light Sources

The application in FM puts distinctive requirements on excitation light sources (Nolte et al. 2006): owing to the Stokes shift they have to emit light at low wavelengths. They also need to provide high intensity to generate sufficient fluorescence, and should allow for uniform illumination of the specimen. Today, the main types of light sources are high pressure arc lamps and lasers.

Arc lamps are the most routinely used light sources (Dobrucki 2013). They provide enough intensity for live-cell imaging and are available as different types that are distinguishable in their lifetime and emission spectra. The latter is either continuous or has several sharp maxima. The selection of a certain type is therefore highly dependent on its application. Despite their popularity, they have severe limitations for quantitative microscopy since they provide non-uniform illumination, and their intensity exhibits fluctuations and diminishes within an operational time of days.

Lasers are a more costly alternative to arc lamps, but exhibit high temporal and spatial emission stability (Gratton and vandeVen 2006). They provide very specific wavelengths and achieve hence much higher intensities in their spectral region. As an additional characteristic, they emit highly collimated light beams (Axmann et al. 2013). Collimated light can be used to focus into very small regions, which is exploited in more advanced imaging configurations like they will be reviewed in Sect. 3.3. Lasers can be implemented in many different ways, and the basic types used in FM are described by Cox 2007. An exhaustive list is provided by Gratton and vandeVen 2006.

Recently, also sets of light-emitting diodes (LEDs) have become available (Dobrucki 2013). They are comparatively cheap and are not damaged by repeated on and off switching. These properties make them a promising alternative in the future.

3.1.4.2 *Optical Filters*

Optical filters play a central role in FM. As it was emphasized in Sect. 3.1.2, FM is highly specific owing to the ability to attach fluorophores at individual molecules. However, it will be revealed in Sect. 3.1.4.4 that the majority of the image acquisition devices are sensitive to intensity, but they cannot differentiate the wavelengths. This is accomplished by filters that selectively transmit light of different wavelengths. Despite this fundamental function, they also enable correlation analyses of molecules labeled with fluorophores of different wavelengths. This expands the range of possible applications tremendously.

In the epifluorescence configuration filters are employed at three positions. First, they are used as excitation filters to selectively excite fluorophores and second, as emission filters to separate the intended fluorescence from other wavelengths. The latter is particularly important since even the reflected excitation light is often much more intense than the fluorescence (Robenek 1995). While excitation and emission filters are barrier filters that absorb light, another type, called dichroic mirrors, are special interference filters that reflect the wavelengths that are not transmitted (Cox 2007). They consist of several layers with periodically changing low and high RIs that create selective permeability and reflection by interference effects (Hecht 2009). As the third option, such dichroic mirrors are mounted at 45° in the infinity space. This allows to combine and separate the excitation and emission light paths.

To detect light as efficient as possible, the transmission properties of a set of filters have to be carefully matched. Beside the availability of standard filter blocks, various applications need specific filter configurations. Thus, excitation and emission filters are often separately exchangeable via filter wheels, and multiband dichroic mirrors are available that support several separated Stoke shifts.

3.1.4.3 *Objective Lenses*

The objective is the component mainly responsible for the image quality. So far it has been treated as a single lens, but modern objective lenses are actually very precise sequences of up to 20 lenses (Kubitscheck 2013a). This complexity is required to reduce the impact of diverse aberrations that real lenses exhibit. In contrast to the simplifications made in Sect. 3.1.3, real lenses do not focus all parallel rays exactly into the focal point. This is mainly caused by spherical and chromatic aberrations (Keller 2006, Robenek 1995). Spherical aberrations occur because curved lenses refract outer rays stronger than rays that are close to the optical axis, and chromatic aberrations are caused by dispersion. Therefore, today's objective lenses come in different classes according to the types of aberrations they reduce. A description of these objective classes is provided by Robenek 1995.

The main characteristics of objective lenses are their magnification, numerical aperture (NA), working distance as well as the immersion medium and cover slip thickness they are designed for. Infinity-corrected objective lenses already have a magnification assigned as they internally create a magnified real image that is focused in infinity by the last lens. Another important characteristic is the NA, defined as:

$$NA = n \sin \alpha. \tag{8}$$

Here, n is the RI of the immersion medium between the specimen and the objective, and α denotes half of the angular aperture. The latter represents the maximum angle with which rays from the focal point can contribute to the image (Kubitscheck 2013a). It is therefore a measure of the capability of an objective to gather light.

To achieve high image quality the NA should be as high as possible and the RIs of the objective, the immersion medium, and the specimen should match. Fig. 13 illustrates what happens if the immersion medium has a lower RI than the objective and if the RIs match. Owing to the refraction at the interface of the objective and the immersion medium, the maximum angle α with which light from the specimen can enter the objective is effectively decreased in case of a refractive index mismatch (RIM). Rays with an angle larger than α cannot reach the objective and do not contribute to the image.
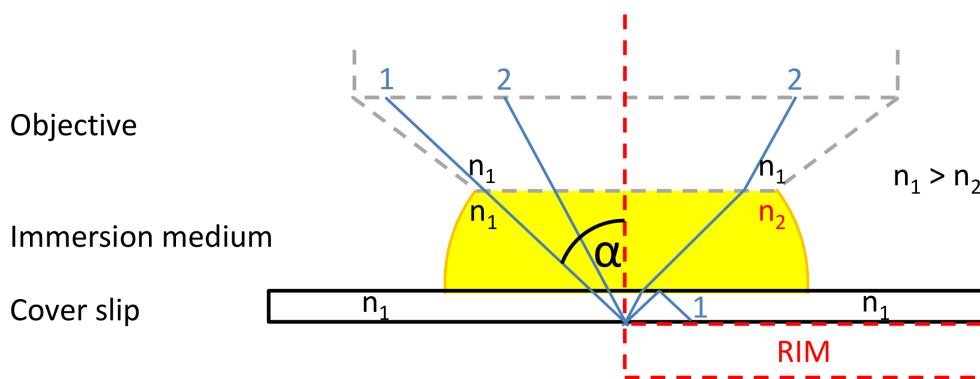

Figure 13: Light paths with and without the RIM at the interface between the objective and immersion medium. In the presence of the RIM, the maximum angle α is effectively decreased because ray 1 cannot contribute to the image.

Similar effects occur at the interface between the immersion medium and the sample if their RIs do not match. They are in detail discussed in Sect. 4.3.5. To optimize the optical conditions for the various applications in live-cell imaging, different types of objective lenses have been designed. They are either dry or immersion objective lenses and are further corrected for use with cover slips or without. The most common immersion objective lenses are designed to match water, oil, or silicone. Water and silicone immersion objective lenses are particularly useful for imaging deep into living tissue since their RIs match those experienced in samples most closely, and their working distances are high. The latter defines the distance from the physical front of the objective to the focal plane (Keller 2006). Still, it is most widely used practice to plate primary cultures on cover slips. Then high-NA oil immersion objective lenses that have been designed to match the high RI of glass can also be used and exhibit superior imaging quality at the very first micrometers within the specimen. An exhaustive list of objective characteristics and corresponding designations that have to be considered for a particular application is provided by Davidson 2013.

3.1.4.4 *Light Detectors*

Today, almost all light detectors for FM are electronic devices (Dobrucki 2013). They exploit the photoelectric effect, where electrons are emitted by materials if they are exposed to light (Hecht 2009). Such light detectors are inherently monochromatic and therefore incapable of differentiating wavelengths due to their functioning being based on the detection of photons. By incorporating filters, color detection systems can be realized, but they are either lacking speed, spatial resolution, or sensitivity (Cox 2007).

Monochromatic light detectors can be divided into point and full-field detection devices (Art 2006). Point detectors detect light without discrimination of its spatial origin, whereas full-field devices detect and spatially separate light from the whole field of view at once.

Photomultiplier tubes and avalanche photodiodes belong to the first category. They feature response times shorter than nanoseconds and single photon detection. Their quantum efficiency (QE), which describes the percentage of absorbed photons that really induce a charge, is 30 % and 90 %, respectively (Dobrucki 2013).

In comparison, full-field detectors, like charge-coupled device (CCD) respectively complementary metal-oxide-semiconductor (CMOS) cameras, exhibit high spatial resolution by composition as arrays of light-sensitive components. In analogy to digital images these components are often referred to as pixels. For CCD cameras, the pixel size is 5-30 μm (Pawley 2006a), the QE can reach 95 %, and the response time for a full image is in the range of several tens of milliseconds. CMOS cameras have similar characteristics, but are faster and have lower QEs. However, they can be produced with smaller pixel sizes allowing for an increase of the number of pixels in an array (Saurabh et al. 2012).

For the present work, electron-multiplying CCD (EMCCD) cameras have been employed because the focus is on the analysis of molecular dynamics, which requires fast observation at low light emission. Their functional principle will now be reviewed in more detail.

Fig. 14 illustrates the overall architecture of an EMCCD camera. Each individual pixel element of an array accumulates the electric charge released by the photoelectric effect.

To obtain QEs up to 95 %, its silicon layer can be thinned, and the pixels are illuminated from the back so that the electrical wiring does not absorb photons. To parallelize exposure and readout, all charges are first of all shifted from the sensor region into a covered read register. This is called frame transfer and is accomplished very fast. The charges in the read register are then shifted line by line into the serial shift register that forwards the charges to the electron multiplication register. This register consists of ~ 500 charge-coupled elements that shift the charges with a much higher transfer voltage than normal (Pawley 2006a). With this voltage shifted electrons can generate additional electrons by collision yielding a chain reaction. The probability with that an electron generates an additional one is proportional to the applied voltage and can yield an electron multiplication gain of $G_{EM} \approx 1000$. The read amplifier finally converts the charges into voltage values that are thereafter digitized to create pixel intensity values.
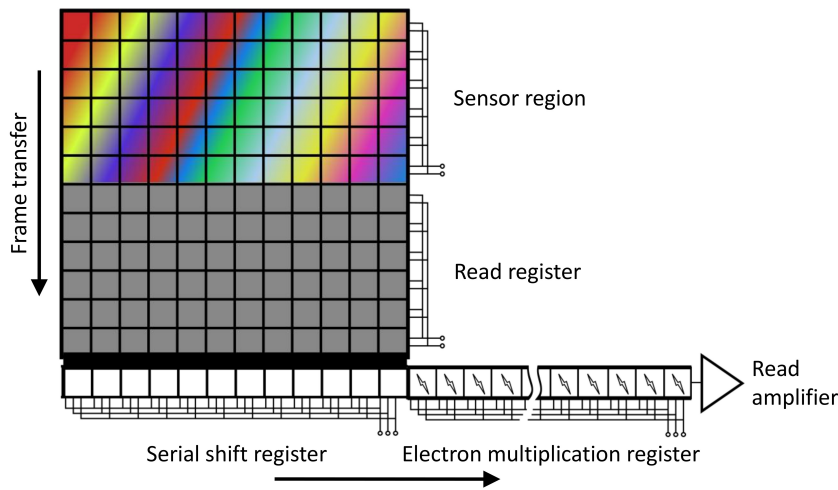
Figure 14: Schematic architecture of an EMCCD camera. (Adapted from `http://commons.wikimedia.org/wiki/File:EMCCD2_color_en.svg`.)

The significance of the electron multiplication register becomes evident when the noise sources of EMCCD cameras are considered. According to Axmann et al. 2013, the overall noise δ at a pixel generated by EMCCD cameras can be computed from all individual noise sources by:

$$\delta = \sqrt{\delta_{mult}^2 \left(\delta_{dark}^2 + \delta_{photon}^2 + \delta_{back}^2 \right) + (\delta_{read}/G_{EM})^2}. \tag{9}$$

Here, δ_{photon} is the noise inherent to the fluorescent signal, and δ_b is the background noise emerging from autofluorescence, unspecific labeling, or light scattering. Both noise sources are inherent to the application of FM and are therefore uninfluenceable by camera engineering.

In contrast, δ_{dark}, δ_{read}, and δ_{mult} originate from the camera design (Dobrucki 2013). δ_{dark} designates dark current noise that occurs at the pixel elements of the camera array and emerges from electrons that are solely created by thermal motion. By cooling the detectors down to about $-100\,°C$, which is already standard for commercial cameras, dark current noise is practically negligible. δ_{read} is the readout noise arising during amplification and digitization. It is usually specified as a fixed standard devia-

tion (SD) for each pixel independently of the actual number of measured electrons. The influence of this error can be decreased by detecting more photons, but typically only a few tens of photons per pixel are detected in live-cell experiments (Pawley 2006b). At such low detection rates the multiplication register can alternatively be used to boost the number of electrons per photon well over the readout noise. This makes it virtually negligible. However, it should only be used at low detection rates because electron multiplication is a statistical process and creates the additional noise factor $\delta_{\text{mult}} \approx \sqrt{2}$ (Robbins and Hadwen 2003). The total noise could otherwise exceed the noise of conventional CCD cameras, although they are subject to readout noise.

3.1.5 Fluorophores

The fundamental advantages of FM are mainly attributed to the exploitation of fluorescence. To make structures of interest visible above the autofluorescent background, fluorophores are used. This section reviews the main types of fluorophores and explains how they can be attached to the molecules of interest.

3.1.5.1 Types of Fluorophores

Fluorophores must first of all absorb light very efficiently and have to be very bright in their particular emission spectrum. There are further very important properties that can be divided into spectroscopic and biochemical properties (Johnson 2006). Spectroscopic properties cover the fluorophores efficiency for optical detection including excitation and emission spectrum, fluorescence quantum yield, and photostability. Biochemical properties determine the compatibility and applicability within the target environment. This includes the size and material of a fluorophore as well as its membrane permeability, binding affinity, and phototoxicity. In order to adjust the properties best for a particular experiment, a wide range of different fluorophores has been developed. According to Nienhaus and Nienhaus 2013 they can be categorized into organic dyes, nanoparticles, and fluorescent proteins (FPs). They are briefly reviewed in the following.

Organic dyes are very small (< 1 nm) planar or cyclic molecules with conjugated systems that have delocalized pi-electrons (Nienhaus and Nienhaus 2013). The traditional types are derivatives of fluorescein and rhodamine, but today newer variants like cyanine and AlexaFluor are available. They feature increased spectroscopic properties and water solubility (Tsien et al. 2006).

Nanoparticles consist of fluorescent materials whose emission wavelength is determined by the size of the particle. Traditional representatives are latex beads, but nowadays quantum dots (QDs) are preferentially used in living systems. QDs consists of a semiconductor core surrounded by an inorganic shell that improves brightness and stability and shields the toxic core (Johnson 2006). This again is encompassed by an organic coating that makes QDs water soluble.

The discovery of the green fluorescent protein (GFP) in the jellyfish Aequorea victoria was published by Shimomura et al. 1962. It consists of 238 amino acid residues, and many different variants have been further developed. Today, they cover different emission spectra and can remain in an excitable state even above room temperature

(Cox 2007). Fig. 15 provides exemplary schemes of the structure of all three categories.


QD (~30 nm)   GFP   Dye (5x)
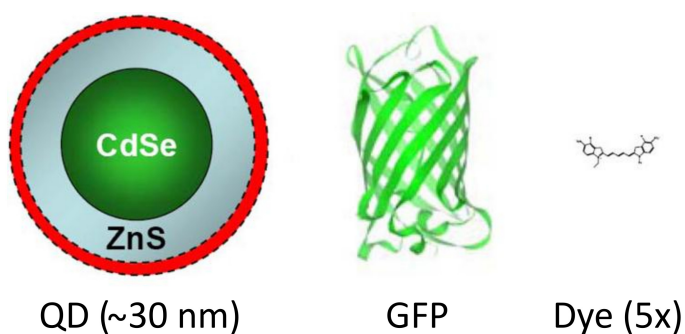
Figure 15: Schematic structure of the three different fluorophore categories. (Adapted from Martin-Palma et al. 2009, originally published in Sensors.)

The three types of fluorophores vary considerably in their properties, and a detailed tabular comparison is presented by Nienhaus and Nienhaus 2013. In summary, organic dyes and FPs have similar spectroscopic properties, but particularly QDs are outstanding in this respect. They exhibit very narrow emission spectra and Stokes shifts larger than 100 nm. This makes experiments with multiple wavelengths possible and allows for the separation of excitation and emission wavelengths. Furthermore, they barely bleach and are brighter than organic dyes and FPs because they can absorb about 100 times more photons at a comparable quantum yield. Noteworthy is also the stochastic blinking that single QDs exhibit. It can be used to ensure that only a single fluorophore is analyzed.

In terms of the biochemical properties, organic dyes and FPs have clear advantages, particularly for application in living cells. Owing to their relatively small size they are less likely to change the molecular functionality (Syková and Nicholson 2008), and they are also less toxic than QDs.

3.1.5.2 Labeling Techniques

Besides their properties, the most important aspect is how a fluorophore can be linked to the molecule of interest. This concerns the questions of how a fluorophore is transported to its target, and how specific is its binding?

FPs are inherently advantageous as the target molecule can be genetically encoded with a specific connection to selected FPs. The corresponding DNA sequence can be transfected into the cell. By transcription of this sequence, the cell expresses the fused construct itself in situ (Tsien 1998).

There are various chemical and mechanical techniques for transfection including the application of cationic lipid reagents, calcium phosphate coprecipitation, or utilization of a gene gun (Cox 2007). A decision for either method is then driven by the sample type and the required expression level in terms of the number of transfected cells respectively the number of expressed molecules within a cell. Also the tolerable cell survival rate after treatment is of importance.

While being extremely specific, it should not be neglected that using FPs may lead to overexpression of the fused protein in comparison to the so called endogenous, original protein. The level of overexpression or if the endogenous protein is even replaced

depends on how well a certain target molecule is regulated. A new construct always has to be tested for effects on the cellular functionality (Nienhaus and Nienhaus 2013).

To bind organic dyes and QDs to the molecules of interest immunostaining is most frequently employed. It is strongly related to the functioning of the human immune system and generally refers to techniques that use antibodies to specifically bind to their corresponding antigens at the target molecules (Cox 2007). To conjugate the fluorophore with the antibody, covalent bonds are established by functionalization of the fluorophore surface. This direct labeling can be very specific, but requires the creation of extra fluorophore-antibody structures for each target. Therefore, indirect labeling is used, where primary antibodies specifically bind to the target, and a secondary antibody, conjugated with the fluorophore, detects the primary antibody. This yields greater flexibility and can also be used to increase the brightness since several secondary antibodies may bind to the same primary antibody. On the downside, this may decrease specificity since one-to-one binding between molecules and fluorophores cannot be ensured.

To transport the fluorophore to the target they simply have to be added to the culture, where they approach the targets by diffusion. The number of tagged molecules has to be experimentally determined by varying the density and the incubation time. More disadvantageous is the fact that antibodies are usually too large to penetrate the cell membrane, which generally limits the application of immunostaining to extracellular molecules in living cells.

3.2 HOW FAR CAN ONE GO: LIMITS OF FM

In the last section the basic principles of FM were reviewed. It was clarified why it has emerged into the primary imaging technique for living cells: it provides images of structures in living cells with high contrast, sensitivity, and specificity. Moreover, it allows to extract functionality and dynamic by one-to-one attachment of single fluorophores to single molecules. However, does it really allow to resolve such information at the molecular scale? The first answer must be no because the spatial resolution of optical microscopes is fundamentally limited by the diffraction of light. This and other limits of FM are the topic of the present section.

3.2.1 *Diffraction Sets a Fundamental Limit on the Resolution*

In light microscopy, resolution defines the smallest spatial distance between two objects with that they can still be distinguished as two separate objects (Hecht 2009). The classical resolution limit was derived by Ernst Abbe. He established the foundations of image formation together with the calculation of optical lenses that are reasonably corrected for chromatic and spherical aberrations (Inoué 2006).

In its famous publication, Abbe 1873 derived the connection between the size of the NA and the distance between periodic line gratings so that they can be resolved. Owing to the diffraction of light at the grating, the information of the structure is only recoverable if the NA of the objective is big enough to capture at least the zeroth and first diffraction order of the resulting diffraction pattern. Since the angle between the diffraction orders increases with finer gratings, he proved that based on the limited NA

of objective lenses, the distance between two lines, so that they can be resolved, cannot be less than $\sim 200\,\mathrm{nm}$ for visible wavelengths.

In its classical definition, Abbe considered the diffraction at illuminated objects instead of the detection of self-luminous point sources like it is the case for FM. In classical light microscopy objects become detectable by altering the properties of the transmitted light. Opposed to that, objects are detected as composites of many fluorophores attached to individual molecules in FM. A fluorescence image contains the signal of many self-luminous point sources. The light of each, even infinitesimal small, point source in the focal plane of the objective is deflected at the aperture of the objective so that the point object appears with a blurred intensity profile in the image plane of the microscope. This point image is generally referred to as the PSF and describes the focusing capability of a microscope (Kubitscheck 2013a). In this purely diffraction-limited case the PSF has the shape of an Airy pattern $I_{\mathtt{Airy}}$ (Airy 1835). The intensity profile of $I_{\mathtt{Airy}}$ is depicted in Fig. 16 and consists of a blurred bright spot surrounded by iteratively dark and bright rings that fade away.

Since fluorophores are independent light sources, they emit incoherent light. Therefore, microscopes can be considered as optical systems that are linear in light intensity (Wu et al. 2008). The Airy pattern then represents the unique impulse response of the microscope, and the observed image $I(x,y)$, which contains multiple point sources, is constructed by convolution of the true objects $O(x,y)$ with the Airy pattern:

$$I(x,y) = O(x,y) * I_{\mathtt{Airy}}(x,y). \tag{10}$$

This process is depicted in Fig. 16. It is apparent that the Airy pattern degrades the resolution of the image since point sources that are too close to each other cannot be distinguished anymore.
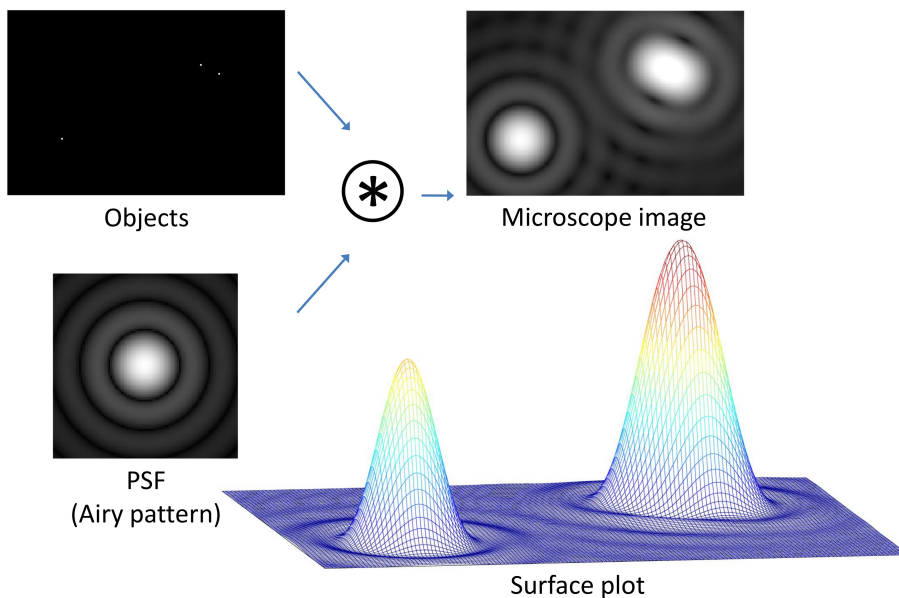

Figure 16: Illustration of the microscope image formation process.

The actual resolution is then defined by the smallest distance between two point sources under which their combined intensity distribution can be perceived as two separate distributions. At this, the so called Rayleigh criterion is commonly applied. It

states that two point sources are separable by eye if their distance corresponds to at least the radius of the inner dark ring of the Airy pattern (Kubitscheck 2013a, Inoué 2006, Rayleigh 1879). The resolution is then defined by the lateral Rayleigh distance:

$$d_R = \frac{0.61\lambda}{n \sin \alpha} = \frac{0.61\lambda}{NA_{obj}}.$$ (11)

In contrast to Abbes's definition, λ is the wavelength of the emitted light and not the illumination wavelength, but both definitions yield similar results as they attribute the resolution capability of a microscope to the NA of the objective and the wavelength of light (Best et al. 2013).

The intensity distribution of the Airy pattern can be well approximated with a 2D Gaussian function (Zhang et al. 2007b). Then the Rayleigh resolution corresponds to the full width at half maximum (FWHM) of the Gaussian. This simplifies the practical estimation of the resolution to computing the FWHM of the PSF's intensity distribution.

To define the axial resolution of a microscope, the 3D diffraction pattern of a point source has to be considered. The 3D PSF is point symmetric in the lateral direction and also symmetric above and below the focal plane along the axial axis (Kubitscheck 2013a). The x,z section together with the lateral and axial FWHM is depicted in Fig. 17. Similar to the Rayleigh criterion, the minimal axial distance d_z between two point
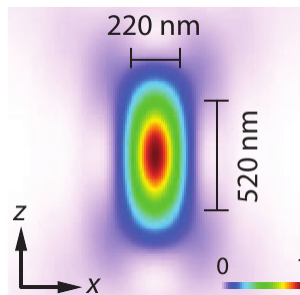
Figure 17: The x,z section of the 3D PSF. The ranges indicate the FWHM. (Reprinted from Huang et al. 2009, originally published in Annual Review of Biochemistry.)

sources is defined by the distance from the axial center to the first minimum along the axial axis (Kubitscheck 2013a, Inoué 2006):

$$d_z = \frac{2\lambda n}{NA_{obj}^2}.$$ (12)

The axial resolution is about three to four times worse than the lateral resolution.

From Equ. 11 and 12 it is apparent that the usage of wavelengths at the lower end of the visible spectrum is preferable for high-resolution applications. Using high-RI immersion mediums the resolution can be further improved. All in all, the theoretical resolution of fluorescence microscopes can approach about 200-300 nm in the lateral and about 500-700 nm in the axial direction (Huang et al. 2009).

3.2.2 *Visibility Defines the Effective Resolution*

In the last section it was shown that the imaging capability of microscopes is fundamentally limited by the diffraction of light. Resolution asks for the ability to recognize

two point sources represented by their finite size PSFs as being separate. This requires contrast. Therefore, the Rayleigh criterion may be considered as the request for 25 % contrast between the intensity of the dip between two PSFs and the intensity at their centers (Kubitscheck 2013a). It is important to understand that such pure diffraction-limited systems are ideal systems (Wu et al. 2008). In reality, chromatic and spherical lens aberrations, alignment errors, or mismatches in the RIs of the immersion medium and the sample blur the profile of the Airy pattern, and the effective resolution is reduced. Furthermore, the obtained contrast depends on the SNR, and today almost all microscope images are acquired digitally. These aspects extend the concept of resolution to the more general question of visibility (Pawley 2006a) and the more important question becomes: is it possible to recognize the contrast between two individual PSFs at Rayleigh distance in digitized images?

Digital images are created by measuring the intensity of an optical image at regular intervals in space and time (Wu et al. 2008). According to the Nyquist-Shannon sampling theorem, the original information can only be reconstructed from the digital representation if it was sampled with a frequency at least twice as high as the highest frequency in the original data (Shannon 1949, Nyquist 1928). Optical images are inherently band-limited as their smallest feature is the PSF. The size of a pixel must not exceed half of the distance defined by the Rayleigh resolution criterion yielding $FWHM_{PSF}/2$ (Pawley 2006b).

Pawley 2006b also states that even if this rule is adhered to, it might not always be possible to achieve the 25 % contrast at the Rayleigh distance between two point sources. To support that finding Fig. 18 illustrates the sampling with the Nyquist rate of an image of two point objects that are separated by d_R. Here, Fig. 18a represents the optimal situation, where the pixels sample exactly the intensity at the center of the two maxima and the valley. Since a pixel actually represents the average intensity of its total area, the contrast will be less than 25 % (see Fig. 18b). Fig. 18c finally depicts the likely situation where the pixels are not centered on the maxima and the valley. This will considerably reduce the contrast and may even eliminate it.
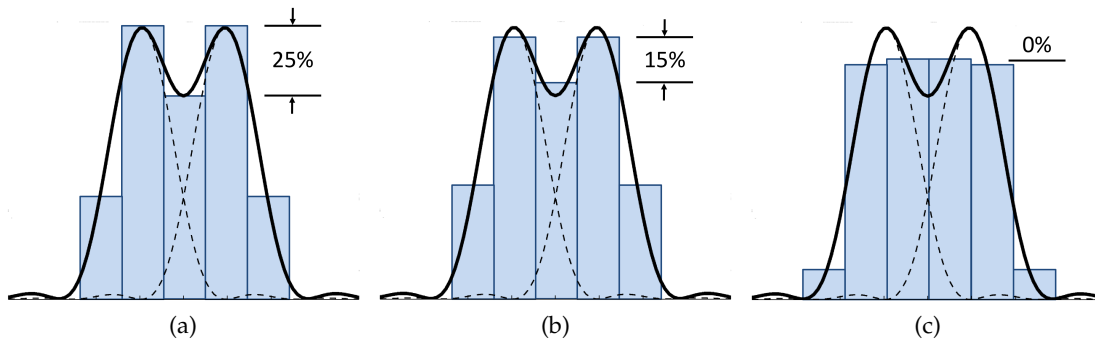
Figure 18: Illustration of Nyquist sampling using the (a) center or the (b) average intensity and (c) if the pixels are not well located with respect to the particles. The black line denotes the combined intensity distribution of two particles and the dashed lines the individual ones. The blue bars represent the pixels and the percents the available contrast.

Although Pawley 2006b acknowledges that by proper reconstruction, for instance using deconvolution, these effects can be mitigated to a large extent, reconstruction

can never be optimal. This is caused by the existence of noise. In Equ. 9, the noise sources of a single pixel were summarized. Considering the photon noise alone, it already introduces an irreducible uncertainty on the number of photons N per pixel (see Sect. 3.1.2). The uncertainty is usually defined by one SD and yields $\pm\sqrt{N}$.

For low light applications, Pawley 2006b shows that the introduced uncertainty can easily reach similar magnitude like the required contrast. To decrease the uncertainty so that the required contrast is reliably available, more photons need to be detected. However, other application dependent noise sources like autofluorescence, unspecific labeling, or light scattering scale with N and are not reducible this way. Particularly the sample type and the labeling strategy have tremendous impact on the achievable visibility in real experiments.

The above considerations about spatial and temporal sampling are very much interrelated: if the spatial sampling shall be increased, then the pixel size could be decreased or the magnification increased. In either case the number of photons collected by a single pixel element will decrease. This, in turn, increases the uncertainty introduced by photon noise. For compensation, either the excitation power may be increased, or the temporal sampling can be reduced. The former is particularly dangerous for live-cell imaging as it accelerates toxic effects that cause cell death. It also yields faster fluorophore saturation, which decreases the available duration of recording. In contrast, reducing the temporal sampling is uncritical for the cells, but limits the capability to capture dynamic processes. Temporal undersampling would again lower spatial resolution owing to motion artifacts.

It is obviously difficult to achieve high visibility for different types of experiments. It must be acknowledged that the fundamental resolution limit that is usually cited in the literature can hardly be approached in practice. As a result, various imaging techniques have been developed that approach or even come below the Rayleigh resolution limit under specific conditions. They are the topic of the next section.

3.3 FM TECHNIQUES FOR LIVE-CELL IMAGING

The available resolution in FM presents a serious limitation since interesting molecular structures like vesicles, the active zone, or the synaptic cleft are in the same range or even much smaller (see Sect. 2.3.2). Various imaging techniques have been developed to increase the resolution, and numerous detailed reviews are available (Weisshart et al. 2013, Schermelleh et al. 2010, Huang et al. 2010, 2009, Heintzmann and Ficz 2006, Stephens and Allan 2003).

In this section, selected techniques will be reviewed and are subdivided into classical and super-resolution techniques. Classical techniques improve the effective resolution, but continue being diffraction-limited. In contrast, super-resolution techniques circumvent the diffraction barrier and provide details in the nanometer regime. They are separately covered in Sect. 3.3.1 and 3.3.2, respectively.

It shall be stressed here that for live-cell imaging the viability of the specimen is just as important as the resolution because biological results could otherwise simply be useless. Viability often stands opposed to resolution since procedures that increase the resolution intensify phototoxic effects and different types of samples set different re-

quirements on the accessibility of the requested information. Therefore, many more factors have to be considered before selecting a particular imaging technique. These include the photon efficiency of the optical system, the employed wavelengths, the size of the biological volume that is excited, the penetration depth in the tissue, the temporal resolution, or the duration of the experiment (Stephens and Allan 2003).

The viability of the specimen also depends on specifications that are not related to the imaging technique. Stephens and Allan 2003 pointed out that a stable cellular environment is vital during the experiment. This includes maintaining constant temperature, CO_2, and humidity conditions.

3.3.1 Classical Imaging Techniques

The most routinely used imaging technique is WF imaging. Its principal configuration was introduced in Sect. 3.1.4. Its success stems particularly from the straightforward implementation and the flexibility in terms of wavelength alternation and temporal resolution. Owing to the homogeneous illumination of the field of view (see Fig. 19a), the image is created at once, and the temporal resolution is only limited by the performance of the detector.

The homogeneous illumination in conjunction with the fact that light from off-focus positions is not filtered out is also its biggest disadvantage. The emission from a fluorophore in focus is superimposed with the emission from neighboring particles in the lateral and axial direction (York et al. 2011). This decreases the SNR and reduces the effective resolution. Furthermore, the available penetration depth is usually low since light scattering yields very blurry images in dense tissue (Inoué 2006). As a consequence, the application of WF microscopes is restricted to thin cell cultures.
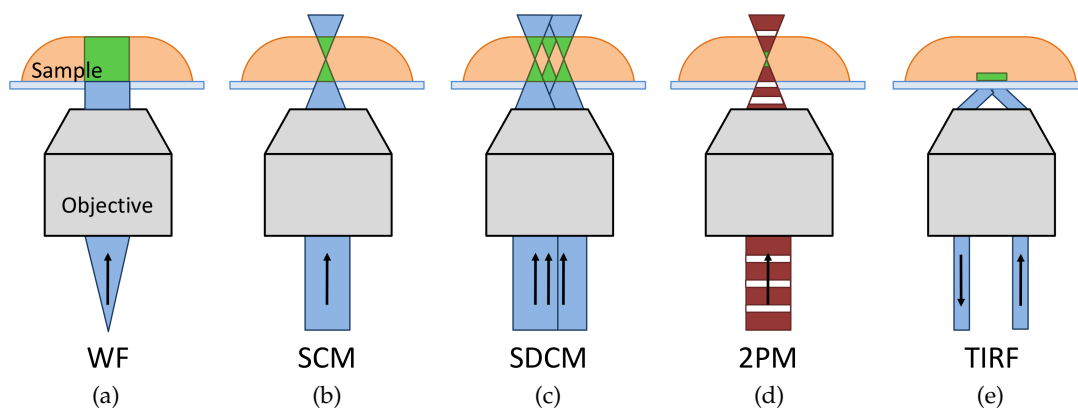
Figure 19: (a)-(e) Simplified illustrations of sample illumination in classical imaging techniques. The green regions illustrate the excited volumes in the sample.

3.3.1.1 Scanning Confocal Microscopy

These issues were addressed by the development of scanning confocal microscopy (SCM) (Minsky 1961) using two major design decisions. First, the excitation light is focused into the sample to excite only a diffraction-limited region (see Fig. 19b). This is nowadays achieved by sending collimated light from a laser into the objective (Naredi-

Rainer et al. 2013) and mainly restricts the lateral detection of light. As a second principle, light from out of focus planes is effectively filtered out by placing a pinhole in the focus of the tube lens.

Thus, point detectors are employed, and the detected light of a diffraction-limited region is represented by one pixel in the image. The full image is obtained by scanning the sample. By restricting the detection of light to such a small confocal volume the SNR is increased, and the effective resolution is significantly improved. It can be shown that by choosing pinhole sizes well below the PSF's FWHM the purely diffraction-limited resolution can be improved by a factor of $\sqrt{2}$, but in practice this improvement is eliminated by the loss in the number of detected photons (Naredi-Rainer et al. 2013, Cox and Sheppard 2004).

The axial sectioning capability of the pinhole is more important since the intensity from the confocal volume falls sharply with the distance to the focal plane. Light from off-focus planes, which would otherwise blur the image, hardly reaches the detector. This makes the axial resolution really available and allows for larger penetration depths in dens tissue (Webb 1996).

However, the increase in effective resolution comes at a significant cost in terms of the reduced temporal resolution (in the order of seconds for an image) and the intensified photobleaching. Both is caused by the scanning procedure.

3.3.1.2 *Spinning Disk Confocal Microscopy*

By scanning the sample in parallel using several pinholes, the invention of spinning disk confocal microscopy (SDCM) (Egger and Petran 1967) combined the advantages of SCM with the high temporal sampling available with WF microscopy (see Fig. 19c). This is accomplished by utilization of a Nipkow disk (Nipkow 1884). It arranges many pinholes in a way that if an object is viewed through the pinholes, each position on the object is evenly sampled after at least one rotation. Today's implementations of SDCM are using two synchronized Nipkow disks; one equipped with microlenses and the second with pinholes (Naredi-Rainer et al. 2013, Toomre and Pawley 2006).

The inner portion of a laser beam is spread apart to achieve uniform collimated illumination for a region of microlenses. This corresponds to the field of view. The microlenses focus parallel beams through the pinholes that create several confocal excitation volumes. Simultaneously, they act as axial sectioning pinholes in the emission path. Owing to the parallel sampling the final image can be acquired using full-field detectors.

The obtained lateral resolution is comparable to that of SCM, but the axial resolution is slightly worse due to cross-talk between the pinholes (Toomre and Pawley 2006). SDCM also suffers from very low photon transmission efficiency ($< 10~\%$). This hinders the acquisition of dim fluorophores, but at the same time decreases photobleaching.

3.3.1.3 *Two-photon Microscopy*

A method that is particularly compatible with living cells is two-photon microscopy (2PM) (Denk et al. 1990). It uses fluorophores that require excitation in the ultraviolet range, which is very toxic for cells and accelerates photobleaching (Cox 2007). Therefore, the fluorophores are excited by two photons at the same time so that each of them needs to carry only half of the required energy, and the excitation light can have twice

the wavelength. To increase the probability that two photons arrive simultaneously the excitation light is focused into the specimen using pulsed lasers (see Fig. 19d).

This results in similar axial sectioning and resolution capability like with confocal microscopy. A pinhole is not required since only in the focal plane the excitation probability is sufficiently high. Furthermore, photobleaching is only present at the focal plane. Owing to the excitation with infrared light the irradiation energy is comparatively low and less damaging for the sample. It also reduces light scattering allowing for penetration depths of several hundred micrometers.

3.3.1.4 *Total Internal Reflection Fluorescence Microscopy*

Another method that excites only a very thin axial section is total internal reflection fluorescence (TIRF) microscopy (Axelrod 2001). Very high-NA aperture objective lenses (NA > 1.4) are employed to focus a collimated laser beam under an angle of total reflection onto the border between the sample and the cover slip (see Fig. 19e). Owing to quantum mechanics, this creates an evanescent wave that reaches up to $\sim 100\,\mathrm{nm}$ into the sample. Only fluorophores in this thin axial region are excited.

This results in images with very high SNRs and increases particularly the axial resolution (Heintzmann and Ficz 2006). However, TIRF is very limited in the number of biological applications since only areas of a cell very close to the cover slip are accessible (Stephens and Allan 2003).

3.3.2 *Circumventing the Diffraction Barrier: Super-resolution Techniques*

Nowadays, the term super-resolution is commonly used to address all methods from the last two decades that achieve effective resolutions well below the diffraction barrier. In the literature it is often stated that the diffraction barrier is now broken. This is misleading since these methods do not break the diffraction barrier directly, but circumvent it by introducing artificial contrast. Abbe and Rayleigh are still right.

Now, what is the underlying idea to circumvent the diffraction barrier? Reconsidering the principle of confocal microscopy, the resolution is improved by detecting only the fluorescence of a single diffraction-limited region at a time. This introduces extra contrast by spatial and temporal separation. The general idea is therefore to further increase the separation by spatial or temporal variation of the light intensities. Then a super-resolution image can be constructed from individually detected small features in the sample (Betzig 1995). In other words: if it is known from which small sub-diffraction-limited region photons do come from, then they can be collected irrespective of their diffraction-limited transmission and be assigned to a smaller region in the image.

According to Huang et al. 2009, the most important techniques achieve separation below the diffraction barrier by (1) spatially patterned excitation or (2) single-molecule localization (SML). These two principles are reviewed in the following.

Of course there are also other principles (Weisshart et al. 2013), but methods based on these two principles have gained major interest and broad application. This is particularly caused by their compatibility with live-cell imaging and their - at least theoretically - unlimited resolution capability.

3.3.2.1 *Spatially Patterned Excitation*

Methods that implement this principle, create sub-diffraction-limited regions by engineering on the excitation pattern and exploitation of fluorophores that can be switched between a bright and a dark state. The first and most fundamental method is stimulated emission depletion (STED) microscopy. It was conceptually presented by Hell and Wichmann 1994 and experimentally verified by Klar and Hell 1999.

The basic setup is similar to that of SCM, and only a diffraction-limited region is excited. Additionally, a second so called STED laser is used. It resets already excited fluorophores to their lowest electronic energy state S_0 (see Sect. 3.1.2) before they can spontaneously emit a photon. To trigger this event, the STED laser has to emit photons with an energy that corresponds exactly to the energy difference between S_1 and the highest vibrational level of S_0. The induced relaxation is also accompanied with the emission of a photon, but now the light has the same wavelength λ_{STED} as the excitation light of the STED laser. This quantum mechanical phenomenon is called stimulated emission.

As a practical result, fluorophores illuminated by the STED laser now emit photons that can be separated from the normal fluorescence using the dichroic mirror. These fluorophores do not contribute to the image anymore and are effectively blanked out.

To realize an effectively sub-diffraction-limited PSF, the excitation pattern of the STED laser is shaped like a doughnut. It leaves only fluorophores in a small circular region in the excited state. This inhibition pattern can be realized using phase masks (Keller et al. 2007).

The FWHM of the effective PSF and in consequence the resolution of the system is defined by the distance (Hell 2007):

$$d_{STED} \approx \frac{\lambda}{2n\sin\alpha\sqrt{1 + i_{max}/i_{sat}}}. \tag{13}$$

Here, i_{max} and i_{sat} are the maximum intensity of the STED laser and the saturation intensity that is sufficient to relax the fluorophores, respectively. The resolution is then adjusted by i_{max}. Since even the intensity in the boundary regions of the doughnut will eventually exceed i_{sat}, the width of the depletion pattern will increase in practice. As a consequence, the resolution can theoretically be infinitely high and has already been realized at the nanoscale by Rittweger et al. 2009.

The high-resolution image is finally constructed by scanning the sample with the effective PSF and collecting the fluorescence using point detectors. The system is thereby still diffraction-limited in the excitation and emission light path. The resolution of the constructed image is solely defined by the known size of the effective PSF.

STED is not the only option to implement dark and bright states of fluorophores. Alternatively, ground state depletion (GSD) can be used (Hell and Kroug 1995), where fluorophores are caught in a so called triplet state by additional excitation. They do not relax to the ground state S_0 until the excitation light is turned off. During this period these fluorophores are therefore effectively bleached.

At the present time the ultimate technique is the application of fluorophores that can be switched on and off. This has first been shown by Hofmann et al. 2005. Proteins that undergo conformational changes between excitable and non-excitable states, by illumination with light of different wavelengths, are employed. The reported switch-

ing intensities are in the range of a few W/cm^2 and are compatible with living cells. Methods that employ such switchable fluorophores to achieve super-resolution have also been generalized under the term reversible saturable optical fluorescence transitions (RESOLFT) (Hell 2007, Hofmann et al. 2005).

Using RESOLFT methods, lateral resolutions of $\sim$ 70-90 nm have been achieved in biological samples (Nägerl et al. 2008, Westphal et al. 2008), but the axial and the temporal resolution as well as the penetration depth remained similar to that of SCM. Owing to the success of RESOLFT technologies, there is currently ongoing development in many directions: improved switchable fluorophores have been developed and employed. They enable multiple switching cycles and exhibit increased photostability so that repeatable and long-term experiments are available (Grotjohann et al. 2012, Testa et al. 2012, Fernández-Suárez and Ting 2008). The axial resolution could be dramatically improved to $\sim$ 100-200 nm by axial PSF engineering (Harke et al. 2008, Klar et al. 2000) or by combination with other imaging techniques (Friedrich et al. 2011, Wildanger et al. 2009, Punge et al. 2008, Dyba et al. 2005). The temporal resolution was improved by parallel scanning of the sample (Chmyrov et al. 2013, Bingen et al. 2011).

3.3.2.2 *Single-Molecule Localization*

Single-molecule localization methods use WF illumination instead of scanning techniques. Reconsidering the image construction process, it can be considered as the convolution of the point sources in the object with the PSF of the microscope. Hence, two point sources cannot be resolved if they are located within the FWHM of their blurred images (see Sect. 3.2.1). However, if it would be possible to image the particles separately, then at least their center positions can be determined with much higher precision than the actual resolution (Betzig 1995). The corresponding localization algorithms are the topic of Sect. 4.3.3.

If individual fluorophores are iteratively localized over time, then a super-resolution image that allows to distinguish nearby fluorophores can be created from these positions. This is exemplarily illustrated in Fig. 20.

In comparison to RESOLFT methods, the image is not directly detected. It is subsequently constructed from several images acquired by full-field detectors. The fundamental principle is still spatial and temporal separation. In contrast to RESOLFT, this is not accomplished by defined sub-diffraction-limited excitation, but by stochastic detection of individual fluorophores. They are inherently the smallest entity that can be resolved. It is the localization accuracy (LA) with which their position can be determined that defines the actual resolution. The two major aspects of SML, the obtained lateral resolution and the particle separation procedure, are now discussed in more detail.

Each photon emitted by a single fluorophore that arrives at the detector is a measure for the position of that fluorophore. The position error of each photon measurement is the SD of the PSF because the normalized PSF represents the Gaussian probability distribution for the spatial position of all detected photons. According to Thompson et al. 2002, the average of all photon measurements then provides the best estimated
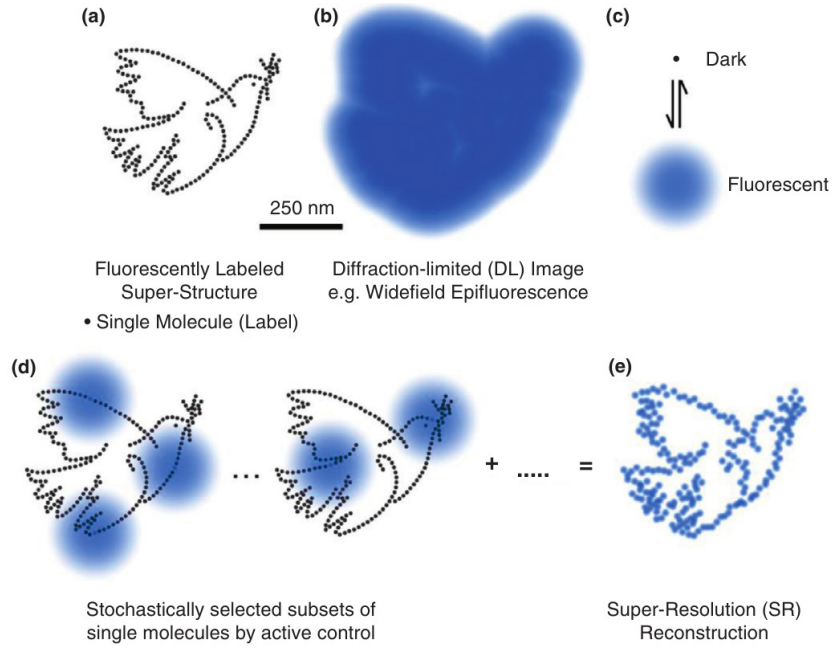
Figure 20: Principle of single molecule image creation. The true particle positions (a) cannot be recovered by conventional diffraction-limited FM (b). If fluorophores can be stochastically switched on and off (c), then individual fluorophores can be localized over time (d) and assembled to a super-resolution image (e). (Reprinted from Sahl and Moerner 2013, with permission from Elsevier.)

position of the fluorophore. The uncertainty Δs with which its position is determined can be estimated by:

$$\Delta s \approx \frac{\sigma_{PSF}}{\sqrt{N}}. \tag{14}$$

This is simply the standard error of the mean and defines the purely photon-limited LA. More realistic theoretical treatments have been derived by Mortensen et al. 2010, Abraham et al. 2009 and Ober et al. 2004. Their findings are based on Fisher's information limit and consider various experimental and imaging conditions.

The spatial resolution of the compounded image can be estimated by considering the image construction process (see Fig. 20). Each detected spot is usually drawn into the image as a 2D Gaussian. Its height then corresponds to the intensity, and its SD is given by the respective Δs (Betzig et al. 2006). Since Δs takes the number of photons into account, it is much smaller than the SD of the original PSF. By substituting Δs with the FWHM in Equ. 14, the theoretically achievable spatial resolution in the image is defined by the distance:

$$d_{SML} = \frac{\sigma_{PSF}}{\sqrt{N}} \cdot 2\sqrt{2\ln 2}. \tag{15}$$

By detecting more and more photons per particle, the resolution can in theory again be infinitely high and ångström-level resolution has already been experimentally proven (Abbondanzieri et al. 2005).

Precise localization of single fluorophores is only achievable if photons can be clearly assigned to a single fluorophore. Thus, only a subset of spatially well separated particles can be imaged at once. Fig. 21 summarizes the principal concepts for single molecule separation.
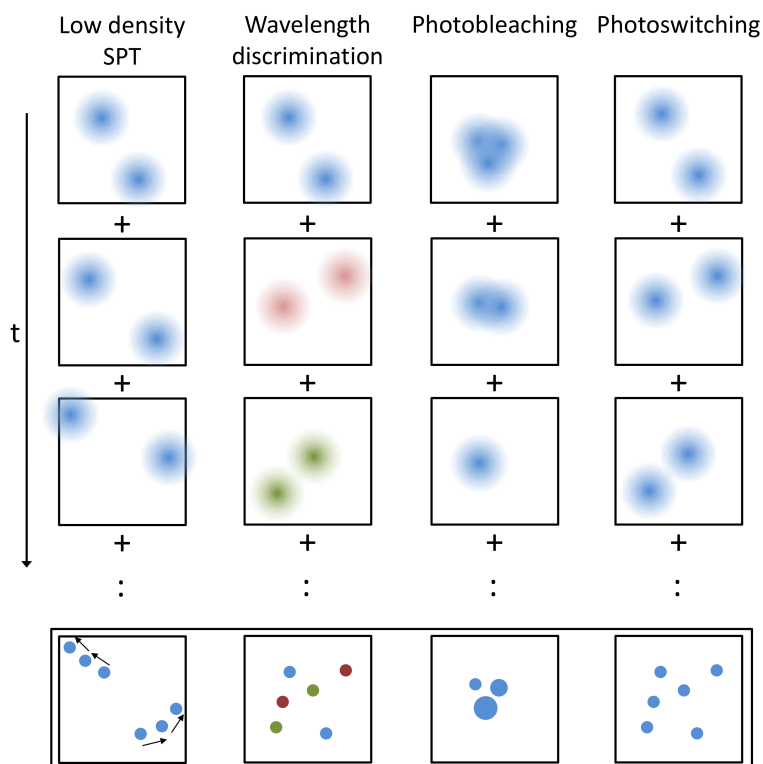
Figure 21: Principles of single molecule separation. The blurred spots represent the particles like they are observed in the individual acquisitions, and the filled circles represent the LA with that they are drawn in the final image.

Early approaches have kept the particle density sufficiently low so that the fluorophores are sparsely distributed. They focused on the detection of molecular dynamics in SPT applications (Yildiz et al. 2003, Kubitscheck et al. 2000, Schmidt et al. 1996). The resolution of particles within biological compartments smaller than the diffraction limit has been achieved by wavelength discrimination (Schütz et al. 1998, Oijen et al. 1998) and by separation based on photobleaching (Simonson et al. 2011, Qu et al. 2004, Gordon et al. 2004). In the latter, single fluorophores are successively bleached out. Starting from the last remaining particle, the combined intensity distribution is computed. This allows to draw conclusions on the individual particle positions. Similar algorithms have also been used to resolve nearby QDs that undergo stochastic blinking (Lagerholm et al. 2006, Lidke et al. 2005). More generally, intrinsic blinking and bleaching, common to all fluorescent molecules, was exploited by Burnette et al. 2011.

It was first pointed out by Lidke et al. 2005 that SML techniques are capable of drawing high-resolution images from localized point sources in a pointillistic fashion. This has ultimately been achieved by using photoswitchable fluorophores. They allow to resolve high molecular densities with as many as millions of fluorophores in a single image. Such methods have been individually developed by different labs and were termed photoactivated localization microscopy (PALM) (Betzig et al. 2006), stochastic optical reconstruction microscopy (STORM) (Rust et al. 2006), and fluorescence photoactivation localization microscopy (FPALM) (Hess et al. 2006). They create high-resolution images by stochastically switching on and off subpopulations of fluorophores. For it, lasers of different wavelength are used, and the whole process can be repeated a few

thousand times (Schermelleh et al. 2010). These methods differ in the type of employed fluorophores and the way they are switched. Nowadays many different fluorophores are available from the stock, and a selection is provided by Huang et al. 2009.

The original methods achieved high SNRs by imaging fixed preparations at the interface of the cover slip using TIRF (Betzig et al. 2006, Rust et al. 2006) or WF (Hess et al. 2006) configurations. Nowadays, they are routinely used with living cells, and effective resolutions of $\sim$ 50-70 nm are achieved (Shroff et al. 2008, Hess et al. 2007). Their applicability has also been broadened by showing that also conventional fluorophores can be used (Heilemann et al. 2008). Relying on WF imaging, the penetration depth is inherently limited, but the field of view is large and does not compromise with the temporal resolution. However, owing to the iterative acquisition the temporal resolution is still in the range of seconds per image (Shroff et al. 2008), but highly dynamic processes, which are only limited by the photon budget and the acquisition speed of the camera, can be assessed by combining PALM with SPT. This has led to the development of sptPALM (Nair et al. 2013, Manley et al. 2008).

Current improvements mainly focus on the extension to 3D. They are in detail addressed in Sect. 4.3.4. Still, as it was pointed out by Weisshart et al. 2013, routine 3D acquisitions in living samples remain to be challenging. The next chapter provides an approach to make such experiments readily available.

FAST 3D MOLECULAR DYNAMICS ANALYSIS IN BRAIN SLICES

This chapter addresses the analysis of molecular dynamics in complex biological samples. Such analyses allow to investigate the local arrangement, mobility, and interaction of signalling molecules in small neuronal compartments.

At first it must be proven that 2D molecular dynamics are also accessible in complex organotypic brain slices. To enable 3D diffusion analyses the major objective is the automatic adjustment to depth-dependent optical aberrations. Since fast dynamic processes in nanoscale compartments shall be analyzed, the method must be feasible with spatial accuracies of less than 100 nm and with at least 30 Hz temporal resolution. Furthermore, a simple imaging configuration shall be employed so that the method can become available to a broad community. Finally, it is a great demand that the technique is fast and routinely applicable so that the viability of the specimen is maintained and robust statistics can be obtained.

Before the actual workflow is presented, at first the available readout from dynamics analyses is quantified, and the corresponding state-of-the-art methods are reviewed.

4.1 DETECTION SCHEMES FOR STUDYING MOLECULAR DYNAMICS

Available optical tools for studying molecular dynamics are briefly summarized in the following. Several related tools provide readouts for molecular dynamics based on photobleaching. The basic methodology was established by Peters et al. 1974 and has lead to the fundamental method today known as fluorescence recovery after photobleaching (FRAP). It uses a focused laser beam to shortly illuminate a small region with an intensive excitation pulse leading to instantaneous and irreversible photobleaching of the fluorophores within that region. The subsequent diffusive influx of non-bleached fluorophores from the surrounding region then recovers the fluorescence. This temporal process can be imaged at standard laser powers. The resulting intensity recovery curve allows for computation of the type of motion, the absolute diffusion coefficient, and the immobile fraction of molecules (Axelrod et al. 1976). Since the bleached region cannot be infinitesimal small, these are always average results for a population of molecules. Beside the simple implementation of FRAP and its high temporal resolution, the strong dependency of the diffusion measurement on the exact knowledge of the geometry of the bleached region as well as the light-induced cell damage are disadvantageous properties.

An alternative implementation is continuous fluorescence microphotolysis (CFM) (Peters et al. 1981). It employs intermediate laser powers to induce photobleaching at a certain level while simultaneously imaging that region. The measured intensity decay reflects the two competing processes of irreversible bleaching and diffusive influx of new fluorophores. CFM allows for the same readout as FRAP, but works with lower fluorophore density, provides higher SNR, and requires less instrumentation.

fluorescence loss in photobleaching (FLIP) (Cole et al. 1996) and fluorescence localization after photobleaching (FLAP) (Dunn et al. 2002) are FRAP variants that provide

additional information. During FLIP, the region is repetitively bleached. The continued influx and subsequent bleaching of new fluorophores leads to a slow decrease of fluorescence in the surrounding regions and allows to draw conclusions on the connectivity of different cellular compartments. Alternatively, FLAP labels single molecules with two different fluorophores and performs simultaneous two color imaging. Bleaching of only one kind of fluorophore allows for additional determination of the diffusing bleached molecules using simple difference image analysis.

Another method that is also capable of measuring diffusion properties is fluorescence correlation spectroscopy (FCS). It is sensitive enough to detect different diffusive subpopulations (Lippincott-Schwartz et al. 2001). It is a photon counting technique, and its application to living cells relies on the detection of fluorescence in a very small confocal volume. Measuring the intensity fluctuation, driven by individual fluorophores that diffuse in and out of that volume, allows to determine fluorophore correlation times. Subsequently, diffusion coefficients, concentrations, and affinity constants for molecule-molecule interactions can be derived (Lippincott-Schwartz et al. 2001). To achieve such high specificity, the density of labeled molecules has to be kept reasonably low. Other drawbacks are the required specialized instrumentation and the difficulty to define the size of the volume.

The utilization of SPT for mobility analyses of individual molecules in living cells is relatively new (Schütz et al. 2000a, Kubitscheck et al. 2000). Tracking single fluorophores with nanometer LA allows for dynamics analyses of populations and individual fluorophores using diffusion measurements (Saxton and Jacobson 1997). Hence, different types of motion and absolute diffusion coefficients can be determined, and molecular interactions can be investigated at the nanometer scale. Relatively sparse distributions of labeled molecules and photostable fluorophores are a prerequisite (Nienhaus and Nienhaus 2013).

A conceptually different approach is based on Förster resonance energy transfer (FRET) (Lakowicz 2006). It occurs when the emission spectrum of the so called donator fluorophore overlaps with the excitation spectrum of the acceptor fluorophore and involves non-radiative energy transfer through dipole-dipole coupling. If a donator is excited and FRET can occur, then the practical implication is that fluorescence is emitted by the acceptor instead of the donator fluorophore (Lippincott-Schwartz et al. 2001). In FRET microscopy this is exploited to measure the spatial relationship between fluorophores since the FRET efficiency and therewith the emitted fluorescence are distance dependent. Molecular distances of several ångström can be resolved.

Such molecular interactions can alternatively be detected using fluorescence lifetime imaging microscopy (FLIM) (Bastiaens and Squire 1999). It determines the lifetime of a fluorophore in the excited state before it returns to the ground state S_0. Since the fluorescence lifetime is sensitive to the occurrence of FRET, interactions can be detected by a shift in the mean fluorescence lifetime (Day and Schaufele 2008).

In this thesis SPT is chosen as the preferred analysis tool for several reasons: (1) most importantly, it provides ultimate specificity since selected molecules can be analyzed individually. (2) the individual spatial LA reaches sub-diffraction nanometer precision allowing for investigation of dynamics in very small compartments. (3) the temporal resolution is only limited by the photon efficiency of the detectors, and varying time scales for the analysis of dynamics can be maintained. The latter notably allows to identify changes in the type of motion over the trace of a single molecule. Finally, (4) SPT is

capable of revealing the 3D trajectory. This is important for anisotropic motion that can for instance be experienced with surface molecules at curved neuronal compartments.

4.2 CHARACTERIZING THE READOUT OF SPT

The characteristics that can be extracted by analysis of SPT data are manifold. The most basic properties are derived from motility and velocity measurements (Meijering et al. 2012). The former category might include the total trajectory length and time, the relative distance from the initial position, or the directional change. Properties like the instantaneous speed, the mean curvilinear speed, or the acceleration, which deal with the rate of displacement, are available from velocity measurements. In contrast, analyzing large numbers of particle trajectories can be used to extract morphological characteristics like the area or contour of biological structures (Nair et al. 2013) or to probe for interactions between molecules by aggregation detection (Jaqaman et al. 2008).

To analyze molecular dynamics, diffusion measurements are most frequently employed (Manley et al. 2008, Saxton and Jacobson 1997). This mainly involves the computation of the mean squared displacement (MSD). It can be interpreted as the volume randomly moving particles have explored after a certain period. It also allows to identify different types of motion and to extract the absolute diffusion coefficients. This information is helpful in many ways. It supports analysis of populations, for instance if different molecules exhibit distinct types of motion or if diffusion parameters are locally varying. Confined regions and their size as well as the dwell times and escape probabilities of particles can be individually detected, and even the location and time of transitions in the type of motion of individual particles can be determined.

The MSD is a measure for the average distance a particle travels during a given time interval τ and is usually calculated as the second-order moment of displacement (Michalet 2010, Qian et al. 1991):

$$\mathrm{MSD}(\tau = m\Delta t) = \left\langle \frac{1}{M-m} \sum_{u=1}^{M-m} |\vec{p}_{u\Delta t + m\Delta t} - \vec{p}_{u\Delta t}|^2 \right\rangle, \quad m = 1, ..., M-1. \quad (16)$$

Here, $\vec{p}_t$ is the position of a particle at time t, Δt is the temporal sampling interval, M denotes the number of position measurements in the trajectory, and m adjusts the usually discrete τ. The outer brackets represent the average over multiple particles. Alternative calculations of the MSD, notably for higher-order moments of displacement (Sbalzarini and Koumoutsakos 2005) or incomplete trajectories (Michalet 2010) are also available.

If the MSD is plotted as a function of τ, the shape of the slope is an indicator for the type of molecular motion. According to Saxton and Jacobson 1997 one can differentiate four types

- directed motion with diffusion $\quad\quad \mathrm{MSD}(\tau) = 2dD\tau + (V\tau)^2$

- normal diffusion $\quad\quad \mathrm{MSD}(\tau) = 2dD\tau$

- anomalous diffusion $\quad\quad \mathrm{MSD}(\tau) = 2dD\tau^\alpha$

43

- confined motion
$$MSD(\tau) \simeq R_c \left[1 - a_1 e^{\frac{-2da_2D\tau}{R_c}} \right].$$

The corresponding MSD curves are depicted in Fig. 22a and their course can be approximated with the stated analytical functions. These are based on the Einstein relation and relate the trajectory of a particle with its diffusion coefficient D (Crocker and Grier 1996). The parameter d always denotes the spatial dimension, V is the velocity, $\alpha < 1$ an anomaly parameter, R_c corresponds to the size of the confined region, and a_1 and a_2 also relate to their geometry and are positive constants.
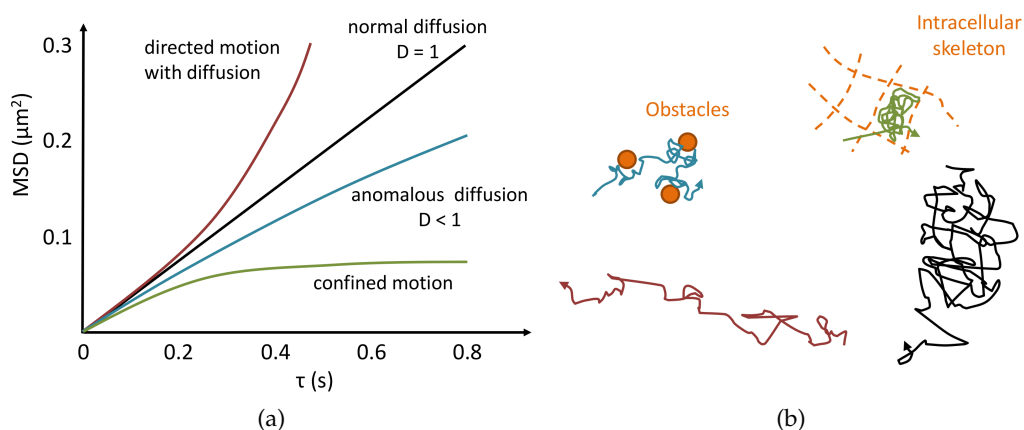

Figure 22: (a) MSD curves for different types of diffusion. (b) Corresponding exemplary trajectories.

Following Saxton and Jacobson 1997, a particle exhibits normal diffusion in the presence of pure Brownian motion. This is reflected by a straight line in the MSD curve where D defines their slope. Anomalous diffusion is represented by a lagging MSD curve indicating impeded motion, owing to interactions with obstacles or traps with varying binding energies or escape times. If a particle's motion is confined to a certain region, its MSD curve approaches a maximum value that relates to the size of this region. This may result from differences in membrane viscosity, embedment in the intracellular skeleton, or tethering to immobile structures. The curve of particles that undergo directed motion is steeper than that of particles with normal diffusion. These particles probably interact with a cytoskeletal motor. Corresponding particle trajectories are exemplarily illustrated in Fig. 22b.

To classify a track according to which motion it most likely corresponds to, several methods have been proposed. The most direct method fits all four motion functions to the MSD curve, and the version revealing the best goodness of fit is selected (Wilson et al. 1996, Anderson et al. 1992). In contrast, Feder et al. 1996 just fit the function for anomalous diffusion and classify into directed motion, normal diffusion or confined motion on the basis of α. Since the corresponding function is nonlinear, the fit is applied to their logarithm to converge more consistently. Kusumi et al. 1993 also reduce the shape of the MSD curve to a single parameter. It represents the ratio of the local diffusion coefficients D_l of the measured MSD and the MSD of normal diffusion. If the ratio falls on either side of the distribution of simulated random diffusion ratios, the particular deviation from normal diffusion can be detected again. To achieve the same classification, Saxton 1993 employs asymmetry measures from the shape of random

walks (Rudnick and Gaspari 1987). These measures of a given trajectory are tested against the probability that they could also accidentally occur in pure normal motion.

Knowing the dominant type of motion allows for the most accurate estimation of the individual diffusion coefficients by MSD curve fitting. The relative fractions of motion types within a population can also be computed. If the type of motion is unknown or difficult to gauge, for instance due to short trajectories (Saxton and Jacobson 1997), a reasonable alternative is the approximation of D by the already introduced local diffusion coefficient D_l. It is computed by fitting a straight line to the very first MSD data points (Kusumi et al. 1993, Qian et al. 1991). By evaluation of the analytical functions, Qian et al. 1991 demonstrated that D_l is fairly independent of the type of motion because the individual motion components dominate the MSD only for large values of τ. On average, D_l overestimates D only by $\sim 20\ \%$ (Kusumi et al. 1993).

These results are always only averages and assume that particles undergo only one type of motion during acquisition. In fact, this assumption is usually not justifiable for long-term observations since particles randomly interact with other molecular structures (Kusumi et al. 2012). As one of the first to determine motion transitions in single trajectories, Simson et al. 1995 detected temporary confinement. Assuming Brownian motion, they divide trajectories in independent segments and search for temporary confinement that is retained longer as would be expected from the probability of random confinement (Saxton 1993). The classification of segments simply relies on probability thresholding. To detect the exact location of transition points, Montiel et al. 2006 compare two running windows and determine significant local shifts in D by means of a log-likelihood ratio test.

Approaches that additionally classify the types of motion have been proposed by Helmuth et al. 2007, Huet et al. 2006. For this purpose, Huet et al. 2006 employ three classification parameters. Immobility is represented by a D_l estimate, confined motion is indicated by a MSD ratio similar to the one proposed by Kusumi et al. 1993, and the shape asymmetry introduced by Saxton 1993 is used for detection of directed motion. Computation of these parameters for a running window with variable size allows for temporal motion classification by thresholding the parameter tracks. Unclassified periods of the trajectory are assumed to have normal diffusion. In comparison, Helmuth et al. 2007 classify motion by feeding a supervised support vector machine with geometrical trajectory features computed on a running window of fixed size.

Finally, some computational aspects of MSD curve fitting shall be considered. Particularly the influence of particle localization errors, quantified by Δs, are of interest. The related questions are: (1) what is the most accurate fitting method, and (2) how many MSD data points should be included for accurate estimation of D? Concerning the first question, Michalet 2010 showed that least-squares (LSQ) fitting can be considered as being optimal since MSD values follow a normal distribution in most cases. Unweighted and weighted fitting yield similar results, which is advantageous since there is no need for estimation of the SD of the MSD. However, the latter holds only true if an adequate number of fitting points is used.

This leads to the second question. First of all, it has to be considered that trajectories should be as long as possible respectively as many particles as possible should be measured to avoid strong statistical fluctuations in the MSD (Qian et al. 1991). However, this would result in only averaged diffusion measurements, and individual type of motion changes or subpopulations with various characteristics are undetectable (Saxton and

Jacobson 1997). In order to maintain specific results, the number of measurements for each MSD data point is usually low. More measurements could be obtained by increase of the temporal resolution, but this reduces the LA because it scales with the inverse of the $\sqrt{N}$ (see Equ. 14). Since the influence of localization errors is unavoidable, Martin et al. 2002 showed that the introduced uncertainty results in a constant offset for any MSD curve and must be considered as an additional fitting parameter. Furthermore, they proved that the existence of localization errors is in fact the reason for the reported probability that trajectories might suggest other motion than the correct one (Saxton 1993).

To deal with the obvious consequence that MSD curves become noisy, Saxton and Jacobson 1997 suggest to analyze only MSD values for $\tau < 1/4$ of the length of the trajectory since otherwise the average does not contain enough measurements. Although they limited their analysis to isotropic mediums and Brownian motion, a more detailed guideline was proposed by Michalet 2010. They argue that the optimal number of considered MSD points is a trade-off between including large time intervals to compensate for the uncertainty at small τ dominated by the localization error and taking only the very first values to exclude the poorly averaged MSD points towards the end of the curve. Therefore, they introduce a reduced localization error $\Delta s_r = \Delta s^2/D\Delta t$ that corresponds to situations where the localization error dominates the effect of diffusion. Based on Δs_r, they provide an empirical approximation for the number of included MSD data points that minimize the error on the fitted curve parameters:

$$m_{min} = \text{Round}(2 + 2.7\sqrt{\Delta s_r}). \tag{17}$$

In practice, an estimate for the LA of the imaging system must be available and D can initially be approximated by D_l. Iterative MSD curve fitting and D estimation will then rapidly lead to optimal values for m_{min} and D.

Since diffusion and MSD calculations depend on the number of available measurements as well as the LA, they can lead to reasonable uncertainty in the estimation of D (Michalet 2010, Qian et al. 1991). It is therefore good practice to provide the distribution of diffusion coefficients rather than an averaged D (Wu et al. 2008). The analysis of the shape of the distribution then allows to determine deviations from the expected normal distribution. In case of deviation, immobile and mobile fractions could alternatively be already assessed from this shape instead of performing dedicated motion type analyses.

The next section now reviews state-of-the-art SPT techniques. It explains how accurate particle positions and trajectories can be determined and reveals the current shortcomings with respect to the determination of 3D information in brain slices.

4.3 RELATED WORK ON SPT

SPT is the ultimate tool in terms of specificity since it allows to analyze the dynamic of individual molecules. Although the principal concepts have long been known, it was not until the 1980s that the sensitivity of the instrumentation made imaging single molecules available at all (Deschout et al. 2014). It took then several more years until single molecule microscopy became a widely available standard tool for analyses in living cells (Schütz et al. 2000a, Kubitscheck et al. 2000).

Since then, research has focused on the precise localization and tracking of multiple particles in digital images, which has led to a variety of computational methods. They are the topic of this section. It follows the general procedure of (1) detecting the particles above background, then (2) determining their lateral and axial position with nanometer precision and (3) linking the individual locations to trajectories. It has to be stated that applications do not always follow this strict distinction between detection that only generates indications of particle positions and subsequent precise localization. Not all presented algorithms are particularly designed for SPT applications. Instead, they often address spot detection in general, which is a common task in microscopic images.

In this workflow the correct detection of all particles in the image is very crucial for any experiment since false positive detections yield biologically misleading results, and missing out too many particles requires to acquire more images for obtaining robust statistics. The performance of the overall SPT procedure heavily depends on accurate localization as otherwise tracks might be unnecessarily interrupted or correct partial tracks might be erroneously linked to intermediate false detections.

Single particle detection and localization are sophisticated tasks. Owing to the one-to-one labeling, single molecules are only represented by a single fluorophore, which requires acquisition at the detection limit and yields generally low SNRs. This is aggravated by simultaneous optimization for the speed of acquisition and for the fact that the excitation intensities cannot be dramatically increased to prevent photobleaching and phototoxicity (Meijering et al. 2006, Sage et al. 2005). Furthermore, single particles are only represented by the diffraction-limited PSF in the image, but do not necessarily have the same SNR since in biological samples usually not all particles lie in-plane with the focal plane of the microscope. Finally, particles often have to be determined in close proximity to neighboring particles or above a non-uniform background created by unspecific autofluorescence or off-focus particles. These properties are illustrated in Fig. 23).

4.3.1 *Preprocessing*

The generally low SNR in biological images is one of the most aggravating parameters for the performance of SPT methods. It is common to enhance the SNR by preprocessing the data. Deconvolution techniques are a powerful tool to reduce blurring and increase the contrast (Sibarita 2005). Although it is generally recommended to apply these techniques to microscopic image data (Pawley 2006a), it seems to be less effective for SPT applications. This is reasoned by the fact that localization algorithms often already perform some kind of implicit deconvolution through the inclusion of shape assumptions (Wu et al. 2008).

Noise reduction is much more frequently applied and is highly reasonable since microscopes are inherently band-limited by the diffraction of light. Thus, any image feature smaller than the PSF can be considered as noise and should be removed. Image denoising techniques can be generally divided into linear and nonlinear methods. Examples for linear filters are simple local averaging (Goulian and Simon 2000) and the very commonly applied Gaussian smoothing (Crocker and Grier 1996). They are easily parameterizable and effectively reduce noise, but at the same time also blur the image, which removes small image features. In contrast, nonlinear methods pre-

serve edges between objects. For biological images, simple median filtering (Bornfleth et al. 1999) as well as more advanced anisotropic diffusion techniques (Uttenweiler et al. 2003, Tvaruskó et al. 1999) have been applied. However, edge preservation is not so important for SPT applications because the boundaries between particles are rather fuzzy. Further sophisticated methods include wavelet thresholding (Starck et al. 2007) or patch-based noise reduction (Boulanger et al. 2008).

4.3.2   *Particle Detection*

Before introducing particle detection methods, the definition of what can be considered a particle is crucial. For general spot detection in FM, they are usually defined as objects of variable size and shape with an intensity profile higher than their local environment, but separated only by a fuzzy boundary without distinct edges (Olivo-Marin 2002). In the specific case of SPT, their intensity profile simplifies to being round and Gaussian-shaped. For the present work this definition is extended to elliptical Gaussian shapes, like they are observable in Fig. 23. This is owed to the requirements of 3D SPT that will be considered later in this chapter. Based on the usually diffraction-limited size of the particle images, the number of distinguishing characteristics is rather small. This limits the type of applicable methods to thresholding and shape-based approaches.
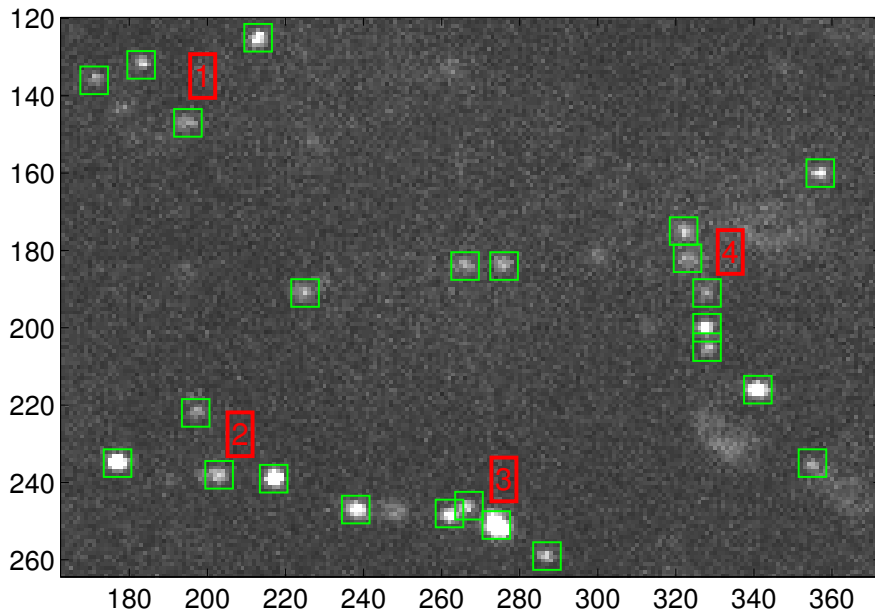

Figure 23: Detected particles in an exemplary acquisition in brain slices are indicated by green boxes. Particles appear as diffraction-limited spots with varying shapes (mark 1) and SNRs (mark 2). They may have overlapping intensity distributions (mark 3) and may have to be distinguished from unspecific background (mark 4).

4.3.2.1   *Threshold-based Methods*

The most basic approaches are purely threshold-based and try to categorize pixels only at the basis of their intensity value. This is generally achieved by estimating the mean

background intensity i_b and computing a threshold t_p by adding a constant factor k times an estimate of the background noise δ_b:

$$t_p = i_b + k\delta_b. \tag{18}$$

Typical estimations for the noise are $\delta_b = \sqrt{i_b}$ (Betzig et al. 2006), taking the median absolute deviation $\delta_b = \tilde{i}_b$ (Olivo-Marin 2002) or, if the particles are sparsely distributed, $\delta_b = \sigma_i$ (Thompson et al. 2002). For the latter, σ_i denotes the SD of the intensity of all pixels. In order to perform well, k requires careful adjustment to the particular image data, which limits the unattended operation of these approaches.

This drawback can be attenuated by using threshold estimation techniques. The classical method suggested by Otsu 1975 analyzes the histogram and assigns pixels to classes by maximizing some discriminant criterion measures of class variances. As was pointed out by Coudray et al. 2010, this common technique is in general not appropriate for unimodal histograms that microscopic images usually exhibit. Owing to the low SNR and the relatively sparse distribution of particles with respect to background structures, the resulting unimodal histograms usually consist of two strongly overlapping distributions. The one representing the particles is normally much smaller than the one containing background pixels. Approaches that are capable of thresholding such unimodal histograms include the histogram-shape-based triangular methods (Rosin 2001, Zack et al. 1977), a method based on linear diffusion in the scale-space (Baradez et al. 2004) as well as the T-point algorithm that minimizes the residuals of two line fits to the descending slope of the histogram (Coudray et al. 2010).

In their basic implementation these are all so called global thresholding methods that show reduced performance for non-uniform background and strong variations in the particle intensities. They should, therefore, be used as locally adaptive versions by separate application to non-overlapping smaller image regions and interpolation of the spatially distributed regional thresholds (Wu et al. 2008). To further improve the separation of true signal from noise, shape knowledge can be incorporated.

4.3.2.2 Shape-based Methods

The basic principle of all shape-based algorithms is signal enhancement by transforming the shape information again into some sort of intensity representation so that thresholding methods can finally be applied more robustly. They can be classified into dynamic thresholding, spot-enhanced filtering, morphological grayscale, wavelet decomposition, and supervised methods.

The top hat (Bright and Steel 1987) and its rectangular and smoothing version, the top hat box filter (Breen et al. 1991), scan the whole image and act like locally dynamic threshold setting operations. They leave a pixel with its original intensity value if the maximum respectively mean pixel intensity of a concentric circular top region, is about a constant threshold value higher than the maximum or mean intensity of a surrounding brim region. Otherwise the pixel is assigned zero. The size of the two concentric regions hence defines the expected particle size and distance.

The spot-enhancing procedure proposed by Sage et al. 2005, can be interpreted as a continuous implementation of the top hat filter. It uses a Laplacian of Gaussian (LoG) filter that is convolved with the image. The authors show that this corresponds to a whitened matched filter, that optimally enhances Gaussian-like structures in additive

independent noise experienced in SMALL-CAPS-FM images. At the same time it suppresses local background. Thus, noise reduction is implicitly included and the only parameter is the SD of the LoG filter that must be tuned for the expected particle size.

The most basic method that is based on morphological grayscale operations, is local maxima detection using grayscale dilation (Crocker and Grier 1996). More advanced composite methods find peak indications using morphological top hat filtering (Wu et al. 2008) or employ the h-dome transform that performs grayscale reconstruction (Vincent 1993). In the former, the size of the circular shape must be larger than the largest particle to be found and the h-dome transform requires a threshold parameter that relates to the SNR in the image. These techniques have been extended by multiplying the intensity at peak indications with the local curvature based on the determinant of the Hessian matrix (Thomann et al. 2002) or by using the h-dome transform as an importance sampling function for a subsequent clustering algorithm (Smal et al. 2008b).

Wavelet-based approaches exploit the decomposition of the image at different scales. Izeddin et al. 2012b employ a B-Spline wavelet of third order and particle candidates are extracted from the wavelet coefficients at the second scale, using a threshold estimated from coefficients at the first scale. Assuming that in contrast to noise, particle features tend to propagate across scales, Olivo-Marin 2002 computes the multi-scale product after hard-thresholding the coefficients at each scale individually. This tends to be more robust and only requires to define the scale that corresponds to the expanse of the largest particle. Using Jeffreys's noninformative thresholding scheme (Figueiredo and Nowak 2001), this approach was extended to detect also very weak objects (Genovesio et al. 2006). Another method based on image denoising uses a multi-scale variance-stabilizing transformation and reconstructs the image after selecting significant coefficients by multiple hypothesis testing (Zhang et al. 2007a).

Supervised methods are trained on annotated sub-images that either contain a particle or only background structures. These sub-images are decomposed by many small Haar features that altogether describe the object by their intensity, shape, size and position. Based on these combined responses for each sub-image the machine learning algorithms AdaBoost (Jiang et al. 2007) and Fisher Discriminant Analysis (Smal et al. 2010) have been applied to biological images.

After signal enhancement, all shape-based algorithms still require the definition of a suitable threshold. As most of them perform local background subtraction indirectly, they can draw on simpler thresholding schemes that are related to the required SNR and conceptionally similar to Equ. 18.

Evaluation

The majority of the presented algorithms has been evaluated in an extensive study by Smal et al. 2010. They conducted performance measurements on synthetic and real biological images, where the SNR, the object shape as well as the parameter settings of the algorithms were varied. The authors conclude that no detection scheme generally outperforms all others. However, for very low SNRs $\leqslant 4$, supervised algorithms show the best overall performance, closely followed by the multi-scale variance-stabilizing transformation, h-dome-based clustering, LoG-based spot-enhancement, and morphological top hat filtering. They also emphasize that the presented unsupervised algorithms are fairly insensitive to their parameterization, which is important for practical application.

4.3.3 *Lateral Particle Localization*

Having pixel grid indications of particle positions, the next step is their refinement to sub-pixel positions, yielding nanometer-scale LAs for particles in the object (see Fig. 24). At first, the fundamental approaches to sub-pixel refinement are introduced.


2D image $\longrightarrow$ Intensity profile $\longrightarrow$ Gaussian fit $\longrightarrow$ Sub-pixel localization
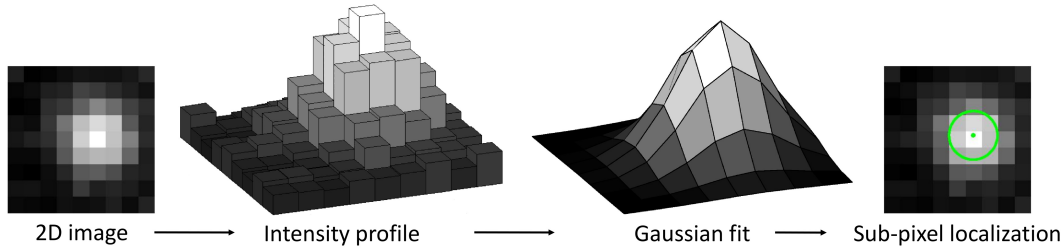
Figure 24: Principle of sub-pixel refinement by means of a fitting algorithm.

4.3.3.1 *Fundamental Localization Algorithms*

As already pointed out, a particle is considered as a round or elliptical Gaussian-shaped object in the image. In the simplest case, its center position x_c, y_c can be estimated by centroid computation (Patwardhan 1997), yielding:

$$x_c = \frac{\sum x i_{x,y}}{\sum i_{x,y}} \quad \text{and} \quad y_c = \frac{\sum y i_{x,y}}{\sum i_{x,y}}, \tag{19}$$

with the weight $i_{x,y}$ being the intensity of an included pixel. This estimation is fairly insensitive to particle shape variations, but easily biased by noisy weights and the chosen region of interest (ROI) (Cheezum et al. 2001). Due to the former, it is usually not directly applied to raw intensity images. Instead, the centroid is computed after cross-correlation of the image with a suitable kernel (Gelles et al. 1988), background subtraction, and low-pass filtering (Ghosh and Webb 1994, Lee et al. 1991) or wavelet decomposition at the second wavelet plane (Izeddin et al. 2012b). Since centroid computation is biased towards the center of the ROI, Berglund et al. 2008 proposed an iterative algorithm that adjusts the ROI using fractions of pixels so that the particle always resides in the center of the ROI.

An extension that excludes the background implicitly is the so called Gaussian mask algorithm (Thompson et al. 2002). It is similar to the former in the sense that the centroid computation is weighted with a function G leading to:

$$x_c = \frac{\sum x i_{x,y} G(x,y)}{\sum i_{x,y} G(x,y)} \quad \text{and} \quad y_c = \frac{\sum y i_{x,y} G(x,y)}{\sum i_{x,y} G(x,y)}. \tag{20}$$

Here, G is computed from a Gaussian function, integrated over each pixel. Because G is centered at x_c, y_c, the position estimation is iterated to minimize the χ^2 sum of the Gaussian mask and the peak intensities.

Alternatively, Parthasarathy 2012 exploits the radial symmetry of the intensity distribution of a particle. The key idea is that the gradients of a radial symmetric function intersect at the coordinate origin of the distribution. The point having the smallest distance to all gradient lines is taken as the estimate for the particle location. To com-

pute the gradient lines, the author uses a Roberts cross operator on the four diagonal neighbors of each pixel. The distance d_u between x_c, y_c and each gradient line $y = y_u + m_u(x - x_u)$ is computed by:

$$d_u^2 = \frac{\left[(y_u - y_c) - m_u(x_u - x_c)\right]^2}{m_u^2 + 1}. \tag{21}$$

The center coordinates are analytically determined by minimizing $\sqrt{\sum_u d_u^2 w_u}$, where w_u is a weight for each pixel that can represent its intensity or distance to the estimated origin.

Another class of algorithms performs fitting of a PSF model incorporating shape and noise information. The typical procedure takes a full nonlinear LSQ fit of a Gaussian function G to the intensity distribution of a particle in the image (Kubitscheck et al. 2000, Anderson et al. 1992). This introduces more complexity than the Gaussian mask algorithm because all free parameters of G are fitted including the SDs σ_x, σ_y, the peak height h, and the background offset o_b:

$$G(x, y) = o_b + h \cdot e^{-\left(\frac{(x-x_c)^2}{2\sigma_x^2} + \frac{(y-y_c)^2}{2\sigma_y^2}\right)}. \tag{22}$$

The fitting routine minimizes the objective function (Kay 1993):

$$\sum_{x,y} (G(x, y) - i_{x,y})^2 \tag{23}$$

and therewith also accounts for the noise. For that reason, algorithms that locate particles in the LSQ sense do not require preceding noise reduction routines. However, LSQ estimation is suited for data exhibiting Gaussian noise, but in FM the intensity at any pixel is dominated by photon noise, which follows a Poisson distribution. LSQ fitting is not optimal because it gives constant weight to every pixel and Gaussian noise is different from Poisson noise particularly for low photon counts. To better account for the photon noise, any pixel can be given a weight $1/N_{x,y}$ in the objective function yielding weighted LSQ fitting (Mortensen et al. 2010).

Estimating the free parameters using maximum likelihood (MLH) instead of LSQ fitting allows to correctly account for Poisson noise (Ober et al. 2004). The joint likelihood L of the free parameters of G is maximized with respect to the measured pixel intensities that are subject to Poisson noise:

$$L = \prod_{x,y} \frac{G(x, y)^{i_{x,y}} e^{-G(x,y)}}{i_{x,y}!}. \tag{24}$$

The last algorithm considered here, is particularly designed for particle fitting on locally non-uniform background and is termed polynomial-fit Gaussian weight (PFGW) method (Rogers et al. 2007). It fits a quartic polynomial function:

$$I_{fit}(x, y) = \sum_{u=0, v=0}^{u+v=4} F_{u,v}(x - x_n)^u (y - y_n)^v \tag{25}$$

in the LSQ sense to the peak indications. This is further weighted by a Gaussian function that is centered at the current position estimate x_n, y_n. As these center coordinates are estimated from the quadratic part of I_{fit}, the algorithm involves an iterative sub-pixel correction step. The refinement stops when the current center position x_n, y_n has a distance less than a given threshold from the previous position x_{n-1}, y_{n-1}. The combination of Gaussian weight and polynomial fitting has the advantage that the center of the particle is used for fitting and the fitted function has enough freedom to incorporate the particle into locally non-uniform background.

Although various background subtraction techniques exist (Piccardi 2004), this topic has barely been addressed in SML techniques (Small and Stahlheber 2014). In general, locally uniform background that varies smoothly only over larger spatial distances is assumed. This is reasonable owing to the sparse signals and the narrow emission bands of optical filters. Simple procedures are sufficient when the background is not considered in the localization procedure. This includes subtraction of the average intensity derived from local (Baddeley et al. 2009) respectively global (Hess et al. 2007) image regions or using more robust temporal median filtering (Hoogendoorn et al. 2014).

Evaluation

These fundamental approaches have been extensively studied in the literature. As one of the first, Cheezum et al. 2001 compared centroid computation and LSQ fitting for diffraction-limited spots modeled by the Airy pattern with noise added from a Poisson distribution. They stated that LSQ fitting generally outperforms centroid computation since the absolute bias and the LA Δs are independent of the relative position to the pixel grid. Furthermore, for LSQ fitting Δs scales well with the SNR. The authors conclude that the limiting SNR for LSQ fitting is 4 since at this SNR Δs decreases to only 100 nm, which is, assuming Nyquist sampling, no sub-pixel precision anymore. Later, Thompson et al. 2002 showed that, although being computationally simpler, the Gaussian mask algorithm performs only slightly worse than LSQ fitting. The PFGW shows similar performance like LSQ fitting, but maintains it even for complicated backgrounds (Rogers et al. 2007).

Abraham et al. 2009 compared MLH with LSQ fitting, using Airy and Gaussian shapes. They demonstrated that MLH fitting yields indeed smaller Δs than LSQ fitting, but this is noticeable only at the limit of low photon counts. Additionally, MLH fitting showed to be more robust to deviations in the PSF shape as they occur for instance due to optical aberrations. Ober et al. 2004 proved that using MLH fitting, predicted theoretical limits for Δs can in fact be reached for digital images with limited photon counts and mixed Gaussian and Poisson noise sources.

The most comprehensive study was conducted by Mortensen et al. 2010. In contrast to other studies, they fitted theoretical PSF models derived from findings of Enderlein et al. 2006 and Bartko and Dickson 1999, who showed that fluorophores have to be considered as dipoles whose 3D orientation changes their intensity distribution. Again, MLH fitting proved to be optimal. A surprising finding was that due to being easily biased by pixels with low photon counts weighted LSQ fitting only performs better than the unweighted version if the background is high or artificially increased.

However, fitting such sophisticated PSF models is only required for imaging fixed dipole emitters. Stallinga and Rieger 2010 showed that Gaussian PSF approximations are fine for freely rotating dipoles, but can result in additional deviations up to several

tens of nanometers for fixed dipoles. Since fixed dipoles might only be imaged if the fluorophore is rigidly linked to a stationary structure (Deschout et al. 2014), this is in practice not required for dynamic live-cell imaging (Small and Stahlheber 2014).

In conclusion, fitting methods are computationally slower, but perform with higher precision owing to the inclusion of shape and noise information. This can also be disadvantageous. If the real measurements deviate from the theoretical assumptions, non-fitting methods may be favorable (Deschout et al. 2014, 2012). Possible additional experimental factors are sample drift, particle movement during exposure, label displacement at the particle, or optical aberrations. Therefore, no estimator suits all experimental conditions and careful selection of the appropriate localization algorithm is necessary.

4.3.3.2 *Localization at High Particle Densities*

Till now it was implicitly assumed that the particles are well separated so that small image sub-regions, containing only single particles, can be extracted and subsequently fed to the position estimators. There are many separation approaches trying to meet this prerequisite (see Fig. 21). Nevertheless, occurrences of densely distributed particles being neighbored, having partially overlapping intensity distributions or even being indistinguishable, are still frequent in practice.

A very reasonable procedure is the detection of such occurrences and their rejection from further processing. This is indeed simple for particles with only partially overlapping intensity distributions. Particles with distances much below the resolution limit are hard to differentiate just by inspection of the intensity distribution (Lidke et al. 2005). Additional shape information can be employed to reject detected particles on the basis of their radius, eccentricity, or SNR (Rogers et al. 2007). The obvious drawback of this procedure is the reduced number of data points and fewer or shorter trajectories, particularly for SPT applications. Another consequence of including nearby particles is the loss of achievable LA. Wolter et al. 2011 showed that for maintaining reasonable LA, the particle density should not exceed ~ 0.5 particles per μm^2. Since higher local densities are frequently observed owing to the mobility of the particles, the LA, the amount of collected data and, very importantly, the viability of the living samples have to be balanced (Small 2009).

In order to reduce the acquisition time, localization algorithms for very dense particle distributions have recently come into focus. This has been supported by the finding that even particles closer than the classical resolution limit can be localized with similar uncertainty than separated particles, given sufficiently high numbers of detected photons (Chao et al. 2009, Ram et al. 2006). Based on the assumptions that the number of particles is known and the combined intensity distribution is drawn from point sources that emit photons with identical, but independent spatial distributions, densely distributed particles can be localized by treating them like mixture intensity distributions (see Fig. 25). This has been formulated by Ram et al. 2006 as a new resolution measure in the sense of how accurate the distance between the center of two point sources can be determined. It was further extended to the axial resolution by Chao et al. 2009. Without wanting to deepen this further, this again emphasizes that the Rayleigh criterion is actually somewhat arbitrary. It is based on a notion of contrast detected by eye, but given sufficient photon statistics the limit can also be driven down.

| 2D image | → | Intensity profile | → | Gaussian mixture fit | → | Sub-pixel localization |
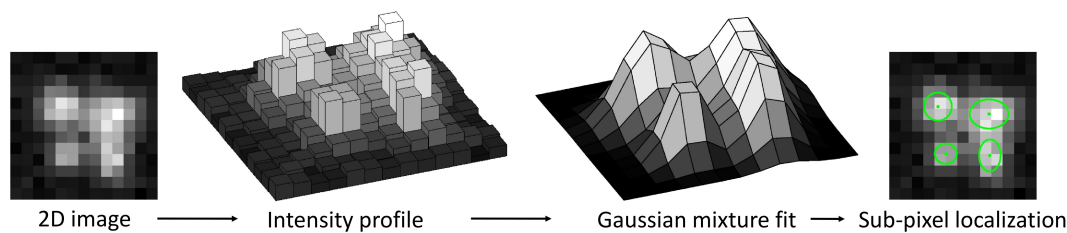
Figure 25: Principle of sub-pixel refinement for multiple neighboring particles by means of a fitting algorithm.

The following algorithms try to approach the proposed resolution limit for dense particle distributions. One of the major difficulties is the correct estimation of the number of involved particles because only on the basis of the intensity distribution, their determination is still inherently hindered by Rayleigh's resolution criterion. In the simplest case when the intensity distributions of different particles are overlapping, but are clearly distinguishable, a standard watershed algorithm can be applied for spatial separation (Izeddin et al. 2012b). It has to be ensured that the region contains enough background pixels as otherwise the fitting routines cannot estimate the offset correctly (Mortensen et al. 2010, Sergé et al. 2008). The major drawback of cutting the combined intensity distribution is the incorrect assignment of photons from either distribution in the overlapping region, which biases the localization. An improved alternative procedure is based on particle deflation through iteration over the detection and localization steps (Sergé et al. 2008). The brightest particles are fitted first. Then they are subtracted from the image to allow for subsequent fitting of nearby dimmer particles. This procedure is iterated until only noise is detected.

The most direct implementation of the findings of Ram et al. 2006 is parallel fitting of multiple particles by means of a Gaussian mixture distribution. Assuming that any emitter contributes independently to the intensity at a pixel, the function G in Equ. 24 is then extended to contain the sum of the intensity distributions of several particles. There are many such algorithms and they mainly differ in the implementation of the second assumption that requires to know the correct number of particles beforehand. The algorithms of Huang et al. 2011 and Holden et al. 2011 are very similar because they rely on particle deflation as introduced by Sergé et al. 2008, but fit the determined number of particles altogether at each iteration. The model with the best likelihood is finally selected.

Another iterative procedure was suggested by Quan et al. 2011 and optimized for performance by Wang et al. 2012. It is initialized with an optimistic number of particles including many false positive indications. The algorithm fits this initial model to the data, then removes the particle with the smallest fitting amplitude and repeats these steps until only a single particle is left for fitting. Subsequently, the Bayesian information criterion (BIC) is computed for each of these models and the optimal model is selected by means of the lowest BIC value. As the BIC includes a penalty term for the number of parameters in a model, this procedure also reduces the probability for overfitting of the data. This Bayesian approach has been extended for time series analysis by Cox et al. 2012. Including connections over several frames can increase the effective density by exploiting blinking, bleaching and added particles. Also the LA may be

increased by combining photons of reoccurring particles. However, these advantages come at the cost of high computational effort and decreased temporal resolution.

Another class of algorithms is based on compressed sensing, which is a quite recent statistical paradigm. It states that a signal can be reconstructed from underdetermined linear systems of measurements in a basis different from that of the original signal given that the signal is sparse in this initial basis (Càndes 2006). In the context of particle localization, Mukamel et al. 2012 and Zhu et al. 2012 model the image on a pixel grid much smaller than the resolution limit by convolution of the particle distribution with the PSF. They take a sparse representation of the image, using the PSF as the fixed basis, to recover the original image. Then the residual between the model and the true image is minimized. The number of particles must not be known beforehand, and the LA correlates with the pixel refinement. These approaches achieve slightly worse LA, but work with higher particle densities than the algorithms that fit mixture distributions. A drawback is that particles are represented by a known and constant shape, which requires all particles to be perfectly in focus.

An extensive evaluation of the different classes of algorithms for densely distributed particles is yet not available.

4.3.4 *Axial Particle Localization*

The most obvious approach to extend the localization principle to 3D is axial scanning of the sample and creation of so called z-stack images. The 3D center position of individual particles can then be found by either cross-correlating (York et al. 2011) or fitting an experimental (Zhang et al. 2011) or theoretical (Aguet et al. 2005) 3D PSF to the image stack.

As an alternative to using the full PSF, an analytical model function can be fitted to a feature of the PSF. A common feature is the lateral width of the PSF. In a first approach, the width of the 2D PSF was described as a function of the axial scanning position by a focused Gaussian beam waist. Then the minimum of the function indicated the axial center of the particle (Oijen et al. 1998). This was later improved by showing that the theoretically predicted axial dependency of the PSF's FWHM ω (Niedrig 1993):

$$\omega(z) = \omega_0 \cdot \sqrt{1 + \left(\frac{z}{d}\right)^2} \tag{26}$$

is in accordance with experimental measurements (Schütz et al. 2000b). Here, z is the relative axial position, ω_0 is the FWHM in focus, and d is the depth of field. The latter is defined as the maximum axial distance of two objects that simultaneously appear sharp at one focus setting (Inoué 2006). By fitting Equ. 26 to the particle widths of the individual z-stack images, the axial center position can be determined with nanometer accuracy (see Fig. 26).

The major drawback of such approaches is their low temporal resolution. This is owed to the necessity to acquire entire image stacks. If particles move during the acquisition, the 3D center position cannot be reliably estimated because the relative axial positions of the measurements have changed. To increase the temporal resolution, two classes of algorithms have been developed. One focuses on tracking only single parti-
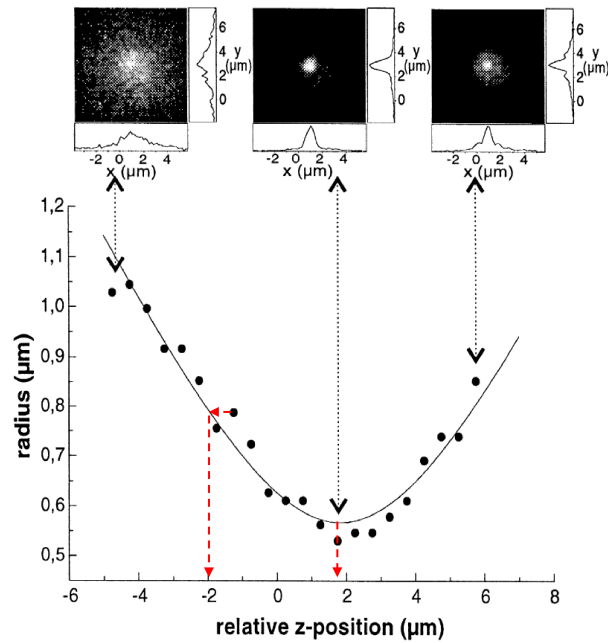
Figure 26: The varying width of the PSF can be used to determine the axial center position of a particle. The exemplary images on top illustrate this variation with respect to the relative axial position. The black curve is a correlation function determined as the best fit to the measured particle positions. The right red arrow indicates the center position, but knowing the parametrization of the correlation function also allows to determine any relative axial position from a single image. (Adapted from Oijen et al. 1998, with permission from Elsevier.)

cles in a feedback approach while the other acquires multiple particles in parallel and determines their 3D position using off-focus imaging.

In the so called feedback approach, Levi et al. 2005 used 2PM to consecutively orbit a focused laser beam around a single particle at two different focal planes. The 3D position is then determined from the resulting periodic intensity profile. They do not require an exact model of the PSF because the computation of the center position is only sensitive to the determination of distinct intensity minimums. The determined 3D position is used to define the scanning position for the next iteration. The system achieves a temporal resolution of 30 Hz and an axial detection range only limited by the objective's working distance. Katayama et al. 2009 implemented the same algorithm, but used two pinholes in a confocal setup to orbit the particle at two focal planes in parallel. They also acquired WF images so that the ROI can be selected automatically, and the trajectory of a particle can be correlated with the cellular environment. Similarly, Lessard et al. 2007 used a confocal configuration, but focused the image into four optical fibers. They act like confocal pinholes so that their back projection yields four different confocal volumes arranged by a tetrahedral geometry in the sample. By maintaining an axial offset between the two pairs of fibers, the measured intensity distribution is used to compute the full 3D position of a particle. This was again implemented in an iterative procedure and facilitates temporal resolutions in the kHz range.

In contrast, off-focus imaging does not require any feedback scanning procedure and is used with standard WF configurations. The basic idea was first proposed by Speidel et al. 2003. They found that the radius of the outer ring of a particle's diffraction pat-

tern scales linearly with the axial focal distance to the real center of the particle. This correlation holds true for focal distances larger than 0.5 μm above the particle and is applicable as long as the particle is detectable off-focus. The axial range is limited to a few micrometer. Well separated particles can be simultaneously measured, and the temporal resolution is only limited by the photon efficiency of the imaging system. The determined correlation function has been further analyzed by Wu et al. 2005. They showed that due to spherical aberrations of the lens, a monotonically changing dependency should be calibrated.

It can be concluded that the fundamental concept, initiated by off-focus imaging, has prevailed. This is particularly due to its compatibility with SML techniques like PALM, STORM and FPALM that have found tremendous application. The ability to obtain large number of trajectories has proven to be more relevant than the detailed analysis of a few single trajectories. The work of Speidel et al. 2003 has been improved and generalized to the concept of exploiting the relationship between 2D features of the PSF and the relative axial center position of a particle with respect to the imaging plane. Given that such an axial correlation is known, it allows for very fast determination of the 3D center position from a single 2D image. The accuracy is only limited by the number of detected photons.

The primarily utilized property of the PSF is their width ω. Based on the axial correlation function described in Equ. 26, it determines the relative axial position of the focal plane to the center of the particle (see Fig. 26). However, extraction of the axial position has proven difficult for two reasons: (1) owing to the axial symmetry of the PSF it cannot be distinguished if a particle is above or below the focal plane, and (2) the shape of the PSF contains only limited information about the axial position of the particle within the depth of field of the microscope.

These difficulties have led to the development of approaches that encode the complete 3D position in the 2D PSF. They can be classified into (1) astigmatism-based off-focus imaging, (2) PSF engineering, (3) multifocal plane detection, and (4) interferometric dual-objective imaging. Their concepts are introduced in the following, and schemes of their most dominant representatives are illustrated in Fig. 27.
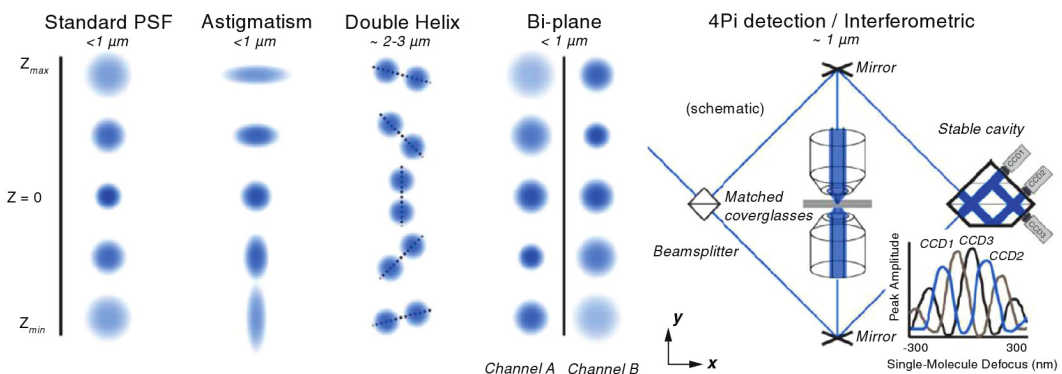

Figure 27: Schematic illustration of how the most dominant representatives of astigmatism-based off-focus imaging, PSF engineering, multifocal plane detection and interferometric dual-objective imaging encode the axial position in the 2D PSF. (Adapted from Sahl and Moerner 2013, with permission from Elsevier.)

4.3.4.1 *Astigmatism-based Off-focus Imaging*

Astigmatism-based off-focus imaging breaks the axial symmetry of the PSF and adds additional axial information by intentional introduction of optical aberrations into the light path. The most basic approaches are uniaxial bending of the dichroic mirror (Ragan et al. 2006) and the introduction of a cylindrical lens in the emission light path (Kao and Verkman 1994). Both approaches yield a PSF that becomes elliptical instead of rotationally symmetric (see Fig. 27). The introduced ellipticity now allows for unambiguous determination of the relative axial position of a particle. This can be implemented by computation of a correlation function using the generalized moment (Ragan et al. 2006) or by separate axial analysis of the two lateral widths. The latter can be obtained from either the distance between the minimum and maximum of the lateral derivatives (Kao and Verkman 1994) or the fit of an elliptical Gaussian function (Holtzer et al. 2007). The ellipticity is not considered as a rejection criterion anymore, instead it is intentionally introduced and looked for during the localization procedure. As the lateral position is unaffected by the introduced astigmatism the 3D position can already be obtained from each individual 2D image.

Owing to its broad applicability, the simple adjustment of the strength of the astigmatism and the smooth integration into the well understood localization framework, the combination of a cylindrical lens and fitting of a Gaussian function has become the preferred configuration for astigmatism-based imaging. It has already been applied to live-cell SPT with QDs as fluorophores (Holtzer et al. 2007). The authors also showed that Equ. 26 is still a valid description for the axial dependency of the individual lateral widths, which allows for direct computation of the axial position. Furthermore, computation of the theoretical limits for the LA was extended to all three directions accounting for mixture of Gaussian and Poisson noise. The results indicate that the axial accuracy is largely improved, particularly in the vicinity of the particle center, while the lateral precision is only marginally reduced. Besides these analytical efforts, broad application of astigmatism-based imaging has been triggered by implementation as 3D STORM (Huang et al. 2008b) and by subsequent extension to a larger analysis range by axial scanning of the probe (Huang et al. 2008a).

Astigmatism-based 3D imaging has been improved in many directions. For instance, Spille et al. 2012 have moved the analysis down to 200 μm deep into living tissue using light sheet fluorescence microscopy (LSFM) (Ritter et al. 2010). LSFM is different from the standard epifluorescence configuration in that the excitation light is focused from the side into the sample, yielding similar optical sectioning like SCM. Extension to high particle densities has been presented by Babcock et al. 2012. They adapted the high density algorithm of Holden et al. 2011 to astigmatism-based imaging by allowing for variable sized PSFs. However, high particle densities can only be resolved if minimal lateral distances are maintained. Pure axial distances cannot be resolved with 2D imaging, unless the number of particles would be known. Finally, scientists have tried to improve the image quality. Izeddin et al. 2012a generated an optical astigmatism with improved quality, using adaptive optics (AO) instead of cylindrical lenses. The employed deformable mirror detects and corrects the optical wave front for spherical aberrations, but at the same time also induces the required astigmatism. They could report improved LAs. Another approach for precision improvement was presented by Xu et al. 2012 who used two opposed objective lenses for image acquisition. Besides

doubling the photon collection efficiency, this also suppressed noise by averaging of two images and yielded considerable improvement of the axial LA.

4.3.4.2 *PSF Engineering*

Technically more demanding engineering of the PSF profile was reported by Pavani et al. 2009. They use a phase mask that performs phase-only spatial modulation of the light beam. This produces a double-helix PSF whose relative angular orientation of the two lobes encodes the relative axial position of the particle (see Fig. 27). The lateral position is derived from the center between the lobes. The lobe coordinates are computed from individual Gaussian fits to their intensity shape. This allows for simultaneous tracking of multiple particles as long as they are spatially well separated. In a subsequent application of this approach, Thompson et al. 2010 tracked QDs in living cells and analyzed the dependency of the 3D localization on the number of photons and the relative axial position.

A phase mask modification that creates only a single helix, termed corkscrew PSF, was proposed by Lew et al. 2011. They argue to be more photon efficient and to cover a larger axial range at the cost of having to acquire two consecutive images that are rotated by 180°. To simplify the setup, the use of only standard optical elements like pairs of nearly parallel mirrors (Sun et al. 2009) or prisms (Yajima1 et al. 2008) has also been proposed. These techniques create two images of the same scene, but maintain lateral shifts between the images that encode the axial position.

4.3.4.3 *Multifocal Plane Imaging*

Multifocal plane imaging adds additional axial information by simultaneous acquisition at multiple focal planes without scanning. Although the shape and axial symmetry of the PSF is not altered, knowing the order and distance of the different focal planes along the optical axis also allows for unambiguous determination of the axial position (see Fig. 27).

Simultaneous imaging of several focal planes can be accomplished by installing a beam splitter into the emission pathway. By implementation of different lengths for the resulting light paths, using either several cameras at different distances (Ram et al. 2008, Prabhat et al. 2004) or additional lenses that focus them differently on separated regions of one camera (Watanabe et al. 2007, Toprak et al. 2007), each camera or region effectively images a different focal plane in the sample. A less frequent alternative is the introduction of a distorted diffraction grating that changes the direction of light according to its diffraction order (Dalgarno et al. 2010). This directly projects several spatially separated focal plane images onto one camera.

These configurations have initially only been used for continuous 2D tracking over an enlarged axial range (Prabhat et al. 2004) or to improve the lateral LA of off-focus imaging (Toprak et al. 2007). The information of the additional planes can also be exploited to obtain an improved axial position estimate, particularly in the vicinity of the particle center. This has been accomplished by combined fitting of either analytical (Ram et al. 2008) or experimental (Juette et al. 2010) 3D PSFs to the different focal plane images or by creation of correlation functions from either normalized intensity differences (Watanabe et al. 2007) or image sharpness metrics (Dalgarno et al. 2010) of individual planes. Such configurations have been applied to 3D live-cell SPT applications using QDs (Ram

et al. 2008, Watanabe et al. 2007). Analogous to astigmatism-based imaging, they have found broad application after successful combination with FPALM (Juette et al. 2010).

Improvements of multifocal plane imaging focused for instance on increasing the temporal resolution. Juette and Bewersdorf 2010 report temporal resolutions in the kHz range for tracking single particles. They were continuously imaged in the focus of a laser beam by means of a movable mirror. These extremely high acquisition rates had been achieved because tracing just a single particle only requires to readout a few lines of the camera and focusing on a small image region yields strong local fluorescence.

An additional orthogonal view of the same region in the sample was obtained by Tang et al. 2010. They used a second focal plane to focus on an angled mirror that was placed inside the sample. After coordinate transformation, this yields nearly isotropic 3D LA because both planes effectively image the particle in focus. 2D localization algorithms can be similarly employed for all directions. However, only few and very well separated particles can be tracked.

4.3.4.4 *Interferometric Dual-objective Imaging*

With respect to the number of detected photons, interferometric PALM achieves the highest 3D LA (Shtengel et al. 2008). This technique exploits the wave-particle duality of light by self-interference of a photon that traveled over two distinct optical paths. It acts as its own coherent reference beam. The self-interference takes place in a 3-way beam splitter and modulates the relative intensity of three output beams. By using three cameras, the axial position can be determined from the relative particle intensities in the images (see Fig. 27). This technique could until now only be applied to fixed samples, and since the relative axial emitter position is essentially encoded in the relative phase of the beams, it can be unambiguously determined only in the range of $\sim \lambda/2$. By evaluation of higher moments of the PSF, Aquino et al. 2011 could extend the axial range to $\sim \lambda$.

Evaluation

At present, there is no study that compares the performance and properties of all algorithms. A selection just based on the data presented in the respective publications is difficult because different samples and fluorophores have been used. Complete information including the 3D accuracy, the number of signal and background photons, the axial detection range, or the frame rate has not always been provided. On these grounds, the specifications provided in Fig. 27 have to be taken with caution and are only directly valid for the specified reference.

Two studies that evaluate typical representatives of the main approaches are available. Mlodzianoski et al. 2009 assessed the performance of astigmatism-based and multifocal plane algorithms. They used the reports of Huang et al. 2008b and Holtzer et al. 2007 respectively that of Juette et al. 2010 for the selection of realistic experimental parameters. Badieirostami et al. 2010 also included the PSF engineering algorithm of Pavani et al. 2009. Both studies mainly differ in their type of performance analysis. Mlodzianoski et al. 2009 measure the respective PSF model and assess the performance of the algorithms from repetitive acquisitions experimentally. Badieirostami et al. 2010 involve analytical PSF models and compare only theoretical predictions.

Both studies consider varying signal and background levels and arrive at similar conclusions that can be qualitatively summarized as follows. Analogous to the lateral LA, the axial LA of all techniques scales with the number of photons and is about 2.5-5 times worse than the lateral LA. Although the obtained accuracy is comparable, astigmatism- and multifocal plane-based approaches are dependent on the relative axial position and maintain reasonable accuracies only in a range of $\sim 1\ \mu\mathrm{m}$ around the native focal plane. In comparison, double-helix localization exhibits effectively constant accuracy over an axial range of $\sim 2\ \mu\mathrm{m}$. Multifocal plane detection is also capable of imaging in this extended range, but with considerably reduced axial accuracy. Astigmatism-based approaches can be advantageous for low photon count experiments because multifocal plane detection employs beam splitting that distributes the light on twice as many pixels. Temporal resolution is not an issue of any of these techniques because they are usually implemented in WF configurations.

All in all, PSF engineering and interferometry techniques are generally accepted to provide the best overall LA, but the other techniques have found more widespread application. This is particularly reasoned by their considerably lower experimental complexity and their simple integration into various imaging configurations.

The influence of important aspects like high particle density or optical aberrations has not yet been considered. Current studies are only based on theoretical analyses or isolated fluorescent beads rather than realistic experimental environments. For these reasons, the above conclusions have to be considered as guidelines, but the true performance of a particular implementation always has to be determined experimentally.

All presented methods require proper calibration of their axial correlation functions. However, so far their availability has been taken for granted and was not considered. This aspect is the content of the next section.

4.3.5 3D Particle Localization in Complex Tissue

There are a few approaches that tried to employ the presented 3D localization methods for diffusion parameter estimation deep in living brain tissue (Spille et al. 2012, Izeddin et al. 2012a, Huang et al. 2008a, Aguet et al. 2005), but none adequately addresses the RIM whose influences strengthen with increasing imaging depth and is therefore not negligible anymore.

So far, the RIM has been merely introduced as an effect that reduces the influx of light into the objective by effectively decreasing the angular aperture (see Sect. 3.1.4.3). However, the resulting effects are manifold and have been extensively studied theoretically (Sheppard and Török 1997, Hell et al. 1993) and experimentally (Neuman et al. 2005, Diaspro et al. 2002). In short, the RIM results in a focal shift because of geometrical distortions and yields a loss of spatial resolution as well as intensity owing to spherical aberrations. These effects are now introduced in more detail followed by a review of approaches that try to compensate for these effects.

4.3.5.1 Influence of the RIM on 3D Localization Methods

Fig. 28a illustrates the imaging situation without and in the presence of the RIM for objective lenses corrected for use with cover slips. Then the RIM occurs at the interface between the sample and the cover slip. For objective lenses that do not require cover

slips, the RIM would arise at the interface between the actual neuronal tissue and the immersion medium.

In consequence of the refraction of light at the interface between the mediums, the true actual focal position differs from the expected focal position. In the most frequent case where $n_1 > n_2$, the actual focus is shifted towards the cover slip. This means in practice that any axial movement of the objective results in an actually shorter focal movement inside the sample, and the axial image appears elongated. The RIM also induces spherical aberration. Rays from a point source at the focal plane are refracted to a different degree at the interface. This depend on their angle of incidence. Outer rays are stronger refracted than central rays and are no longer exactly focused into the same spot at the back focal plane. This results in a blurring of the PSF, which intensifies as a function of the imaging depth and primarily deteriorates the axial resolution. On top of that, the PSF becomes more and more asymmetric with respect to the axial axis as the imaging depth increases. Since the spherical aberration blurs the excitation as well as the emission PSF, excitation light is further spread into regions out of the confocal volume and less emission light passes the pinhole. The maximum detectable intensity also decreases with the imaging depth. The absorption of light by the material is negligible. The described impacts on the observable 3D PSF are presented in Fig. 28b.

Now, what are the consequences for the application of 3D localization methods deep in living tissue? The exponential decrease in intensity certainly lowers their achievable LA, but does not inherently preclude their utilization. The focal shift has a virtually linear relationship with the depth in the tissue and can be considered using a constant scaling factor for the axial positions (Hell et al. 1993). Since diffusion analyses only consider relative distances, the scaling factor can actually be neglected. It only has to be considered if the absolute depth of a particle is of interest.

The situation is different for the loss in resolution and the asymmetry of the PSF. These effects change the local relationship between features of the PSF and the relative axial position of a particle. Many applications of 3D localization methods still assume that a single 3D PSF and consequently a constant relationship is valid across the sample (Wang et al. 2013, Babcock et al. 2012, Huang et al. 2008b). This might be acceptable in primary cultures, where images are often acquired in close proximity to the cover slip, but in order to image cells in their natural environment the assumption of a constant 3D PSF is apparently not valid. Instead, the required axial relationship varies as a function of the imaging depth and the ratio of the RIs. By ignoring this fact, current techniques do not only experience a decrease in their axial LA, the computed axial positions also exhibit a depth dependent systematic error (SE) (Sokoll et al. 2011, Deng and Shaevitz 2009). They are simply incorrect although the accuracy with that these false values are computed might be high.

To compute the correct axial position the unique relationship between features of the 2D PSF and the relative axial position has to be known at every depth. Approaches that address this issue can be classified into (1) strategies that minimize the influence of the RIM, (2) methods that perform prior depth-dependent calibration measurements, and (3) computational techniques that try to predict the aberrated 3D PSF.
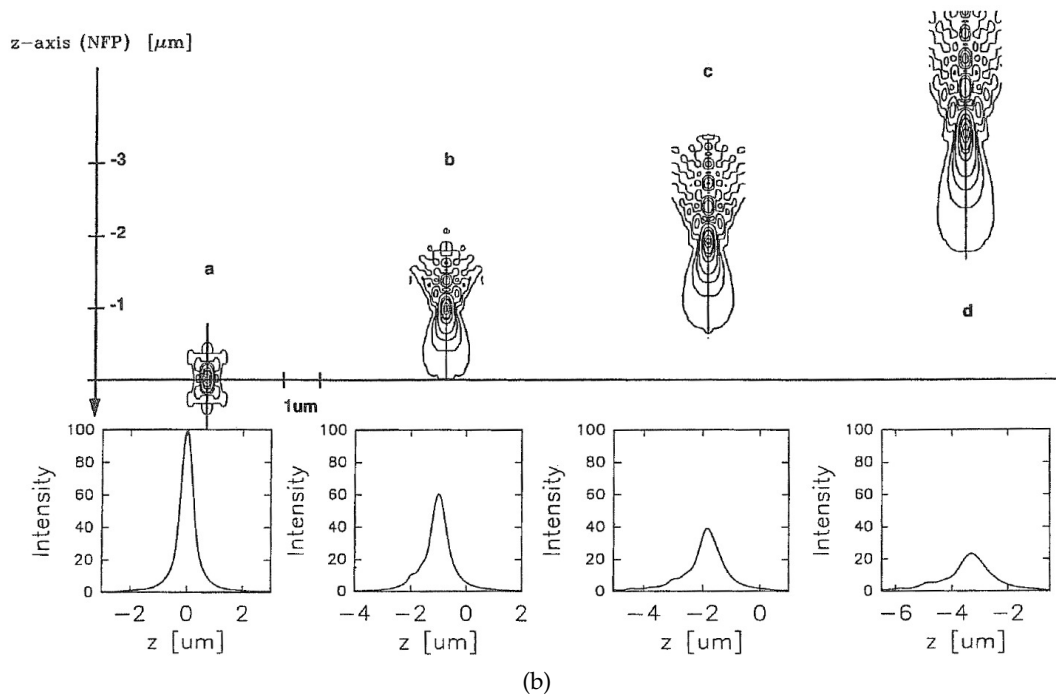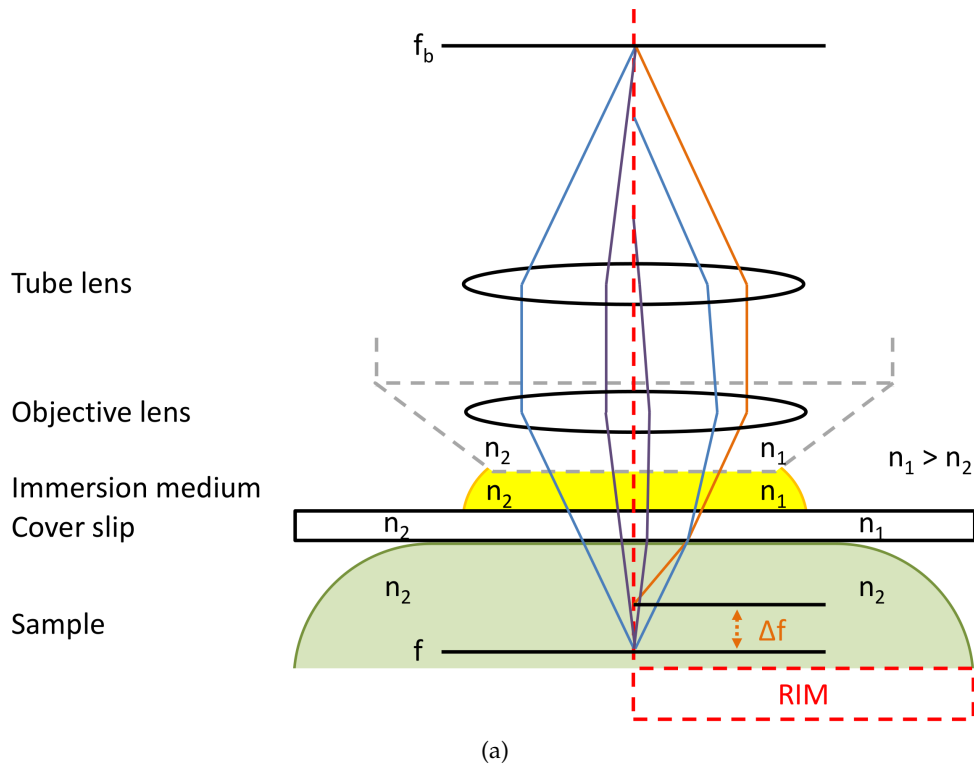
Figure 28: (a) Imaging situation without and in the presence of the RIM. As a result of the RIM, the actual focus is shifted (orange ray) and central (purple) as well as outer (blue) rays are not focused into the same spot. (b) Impact on the PSF. It appears elongated, blurred, axially asymmetric and the intensity decreases. (Reprinted from Hell et al. 1993, with permission from John Wiley and Sons.)

4.3.5.2 *Minimizing the Influence of the RIM*

Since the imaging depth and the RI of the sample are the major parameters for the deteriorating influence of the RIM (Sheppard and Török 1997), the most consequent

practical strategy is the usage of an appropriate objective. Water (Nägerl et al. 2008), silicone (Shimozawa et al. 2013), or glycerol (Urban et al. 2011) immersion objective lenses have been used to most closely match the RI of the samples. The RIs of common mounting mediums as well as of different tissues and organs are for instance listed by Bacallao et al. 2006. Further practical guidelines like the adjustment of the pinhole size or the mixing of mounting mediums are provided by Egner and Hell 2006.

If matching the RIs is not practical, Sheppard and Gu 1991 showed that spherical aberrations can be compensated by adding a correction lens. This alters the effective tube length of the objective and introduces an opposite-sign spherical aberration. Therefore, modern objective lenses are often equipped with correction collars to manually fine adjust for varying cover slip thicknesses, depths in the tissue, and temperature-dependent RI changes (Keller 2006).

Since in biological samples the aberrations introduced by the RIM are usually too complex to be fully compensated by such static methods, AO schemes from the field of astronomy have recently been applied to microscopy (Schwertner et al. 2004). The key idea is to measure the aberrated wave front and to introduce opposed spherical aberrations for compensation. In so doing, AO schemes are capable of restoring the original PSF shape. Their direct implementation using point-like reference sources is more complicated in live-cell imaging. In thick biological samples the references usually do not appear point-like, and background as well as out-of-focus light creates ambiguities (Booth 2007). Still, reasonably improved PSF shapes have been reported for confocal (Azucena et al. 2010), WF (Izeddin et al. 2012a), and STED (Gould et al. 2012) imaging configurations.

An alternative to directly measuring the wave front, is maximization of the local signal intensity. Optimization schemes like genetic (Izeddin et al. 2012a, Sherman et al. 2002) or hill-climbing algorithms (Marsh et al. 2003) have been applied. These approaches require less instrumentation, but rely on iterative image acquisitions to optimize the shape of the induced compensatory aberrations.

4.3.5.3 *Doing Prior Depth-Dependent Calibration*

Calibration-based methods accept the aberrations induced by the RIM and consider them by adjustment of the axial relationship according to the imaging depth. This involves depth-dependent calibration prior to the actual experiment. One option is the measurement of 3D PSFs by axial scanning at various imaging depths. This can be done using fluorescent markers in an extra sample (Quirin et al. 2012) or by directly adding fiducial markers to the sample under observation (York et al. 2011). The latter variant prolongates the duration of the experiment, but is generally more precise. In either case, it is important to employ markers with spectroscopic properties similar to the actual fluorophores. For analysis, the reference images corresponding to the imaging depth of the acquisitions can be used to compute the correct axial relationship.

Alternative to calibrating the full PSF, the variation of the induced positioning error can be calibrated. Huang et al. 2008a implemented this idea in an astigmatism-based method and corrected the varying parabolic relationship of the PSF's width to the relative axial position. They found an approximately linear correlation between the true relative position at a certain imaging depth and the measured relative position. The latter was obtained using the, at this point incorrect, symmetric calibration curve measured at zero depth. The linear correlation is different for positions above and below

the focal plane, and the two corresponding scaling factors were used to correct the relative positions. By calibration of the course of the scaling factors as a function of the imaging depth the SE of the axial position could be compensated during analysis.

4.3.5.4 *Predicting the Aberrated 3D PSF*

In contrast to experimental calibration, computational methods predict the variable 3D PSF for a certain depth and fit it to the acquired data. The axial position can be computed with respect to the induced aberrations. Vectorial (Török et al. 1995, Hell et al. 1993) and scalar (Gibson and Lanni 1991) PSF models have been proposed. The latter is computationally much simpler since it depends only on a few standard parameters of the objective and the specimen. It was further extended by Hiware et al. 2011 to account for spatially varying RIs within a sample.

The model of Gibson and Lanni 1991 was used by Aguet et al. 2005 in a MLH-based fitting method. Initially, they need to acquire z-stack images of reference beads in the sample so that they know the absolute axial position of their focal plane with respect to the cover slip. Once they know their imaging position in the sample acquisition of single images is sufficient to compute the position of any other particle. The accuracy with that axial positions of fast moving particles can be obtained also depends on the feasibility to scan immobile reference beads. The determination of absolute positions from z-stacks was also implemented by Kirshner et al. 2013. They fit the same PSF model, but in the LSQ sense. They also included the model of Hiware et al. 2011 and adapted it for different courses of spatially varying RIs. Finally, McGorty et al. 2014 proposed to experimentally measure the PSF near the cover slip and predict their distortion with respect to the imaging depth and the RIM. They were also able to account for aberrations specific to the instrumentation by evaluation of the derived axial calibration curves.

Evaluation

All in all, it is apparent that there is currently a strong development towards analysis of biologically more relevant brain slices. Although, the mismatch in the optical system should always be reduced as much as possible, such static methods are not always viable or require continual manual interaction and subjective adjustment. AO are usually more effective, but are very demanding in terms of their technical instrumentation and setup. Furthermore, they exhibit the same basic disadvantage like calibration or computational approaches: they rely on some sort of calibration either before or during the experiment. To incorporate the current experimental conditions, which can significantly vary as a result of cover slip thickness tolerances, varying temperatures, or imperfect specimen contact to the cover slip, immobile reference point sources are required. These are hard to implement or to ensure in living brain tissue. Computational methods still rely on rather basic parameters of the objective and the specimen. Moreover, preceding measurements have to be conducted to adjust to the actual specimen.

4.3.6 *Linking Particles Over Time*

Next to the full spatial information, analysis of molecular dynamics also requires the information of the temporal domain. This involves linking multiple particle positions

over several frames to trajectories. Solving this association problem is especially difficult for tracking fluorescent particles in biological samples (Meijering et al. 2012, Jaqaman et al. 2008). Temporarily high particle densities and particles with varying types of motion are common. The number of particles usually varies over frames as particles might appear or disappear at the focal plane or undergo blinking (see Fig. 29), and it might look like particles split or merge, owing to the limited spatial resolution of the imaging system. Finally, linking can suffer from false or missing particle detections in the preceding steps. On top of that, only few information is available to resolve consequent ambiguities. Because particles appear as diffraction-limited spots in the image, next to their position, only simple properties such as intensity, velocity or acceleration can serve as additional features (Wu et al. 2008).
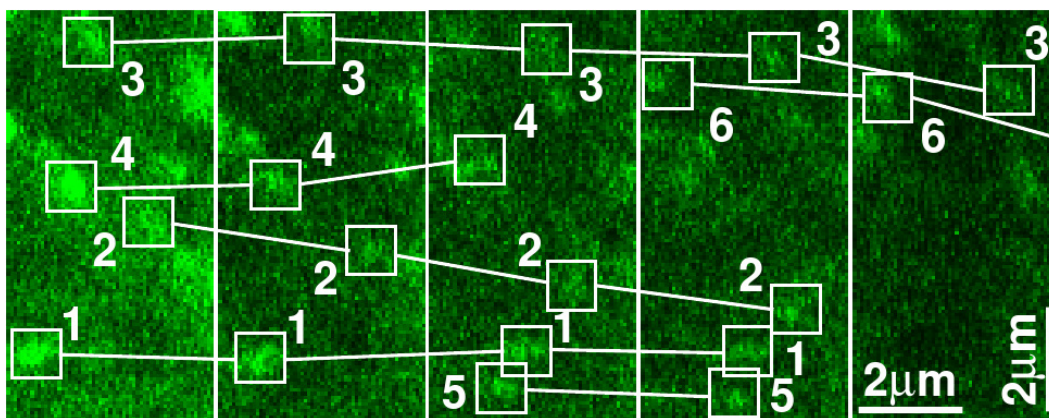

Figure 29: Linked particles in a set of time lapse images. Particles may closely approach each other (track 1 and 5), newly appear (track 5 and 6) or disappear (track 4). (Reprinted from Smal et al. 2007, copyright (2007) IEEE.)

To solve such multiple target tracking problems, multiple hypothesis tracking (MHT) has generally been accepted as the preferred method because it is almost globally optimal in space and time (Jaqaman et al. 2008, Blackman 2004). Based on measurements of particle positions and assumptions on the particle behavior, MHT computes the probability tree for all possible associations over all frames. Multiple assignment of a particle with particles in adjacent frames is explicitly allowed. Potential conflicts are not resolved immediately, instead it is assumed that future data will clarify it. The most probable paths that are non-conflicting, thus, do not contain identical particles in any frame, are eventually chosen as the solution for the tracking. Although an algorithmic formulation for MHT exists (Reid 1979), it is generally not applicable to scenarios with more than a few particles and frames owing to the exponential increase in complexity (Jaqaman et al. 2008). Established algorithms usually attempt to approach the globally optimal solution by temporal separation and determination of locally optimal solutions.

They can be divided into local linking approaches that consider only two consecutive frames and global linking approaches that take multiple adjacent frames into account (Meijering et al. 2012). Considering local strategies, the simplest approaches just look for the nearest neighbor of each particle in a circular region in the consecutive frame. Linkage of two particles is only performed if only a single particle is found in the respective search region. Their size can be defined by the user (Goulian and Simon 2000, Marston et al. 1996) or drawn from biophysical knowledge, for instance based on

the expected diffusion constant (Wieser and Schütz 2008). In high density situations this may still lead to multiple particle assignments that have to be resolved.

So called global nearest neighbor algorithms enforce a uniqueness constraint stating that each particle can only belong to a single trajectory. To ensure uniqueness, potentially conflicting assignments are resolved by taking the distance to a potential linking candidate as a weight in a bipartite graph and finding the optimal assignment defined by the minimal global weight (Vallotton et al. 2003, Schmidt et al. 1996). To increase the significance of the weights, further similarity measures can be included. Thomann et al. 2002 and Anderson et al. 1992 also integrated a relative change of intensity measure and Tvaruskó et al. 1999 combined distance, velocity, intensity, and shape area using fuzzy rules.

Global linking strategies still rely on locally optimal associations between consecutive frames. However, they construct complete trajectories over the whole image stack by considering multiple frames and trying to reconnect across gaps or capturing splitting and merging events. They can be classified into deterministic algorithms performing (1) spatio-temporal tracing or (2) graph-based optimization as well as (3) Bayesian estimation-based probabilistic methods.

4.3.6.1   *Deterministic Spatio-temporal Tracing*

Deterministic spatio-temporal tracing methods track particles under consideration of previous results and multiple frames ahead. They mainly attempt to close gaps in trajectories occurring from temporally dim, blinking or off-focus particles. Sage et al. 2005 particularly considered finding the path of well separated particles in noisy images. The path of a single particle is described by a cost function over all frames that includes the distance, a smoothness weight and the absolute intensity difference for the position at each frame to the previous. Since they define constraints on the particle movement, they can formulate it as a global optimization problem. After computing the weights of all possible local connections, the optimal path is then found by means of dynamic programming.

A conceptually similar approach was proposed by Bonneau et al. 2005, but they enforce smoothness by treating particle paths as geodesics in a Riemannian metric and are capable of tracking multiple particles. This is done on the expense that particle trajectories are no longer globally optimal. They compute initially unambiguous partial tracks based on some maximal traveling distance between consecutive frames. These are subsequently combined to complete tracks by finding geodesics between end and start points of partial tracks using a variant of the fast marching method. Taking the diffusion constant estimated from the corresponding partial tracks and the intensity in the image into consideration, this minimizes the energy of paths across gaps.

Relying on the sub-pixel LA produced by their deflation strategy, Sergé et al. 2008 provide multiple particle tracking at high densities. They iteratively extend the tracks by finding the most likely connections according to the product of three weights defined by probability laws. All weights include past information using a sliding temporal window and are also computed for particles possibly reconnected over several frames. They integrate a probability for the expected position that extends over temporal gaps according to the estimated local diffusion constant. Furthermore, they treat bleaching as being negligible and enforce constant intensities by a probability law derived from the preceding intensity distribution because the algorithm is particularly

designed for QD experiments. Their third weight consists of a reappearance probability for discontinued tracks that decays exponentially over time.

4.3.6.2 *Deterministic Graph-based Optimization*

Graph-based algorithms construct weighted bipartite graphs that represent connections over several frames and solve this assignment problem (Burkard and Çela 1999). Sbalzarini and Koumoutsakos 2005 construct a bipartite graph for each frame that links all particles in that frame with all particles in a preset number of subsequent frames. This allows for consideration of blinking events. The links are given costs computed from the quadratic distance and the quadratic differences in the intensity moments of first and second order between two particles. Splitting and merging events are explicitly excluded. Dummy particles are introduced to cope with varying number of particles between frames. To find the optimal set of links, they extend the algorithm of Dalziel 1993, which is based on the transportation problem, to deal with multiple frames.

Jaqaman et al. 2008 explicitly designed their method for high particle densities and treat splitting and merging as additional separate events. They first create partial tracks by frame-to-frame particle linking similar to Sbalzarini and Koumoutsakos 2005, but consider only two consecutive frames at a time. Subsequently, a second bipartite graph is constructed that links the end and start points of the partial tracks. Each track appears in each of the temporal events track initiation, termination and reconnection as well as splitting and merging. Because splitting and merging events might happen at intermediate positions of a partial track, even the individual frame positions of each track are included in the graph. Both linking steps are formulated as linear assignment problems, where the first considers the particle and the second the partial track assignment. The corresponding cost matrices include distance and intensity properties. By solving the linear assignment problem, they find a global solution in space and time because all tracks compete with each other.

4.3.6.3 *Probabilistic Methods*

Recently, probabilistic methods experienced major attention. They generally rely on spatio-temporal tracing, but employ a Bayesian estimation framework. Instead of making hard decisions at every step, they model the uncertainty about potential particles and their potential associations by assigning probability (Meijering et al. 2009). This uncertainty is kept up during tracking until eventually hard decisions have to be made to decide for a final solution. They also include knowledge about the dynamic behavior of the particles and combine these predicted measurements with measurements obtained from the image.

Within the Bayesian framework, this strategy is implemented by sequential state estimation, where a state describes the information about a system at a certain time point. This is the information that is to be estimated and may include the particle position, intensity, velocity or acceleration. Given a sequence of measurements, the state of each time point is then estimated in a recursive two-step procedure (Godinez 2013, Wu et al. 2008). First, the posterior distribution of the current state is predicted by evolving the prior state distribution with a dynamic model. And second, Bayes's theorem is applied to update the current posterior state distribution with the measurement model that de-

fines the probability of the observed measurements given the current state. In so doing, all previous measurements are exploited to evolve the state of individual particles over time.

This can be analytically computed using the well-known Kalman filter and has been implemented in a tracking algorithm by Genovesio et al. 2006. Since the dynamics of particles are the information to be determined from the measured trajectories, including a particular motion model is critical. Therefore, they incorporate several different Kalman filters in an interacting multiple model algorithm.

A more suitable analytical computation scheme is the particle filter (Isard and Blake 1998). It can handle nonlinear and non-Gaussian dynamics as well as noise. The key idea is the representation of the posterior state distribution with random state samples and associated importance weights. By means of these random samples, multiple image positions are queried in parallel to determine the position of an object. This abolishes the former separation of detection and linking procedures and yields greater robustness to preceding errors during the detection step (Godinez 2013). Propagation of multiple particles can be modeled by using a single mixture model (Smal et al. 2007) or several independent particle filters (Godinez et al. 2009). Both approaches have been combined by Smal et al. 2008a in order to adjust to the local particle density. They also incorporated different motion models. Chenouard et al. 2009 increased the competition of tracks by allowing for MHT over some future frames. By evaluation of the probabilistic model for these frames, the algorithm can cope with false measurements using future data.

Evaluation

Two studies have compared biologically motivated tracking algorithms of different classes. A classical study was conducted by Godinez et al. 2009. They compared deterministic and probabilistic algorithms on simulated and real images and considered gap closing, spurious particle detections and varying SNRs. For deterministic algorithms they solely involved local strategies, which are clearly not competitive. In contrast, Chenouard et al. 2014 performed an open competition and invited scientists to apply their algorithms to a published data set. Although this also does not ensure to be entirely representative, it complies with the general criticism that public data sets are unavailable (Saxton 2008). Their purely synthetic data set particularly addressed varying particle dynamics, density and SNR. They analyzed the total workflow of SPT algorithms disallowing for assessment of the individual steps.

Notwithstanding their conceptual differences, both studies arrived at similar conclusions: global linking strategies are generally to be preferred over local strategies. Within global strategies, probabilistic methods tend to provide less fragmented results. This is notably due to the inclusion of dynamic models and the reliability of the measurements, allowing to cope with spurious detections. Chenouard et al. 2014 also emphasized that the best algorithms were perhaps overtrained for the particular data set. The expected particle density and the SNR are the main factors that have to be considered for appropriate algorithm selection.

These studies and also the majority of the individual methods did not directly address the desire for 3D tracking. Nonetheless, it can be expected that virtually all algorithms are extendable to 3D linking. This can be achieved by adjustment of the distance measures as well as other criteria such as velocity, acceleration or dynamic models.

4.3.7 *Implications for the Thesis*

In this section the state-of-the-art methods for all components of the complete SPT work-flow were reviewed and individually assessed. Since this thesis particularly addresses their application in brain slices, counteracting the influence of the RIM is the primary requirement.

By reviewing the proposed solutions, it has to be concluded that current methods are generally impractical owing to their specialized technical implementation or parallel calibration for each acquisition. The manual experimental efforts are generally high and have impeded the widespread application of current approaches until today. This is also reflected in the fact that these methods seem to have been used so far only for static, but not for dynamic analyses in brain slices (Deschout et al. 2014, Specht et al. 2013, Gould et al. 2012). For dynamic analyses in living tissue, acquisitions have to be immediately executable without delaying calibration procedures that impair the viability of the sample.

On these grounds, an online calibration method for astigmatism-based 3D SPT techniques will be developed in the following sections. It determines the varying relationship between the width of the 2D PSF and the relative axial position of a particle directly from the acquired 2D image stream. This is accomplished with only minor preconditions and without individual calibration procedures. Thus, this method intends to solve the demand for making 3D SPT in living brain slices readily available. This enables analyses that maintain the viability of the sample, but does not add additional experimental efforts or compromises for the experimenter.

Since the accuracy of the proposed online calibration method strongly depends on the quality of the obtained particle shape parameters, emphasis is also put on the corresponding procedure. For 3D localization of multiple neighboring particles, the major difficulty is that owing to the required high number of free fitting parameters the likelihood function can become quite complex and may be difficult to maximize. In order to maintain robust estimation, reduction of the number of fitting parameters by fixing the peak intensity (Huang et al. 2011) or by proprietary optimization schemes (Babcock et al. 2012) have been proposed. Owing to the requirement of imaging particles off-focus, the former solution is not applicable. In order to avoid a proprietary optimization scheme, it will be proposed here to employ a standardized expectation maximization (EM) algorithm.

Both aspects have been incorporated into a 3D SPT workflow that is presented in the following.

4.4 3D SPT IN BRAIN SLICES - ALGORITHM OVERVIEW

A schematic overview of the proposed workflow for fast nanoscale 3D SPT deep in living samples is presented in Fig. 30. It basically follows the general guideline for SPT applications. Particle candidates are detected first. Then their sub-pixel locations and shape parameters are determined. Finally, they are linked to trajectories.

To extract the required 3D information an astigmatism-based method, employing a cylindrical lens, is used. It was chosen for its ease of implementation, the ability to track multiple particles in parallel, and because the method itself sets no limit on the temporal resolution. Furthermore, it is applicable to various imaging configurations.

Owing to the depth-dependent aberrations induced by the RIM, the axial position cannot be immediately accessed just by prior calibration of a single axial correlation function. For that reason, the workflow additionally includes an online calibration procedure that estimates the required axial calibration curves directly form the 2D image stream. As it will be explained later, the online calibration method has relatively low prerequisites, but draws on 2D particle trajectories. Therefore, a preceding 2D linking procedure is introduced.
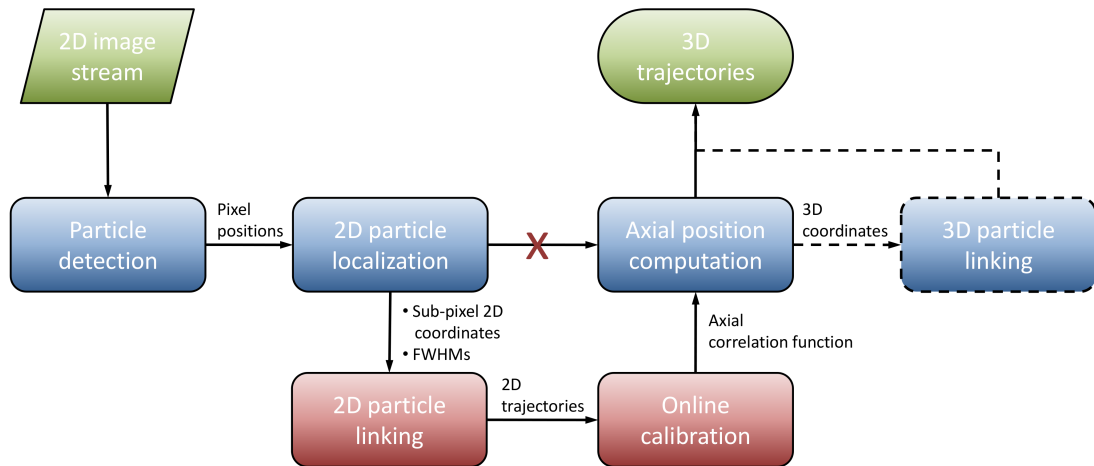
Figure 30: Workflow of the 3D SPT algorithm. In contrast to the general guideline, it additionally includes a 2D linking and an online calibration procedure. The dashed lines indicate optional procedures.

Since this thesis focuses on the online calibration and the shape estimation procedures, but the total SPT workflow has to be implemented for proving their functioning, well-established methods were implemented for the particle detection and the 2D linking procedures. It was not attempted to achieve further development in these areas. Also, some simplifications have been made, and they will be addressed in the corresponding sections. Since a multitude of powerful 3D linking tools is already publicly available (Meijering et al. 2012), the final 3D linking is considered as an optional procedure and was not implemented in this thesis.

In the remainder of this chapter, the fundamental capability to derive 2D diffusion properties deep in brain slices will be proven first. Sect. 4.6 and 4.7 focus on the particle detection and localization procedures. The latter also includes the estimation of each particle's individual FWHMs. In Sect. 4.8 it will be described how the particle locations are used to create the required 2D trajectories. This is followed by Sect. 4.9 that analyzes the influence of the RIM in detail and explains the proposed axial online calibration method. Sect. 4.10 finally presents experimental results.

4.5 THE PROOF OF PRINCIPLE: 2D SPT IN BRAIN SLICES

Before the 3D SPT workflow is presented, a suitable imaging configuration as well as fluorophores for application deep in living brain tissue have to be selected. It is the purpose of this section to prove that diffusion characteristics are in fact accessible in brain slices. The corresponding line of argument has originally been published in Biermann et al. 2014. It was the joint work of members of the group Molecular Physiology

at the LIN in cooperation with scientists from Bordeaux, Hamburg and Münster. In the following, the key results are presented.

Owing to the deterioration of the optical signal, application of the various imaging configurations to thick biological samples remains a major challenge until today (Schermelleh et al. 2010, Triller and Choquet 2008). Relatively few approaches have been reported. For instance, STED microscopy has been used to localize synaptic molecules in living mouse brains (Testa et al. 2012, Berning et al. 2012). They report maintenance of high spatial resolution down to 50 µm within the specimen, but the general problem of this technique remains: the temporal resolution is only in the range of several seconds, even for small fields of view. Also, STED microscopy does still not allow for direct observation of individual molecules in such complex environments. WF based SML methods are an alternative. They have been applied to whole cells, and frame rates up to 100 Hz have been reported (Huang et al. 2008a, Juette et al. 2010). Since optical sectioning is inherently missing, the penetration depth of these methods is limited to only a few micrometers. Photobleaching and photoactivation of fluorophore populations is still challenging with WF excitation across the whole sample (Zanacchi et al. 2011). To cope with these disadvantages, SML has been combined with 2PM that provides the required optical sectioning (Vaziri et al. 2008, Fölling et al. 2008). The penetration depth could be increased to 15 µm. 2PM has also been classically used with fluorescent nanoparticles (Ragan et al. 2006). This yields imaging depths down to 100 µm, improved SNRs and frame rates up to 100 Hz. Similar temporal resolution and sensitivity can also be obtained by using quite novel LSFM. Extension of the imaging depth down to 200 µm has been reported using QDs in an aqueous solution (Ritter et al. 2008) or fluorescent beads in salivary gland cells (Spille et al. 2012).

To investigate molecular dynamics of lipids and transmembrane proteins in correlation with synaptic membrane compartments the usage of SDCM in combination with QDs is proposed here. Owing to their outstanding spectroscopic properties, QDs are very appropriate for SPT applications. In comparison with other types of fluorophores, they are very bright, exhibit high photostability, have very narrow emission spectra, exceptionally large Stokes shifts, and the surface of QDs can be functionalized for a large variety of molecules (Michalet et al. 2005). Although genetically encoded FPs are unbeatably specific labeling membrane proteins via antibodies has several advantages for the envisaged purpose. First, depending on the membrane turnover of the molecule of interest only the surface population of this molecule is detected, and second, the most suitable QD variant can be selected for a particular application. Finally, endogenous membrane molecules can be investigated in their native cellular environment without overexpression.

To access QDs deep in living tissue, LSFM and 2PM seem to be the preferred tools. However, by the time of selection, LSFM has not been commercially available (Santi 2011), and because the maintenance costs are very high, 2PM was simply not affordable by the group Molecular Physiology. Therefore, SDCM was chosen since it is conceptually similar to 2PM, but comes at lower costs. A setup that at its core is based on a confocal spinning disk unit (CSU) was established. It is presented in Fig. 31. It allows to image living samples at depths of several tens of micrometers (Shimozawa et al. 2013) with a large field of view, while maintaining high temporal resolution that is only limited by the speed and sensitivity of the camera. To allow for imaging into brain slices with

and without a cover slip, an upright configuration was chosen. It can be expected that by using such a well-established, commercially available, and affordable setup, the findings presented in the following become widely accessible and reproducible.


Figure 31: The confocal spinning disk setup that was established by the group Molecular Physiology. The major components are the upright microscope Olympus BX51WI and on top the Yokogawa confocal scanner unit CSU-X1 as well as the EMCCD camera Andor iXon^{EM}+ 897. The lasers and the control units are located in the racks on the right.

The major contributions that will be provided in the following are the answers to the questions: (1) can QDs deeply penetrate and specifically bind to membrane molecules at cells in cultured brain slices? (2) is the extracellular space permeable enough to enable diffusion measurements with QDs, and, more specifically, (3) is a CSU-based imaging system sensitive enough to distinguish between different cellular compartments and subpopulations of molecules by means of diffusion?

4.5.1 *Quantifying the Performance of the SDCM Setup*

Before these questions are finally addressed, first of all the performance of the established setup shall be assessed. The related question is: what is the maximum achievable performance using QDs? This effort is reasonable since it enables derivation of the most effective parametrization and subsequent assessment of the influence of the sample. Also, the performance limits can be identified so that the obtained measurements can be checked for being plausible.

A related, technically and biologically very important, parameter is the excitation power. It controls the imaging quality and the viability of the specimen. It is known that the photon transmission efficiency is relatively low for SDCM (Toomre and Pawley 2006).

To still enable reasonable SNRs at large imaging depths, a tuneable laser[1] providing up to 1000 mW was additionally installed. The measured transmission efficiency of the presented imaging configuration is depicted in Fig. 32a. As expected from the fiber coupling and the light transition through the spinning disks, the resulting excitation power in the infinity space between the CSU and the objective is only about 8 % of the input laser power.

In order to determine realistic upper bounds for the key performance characteristics of the setup, 655 nm emission wavelength QDs[2] were immobilized on cover slips and imaged using a water immersion[3] and an oil immersion objective[4]. 655 nm emission was chosen to improve the SNR since autofluorescence of cells occurs mainly in the green region of the spectrum and is reasonably low in the red region (Nienhaus and Nienhaus 2013, Schütz et al. 2000b). The water immersion objective was tested to achieve high imaging depths since it matches the RI of the sample most closely. The oil objective was expected to provide better imaging quality at intermediate depths, owing to its higher NA. From Fig. 32a it is also apparent that the resulting excitation powers at the focal plane of the objective lenses are about 5 % and 3 % of the input laser power for the water and oil objective, respectively.

For the following measurements, immobilized QDs were embedded in purified water respectively in Zeiss Immersol 518 F oil. With the oil objective, QDs had to be imaged through a cover slip. Fig. 32b-32c plot the SNR and the lateral LA as functions of the input laser power for each objective. The frame rate was always 30 Hz. The SNR was computed according to Cheezum et al. 2001. As expected, it clearly improves as the excitation increases. Although the total light throughput of the water objective was higher, the obtained SNR is about twice as good for the oil objective. This is most likely due to the fact that the oil objective focusses the excitation light much better, and consequently the resulting intensity is higher.

With respect to the lateral LA, many publications often only provide a theoretical value, but this predicts just the lower bound for the achievable LA, based on the considered imaging conditions. Experimental assessment is more realistic since the fitting procedure as well as experimental factors like optical aberrations or the thermal drift of the microscope are considered. Consequently, both versions are provided here. Experimental derivation involved iterative measurement of immobilized QDs and calculation of the SD of their center coordinates. This is taken as the measure for the LA (Kubitscheck et al. 2000). The theoretical prediction is based on the number of photons per particle N_p, the background noise σ_b, and the pixel size in the object space d_{po} (Thompson et al. 2002):

$$\left\langle (\Delta s)^2 \right\rangle = \frac{\sigma_{xy}^2 + d_{po}^2/12}{N_p} + \frac{8\pi\sigma_{xy}^4\sigma_b^2}{d_{po}^2 N_p^2}. \tag{27}$$

As expected, both procedures reveal similar trends in the course of the LA, but the theoretical prediction yields better absolute values. In summary, the LA always improves as a function of the input power and reaches a range of a few tens of nanometers.

---

1 Genesis Coherent laser: 488 nm wavelength, max. power 1000 mW
2 QD Invitrogen Molecular Probes: 655 nm emission wavelength, 45 nm diameter
3 Olympus LUMFI objective: 60x magnification, 1.1 NA
4 Olympus UPlanSApo objective: 100x magnification, 1.4 NA
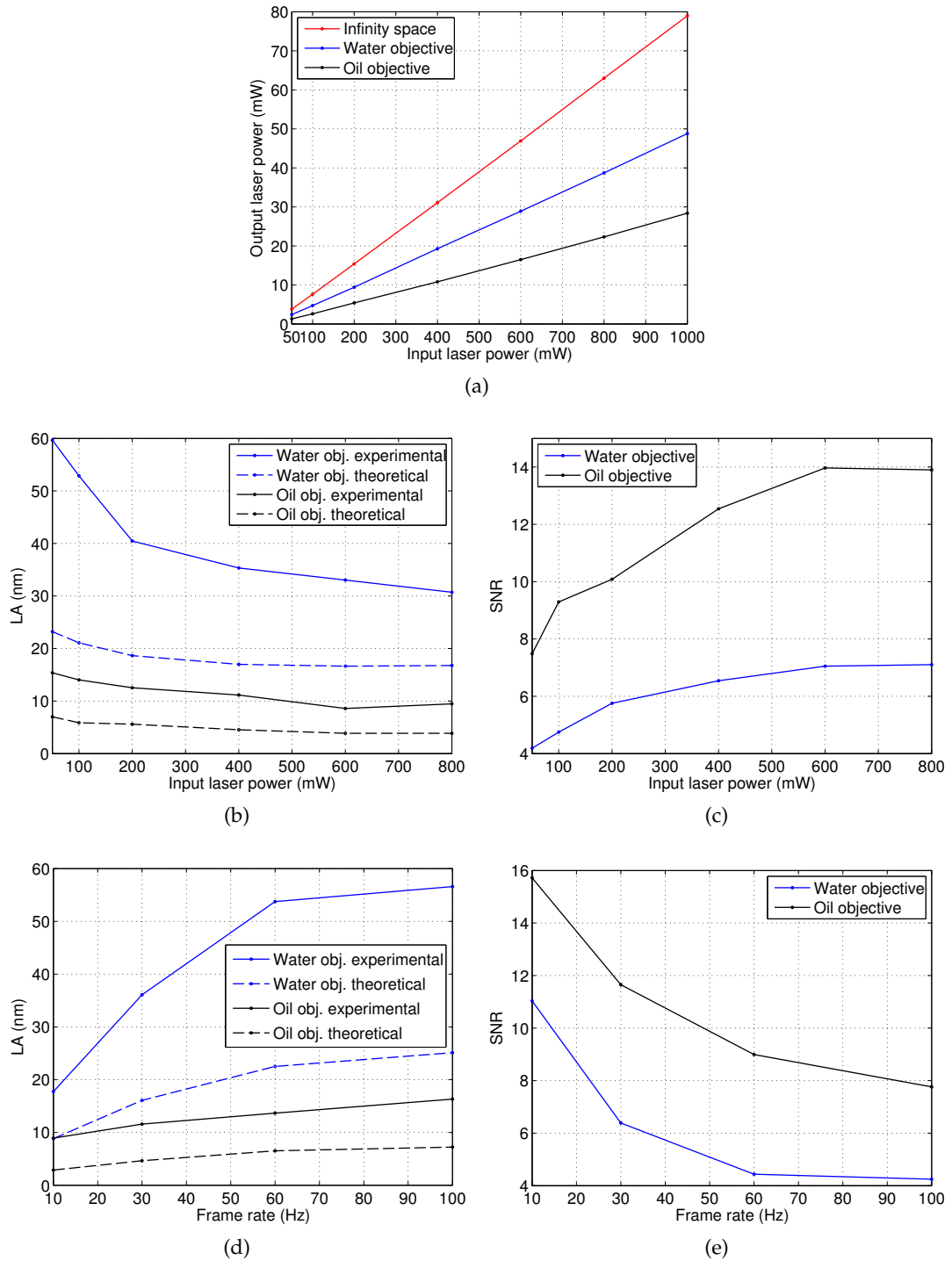
Figure 32: (a) Efficiency of light transition through the CSU and a water respectively an oil objective. LA and SNR for the same objective lenses as functions of (b)-(c) the input laser power and (d)-(e) the frame rate.

Please note that the presented results are taken from the initial publication (Biermann et al. 2014). At this early stage, only a standard weighted LSQ fitting procedure, including a peak detection procedure based on Thompson et al. 2002, had been implemented. A complete software package from collaborators in Bordeaux was used for diffusion analysis. Since the range of functions of the SPT workflow presented in this

76

thesis is not as complete as that of the software package, particularly the diffusion results could not be equivalently repeated. The presented performance results are consequently not one-to-one comparable, but this does not put the generality of this proof of principle into question.

The dependency of both measures on the temporal resolution was also analyzed. A clear tendency for deterioration towards higher frame rates is observable in Fig. 32d-32e. Apparently, frame rates up to 100 Hz still yield reasonable performance, however, 30 Hz were selected for real experiments since worse performance is expected within the tissue. Although Kusumi et al. 2012 pointed out that the molecular motion is actually about 1000 times faster, video-rate analyses continue to be frequently used since they already allow to detect changes between populations of molecules.

The presented results were obtained using $400\ mW$ and $100\ mW$ laser input power for the water and the oil objective, respectively. This is also the parametrization used for all following experiments in brain slices. Since there are no noticeable points of saturation in the curves of Fig. 32c-32c, this parametrization has been derived from experimental experiences with the vitality of the slices. It was experienced that higher excitation powers for either objective led to recognizable acceleration of photobleaching and visually detectable cell death.

4.5.2 *Accessing Diffusion Parameters in Brain Slices*

To validate the applicability of the presented configuration, organotypic hippocampal brain slices from mice were prepared, and glycosylphosphatidylinositol (GPI) as well as neuroligin1 (Nlg1) were monitored. GPI is a surface molecule in the neuronal membrane and has no direct interactions with intracellular scaffold proteins or extracellular binding partners. It has therefore been used to investigate lipid subdomains of the neuronal membrane (Eggeling et al. 2009, Renner et al. 2009) and was employed here as a reporter for varying diffusion in different membrane compartments. Nlg1 is a post-synaptic cell adhesion molecule that reaches out of the membrane and interacts with other proteins to maturate and stabilize synapses (Bang and Owczarek 2013). Its impeded diffusion compared with GPI allows to probe for molecular subpopulations by means of diffusion.

To label GPI and Nlg1, the slices were transfected by use of a gene gun to express GPI and Nlg1 in neurons with GFP- respectively hemagglutinin (HA)-tags. QDs then bind via specific anti-GFP or anti-HA antibodies. The slices grew in well plates (see Fig. 33a) and were incubated with QDs directly before imaging. To image into brain slices, the water objective can directly be pointed to the slices since the required RI matches that of the extracellular solution that supports the cells during the experiment. A specific imaging chamber had to be build for the oil objective (see Fig. 33b). It uses a net to attach the slice below a cover slip, while at the same time keeping it embedded in the extracellular solution.

4.5.2.1 *Can QDs Penetrate and Bind to Membrane Molecules in Slices?*

Indeed, it was possible to detect QDs within the tissue (see Fig. 34a), proving that the penetration of QDs through the outer surface into cultured brain tissue is not substantially hindered by adding the GFP antibody. Specific labeling was observed at trans-
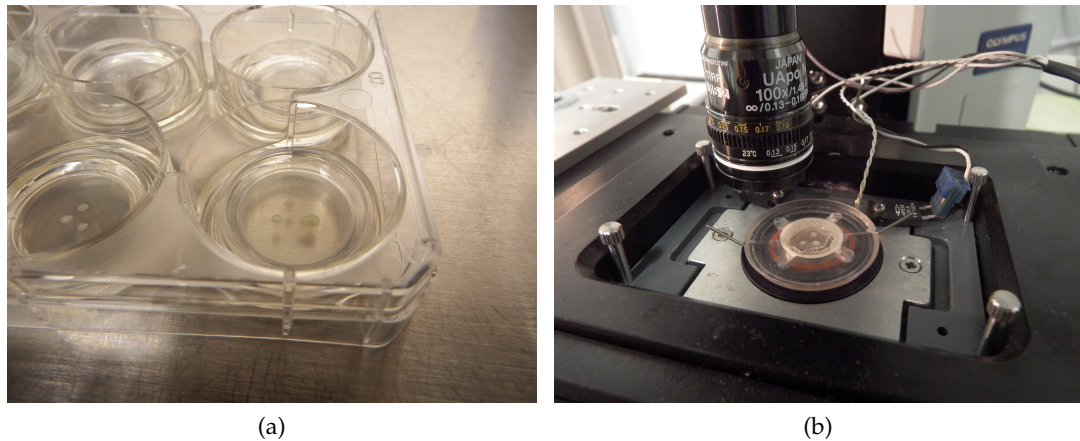
Figure 33: (a) Alive brain slices of rat (the white spots) that are cultured in a 6-well plate. (b) The custom-made imaging chamber. It is heated and filled with extracellular solution. A net fixates the brain slices at the cover slip so that they can also be imaged using an oil objective.

fected neurons. They were identified by preceding imaging of GPI-GFP. The relative labeling density as a function of the depth in the tissue is depicted in Fig. 34c. It represents the ratio between the number of QDs that correlate with transfected cells and the detected number of QDs at 3 μm penetration depth. The absolute density of QDs at the membrane of transfected cells could be controlled by the concentration of QDs in the incubation media and the time of incubation[5].

The relative labeling density constantly decreases and vanishes at about 60 μm imaging depth. This is reasoned by the deteriorating detection rate, mainly owing to the employed one-photon excitation, light scattering, and the RIM. It also explains the faster deterioration for the oil objective since here the RIs of the specimen and the immersion medium deviate much more. To prove that these trends are indeed artifacts of the particle detection instead of impeded penetration capability, collaborators in Hamburg repeated these measurements using 2PM. As apparent from Fig. 34b and the effectively constant labeling density presented in Fig. 34c, QDs really penetrate the tissue and entirely label transfected neurons without loss of specificity for at least 150 μm depth. These findings already indicate that the extracellular space is much more permeable than suggested by ultrastructure investigations of fixed tissue (Syková and Nicholson 2008, Van Harreveld et al. 1965). Furthermore, they confirm predictions about the form of the extracellular space, described as fluid-filled pores of about 38-64 nm (Thorne and Nicholson 2006).

Before the analysis of molecular diffusion in slices is addressed, first of all the achievable LA is assessed as a function of the imaging depth (see Fig. 35a). Particles that seemed to got stuck in the tissue were manually selected by visual inspection, because QDs cannot be immobilized in living samples without changing the optical properties of the tissue. Since this procedure is subjective, and particle motion cannot be perfectly excluded, the presented values tend to underestimate the true LA. It is most likely slightly better. The general trend of reduced performance towards larger depths in the tissue as well as the superior performance of the oil objective at intermediate imaging

---

5 Typically, 5 minutes incubation with mixture of ∼ 100 ml extracellular solution and 1 μl QD solution
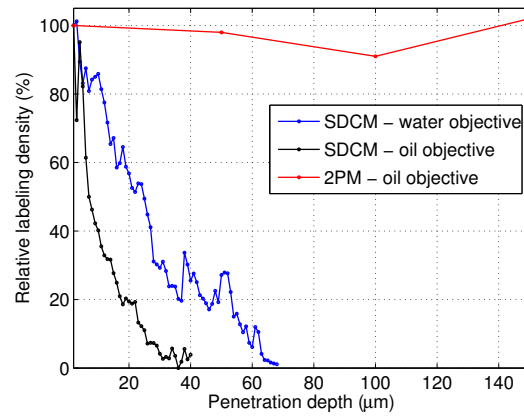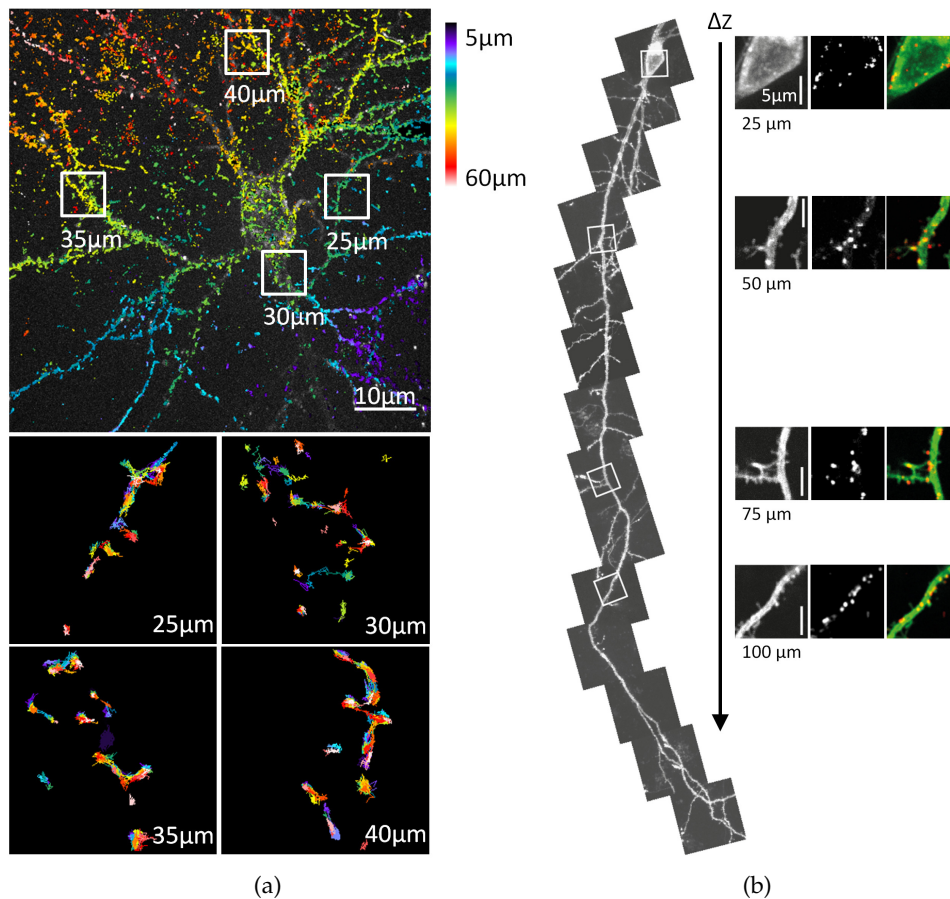
Figure 34: (a) QD labeling at transfected neurons in brain slices. The color encodes the depth in the sample and the sub-figures present measured QD trajectories at different depths. (b) A traced neuron using 2PM. The sub-figures on the right present the GPI-GFP and the corresponding QD acquisitions as well as both overlayed. (c) Relative labeling density as a function of the imaging depth for different imaging configurations.

depths are recognizable. The performance reduction in comparison to the measurements without tissue (see Fig. 32b-32c) is remarkably high. Apart from the stated problem of the particle selection, this is most likely due to the effects introduced by the RIM, the movement inherent to the tissue and the decreased SNR. The latter was found to

constantly deteriorate for both objective lenses from 5 to 3.5 as a function of the imaging depth. Nevertheless, these results clearly suggest that particularly the assumed LA always has to be measured for every setup and imaging condition individually, so that reasonable values are obtained.

From a biological perspective it can be concluded that reasonable LAs are achievable for analysis of the first cell layers. Using cultured organotypic slices, all cells are already integrated into the complex neuronal network at low depths. The viability of such neurons close to the surface was tested by whole-cell patch-clamp recordings and normal electrical properties and spontaneous activity was found.

4.5.2.2 *Is the Extracellular Space Permeable Enough for Diffusion Measurements?*

To identify whether QDs are suitable for quantification of mobility in brain slices, the water objective was taken for its larger penetration depth. The highly mobile GPI-GFP was recorded using the previously stated parametrization. For comparison, also the dynamics of GPI-GFP in transfected neurons of primary hippocampal rat cultures were analyzed. They represent the system often used for molecular analyses.

To analyze the image data, a software package[6], provided by collaborators in Bordeaux, was used. Particles are detected and localized based on image wavelet segmentation and individual centroid determination (Izeddin et al. 2012b). In comparison to Gaussian fitting approaches, this method has about 10 % lower LA, but is particularly suited for low SNR and performs more than one order of magnitude faster. Especially the gain in computation time was a strong argument, considering the large amount of data that had to be processed. To construct the trajectories, the software draws on a deterministic global linking strategy based on simulated annealing (Racine et al. 2006). It allows to capture particle appearance and disappearance as well as splitting and merging events. This is particularly valuable for imaging in slices since particles occasionally interfere or leave the focal plane, owing to the 3D extension of neurons in the thick tissue.

The resulting trajectories are most probably correct, but relatively short (see Fig. 35b). To exclude QDs that did not bind to the target molecule, usually recognizable by their short dwell times in the focal plane, only trajectories with lengths ≥ 12 were analyzed. ~ 40 % of all trajectories remained for analysis. More than ~ 60 % of the trajectories were longer than 12 measurements in primary cultures. This is most likely because of the more planar cellular architecture.

Since the LA is significantly lowered in slices and the trajectory length is relatively low, diffusion was quantified based on the distribution of D_l. For the present configuration, using the rule of thumb of Saxton and Jacobson 1997 would suggest to take 3 points to maintain statistically significant MSD values. In contrast, using Equ. 17 even suggests to include more than 10 points to reduce the influence of the LA. Here, 8 MSD points were used as a compromise between the LA and the trajectory lengths so that the last MSD point is still averaged by at least 4 measurements. D_l was then computed by fitting a straight line at these MSD points.

The distribution of D_l is depicted in Fig. 35c for molecules in dendritic compartments. It is apparent that the diffusion is very similar for primary cultures and slices.

---

6 Meanwhile the software is commercially available at http://www.moleculardevices.com/systems/metamorph-research-imaging/metamorph-microscopy-automation-and-image-analysis-software
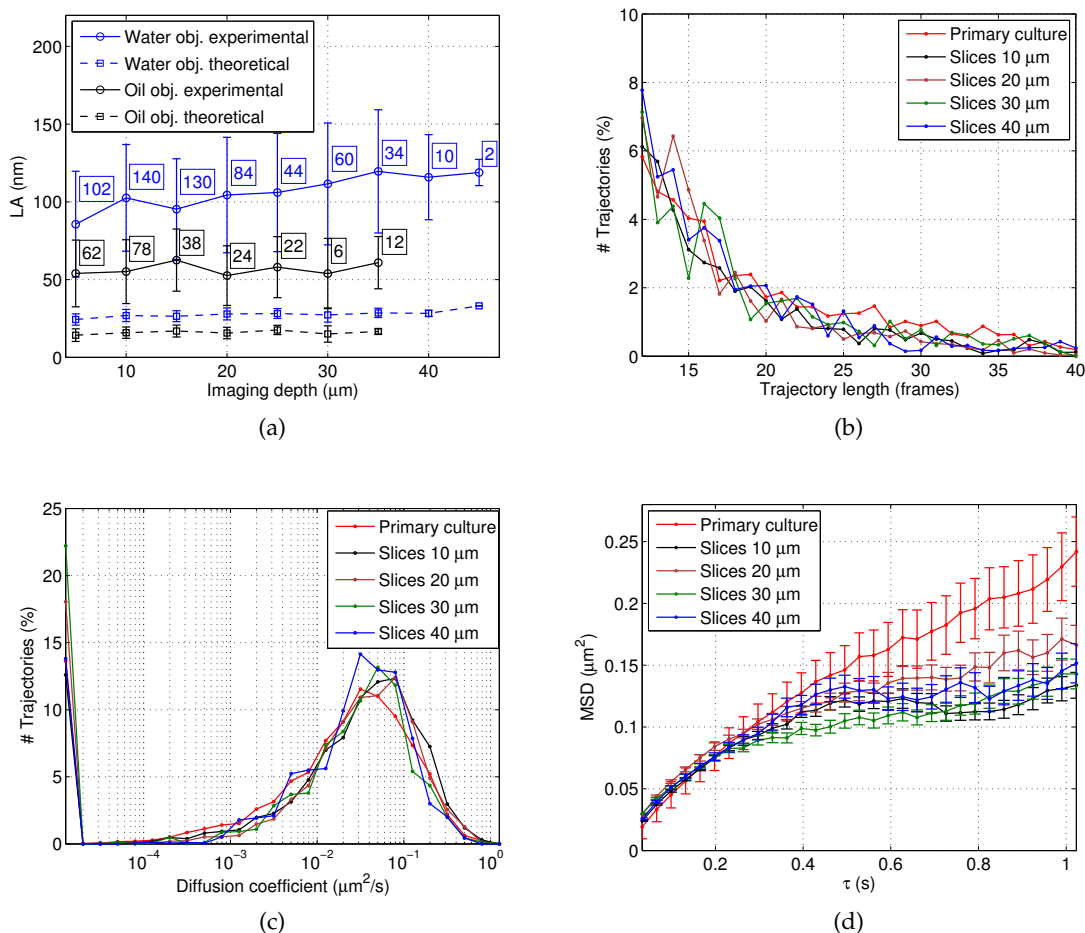
Figure 35: (a) LA as a function of the imaging depth for the water and the oil objective. (b) Distribution of the analyzed trajectory lengths of GPI-GFP measured in primary culture and at various depths in slices. (c) Distribution of D_l and (d) the corresponding MSD curves of GPI-GFP for the same preparations.

It does not significantly change as a function of the imaging depth in slices. The corresponding MSD curves are presented in Fig. 35d. The slope of the MSD curves is identical for cultures and slices. However, for larger time scales the mobility appears to be more constrained in slices than in primary cultures. It can be assumed that the more confined motion is justified by the more complex cellular environment that leads to compartmentation owing to the size of the QDs. From these results it can be concluded that the extracellular space is indeed permeable enough to analyze the local diffusion of molecules in slices at biologically relevant depths. Although propagation seems to be restricted at a larger scale, the local mobility is not significantly hindered by labeling with QDs. The finding that local diffusion is similar in slices and primary cultures is of utmost importance.

4.5.2.3 Can Cellular Compartments and Subpopulations of Molecules be Distinguished?

Now the final question, whether it is indeed possible to detect subpopulations by means of diffusion, is addressed. To distinguish such usually small differences, the

oil objective with its about twofold better LA than the water objective, was used. Again, the surface mobility of GPI-GFP was measured, but the preceding acquisition of GPI-GFP fluorescence was used to assign trajectories to axons, dendrites, and synaptic compartments. The corresponding distributions of D_l are presented in Fig. 36a. Differences in the mobility between neuronal compartments are clearly visible. Without explicitly presenting it here, similar results have been obtained for repetition of these measurements in primary cultures. They are also comparable to results previously reported by Renner et al. 2011 and Renner et al. 2009.
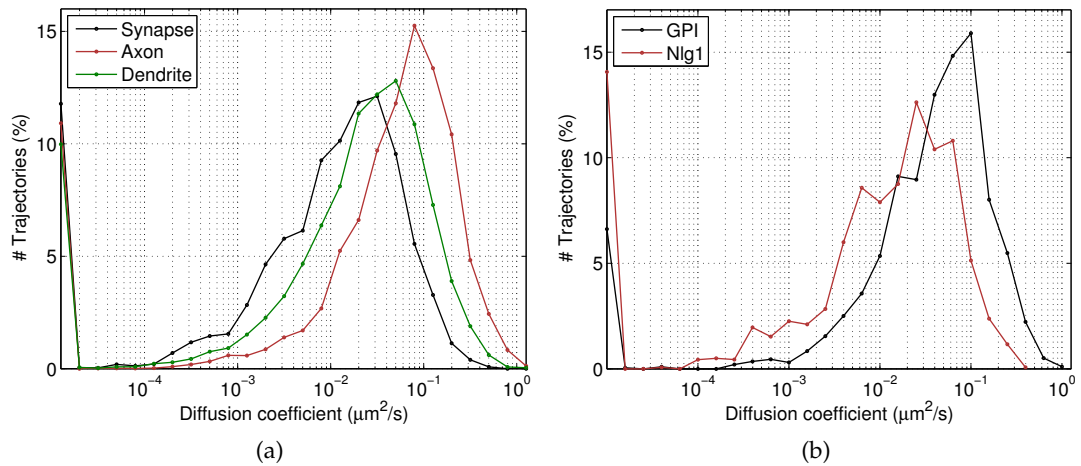

Figure 36: (a) Distribution of D_l for GPI-GFP measurements at different compartments. (b) Distribution of D_l for GPI-GFP and Nlg1-HAmeasurements.

In a second set of experiments Nlg1-HA was also imaged at dendrites, and its diffusion was compared with that of GPI-GFP (see Fig. 36b). As expected from its synapse stabilizing function, the population of Nlg1-HA molecules is on average considerably slower than the only passively interacting GPI-GFP. These results demonstrate that mobility differences between neuronal membranes at various subcellular compartments as well as different molecular populations are indeed verifiable using the proposed imaging configuration.

4.5.3 *Conclusion*

It can be concluded that the presented SPT application allows for verification of interactions found in biochemical or molecular biology experiments in primary neuronal cultures. The achieved temporal and spatial resolution is sufficient to quantify effects on subpopulations of membrane-associated molecules in organotypic slices. Therefore, this application can support other scientists to gain more detailed information about the molecular organization and dynamics in complex living brain slices. Owing to the technical scope of this thesis the line of argument has mainly focused on the proof of principle in terms of the accessibility of varying mobility. More detailed analyses and discussion of the biological impact are presented in the original publication (Biermann et al. 2014). It also provides further biological details. These are for instance the preparation of the samples, the protocols for coupling the QDs with antibodies and how to

transfect the samples. The electrophysiological properties of neurons in brain slices are also provided.

In the following, the individual components of the developed 3D SPT workflow are presented in detail.

4.6 PARTICLE DETECTION

To identify particle candidates, unsupervised and supervised techniques have been developed. Supervised techniques were found to generally perform best, but at the expense of heavily relying on good training data that reflects the expected data very well (Smal et al. 2010). Due to imaging at different depths in the samples, the shape and SNR of the acquisitions vary significantly. Therefore, supervised techniques are expected to require frequent retraining and are consequently not considered as being suitable for this type of application. Instead, a procedure based on the spot-enhancement filter is used (Sage et al. 2005). It exhibits good overall performance, is reasonably insensitive to variations in the shape, and requires only a single easily tunable parameter (Smal et al. 2010). Furthermore, it implicitly smooths the data and suppresses the local background. Explicit preprocessing procedures can be avoided.

The present particle detection procedure is then as follows:

> **Data** : Image stream
> **Result** : Pixel positions of particle candidates
> **for** *each image* **do**
> > Convolve the image with a LoG filter;
> > Segment image using a global threshold t_p;
> > Compute watershed transformation;
> > Use watershed lines to separate interconnected particle regions;
> > Compute region centers from minimum values;
> **end**

First, each image is convolved with a LoG filter of size 11 and kernel SD of 1.5 pixel (see Fig. 37a). This results in strong negative responses at bright particle positions. The chosen parametrization corresponds well to the maximum FWHM value of detected off-focus particles with the present imaging configuration (see Fig. 40a). Before convolution, the image is mirror-reflected at its boundaries so that truncated boundary particles are still detectable.

Subsequently, a global threshold t_p is computed for the LoG-filtered image by $t_p = i_b + k\delta_b$. Since the image fraction that is occupied by background pixels is usually high, robust estimates of i_b and δ_b are obtained by computation of the median and the median absolute deviation, respectively. Owing to unavoidable photobleaching over time, these parameters have to be estimated for each image individually.

For the user-defined factor k, a value of $k = 8$ has been empirically found to be reasonable for real acquisitions as well as synthetic images. This setting never had to be changed during this work. However, k should not be set too high since otherwise dim off-focus particles can easily be missed. In contrast, it is relatively save to chose rather lower values since more information about particles is available in later stages of the algorithm. Rejection of particle candidates is then more reliable.
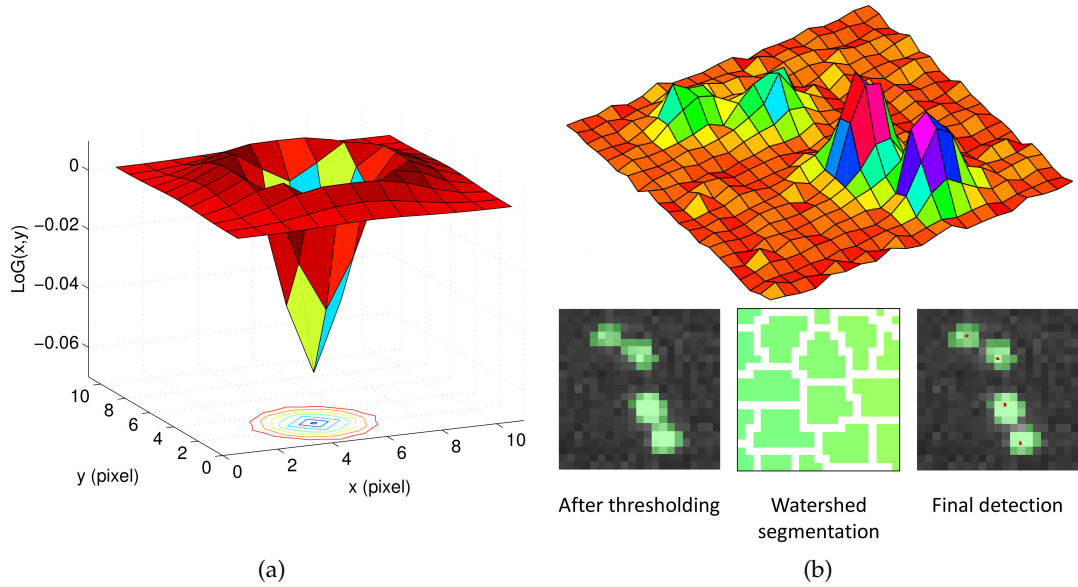
Figure 37: (a) Kernel of the applied LoG filter. (b) Illustration of how the additional watershed segmentation allows to distinguish neighboring particle candidates. The current segmentation that is based on the LoG-filtered image is presented in green on top of the original acquisition. The red dots depict the detected particle positions with pixel accuracy.

The application of t_p is likely to result in a segmentation that contains interconnected regions of nearby particles. Therefore, a watershed algorithm that uses the 8-connected neighborhood is applied to the LoG-filtered image. Removal of the watershed lines from the segmentation allows for separation of neighboring particles without further parametrization (see Fig. 37b). The pixels with the lowest value in each region are finally selected as particle candidates.

4.7 PARTICLE LOCALIZATION AND SHAPE ESTIMATION

2D localization algorithms can be classified into fitting and non-fitting methods. Their basic pros and cons have been discussed in Sect. 4.3.3.1. For the purpose of 3D SPT, a fitting-based method was selected for two reasons: (1) since astigmatism-based 3D localization is employed, an explicit model of the PSF shape is preferable for determination of particle features that provide the required axial relationship. (2) occurrences of nearby particles can be handled to a certain degree by treatment as mixture distributions or based on compressed sensing algorithms.

In a second fundamental decision, fitting mixture models is preferred over compressed sensing algorithms, because they can easily be adapted to elliptical intensity distributions. Compressed sensing algorithms rely on the definition of a single unique intensity distribution. This simplification is not valid for the present application since blurred off-focus particles have to be detected for axial localization, which are additionally altered by the intentional astigmatism. For the fitting routine, MLH estimation is employed because it performs better than LSQ fitting if the noise can be accurately modeled (Mortensen et al. 2010, Abraham et al. 2009). This is indeed the case when

using modern EMCCD cameras. Their dominant source of noise at low signal and reasonable G_{EM} levels is photon noise (Axmann et al. 2013), which is well described by a Poisson distribution (see Equ. 6).

The actual fitting algorithm and the general analysis procedure are now described in detail.

4.7.1 Multiple Particle Fitting

The most common procedure for particle fitting is the isolation of single spots and the individual estimation of their shape parameters. Although the particle density at a neuron can be controlled by the concentration of QDs in the incubation media, closely approaching or superimposing particles are likely to occur owing to the mobility of particles. To reduce the fitting errors in case of neighboring particles, they are explicitly modeled using Gaussian mixture distributions.

When fitting multiple particles in parallel, the likelihood function can become quite complex and may be difficult to maximize. This is already the case if multiple fixed-sized intensity distributions are fit, which is a standard procedure today. In this context, it was pointed out by Huang et al. 2011 that in order to achieve robust parameter estimation, also the intensity parameter had to be predefined. This is effectively a reduction of the number of fitting parameters that is not applicable here. Owing to the required off-focus acquisitions also the intensity is subject to strong variation. In contrast, Babcock et al. 2012 actually fitted multiple particles with individual shape parameters and proposed an optimization scheme where the particles are fitted individually, but in an iterative fashion.

In order to avoid proprietary optimization schemes or limitation of the number of free fitting parameters, it is proposed here to employ an EM algorithm. Its principles and the current implementation for microscopy data are now introduced in detail.

4.7.1.1 The Basic Principle of EM

The EM algorithm is a standard statistical tool developed by Dempster et al. 1977. It replaces the complex nonlinear optimization problem of maximizing the log-likelihood during MLH fitting with an iterative sequence of problems that are easier to solve.

The key idea is the concept of incomplete data, where parts of the data are treated as missing observations. For the general example of estimating the distribution parameters of mixtures, the assignment of single measurements to the corresponding distribution would be the missing information. If the assignments would be known, the problem would reduce to several independent distribution estimations that are easier to solve.

The EM algorithm implements this idea by means of an iterative two-step process consisting of an expectation step (E-step) and a maximization step (M-step) (Chen and Gupta 2010). As the complete data is unavailable, the E-step makes a guess about the complete data and takes the expected value of the complete data log-likelihood instead. The M-step consecutively maximizes this expectation with respect to the model parameters. Given improved estimates for the model parameters they can in turn be used to improve the guess about the complete data. By iteration of the two steps, the observed

data log-likelihood is indirectly maximized by maximizing the expected complete data log-likelihood.

4.7.1.2 *EM Algorithm for Binned and Truncated Data*

For the present application, the EM formulation of Ainsleigh 2009 is used. It is a generalization of the initial work of McLachlan and Jones 1988 that was later extended to multivariate data by Cadez et al. 2002. They showed that for estimating Gaussian mixture distributions in histogram data, whose bins can be treated as statistically independent Poisson processes, almost a closed-form solution for a single update iteration of the EM algorithm exists. Ainsleigh 2009 finally added the consideration of uniform background to the formulation. Therefore, his EM formulation is applicable to digital microscopy images since they are created by discrete sampling of photons that is subject to shot noise.

In microscopy images, the individual photon positions are the actual measurements, but only the intensities, as a relative measure for the number of photons that fall in each pixel, are observable. Hence, next to (1) the assignment of photons to the individual Gaussian distributions, also (2) the individual photon measurements that distribute over each pixel are the missing observations. Cadez et al. 2002 and McLachlan and Jones 1988 showed that (3) the unknown pixel intensities of truncated distributions can also be treated as missing observations. Consideration of truncated distributions is advantageous since they are likely to occur during sub-region creation (see Fig. 38). Ignorance of truncated intensity data, which effectively means treating them as zero values, yields biased parameter estimates.

The underlying component mixture model for microscopy images, that contain the intensity distributions of particles as well as background, can be described by:

$$\mathcal{C}(r; \Theta) = \mathcal{N}(r; \Theta) + \pi_g \left(\frac{1}{v} \right) \qquad r \in \mathbb{R}^2, \tag{28}$$

where $\mathcal{N}(r; \Theta)$ is itself a Gaussian mixture model defined by:

$$\mathcal{N}(r; \Theta) = \sum_{i=1}^{g-1} \pi_i \mathcal{N}_i(r, \theta_i). \tag{29}$$

The g components are separated into $g - 1$ multivariate normal distributions $\mathcal{N}_i$ that represent the particles and a single uniform distribution that describes the background. Here, r is a random variable that represents the sub-pixel positions of the individual photon measurements, and each $\mathcal{N}_i(r, \theta_i)$ has parameter vector $\theta_i = (\mu_i, \Sigma_i)$ with μ_i being the expected values and Σ_i being the covariance matrix. The uniform background distribution is solely parameterized by the total number of pixels v. π is a vector of component mixing proportions subject to $\sum_{i=1}^{g} \pi_i = 1$, $\pi_i \in [0, 1]$ and represents the unconditional probabilities that a photon belongs to a certain component. Θ is the vector of all unknown parameters of the mixture given by $\Theta = (\pi_1, ..., \pi_g, \theta_1, ..., \theta_g)$.

According to Ainsleigh 2009, the update step for the individual parameters π_i, μ_i, and Σ_i of the mixture components at the $t+1$-th iteration of the EM algorithm involves evaluation of:

$$\pi_i^{t+1} = \frac{1}{N} \sum_{j=1}^{\nu} m_j(\Theta^t) \tau_{ji}(\Theta^t), \tag{30}$$

$$\mu_i^{t+1} = \frac{1}{\kappa_i(\Theta^t)} \sum_{j=1}^{\nu} \frac{m_j(\Theta^t)}{\Phi_j(\Theta^t)} \ \pi_i^t \int_{\mathcal{R}_j} dr \ \mathcal{N}_i(r, \theta_i^t) \ r, \tag{31}$$

$$\Sigma_i^{t+1} = \frac{1}{\kappa_i(\Theta^t)} \sum_{j=1}^{\nu} \frac{m_j(\Theta^t)}{\Phi_j(\Theta^t)} \ \pi_i^t \int_{\mathcal{R}_j} dr \ \mathcal{N}_i(r, \theta_i^t) \ rr^T. \tag{32}$$

Note here that the first equation refers to all components of the mixture model, while the remaining equations refer solely to the update steps for the parameters of the Gaussian components. Since the background component contains no unknown parameters, solely its proportion has to be updated.

Ainsleigh 2009 also provided an in-depth theoretical derivation for this solution. Here, it shall be sufficient to have a closer look at some individual variables in order to clarify the basic principle of how this EM formulation deals with the missing observations.

So, $m_j(\Theta)$ denotes the expected intensity at the j-th pixel and is defined for all pixels ν as:

$$m_j(\Theta) = \begin{cases} N_j & \text{if } j = 1, ..., o \\ \frac{N_o}{\Phi_o(\Theta)} \Phi_j(\Theta) & \text{if } j = o+1, ..., \nu. \end{cases} \tag{33}$$

For the observed pixels o, these are simply the number of photons N_j observed at each pixel. The values for the unobserved pixels are computed by extrapolating the total number of observed photons into the truncated regions. This can be done by means of the ratio $\frac{N_o}{\Phi_o(\Theta)}$ that is applied to the unconditional probability that a photon is detected at a certain pixel. In this manner, the derivation of an explicit parameter estimator for the truncated pixels is avoided, and maximization is conducted on a complete set of pixels. The estimation is less biased than it would be by assuming zero-valued pixels. The subscript o denotes all observed pixels, while j denotes only a single pixel.

The unconditional probability $\Phi_j(\Theta)$ for a single pixel is then defined by:

$$\Phi_j(\Theta) = \int_{\mathcal{R}_j} \mathcal{C}(r; \Theta), \tag{34}$$

where $\mathcal{R}$ denotes the sample space of r. It becomes apparent that the observed intensities are linked to the unobserved individual photon measurements by integration of their Gaussian distribution over the pixel regions.

Furthermore, τ is defined as:

$$\tau_{ji}(\Theta) = \frac{\pi_i \int_{\mathcal{R}_j} dr \ \mathcal{C}_i(r, \theta_i)}{\sum_{i=1}^{g} \pi_i \int_{\mathcal{R}_j} dr \ \mathcal{C}_i(r, \theta_i)}. \tag{35}$$

It represents a relative weight that can be interpreted as the probability with that a photon measurement is assigned to the i-th mixture component solely given its position.

Finally, N and $\kappa_i(\Theta)$ denote the total number of photons respectively the number of photons per mixture component.

Using Equ. 30-32, the EM algorithm iteratively updates Θ until a maximum number of iterations t_{iter} is reached. The parametrization $\Theta^{t_{iter}}$ is taken as the fitting result.

The presented EM algorithm has been implemented in Mathematica[7] by Yury Prokazov from the Special Lab Electron and Laserscanning Microscopy at the LIN. This also includes a wrapper for calling the algorithm in MATLAB[8].

4.7.2 *The General Analysis Procedure*

This section describes how the EM algorithm is embedded into the general fitting procedure. Since it explicitly considers the dominant noise source, it is applied to the original data rather than to the LoG-filtered image. For the same reason, the image is gain corrected so that each pixel's intensity value corresponds to the approximate number of photons instead of an arbitrary intensity representation.

Owing to the practically linear G_{EM} of the employed camera, the true number of photons per pixel can be estimated by:

$$N_{x,y} = \frac{i_{x,y} \cdot S_{CCD}}{G_{EM}}, \tag{36}$$

where S_{CCD} is the sensitivity of the analog-to-digital converter representing the number of electrons per digital intensity unit.

Based on the set of particle candidates provided by the detection procedure, the general analysis procedure for each image is as follows:

> **Data** : Image
> **Result** : Particle configurations
> **for** *each particle candidate* **do**
> >   Cut sub-region around candidate;
> >   Select all candidates within sub-region;
> >   Create initial configuration;
> >   **for** 1:t_{init} **do**
> > >   Invoke EM fitting algorithm;
> > >   Compute and store likelihood of fitted particle configuration;
> > >   Update initial configuration with random component;
> >
> >   **end**
> >   Select configuration with highest likelihood;
> >   Store configuration of center candidate;
>
> **end**
> Validate particle configurations;

This is also illustrated in Fig. 38. A sub-region is selected around each particle candidate, and the individual sub-regions are successively fit by the EM algorithm. This multiple particle fitting includes any particle candidate within each sub-region, but only the fitting parameters of the current central particle candidate are retained.
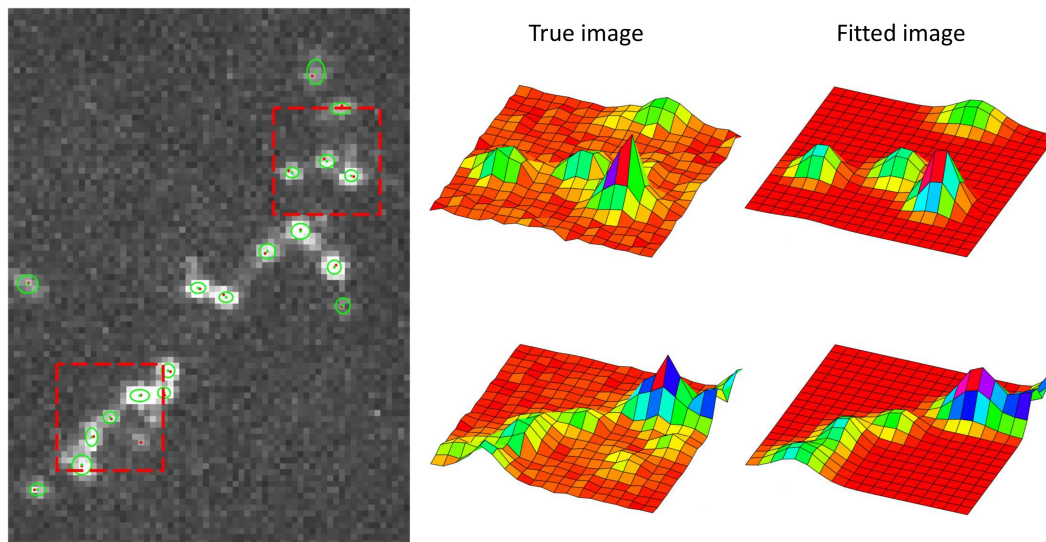

Figure 38: Illustration of the fitting procedure. The red dots denote particle candidates, while the green ones with the contour line represent the fitted particles. The red boxes depict two exemplary sub-regions, and on the right their true image data as well as the fitted image are presented. The intensity distribution of neighboring particles may overlap, and truncated distributions can arise as a result of the sub-region selection.

This iterative procedure was chosen for two reasons: first, to account for the smoothly varying background and, second, to minimize the additional fitting error introduced by truncated boundary particles.

Similar to the experiences made by most of the researchers using cell cultures, images acquired in brain slice were found to exhibit only smoothly varying background. This is reasonable since the narrow emission spectra of QDs allowed for the usage of emission filters with similarly narrow transmission range. Imaging QDs with emission in the red region of the light spectrum rejects most of the autofluorescence that usually occurs in the green region of the spectrum. Owing to the low transfection rate, there are barely neighboring neurons whose particles may additionally add blur to the image. Finally, since off-focus particles at the same neuron are explicitly considered in the fitting procedure, also blurred particles do not contribute as inhomogeneous background.

The analysis procedure relies on sub-regions that are assumed to contain homogeneous background, and the component mixture model of the EM algorithm (see Equ. 28) can be directly applied. An additional global background subtraction procedure is not required.

Although the EM algorithm explicitly accounts for truncated intensity distributions of boundary particles, the accuracy with that their parameters are estimated was found to still being significantly reduced (see Sect. 4.10.1.3). This adds additional uncertainty to the fitting accuracy of particles that neighbor such boundary particles since emitted

photons might be incorrectly assigned to the individual distributions. In order to obtain the best fitting result for each particle, a sub-region is selected that centers each particle individually. This maximizes the distance to the boundary of the sub-region and reduces the impact of the error that propagates from boundary particles.

The boundary size of the sub-region was set to 19 pixels for the present data. This choice represents a compromise between the required distance to the boundary so that the fitting accuracy is not reduced (see Sect. 4.10.1.3) and a preferentially small region to justify the assumption of background homogeneity.

The actual EM algorithm is provided with an initial parametrization that is individually derived for each sub-region and considers the number of particle candidates. For initialization of the mixing proportions π_i, the image region is first smoothed with a Gaussian filter having a SD of one pixel so that the subsequent procedure is more robust. The background proportion is then computed from the minimum photon count in the sub-region times the number of pixels. The remaining photons are distributed to the particle candidates with respect to the number of photons in their peak pixel. Finally, all proportions are normalized so that they sum to one. The centers μ_i of the Gaussian mixture are initialized with the center position of the pixel identified by the particle detection. The FWHM values are always initialized with 380 nm. This corresponds to the average value of the FWHM range experienced in calibration measurements (see Fig. 40a).

After initialization, the EM algorithm iterates $t_{iter} = 100$ times. This is a relatively large value (Cadez et al. 2002) that should ensure that a local maximum in the likelihood can be reached. This is indeed important since EM only guarantees to find at least a local maximum of the likelihood function (Dempster et al. 1977). In order to avoid that the EM algorithm gets stuck in a poor local maximum, it is repetitively started t_{init} times with random initialization (Chen and Gupta 2010). The parameter set Θ with the highest likelihood is selected.

For the present data, where the bins are treated as statistically independent Poisson processes, the normalized observed data log-likelihood is given by (Maus et al. 2001):

$$L = - \sum_{j=1}^{\nu} N_j \ln \frac{N_j}{\mathcal{C}_j}. \tag{37}$$

Here, N_j again represents the number of photon counts at the j-th pixels, while $\mathcal{C}_j$ denotes the expected number of photons at that pixel for the mixture model with parametrization Θ.

After the initial execution of the EM algorithm with the presented parametrization, subsequent starts are initialized with a random deviation of up to 20 % from the initial mixing proportions. The particle positions are randomly altered by ± 1 pixel, and the FWHMs are randomly selected in the range 266-500 nm. All deviations are drawn from an uniform distribution.

Detected particles and their parametrization are finally tested for being reasonable. Particles that do not contain a minimum of 100 photons or have FWHM values outside the range of 200-700 nm are rejected for further analysis.

The identification of occasionally superimposed particles that were too close to have been distinguished by the particle detection procedure (see Fig. 48) is transferred into the temporal domain. Instead of analyzing the noisy intensity distribution, like existing

mixture distribution fitting algorithms do (Huang et al. 2011, Holden et al. 2011), it is proposed here to solve this problem by detection of splitting and merging events. The additional temporal information provided by the image streams is explicitly exploited. This issue is addressed in the next section. Particles with significantly overlapping distributions are detected, but not resolved. Instead, they are excluded from further analysis because the accuracy with that parameters of their intensity distributions are estimated considerably reduces as a function of the distance between two particles (see Fig. 51).

This procedure is reasonable since the focus of this work is on the axial online calibration that heavily depends on accurate shape estimations. Once the axial correlation function is known, particles that have yet not been resolved can also be analyzed. It can also be concluded that the selected spot detection procedure is sufficient since it can resolve particles that are at least 3 pixels apart (see Sect. 4.10.1.2). This correlates with the distance where the LA starts to significantly deteriorate.

4.8 LINKING PARTICLE POSITIONS TO TRAJECTORIES

In order to link particle positions to trajectories, local and global strategies are available (see Sect. 4.3.6). For the present data, a local linking strategy seems to be sufficient for the following reasons: (1) relatively sparse particle distributions are adjusted, (2) very close particles are not considered for analysis owing to the decrease in accuracy, and (3) the trajectory lengths are not required to be extremely long. The latter will become clear in Sect. 4.9.2 as the online calibration can simply combine trajectories from multiple particles. For the current focus on the axial online calibration method, the correctness of the identified trajectories is of much more importance than their absolute lengths. Consequently, a conservative, but reliable strategy is most appropriate, and the following procedure has been implemented:

> **Data** : Particle positions for all images
> **Result** : Trajectories
> **for** *all subsequent images* **do**
> | Connect particles using a local linking strategy;
> **end**
> Bridge small gaps between individual trajectories;
> Detect splitting and merging events;
> Delete trajectories that represent multiple particles;
> Delete trajectories that are too short;

The local linking strategy provided by the implementation of Jean-Yves Tinevez and Yi Cao[9] was employed. The assignment problem between particle positions in consecutive frames is solved via the Hungarian algorithm (Kuhn 1955) based on the nearest neighbor criterion. To account for blinking events, the end and starting positions of different trajectories are subsequently reconnected with respect to a user-defined maximal number of frames and distance.

---

9 Their set of MATLAB scripts is available at `http://www.mathworks.com/matlabcentral/fileexchange/34040-simple-tracker`.

In order to identify superimposed particles that are hardly distinguishable by analysis of their intensity distributions, it was proposed here to exploit the temporal domain. Splitting and merging events are detected after all trajectories have been assembled. It is checked whether at the end of any track another track can be found within a user-defined neighborhood in the consecutive frame. This identifies merging events between trajectories. By running the same procedure backwards, splitting events can be detected. Provided all merging and splitting events are known, all positions after a merging respectively all positions before a splitting event are removed from the corresponding trajectories. If trajectories undergo splitting and merging, only the positions between these events are removed. A minimum track length criterion is applied to the remaining trajectories.

Although the proposed procedure is relatively basic, it suffices to reliably link particles in the present acquisitions and allows to detect superimposed particles.

4.9 ADDRESSING THE RIM

In this section the actual online calibration method is presented. It adjusts astigmatism-based 3D SPT techniques to the aberrations induced by the RIM so that they are applicable deep in living samples. In contrast to existing techniques, this method determines the aberrations directly from the acquired 2D image stream and does not require individual calibration or any other additional effort for the experimenter.

At first, the influence of the RIM will be quantified, and an axial model that describes the induced aberrations is established. By exploiting particle movement and the redundancy introduced by the astigmatism, it is subsequently shown that it is possible to estimate the current axial model from the 2D image stream independently of the imaging depth. The presented results have initially been published in Sokoll et al. 2013 and Sokoll et al. 2011.

4.9.1 *The Axial Correlation Function*

It was explained in Sect. 4.3.4 that 3D SPT techniques achieve high temporal and spatial resolution by evaluation of the axial correlation function. It describes the relationship between features of the 2D PSF and the relative axial distance of the particle to the focal plane.

Considering Gaussian PSF models, there are basically two features that vary with the axial distance of the focal plane to the center of the particle. These are the height h and the FWHM ω. They correspond to the peak intensity respectively the width of a fluorescent spot at each axial position and are depicted in Fig. 39a. Fig. 39b-39c further illustrate that the axial intensity distribution can be approximated with a Gaussian function, and that the width exhibits the well-known parabolic relationship (see Equ. 26). The peak intensity was experienced to be a relatively noisy measure, which is particularly true for QDs. Moreover, the peak intensity varies significantly already for fluorophores of the same type, which prevents the application of a single correlation function. On these grounds, only the axial relationship of the FWHM is a suitable model that can be reliably used for analysis of multiple particles at once.
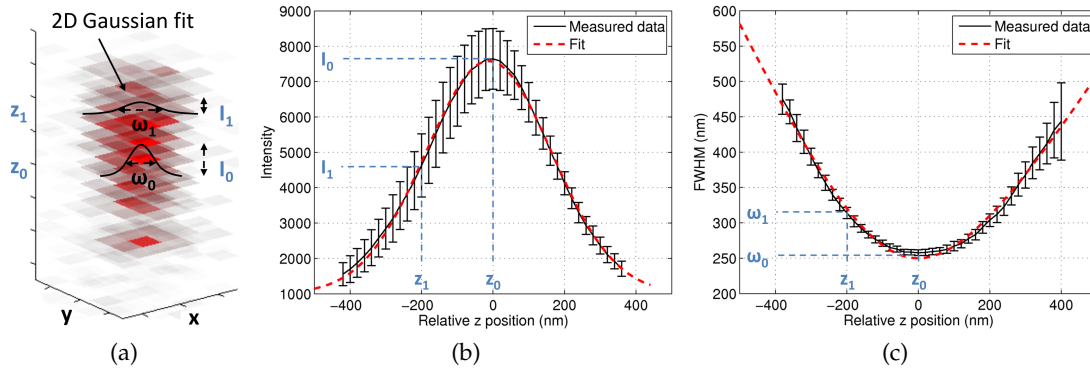
Figure 39: (a) Illustration of the relationship between 2D PSF features and the axial position. (b) Fit of a Gaussian function to the relationship of the intensity with the axial position. (c) Corresponding plot for the FWHM fitting Equ. 26.

4.9.1.1 *Adjusting the Correlation Function to the Influence of the RIM*

To determine the influence of the RIM on the axial correlation function, z-stacks of immobilized 30 nm diameter fluorescent beads with 580-605 nm emission wavelength were analyzed at different depths. To maintain improved LA at reasonable depths in brain slices, again an oil immersion objective[10] was employed. Such sub-resolution-sized beads are typically used for calibration measurements (Hibbs et al. 2006). Here, they were chosen because of their stable fluorescence that simplifies analysis and reduces the number of frames that need to be acquired. These beads were dissolved in Mowiol[11], and drops of this solution were put on cover slips. This procedure enables imaging of immobilized beads at varying depths, because Mowiol is a transparent mounting medium that is curing quickly. Since Binding et al. 2011 showed that the RI of rat brains measured in vivo can be considered being independent of the imaging depth, the usage of Mowiol that exhibits a constant RI is a reasonable experimental setting. Furthermore, the RI of Mowiol is lower than that of the immersion oil and the cover slip. This is identical to the situation in real experiments.

The axial correlation curves for beads at depths of 0-30 μm are presented in Fig. 40a. They are obtained by axial scanning of 20 beads at each depth and plotting of the average FWHM from elliptical Gaussian fits to the 2D PSFs at each relative axial scan position. Each bead was scanned once with an axial step size of 20 nm over an axial range of 2 μm and a temporal resolution of 10 Hz. For negative relative z positions the focal plane is above the center of the particle and for positive positions below. The center of the particle is represented by the vertex of the curve, where the effective resolution is highest.

It is apparent that the well-established parabolic correlation function holds only true for beads located directly under the cover slip, where the RIM is effectively negligible. With increasing depth the 3D PSF becomes more and more distorted resulting in increasingly skewed parabolic correlation curves. Also, the effective resolution at the center of the particle decreases as a function of the depth.

The presented depth dependency is not directly comparable to the one that should be experienced in brain slices or aqueous solutions since there the RIs are much lower.

---

10 Olympus UAPON 100XOTIRF objective: 100x magnification, 1.49 NA
11 Mixture ratio: 0.1-1 μl beads solution to 2 ml Mowiol

Although this could not be proven as Mowiol was self-made and its exact RI was unknown, the observed dependency on the depth is nevertheless expected to be weaker than that for real experiments.
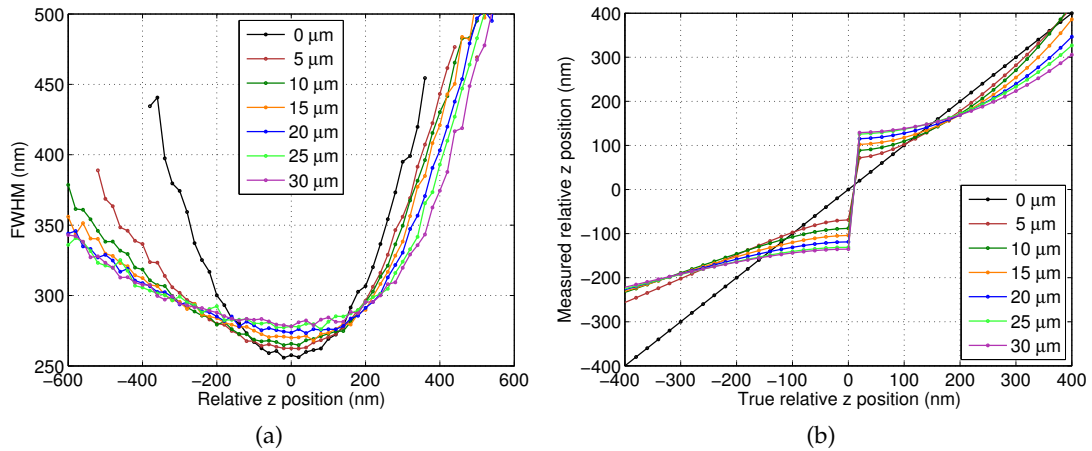

Figure 40: (a) Measured axial correlation curves of immobilized beads at different depths in Mowiol. Each data point represents the average value of $\sim$ 20 beads. The individual numbers may vary owing to reasonability checks on the fitting results and the additional restriction that data points are only included if their intensity is at least 30 % of the intensity at focus. All curves were aligned according to their true vertex before averaging. (b) Deviations from the true axial position if the influence of the RIM is ignored and always the same calibration at zero depth is used. Note that the underlying calculations already draw on modelling the curves using Equ. 38.

If the depth dependency is neglected and the calibration curve at zero depth is utilized for particles imaged deep within the specimen, then the obtained relative axial position will be incorrect. The resulting SEs are presented in Fig. 40b. They increase as a function of the imaging depth. For the given experimental configuration, this can already result in deviations of more than 100 nm from the true axial position. Since the SE originates from wrong depth assumptions, it is obtained no matter how accurate the shape of a particle can be determined.

To compensate for the RIM, Huang et al. 2008a proposed the usage of two depth-dependent scaling factors that individually correct the obtained relative axial positions above and below the focal plane. However, this almost linear relationship was only shown for simulated PSFs, where most likely not all experimental factors were included. The measured results in Fig. 40 clearly indicate that there is no linear relationship. The simulations apparently did not cover the reduction of the effective resolution at the particle center as a function of the depth. In reality, significant deviations already occur in the vicinity of the particle center. Their approach also changes the axial LA by means of the scaling factors, which additionally deteriorates it as a function of the imaging depth. In order to avoid this artificial reduction of the axial LA and since the determined linear relationship seems hardly valid, here an alternative approach is proposed. Instead of post-correcting the localization results, the aberrations of the axial correlation function are directly modelled. Equ. 26 is adapted to:

$$\omega(z) = \omega_0 \cdot \sqrt{1 + \left(\frac{z}{d}\right)^2} + m_r \cdot z. \tag{38}$$

Here, z, d and ω_0 are still the relative axial position, the focal depth and the FWHM in focus. The extra parameter m_r controls the skewness of the correlation function. The proposed extension was empirically established and can be considered as adding a straight line with depth-dependent slope to the symmetric correlation function at zero depth.


(a)

(b)   (c)
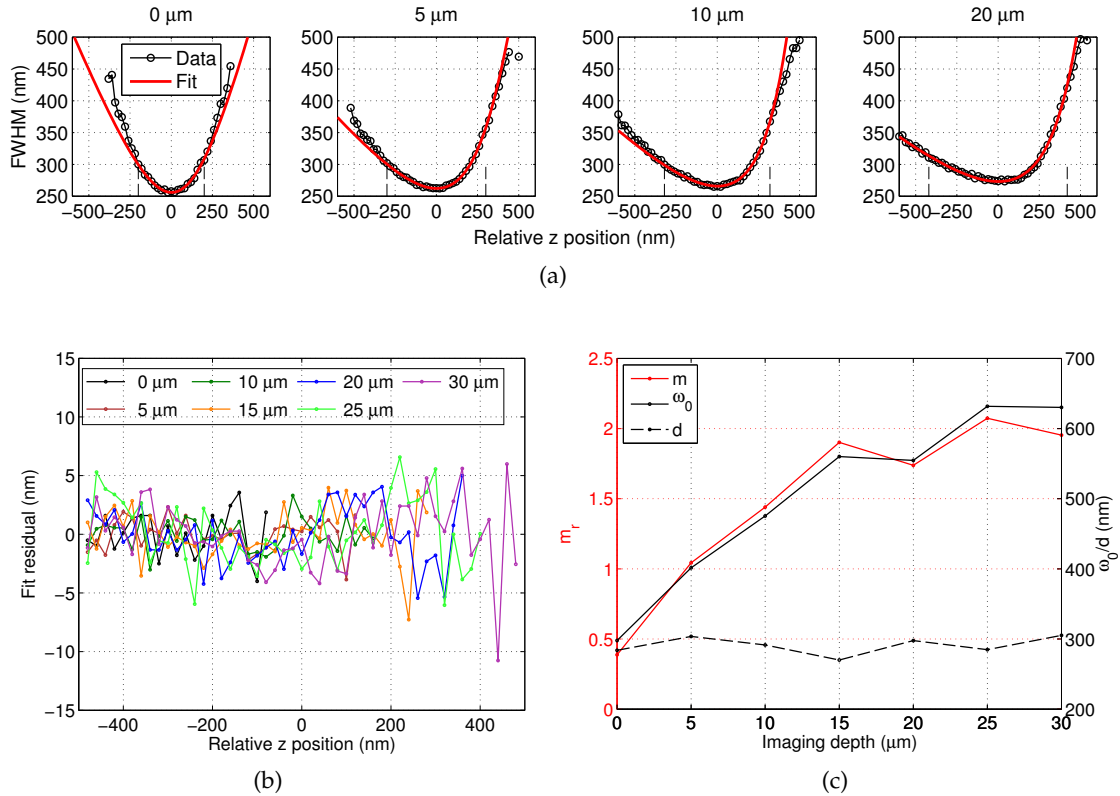
Figure 41: (a) Fits of the proposed correlation function to calibration measurements at selected depths. The individual axial fitting range is indicated by the dashed vertical lines at the bottom of each graph. (b) Individual fitting residuals for all examined depths. (c) Change of the correlation function parameters as a function of the imaging depth.

Fig. 41a illustrates that the proposed correlation function is capable of approximating the induced aberrations independently of the imaging depth. It includes only selected depths since for the given configuration the effects of the RIM are most evident within the first 20 μm. LSQ-based fitting is used to match Equ. 38 with the measured calibration curves.

The fit residuals for all examined depths are presented in Fig. 41b. Apparently, Equ. 38 is a fairly good approximation for the induced aberrations at any depth since the residuals are only in the range of ±5 nm. Note that the fit is obtained only from a limited axial range that increases as a function of the depth. It corresponds to the axial spread of the PSF and was determined from the FWHM of a Gaussian fit to the axial distribution of the peak intensity (see Fig. 39b). This limitation is reasonable since it was experienced that already the well-established standard model deviates outside this range. This could be the result of the much lower number of collected photons or because the shape of the PSF starts deviating from Gaussian approximations as was observed by Izeddin et al. 2012b. If the included data points would be only restricted to

have peak intensities of at least 20 % of the intensity at focus, then the fitting residuals still just increase by a factor of two (Sokoll et al. 2013).

Fig. 41c finally depicts the change of the correlation function parameters as a function of the imaging depth. m_r and ω_0 reflect the strength of the induced aberrations most. Their rate of change decreases as a function of the depth as was already experienced for the course of the calibrations curves.

4.9.1.2 *Breaking the Axial Symmetry by Introduction of a Cylindrical Lens*

Now that a depth-independent description of the axial correlation function is available, still the differentiation whether a particle is located above or below the focal plane has to be enabled. As is illustrated in Fig. 42a, the axial position can only be ambiguously determined since owing to the lateral point symmetry of the PSF effectively only a single width parameter is extracted. Fig. 42a also depicts the critical region around the focal plane where only limited information about the axial position is available. Changes in the axial position are only represented by minor variations in the function value of the correlation function.

(a) (b)
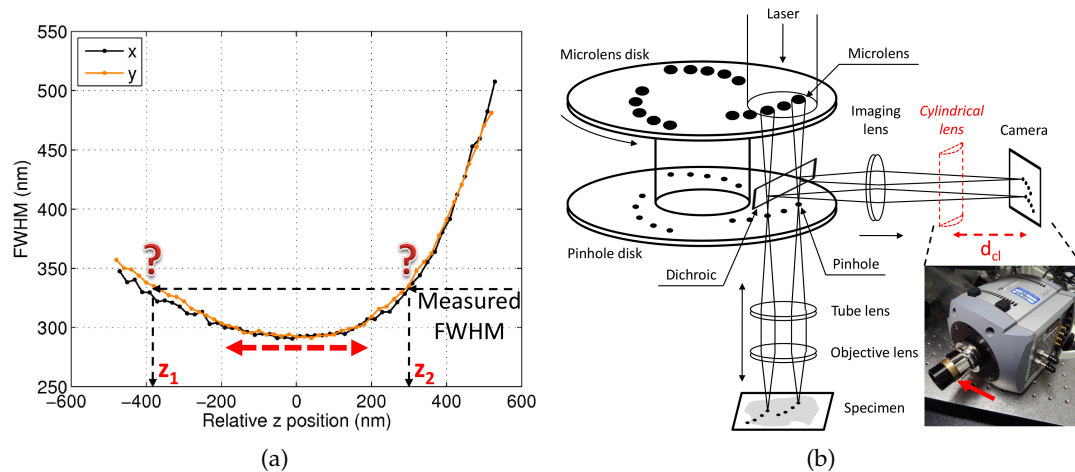
Figure 42: (a) Critical issues of axial off-focus imaging are illustrated on the basis of a real acquisition at 10 μm depth. Clearly, the axial position can only be determined ambiguously, and only limited information about the axial position is available from the flat course of the curve in the vicinity of the particle center (red arrow). (b) Position of the cylindrical lens in the light path of the SDCM setup. The red arrow points at the custom-built housing for the lens.

To address these issues, a plano-convex cylindrical lens[12] was inserted into the light path of the SDCM setup. It was placed with distance d_{cl} directly in front of the camera using a custom-built housing (see Fig. 42b).

This introduction of the lens slightly shifts the focal plane for one lateral direction along the axial axis so that the 2D PSF becomes elliptical instead of rotationally symmetric. Furthermore, the major axis is switching half way between the two focal planes like it is illustrated on the left in Fig. 43a. Breaking the axial symmetry of the PSF introduces additional axial information as now the two lateral widths of the elliptical PSF can be separately analyzed. If they are plotted individually, this creates two correlation

---

12 Thorlabs LJ1516RM, $f = 1000$ nm

96

curves that exhibit an axial shift. It is denoted as focal shift Δ_f in this thesis and is also visualized in Fig. 43a. This allows for unambiguous computation of the relative axial position of a particle since each position is defined by a unique pair of FWHM values. The center between the vertices of the two curves is often interpreted as the axial center of the particle. This is imprecise since the real center of the particle is at the vertex of the correlation curve unaffected by the lens. This is the y curve in the current configuration, and therefore, their vertex represents the zero position throughout this thesis.
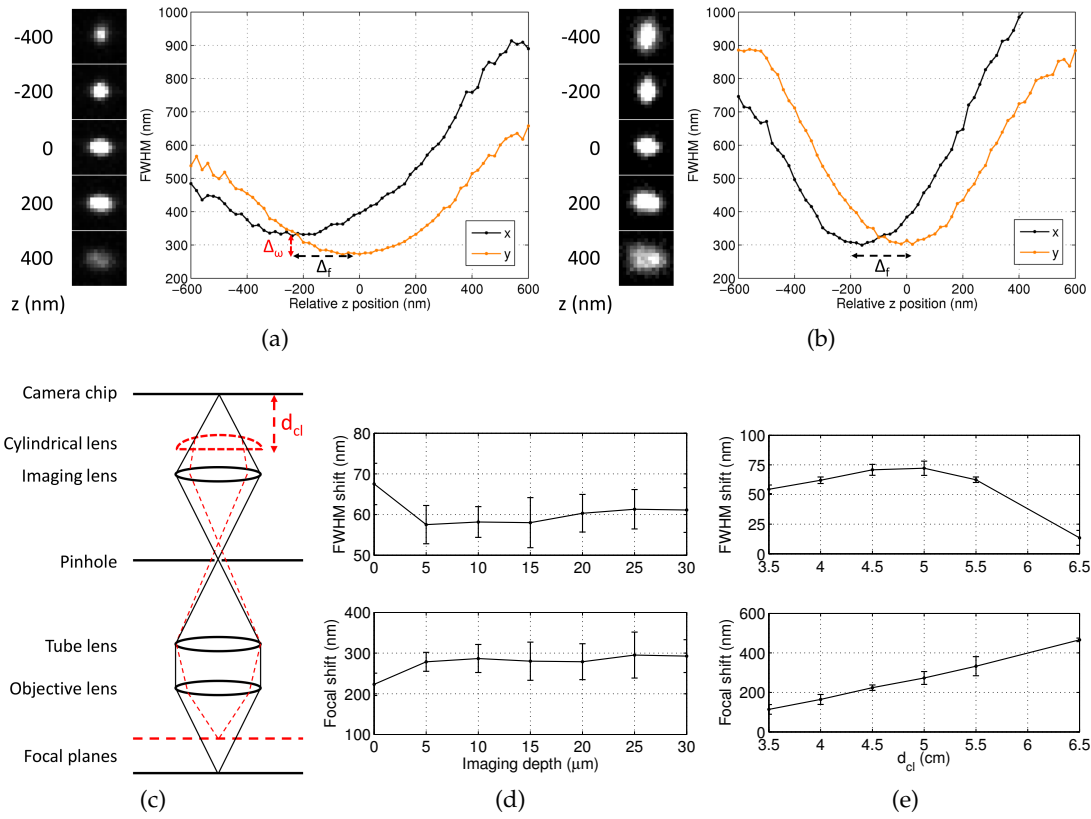
Figure 43: (a) Individual correlation functions acquired in confocal mode. Δ_f and Δ_ω are illustrated. The corresponding acquisitions are presented on the left. (b) Individual correlation functions acquired in WF mode. There is no FWHM shift for this configuration. Again, the corresponding images are presented on the left. (c) Simplified ray diagram for confocal imaging with (red) and without (black) the cylindrical lens. Δ_ω and Δ_f are plotted as functions of (d) the imaging depth respectively (e) d_{cl}.

The expected focal shift between the two calibration curves is clearly observable in Fig. 43b, but also an offset in the FWHM value of their vertices. It will here be denoted as Δ_ω. It can also be recognized by the varying lengths of the major axis above and below the particle center in the real acquisitions on the left.

This offset was determined to be an artifact of using a cylindrical lens with SDCM. As is apparent from Fig. 43b, if the bypass of the CSU is used, thus, the images are acquired in WF mode, only the expected focal shift is obtained, and the major axes are of equal length.

To clarify the principle of operation of the lens, Fig. 43c shows a simplified sketch of the light paths in the setup. This is done separately for the x and the y direction,

where, for the present implementation, the x direction is affected by the lens, but the y direction is unaffected. The image that is focused on the camera chip stems from a different, second, focal plane for the x direction. This is due to the different angle of refraction at the convex interface of the lens. This is actually the desired effect that breaks the point symmetry of the PSF since the width of the 3D PSF varies along the axial axis, but a different axial plane for each lateral direction is now focused into a single image.

To identify the origin of Δ_ω, the actual light path has to be examined. For the y direction, the light at the focal plane of the objective is first focused into the pinhole and then on the camera chip. Since the image for the x direction stems from a different focal plane, the light of this second focal plane is not focused into the pinhole anymore. Instead, its focal point is slightly shifted towards the back of the pinhole. This leads to a loss of resolution in the x direction. Consequently, the PSF is blurred along this lateral direction, which is finally observed as a FWHM offset in the corresponding correlation curve. It must be concluded that the FWHM shift is an inherent artifact of using a cylindrical lens with confocal setups and cannot be avoided.

Next to the focal shift also the FWHM shift has to be known for confocal setups. The course of both shifts as a function of the imaging depth is depicted in Fig. 43d. It is apparent that they are virtually constant and independent from the imaging depth yielding on average $\Delta_\omega = 60.25 \pm 5.71$ nm respectively $\Delta_f = 278.40 \pm 45.37$ nm. A notable deviation is apparent for the measurements at zero depth. Similar to another effect that will be explained later, this could be an artifact of the astigmatism produced by the cylindrical lens. On the other hand, the fact that at zero depth one focal plane may be located in the cover slip while the other is already in the mismatched media might introduce such deviations. It must be admitted, that the cause of this effect could not be clearly determined during this work. However, since molecular dynamics are measured within the samples, this effect can be neglected. The stated average values do not include the measurements at zero depth.

In contrast, both shifts vary as a function of the distance d_{cl} between the lens and the camera chip. In Fig. 43e it is apparent that Δ_f has a linear relationship, whereas Δ_ω first increases as one would expect, but then decays for distances larger than 5 cm. Inspection of the resulting axial correlation curves revealed that at very large d_{cl} their centers are shifted out of the detectable axial range. This results in deviations from the expected relationship. The axial sectioning capability of the CSU, that in the first place renders analysis deep in living tissue possible, now limits the strength of the astigmatism that can be adjusted. Given that for a specific lens the introduced astigmatism is solely adjusted by d_{cl}, it is very reasonable that Δ_ω does not vary with depth.

Consequently, the constant FWHM shift can simply be subtracted from the measurements and does not yield a loss of generality of the proposed approach. Δ_ω is silently accounted for in the remainder of this thesis. $d_{cl} = 4.5$ cm was chosen as a compromise between a reasonable astigmatism and the available axial detection range. This issue is also addressed in more detail in Sect. 4.10.1.9.

Finally, another artifact of the setup that could not be accommodated for in this work has to be revealed. Fig. 40-41 were already drawn from analyses of the y curve of images acquired with a cylindrical lens. This lateral direction is almost unaffected by the lens and results in equivalent curves like if they were measured without a lens (Sokoll

et al. 2011, Deng and Shaevitz 2009). In theory, the cylindrical lens only shifts the focus of one lateral direction so that owing to the rotational symmetry of the PSF both curves should be identical. However, for the present configuration the shifted x curve was found to exhibit deviations from the y curve that cannot be neglected. This is most significant below the particle (see Fig. 44a). The x and y curves are corrected for their shifts and plotted for exemplary depths.
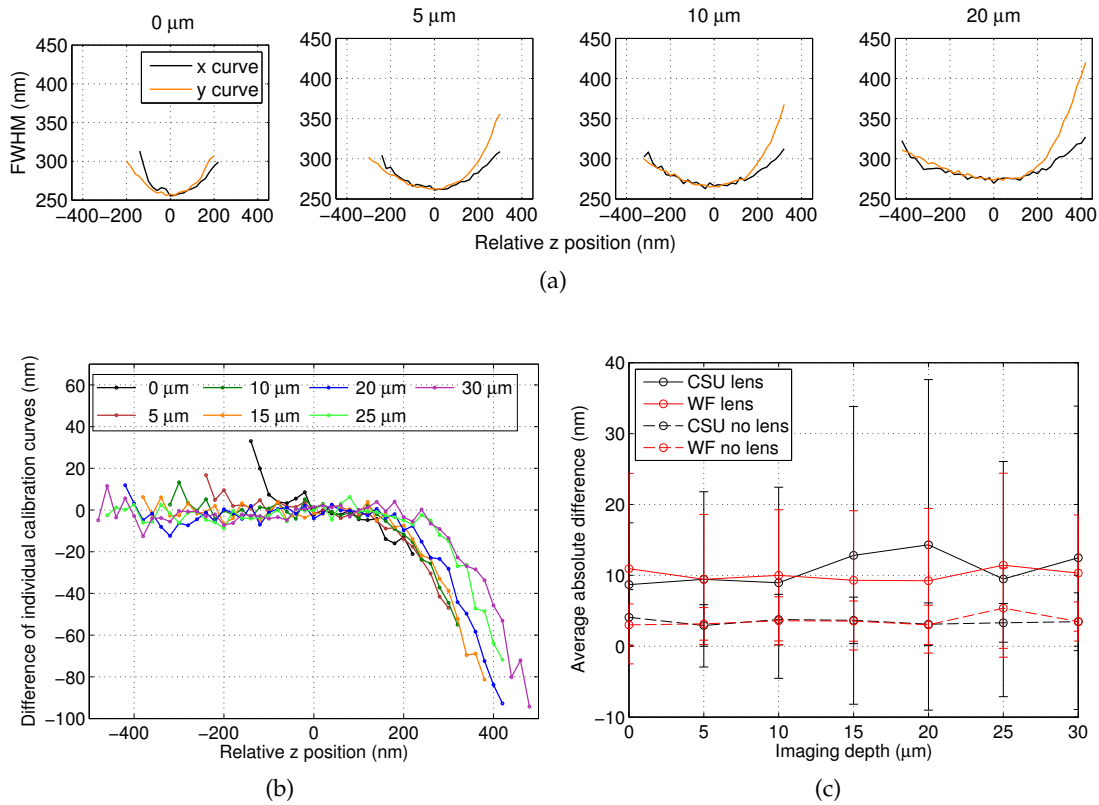

Figure 44: (a) Individual plot of the x and y axial calibration curves of single scans at exemplary depths. (b) Difference of the x curve that is affected by the cylindrical lens from the unaffected y curve at exemplary depths. (c) Total difference between the two lateral calibrations curves for different imaging configurations at exemplary depths. Note that owing to the measurement noise and the calculation of absolute deviations, the average error may never approach zero. The average difference with lens is not increased tremendously because only parts of the curve deviate.

In Fig. 44b the corresponding differences between the individual curves are quantified. Within the available axial range the differences may become as high as 100 nm. The average absolute deviation for the relevant axial range is presented as a function of the imaging depth in Fig. 44c. The total deviation is ~ 11 nm and is almost constant as a function of the depth.

To identify the source of this artifact, Fig. 44c also presents the deviations for different imaging configurations. This includes confocal spinning disk imaging without the lens as well as using the WF mode with and without the lens. Clearly, this artifact must be attributed to the lens since for both imaging configurations the error increases significantly only when the cylindrical lens is installed. Without the lens both curves are virtually identical for the total axial range (see Fig. 42a for an example). Similar results were obtained when using another cylindrical lens of the same type respectively

one with shorter focal length. Consequently, these aberrations are not subject to a single poorly manufactured lens, but instead it must be concluded that the introduced astigmatism of a cylindrical lens is not as perfect as expected. Similar artifacts have also been reported by Izeddin et al. 2012a and were corrected using technically more sophisticated AO. An explanation was not provided.

It has to be stated that although the cylindrical lens could be determined as the source of these aberrations, a satisfying physical explanation could not be found. The artifacts of the present setup that lead to deviations form the expected behavior have to be accepted as they are. Since alternatives are available, the proposed online calibration method nevertheless draws on the expected curve model with identical curves that just exhibit a focal shift.

4.9.2 *The Axial Online Calibration Method*

Up to now, high temporal and spatial resolution have been enabled by computation of the nanoscale 3D particle position from just a single acquisition. The axial analysis range was extended to both sides of the focal plane by introducing an astigmatism using a cylindrical lens, and also a description of the required axial correlation function is available independently of the imaging depth. However, their current parametrization is still unknown.

As it was stated in Sect. 4.3.5, virtually all methods that localize fluorophores deep in tissue rely on some sort of prior calibration. Owing to the continuous motion of molecules this is practically hardly feasible for SPT in living samples. As a result of the minimum time it takes to acquire a full z-stack, particle motion corrupts the correspondence between the expected and the real scan position. Also, matching the current experimental situation is impracticable since the parametrization among different depths varies significantly. So for instance imperfect specimen contact to the cover slip may hinder estimation of the current depth in the tissue, the actual RI of the sample depends on the temperature and the manufacturing variance of the cover slip thickness changes the effect of the RIM.

In order to circumvent such issues, here an online calibration procedure is developed. It attempts to determine the current axial correlation function directly from the 2D image stream that must be acquired to analyze molecular dynamic.

The key ideas of the method are (1) that since the correlation function is defined by three parameters, it can be reconstructed by knowing three coordinates of the curve. (2) for the purpose of obtaining these coordinates, the inherent molecular particle motion can be used, and (3) on that account, the redundancy introduced by the astigmatism can be exploited. The method consists of three steps:

Data : Concatenated particle trajectories and corresponding FWHM values
Result : Parametrization of axial correlation function
(1) Identify vertex frames;
(2) Compute the three required coordinates;
(3) Estimate the curve parameters;

They are now described in detail.

4.9.2.1 Vertex Frame Identification

In contrast to trying to avoid the inherent molecular motion, it is actually demanded and consequently employed to estimate the FWHM of the vertex of the correlation curve. The presented method assumes that a particle passes the two artificial focal planes of the imaging configuration several times during the acquisition of a single 2D image stream. This is not a serious limitation since the diameters of neuronal compartments like synapses, axons, or dendrites are limited, and particles mainly diffuse freely within these compartments.

The most simple case is considered in Fig. 45a, where a particle just moves along the axial axis. It presents the particle's axial position as a function of the current imaging frame. The respective focal planes in the x and y directions are crossed at different frames. The corresponding FWHM measurements of the individual lateral directions are also depicted. The vertex point of the curves corresponds to the moment when a particle is in either focal plane. To identify those images where a particle is in either focal plane and that consequently represent a vertex position, the change of the FWHM values during particle movement is analyzed.
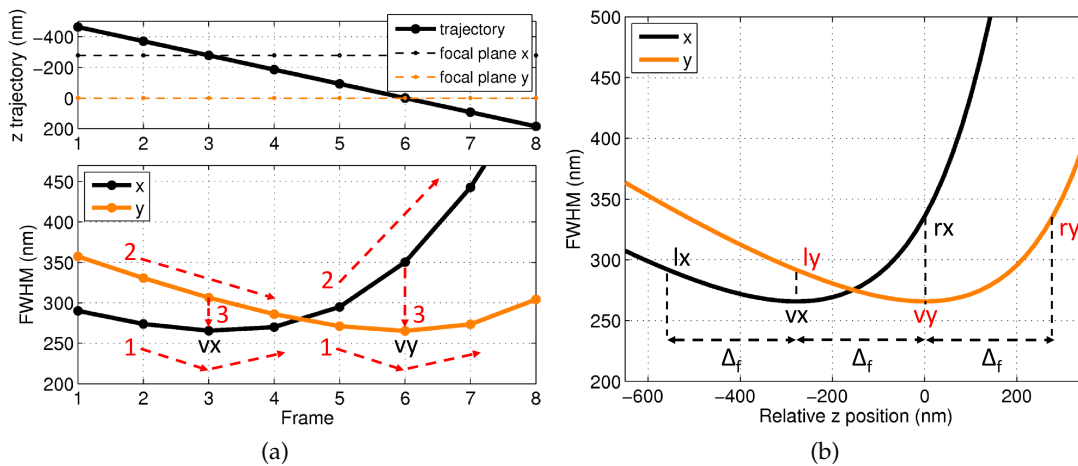
Figure 45: Basic principles of the algorithm. (a) Trajectory of a particle that moves along the axial axis and the corresponding FWHM measurements. The red marks illustrate the vertex identification model. (b) Derivation of the three required coordinates (in red) by exploitation of the redundancy introduced by the cylindrical lens.

The corresponding vertex identification model is then defined as follows: a vertex frame is any image, where the measured FWHM in one lateral direction is smaller than those of the two neighboring images. This is indicated by mark 1 in Fig. 45a. The FWHM values in the other lateral direction have to be either constantly increasing or decreasing in the current neighborhood (see mark 2). Finally, mark 3 refers to the requirement that the FWHM value of v must be smaller than that of the opposite lateral direction. A robust estimate for the FWHM value of the two vertices can then be computed by the median FWHM of all identified vertex frames f_{vx} and f_{vy}.

An inherent problem of this identification model is that it is prone to underestimate the true FWHM value. Because the estimated FWHM values are subject to noise, it is clear that frames with outliers towards low FWHM values are more likely to be selected as vertex frames than the remaining ones. Consequently, the estimated FWHM value of v is

biased towards lower values. To account for this effect, the vertex frame identification is conducted on smoothed images to reduce the noise. The data is convolved with a Gaussian filter of size 9 and kernel SD of 1 pixel (Crocker and Grier 1996) before fitting. Although the vertex frames are identified from the smoothed images, the actual FWHM value is still computed using the fitting results from the original images. This heuristic procedure is reasonable since smoothing stabilizes the relative FWHM differences between the frames.

4.9.2.2 *Computation of the Three Required Coordinates*

Now that an estimate of the vertex FWHM is available, the redundancy introduced by the astigmatism is exploited to derive estimates for two more coordinates left (l) and right (r) of the vertex.

Therefore, the properties of the two correlation functions shall be recapitulated: they are axially separated by Δ_f, which is independent of the imaging depth and is solely defined by the distance d_{cl} of the cylindrical lens to the camera. Apart from that, the curves are identical owing to the rotational symmetry of the PSF. In consequence of that knowledge, l and r are chosen to be the points at axial distance $\pm\Delta_f$ from v. Then all three coordinates can be estimated from the identified vertex frames. This situation is exemplarily depicted in Fig. 45b.

It is apparent that in this setting ly corresponds to the vertex vx and rx to the vertex vy. Since always the widths in both lateral directions are known, the FWHM value of ly can be computed from the median of the FWHM values of the vertex frames f_{vx} in the lateral x direction. Similarly, the FWHM value of rx can be computed from the median of the FWHM values of the vertex frames f_{vy} in the lateral y direction. Since the two curves are identical, the FWHM value of ly is the same as the FWHM value of lx at distance $-\Delta_f$ from vx. Respectively, the FWHM value of rx is the same as the FWHM value of ry at distance $+\Delta_f$ from vy. Consequently, they can be jointly used to construct each individual axial correlation function.

Because the absolute axial position of a particle is not of interest, the axial coordinate of v is simply zero, and the three general coordinates are finally given by:

$$\begin{pmatrix} v \\ l \\ r \end{pmatrix} = \begin{pmatrix} 0 & \tilde{\omega}_{xy}(f_v) \\ -\Delta_f & \tilde{\omega}_y(f_{vx}) \\ +\Delta_f & \tilde{\omega}_x(f_{vy}) \end{pmatrix}. \tag{39}$$

Here, $\tilde{\omega}$ denotes the median of all collected FWHM values. Note that for simplicity only the three general coordinates v, l, and r are stated. The extra notation whether they belong to the x or y curve can be omitted because vx_x is simply $vy_x - \Delta_f$ and so on. As already addressed earlier, Δ_ω is left out in these equations since it can simply be considered by subtraction. It should be noted that the calibration procedure actually also allows for estimation of Δ_ω. It can be computed from the difference between $\tilde{\omega}_x(f_{vx})$ and $\tilde{\omega}_y(f_{vy})$.

4.9.2.3 Estimation of the Parametrization

By use of the three general coordinates, the parameters m_r, ω_0, and d of the axial correlation function can be computed by setting up a nonlinear equation system:

$$\omega(l_x) = l_y \tag{40}$$

$$\omega(v_x) = v_y \tag{41}$$

$$\omega(r_x) = r_y \tag{42}$$

In order to avoid complex solutions, the solution space is restricted by incorporation of the following assumptions on the three coordinates:

$$v_y > 0, \ l_y > 0, \ r_y > 0 \tag{43}$$

$$l_y > v_y, \ r_y > v_y \tag{44}$$

$$l_x < v_x < r_x \tag{45}$$

$$v_x = 0 \tag{46}$$

$$-l_x = \Delta_f, \ r_x = \Delta_f \tag{47}$$

This results in the following relatively compact analytic solutions for the three parameters:

$$m_r = \frac{-l_y + r_y}{2r_x} \tag{48}$$

$$\omega_0 = v_y \tag{49}$$

$$d = \pm \frac{2v_y r_x}{\sqrt{(l_y - 2v_y + r_y)(l_y + 2v_y + r_y)}}. \tag{50}$$

By observation of Equ. 50 it becomes apparent that there exist actually two solutions for each set of coordinates. However, owing to the squaring of d in Equ. 38, both solutions result in the same curve, and effectively an unique real solution exists.

An exemplary analytical solution is presented in Fig. 46a. It is computed for a set of coordinates taken from the calibration experiments at depth 10 µm in Mowiol. Apparently, the resulting curves run well through the three coordinates, but their true vertex is not located at vx respectively vy. This violates an essential assumption of the online calibration, and it must be concluded that although a compact analytical solution exists, it does not comply with all expectations on the solution.

Therefore, an additional equation is necessary that incorporates the required side condition of having the vertex of the curve at the coordinate v. This can be accomplished by adding equation:

$$\omega'(v_x) = 0 \tag{51}$$

to the nonlinear equation system (see Equ. 40-42). Here, $\omega'(v_x)$ denotes the first derivation at v. Since this results in an overdetermined equation system, Equ. 38 is extended with an additional parameter z_s yielding:

$$\omega(z) = \omega_0 \cdot \sqrt{1 + \left(\frac{z - z_s}{d}\right)^2} + m_r \cdot (z - z_s) \tag{52}$$
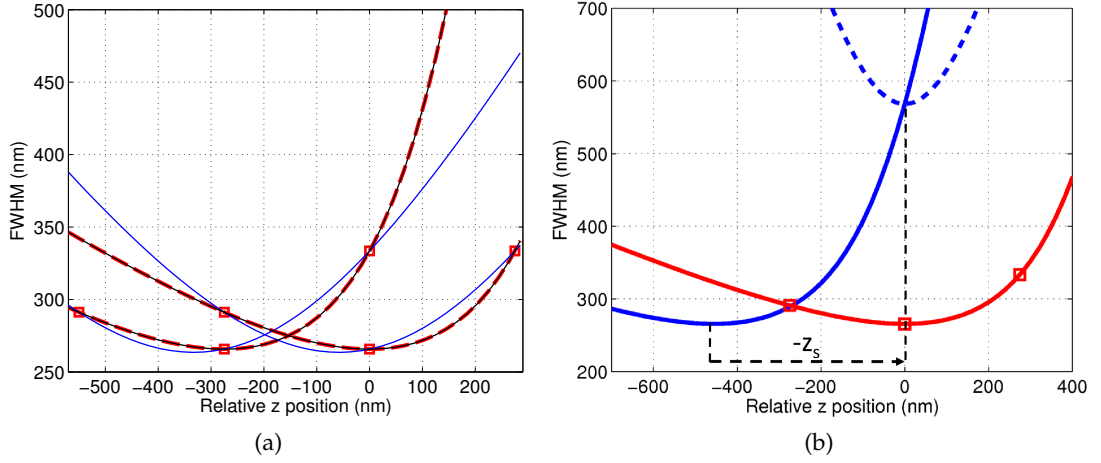
Figure 46: (a) Approximation of the true calibration curve (red dashed line) on the basis of the reference coordinates (red rectangles). The analytical solution (blue line) runs well through the coordinates, but does not have its vertex at the true vertex. In contrast, the proposed numerical solution (black line) approximates the true calibration curve very well. (b) Illustration of the shift z_s. The blue curves have identical parametrization except that the dashed curve has $m_r = 0$ because it is the corresponding symmetrical parabola. Both curves are axially separated by the shift z_s. It must be subtracted in order to have the vertex at the true vertex position of the wanted curve (red line).

and consequently

$$\omega'(z) = m_r + \frac{\omega_0(z - z_s)}{d^2\sqrt{1 + \frac{(z - z_s)^2}{d^2}}}. \tag{53}$$

The principal course of the curve is still the same, but z_s allows to shift the curve along the axial axis in order to maintain the true vertex at v.

Although the fitting procedure involves only four variables, the closed-form solution of the latter system of four nonlinear equations is quite complicated and contains complex solutions. In order to avoid the evaluation of ill-conditioned expressions, a numeric root finding procedure was found to be much more convenient from a practical point of view.

A LSQ-based nonlinear curve fitting procedure is proposed. It has the advantage that complex solutions can be prevented, and instead, always a near real solution is obtained. The fitting procedure relies on the trust region optimization scheme (Coleman and Li 1996) implemented in MATLAB's Optimization Toolbox and is provided with the following bounds:

$$m_r : \quad [-2\ 5] \tag{54}$$

$$\omega_0 : \quad [100\ 1000]\ nm \tag{55}$$

$$d : \quad [100\ 1000]\ nm \tag{56}$$

that are derived from the calibration measurements in Mowiol (see Fig. 41c).

In order to enforce the necessary side condition, although there is now one coordinate less than required parameters, the key idea is the substitution of z_s by the remaining parameters. z_s is defined to be the axial shift of the true vertex position that

originates because the original parabola is skewed by means of the term $m_r \cdot z$. z_s is illustrated in Fig. 46b and can be computed by:

$$z_s = \pm \sqrt{\frac{m_r^2 d^4}{\omega_0^2 - m_r^2 d^2}}. \tag{57}$$

This simply corresponds to the root of the first derivation as the original vertex is by definition at $v_x = 0$ (see Equ. 39). Since the RI of the specimen is typically much smaller than that of the immersion medium, the RIM leads to axial correlation functions with positive shift z_s. Owing to the manufacturing variance of the cover slip thickness, the curve may also be skewed in the opposite direction. This occurs most likely at low imaging depths. Errors in the coordinate estimation may also result in that phenomenon. Therefore, the appropriate solution of Equ. 57 is selected according to whether l_y or r_y is larger.

During the fitting procedure, z_s is not considered as a free parameter, but instead computed by use of Equ. 57 and the current estimates of m_r, ω_0, and d. Consequently, the true vertex of the skewed parabola is always enforced to be at $v_x = 0$ independently of the parametrization. As a result of this substitution, the actually underdetermined problem can be solved using just three coordinates because the fitting procedure indirectly maintains the additional side condition. This procedure yields adequate real approximations to the wanted correlation function as is exemplarily shown in Fig. 46a.

4.9.3 Computation of the Axial Position

Now that the parametrization of the axial correlation functions is known, they can be used as calibration curves to compute the relative axial position of a particle using the measured widths ω_x, ω_y.

There are two different types of techniques: here termed (1) direct computation and (2) distance minimization methods. Techniques of the former type plug the widths into a separate calibration function. The corresponding axial position can be directly read out by computation of the function value from the measured FWHM values. This separate calibration function can be computed using the ellipticity ω_{xc}/ω_{yc} (Spille et al. 2012), the difference $\omega_{xc} - \omega_{yc}$ (Izeddin et al. 2012a), or by insertion of the generalized width $\sqrt{\omega_{xc}^2 \omega_{yc}^2}$ and the square root of the ellipticity into Equ. 26 (Holtzer et al. 2007). ω_{xc} and ω_{yc} denote the FWHM values of the axial calibration curves for each axial position.

The distance minimization method proposed by Huang et al. 2008b searches for the axial position that matches the measured widths best. It minimizes the distances between the measured widths and the calibrations curves by means of the combined distance:

$$D_c = \sqrt{\left(\sqrt{\omega_x} - \sqrt{\omega_{xc}}\right)^2 + \left(\sqrt{\omega_y} - \sqrt{\omega_{yc}}\right)^2}. \tag{58}$$

According to Spille et al. 2012, direct computation methods are faster, but the minimization method is more accurate. It was therefore chosen in this thesis. Since it was experienced that in order to yield robust results the search must be well initialized, the axial position is first computed by direct computation using the difference and subsequently improved by initializing the minimization method with that estimate.

This section evaluates the presented 3D SPT workflow. Evaluation of algorithms that an-alyze real experimental data with nanometer accuracy is inherently difficult for several reasons. Most importantly, the ground truth (GT) is generally not accessible owing to the lack of parallel methods that could assess the same level of information. Further-more, critical parameters like the SNR or the number of focal plane crossings cannot be easily accessed or even be controlled in real experiments. Finally, statistically sig-nificant results can only be ensured using large number of acquisitions, which cannot always be obtained experimentally.

Therefore, the algorithm is evaluated on different types of data: (1) its performance is analyzed on synthetic data so that the GT is available and the dependency on critical parameters can be assessed. (2) the algorithm is applied to semi-synthetic data, which allows for determination of its accuracy in the presence of experimental artifacts of the setup. (3) measurements in brain slices under real experimental conditions have been conducted, and the plausibility of the results was examined.

Since the major contribution of this thesis is the facilitation of experiments in natural brain slices, the evaluation mainly considers the online calibration procedure respec-tively the axial accuracy. The focus was set on minimizing the depth dependent SE since this is an important measure to reveal how well the model assumptions meet the reality. Intermediate results of the 3D SPT workflow are also evaluated.

4.10.1 *Evaluation on Synthetic Data*

Since the online calibration method depends on the quality with which the shape pa-rameters of individual particles are determined, also the particle detection and shape estimation procedures are evaluated. The focus is set on evaluating their performance in the presence of multiple particles with partially overlapping distributions. This is followed by several detailed analyses that evaluate the efficiency of the online calibra-tion method in isolation. This includes (1) assessment by means of the SE and the axial LA, (2) visual analysis of the determined trajectories, and (3) an evaluation of the ob-tainable diffusion parameters. Since the online calibration comprises several steps, also (4) intermediate results are analyzed. (5) the impact of the experimental parametriza-tion is evaluated. Before the results are presented it is described how the underlying images are simulated.

4.10.1.1 *Simulation of Astigmatism-Based 3D Single Molecule Images*

To create synthetic single molecule images that also represent astigmatism-based 3D information, the PSF of individual particles is simulated with an elliptical Gaussian function of the form presented in Equ. 22. This is a common approximation to the induced aberrations (Huang et al. 2008b, Holtzer et al. 2007).

Since the sensor of the camera is well represented by a discrete set of quadratic pixels, this continuous function is integrated over the pixels to simulate photon counts (Huang et al. 2011). The discretized elliptical Gaussian profile is then computed as:

$$N_{x,y} = N_p \Delta I_x(x,y) \Delta I_y(x,y) \tag{59}$$

with

$$\Delta I_x(x, y) = \frac{1}{2} \left[\text{erf} \frac{((x - \frac{1}{2}) - x_c)}{\sqrt{2}\sigma_x} - \text{erf} \frac{((x + \frac{1}{2}) - x_c)}{\sqrt{2}\sigma_x} \right], \tag{60}$$

$$\Delta I_y(x, y) = \frac{1}{2} \left[\text{erf} \frac{((y - \frac{1}{2}) - y_c)}{\sqrt{2}\sigma_y} - \text{erf} \frac{((y + \frac{1}{2}) - y_c)}{\sqrt{2}\sigma_y} \right]. \tag{61}$$

Here, $N_{x,y}$ is the number of signal photons at a pixel per particle, N_p is the total number of emitted photons per particle, and $\Delta I_x(x, y)$, $\Delta I_y(x, y)$ integrate the Gaussian distribution over each pixel using the error function. x_c, y_c are the center coordinates, and σ_x, σ_y represent the SD of the Gaussian profile.

Multiple particles, of number K_p within an image, are simulated by adding up $N_{x,y}$ of all particles. This is reasonable since it can be assumed that any emitter contributes independently to the number of photons at a pixel.

In order to obtain realistic images, they are parameterized and further processed to correspond to the present experimental configuration. σ_x and σ_y are chosen to correspond to ω values in the range of 266-500 nm (see Fig. 40a). The individual FWHMs of each particle are randomly drawn from an uniform distribution in that range. This reflects the situation that particles have elliptical shapes owing to the introduced astigmatism.

The images are also scaled to match the camera's back-projected pixel size in the object space (d_{po}). Based on the TIRF objective with $M = 100$ and the CSU's internal magnification factor of 1.2, 1 µm in the object space is magnified to 120 µm on the camera chip. Since the physical pixel size of Andor's iXon^{EM} + 897 camera is $d_p = 16$ µm, 7.5 pixel represent 1 µm in the object space, and hence each camera pixel corresponds to $d_{po} \approx 133$ nm.

The number of emitted photons per particle is varied in the range $N_p \approx 400$-100000, which corresponds to SNRs of ≈ 4-66. $N_p \leqslant 3000$ respectively SNR $\leqslant 10$ are the values actually experienced in real brain slice experiments (see Fig. 74e). From the same experiences a constant number of background photons $N_b = 40$ is added to each pixel.

To simulate the noise contribution of an EMCCD camera, only δ_{photon}, δ_b, and δ_{mult} have to be considered (see Sect. 3.1.4.4). The signal and background noise sources are added to each pixel using independent realizations p_{pois} of a Poisson distribution with $\lambda_{pois} = \sum_1^{K_p} N_{x,y} + N_b$. The respective λ_{pois} is subtracted from p_{pois} so that it only represents the additive noise component at a pixel. The multiplicative noise that occurs in the electron multiplication register is considered by multiplication of $\delta_{mult} = \sqrt{2}$ with p_{pois}.

In order to effectively eliminate the readout noise, G_{EM} was set to 64. Since G_{EM} is practically linear and the number of electrons per digital intensity unit of the analog-to-digital converter is $S_{CCD} = 12.4$, the photon counts are converted to intensity values similar to what the camera provides by multiplication with $\frac{G_{EM}}{S_{CCD}}$.

Altogether, the intensity value present at each pixel in a synthetic image with multiple particles is finally computed as:

$$i_{x,y} = \left[\sum_1^{K_p} N_{x,y} + N_b + \sqrt{2} p_{pois} \right] \cdot \frac{G_{EM}}{S_{CCD}}. \tag{62}$$

ω	N_p	N_b	d_{po}	λ_{pois}	δ_{mult}	G_{EM}	S_{CCD}
266-500 nm	400-100000	40	133 nm	$\sum_1^{K_p} N_{x,y} + N_b$	$\sqrt{2}$	64	12.4

Table 1: Default parametrization for the simulation of single molecule images.

The parametrization is summarized in Table 1. This is the default parametrization used throughout the evaluation if not stated otherwise.

An exemplary image that was rendered with the presented configuration is presented in Fig. 47. The density was set to 0.5 molecules per μm^2, and it is presented at various SNRs in order to gain an impression of the obtained variance in image quality with which a 3D SPT algorithm has to deal.
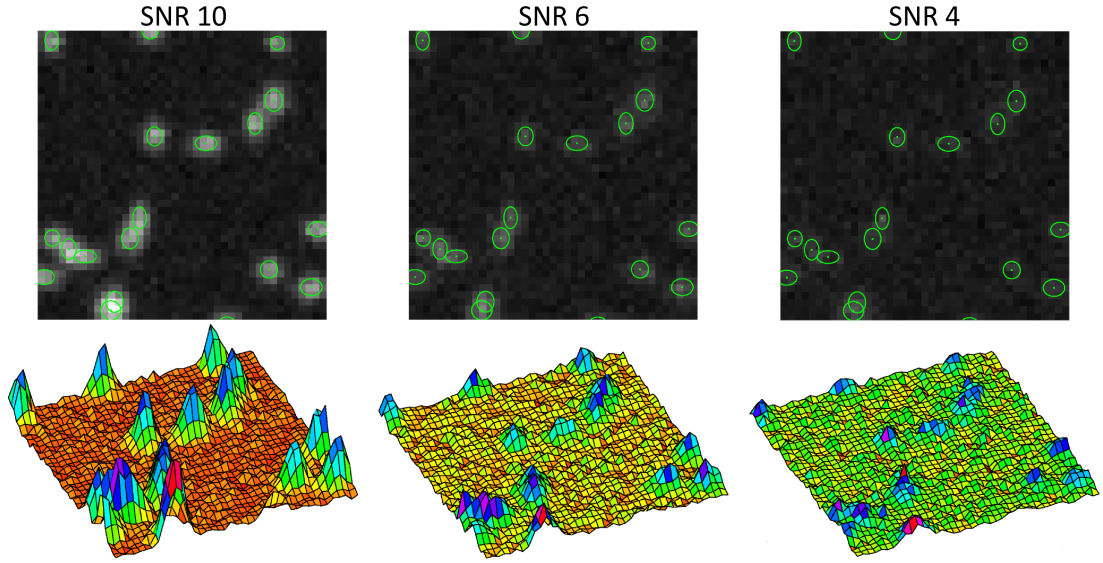
Figure 47: Exemplary simulated image at varying SNRs.

In accordance with Equ. 9, the individual SNR of each particle in the image is defined by:

$$SNR = \frac{\hat{N}}{\sqrt{2\left(\hat{N} + N_b\right)}},$$ (63)

where $\hat{N}$ denotes the number of photons at the peak pixel of a particle excluding noise and background. The factor 2 incorporates δ_{mult}. Note that this definition is valid only for individual particles and may hence overestimate the SNR for overlapping intensity distributions of multiple particles.

Finally, also note that for evaluation the SNR is sometimes kept constant across all particles in an image independently of their FWHMs. This means that for a predefined SNR the number of photons per particle must be individually computed by:

$$N_p = 2\pi\sigma_x\sigma_y\hat{N},$$ (64)

with

$$\hat{N} = \frac{2SNR^2 + \sqrt{4SNR^4 + 8N_bSNR^2}}{2}$$ (65)

derived from Equ. 63. Of course, in real acquisitions the SNR reduces for off focus particles since their photons distribute over a blurred intensity profile, and the total photon number is decreased. However, for the evaluation of the detection and shape estimation performance it is reasonable to maintain a constant SNR. The respective FWHM and SNR definitions will be stated for each evaluation scenario individually.

4.10.1.2 *Particle Detection Procedure*

The particle detection procedure is based on the spot-enhancement filter that was already evaluated in detail for elliptic shapes, varying SNRs, and non-uniform backgrounds (Smal et al. 2010). It was reported to exhibit good overall performance, but its capability to handle overlapping intensity distributions or at least nearby particles was not analyzed. Such occurrences were explicitly avoided by the evaluation procedure. Since particles may occasionally approach each other during diffusion, this issue is addressed here. The particular question is: what is the minimal distance two particles may have so that the spot detection method can still resolve and detect them?

A common approach is the application to images with varying particle densities (Zhu et al. 2012, Huang et al. 2011, Holden et al. 2011). However, the density is just an indicator for the average distance of particles, but lower distances may occur by chance.

Therefore, the detection method is tested on simulated images that contain only two particles at varying distance. One particle is always located in the center of the image, and the second is located at a circular orbit with varying radius that represents the distance. Its exact position on the orbit is drawn from a uniform distribution. This setting is supposed to avoid any dependency on the sub-pixel positions by rendering them variable on the discrete grid. As explained earlier, the SNR of both particles in an image is kept constant, but the FWHMs do vary. Exemplary images are presented in Fig. 48a.
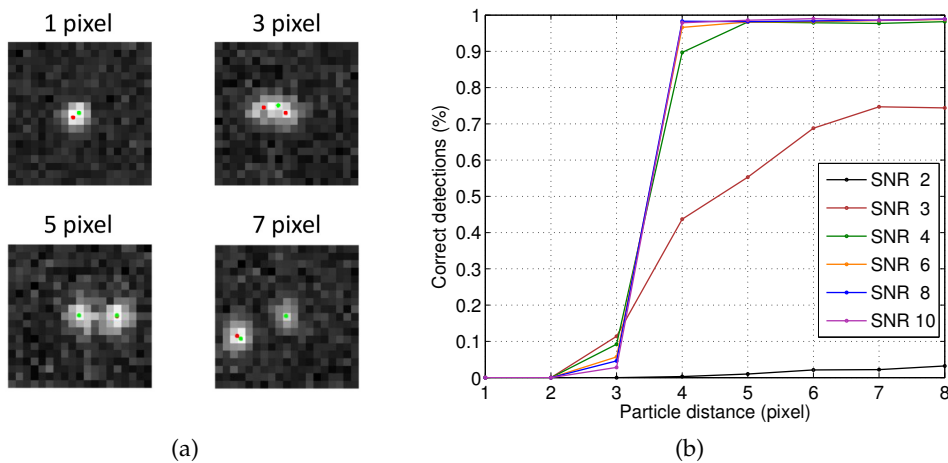

Figure 48: (a) Exemplary simulated images for different particle distances at SNR = 6. The red dots depict the GT and the green dots the detection result of the algorithm. (b) Fraction of correctly detected images as a function of the particle density and the SNR.

The performance was measured by means of the fraction of images that are correctly analyzed. This means that exactly two particles must be detected within one pixel distance to their known rounded pixel position. Any image that has less, more, or inaccurately detected particles is counted as being analyzed incorrectly. One pixel distance was chosen because it is the maximum deviation experienced with that filter for the present type of data. The detection threshold factor k was kept at 8 and never had to be altered for any evaluation scenario. Fig. 48b plots the fraction of correctly detected images as a function of the particle density and the SNR. 1000 images were analyzed for each data point.

Apparently, there is a clear change in the detection performance at distance of 4 pixels. This means that there must be 3 pixels between the center of two particles so that they can be correctly detected. For larger distances the detection rate reaches almost 100 %, which indicates that indeed the maximum deviation from the true particle position is only about 1 pixel. It is also apparent that the detection capability strongly deteriorates for SNR < 4, which is in good agreement with previous reports (Meijering et al. 2012).

Alternative algorithms that fit mixture models, but try to determine the correct number of particles by iteration between detection and localization (see Sect. 4.3.3.2), usually just provide the performance with respect to the density, but not an exact distance that they can resolve. By inspection of their provided images, it becomes apparent that they also require a distance of ~ 2 pixels between particle centers. Therefore, it can be concluded that the simplification for the detection performance, made in Sect. 4.7.2, is reasonable.

4.10.1.3 *EM Particle Fitting Procedure*

This section evaluates the accuracy with that the EM algorithm estimates the intensity distribution of multiple particles. Since for the present 3D application the individual widths of the distributions are of interest, in addition to the LA of the center coordinates also the accuracy with that the individual FWHMs are determined is assessed.

The evaluation covers several scenarios including the robustness of the EM algorithm with respect to (1) the number of random starts and (2) the number of particles. The dependency of its accuracy on the distance (3) between two particles, (4) of a particle to the boundary, and (5) of a center particle to another truncated particle is also investigated.

In order to isolate the accuracy analysis from the detection capability, the spot detection procedure is bypassed. The EM algorithm is provided with the correct number of particles, and their positions are rounded to discrete pixel positions. To simulate the accuracy of the spot detection filter, the positions are given a random deviation of either -1, 0, or 1 pixel in each lateral direction.

The SNR will be the same for all particles in an image irrespectively of their varying FWHMs. This holds true for all evaluation scenarios of this section. The number of simulated images is always 1000 unless stated otherwise.

Robustness to the Number of Random Starts

Since the EM algorithm is known to be a local optimizer, the presented fitting procedure runs it several times with varying random initialization and reports the result with the

highest likelihood. To determine a useful number of random starts for sub-regions of 19 pixels, images containing 4 particles, arranged on a grid with average distance of 5 pixels, were rendered. For the purpose of varying particle distances and sub-pixel positions, random xy deviations, drawn from an uniform distribution in range $[-1\ 1]$ pixels, were added to each particle position. This configuration simulates the envisaged distances between particles that the detection routine can deliver. Exemplary simulated images, together with the corresponding fitting results, are depicted in Fig. 49a. The superimposed contour lines represent the FWHM of each elliptical 2D Gaussian.

(a)

(b)

(c)
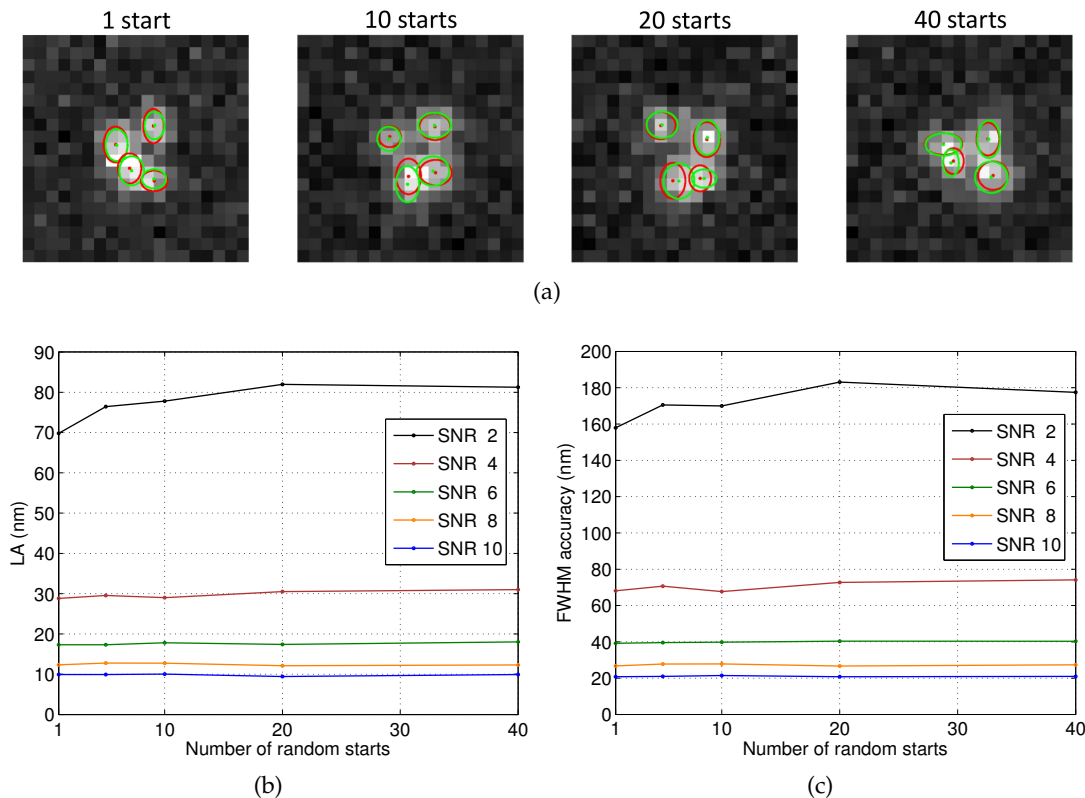
Figure 49: (a) Exemplary simulated images for different number of random starts at SNR = 6. The red shapes depict the GT and the green shapes the fitting result of the algorithm. (b)-(c) The LA respectively the FWHM accuracy as functions of the number of random starts and the SNR.

Fig. 49b-49c plot the LA and the FWHM accuracy as functions of the number of random starts and the SNR. The accuracy is computed using the SD of the distance to the true center position respectively the true individual FWHMs (Kubitscheck et al. 2000). This measure is applicable since the errors are symmetrically distributed. This also holds true for all further analyses.

It is apparent that the FWHM accuracy is about twice as bad as the LA. Consequently, the axial LA will also be worse than the lateral LA, which is in line with previous reports (Badieirostami et al. 2010, Mlodzianoski et al. 2009). This finding will be proved true throughout all following scenarios.

With respect to the number of random starts, it has to be stated that there is almost no effect on the accuracy. If at all, then there is a slight tendency for improvement for higher SNRs, while for lower SNRs the accuracy even seems to decrease. By in-depth examination of the individual fitting results it was determined that the slight deterio-

ration for low SNRs is reasoned by fitting outliers that nevertheless maintain a better likelihood. Most frequently, this occurs if the intensity distributions of two particles are notably overlapping. The EM algorithm sometimes fits the intensity distributions of two particles as one and erroneously includes a nearby, low SNR particle within the noise of the background. With increasing number of random starts it becomes more likely that such a misleading solution is found owing to the additional deviations introduced during random initialization. This can lead to worse accuracies.

It can be concluded that the EM algorithm is reasonably robust with respect to the proposed initialization. This is supported by the fact that even for high SNRs the likelihood just improves by order of less than 10^6. The corresponding gain in accuracy is therefore extremely marginal. If particles are very close, still fitting outliers may emerge. This is mainly a result of the relatively coarse range for reinitialization that was chosen to suit the accuracy of the spot detection procedure.

Consequently, the number of random starts of the EM algorithm was set to $t_{init} = 1$ for all presented computations in this thesis. The majority of evaluation scenarios has also been computed using $t_{init} = 10$, but since the SNRs of off-focus particles are very low, either the results were virtually identical or the fitting outliers even resulted in less accurate results. A practical advantage of this selection was the notable reduction of algorithm runtime.

It should be noted that setting t_{init} to higher values is expected to be advantageous if the correct number of particles is unknown and remains itself a free fitting parameter. Then also the reinitialization should be less coarse. This issue must be addressed if the EM algorithm shall be used for super-resolution images, where the density of particles is high (Zhu et al. 2012, Huang et al. 2011, Holden et al. 2011). It is neglected in this work.

Robustness to the Number of Particles

Owing to the derivation of 3D information, the fitting routine has to deal with two additional free parameters per particle. The EM algorithm was proposed to deal with the increased complexity in the likelihood function. In order to analyze its robustness to the number of particles, varying particle numbers were rendered on a discrete rectangular grid with grid size 5 pixels similar to the previous evaluation scenario. Note that for this scenario the fitting sub-region had always the same size like the total image so that always all particles were fit at once. Exemplary simulated images and the corresponding fitting results are presented in Fig. 50a.

The LA and the FWHM accuracy are displayed as functions of the number of particles and the SNR in Fig. 50b-50c. The accuracies of the respective parameters improve slightly up to 10 particles, but remain virtually stable even for high numbers of simultaneous particle fits. The EM algorithm can consequently be considered as a reasonably robust parameter estimator for the present application. It can robustly handle all free parameters for multiple particles and uses a well-known optimization scheme. Other scientists can easily adopt and extend this approach. It can be concluded that the size of the sub-region is a fairly uncritical parameter as long as uniform background can be assumed.
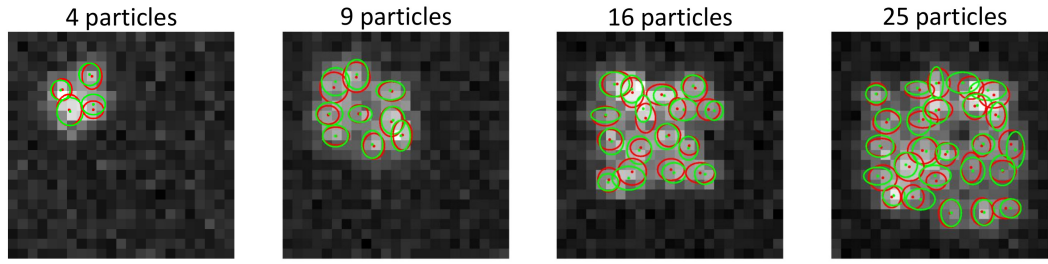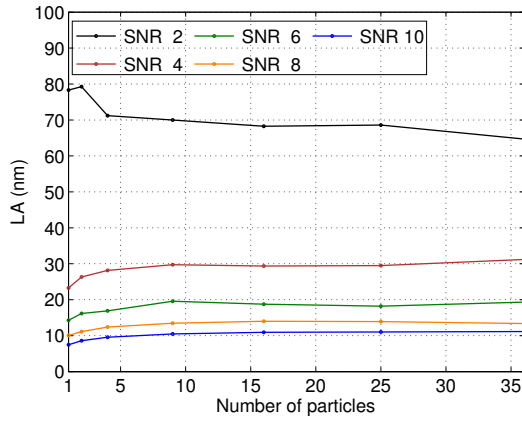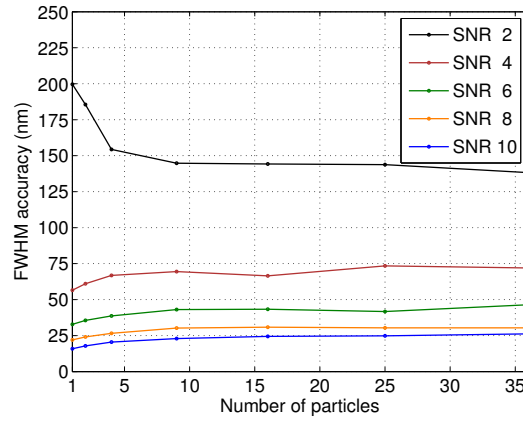
Figure 50: (a) Exemplary simulated images for different number of particles at SNR = 6. The red shapes depict the GT and the green shapes the fitting result of the algorithm. (b)-(c) The LA respectively the FWHM accuracy as functions of the number of particles and the SNR.

Dependency on the Particle Distance

To analyze the dependency on the distance between particles, the image configuration is identical to the distance test of the particle detection procedure. It includes a central particle and a second particle at an orbit with varying radius. In Fig. 51a now also the contour lines are plotted.

Fig. 51b-51c present the LA and the FWHM accuracy as functions of the particle distance and the SNR. Apparently, the accuracies are unaffected by neighboring particles for distances larger than 4-5 pixels. Up to a particle distance of 1 pixel the accuracies deteriorate to ∼ 2-3 times their optimal values. Again, the FWHM accuracy is about twice as bad as the LA.

All in all, it is apparent that the EM algorithm maintains nanometer accuracy for realistic SNRs and dense particles up to 1 pixel distance. The results are in similar range than those reported by Huang et al. 2011, Holden et al. 2011, and Babcock et al. 2012. Note that only the latter algorithm dealt with the same number of free parameters like the present implementation. As a result, application of the EM algorithm can be considered as a robust alternative even for analysis of 3D super-resolution images. For the present workflow it can be concluded that once the axial correlation function has been determined, the proposed algorithm can also be used to compute the 3D position of very dense particles that are currently omitted.
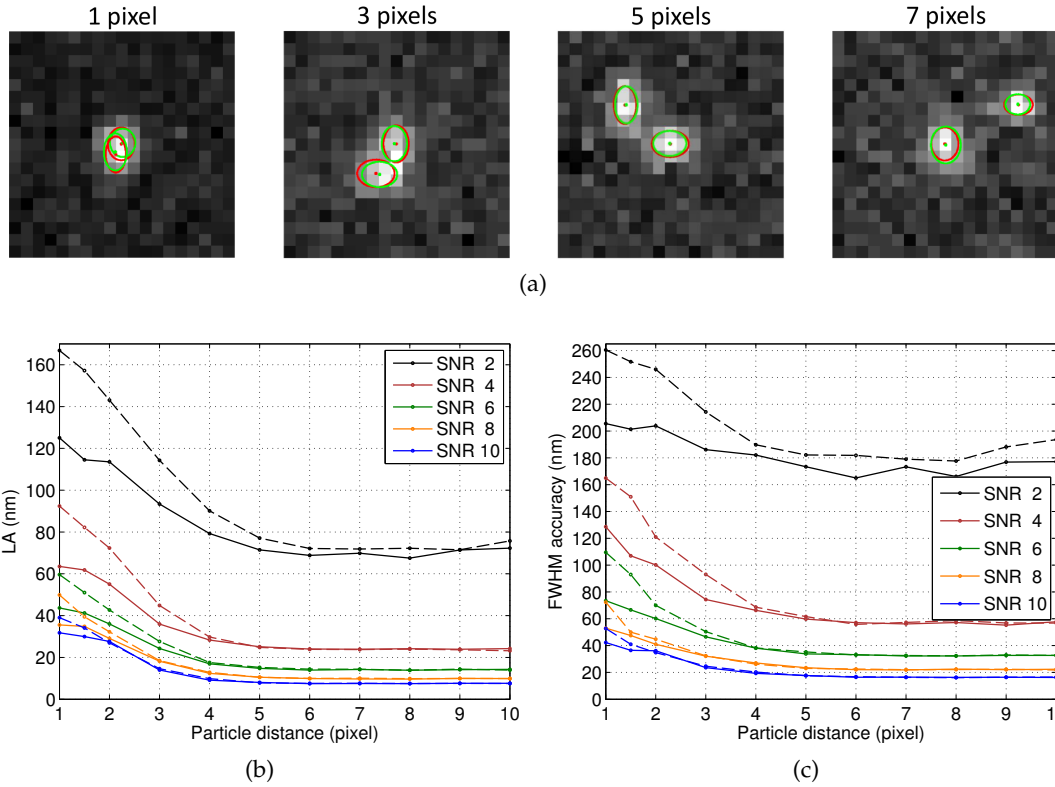
Figure 51: (a) Exemplary simulated images for different particle distances at SNR = 6. The red shapes depict the GT and the green shapes the fitting result of the algorithm. (b)-(c) The LA respectively the FWHM accuracy as functions of the particle distance and the SNR. The dashed lines are the result if the EM algorithm is configured with $t_{init} = 10$.

Fig. 51b-51c also include the results for configuration of the EM algorithm with $t_{init} = 10$. They clearly indicate that fitting outliers occur only at very low particle distances. Their occurrence is raised by multiple random starts only in that range. At larger particle distances the results are virtually identical. This supports the choice of only a single start of the EM algorithm for the present data.

Dependency on the Distance to the Truncating Boundary

Here, it is assessed whether the truncation of intensity distributions has an impact on the accuracy with that shape parameters are determined. Images that contain only a single particle with varying distance to the boundary are rendered. The orbital boundary position was again drawn from an uniform distribution so that the sub-pixel position is varied. Exemplary images, including the fitting results, are presented in Fig. 52a.

Fig. 52b-52c display the LA and the FWHM accuracy as functions of the particle distance to the boundary and the SNR. Truncated pixels effect the accuracy of the shape estimation up to a particle distance of 3 pixels to the boundary. This corresponds to a distance of 3-4 times the SD of the PSF and is a reasonable result since further beyond the Gaussian representation of the PSF approaches zero values.

Although truncated pixels are explicitly considered, the accuracy deteriorates $\sim$ 2-3-fold from boundary distance 3 to 0.5 pixels. This is a clear improvement with respect to the results when truncated pixels are simply considered as being zero valued. Those
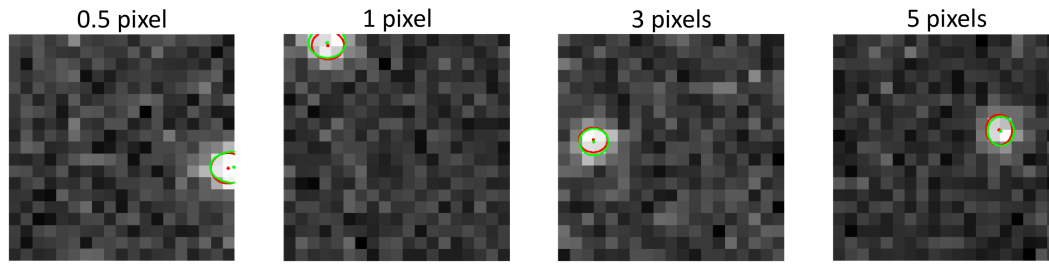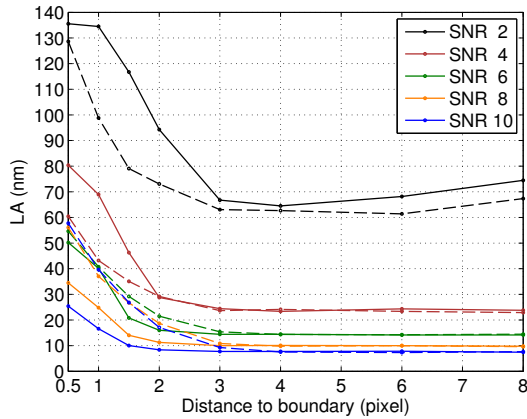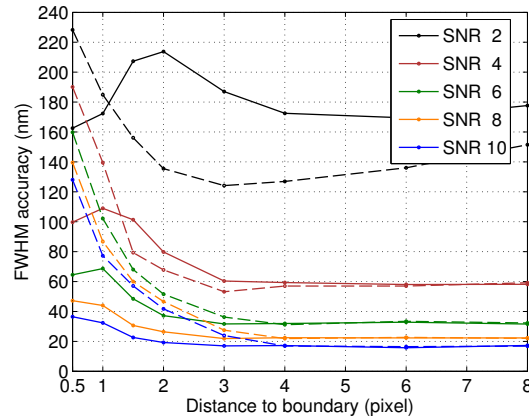
Figure 52: (a) Exemplary simulated images for different particle distances to the boundary at SNR = 6. The red shapes depict the GT and the green shapes the fitting result of the algorithm. (b)-(c) The LA respectively the FWHM accuracy as functions of the particle distance to the boundary and the SNR. The dashed lines are the result if truncated intensity distributions are not considered in the EM algorithm.

are additionally presented in Fig. 52b-52c. The corresponding improvement is most considerable for the FWHM accuracy. This emphasizes the importance of taking truncated intensity distributions for the present 3D application into account.

Dependency on the Distance to a Truncated Boundary Particle

Finally, the error propagation from truncated boundary particles to neighboring particles shall be assessed. The same image configuration like in the previous section was used, but the distance to the boundary was fixed to 0.5 pixel. In addition, always a second particle with varying distance to the boundary particle was included (see Fig. 53a). In order to isolate the influence of the truncation of the boundary particle, other sources of errors, like the influence of the distance between the particles as well as the distance to the boundary itself, were subtracted from the obtained accuracies of the second particle.

Fig. 53b-53c present the relative deterioration of the accuracies that are solely attributed to the truncation of a nearby particle. The error from a nearby truncated particle propagates over ~ 4-5 pixels until it stops to affect the accuracies with that a central particle is determined. This effect is clearly measurable for SNR > 4. For lower SNRs, it was already apparent in Fig. 52b-52c that the extrapolation of photons into truncated regions does not increase the accuracy.

| 1 pixel | 3 pixels | 5 pixels | 7 pixels |

(a)

(b) (c)
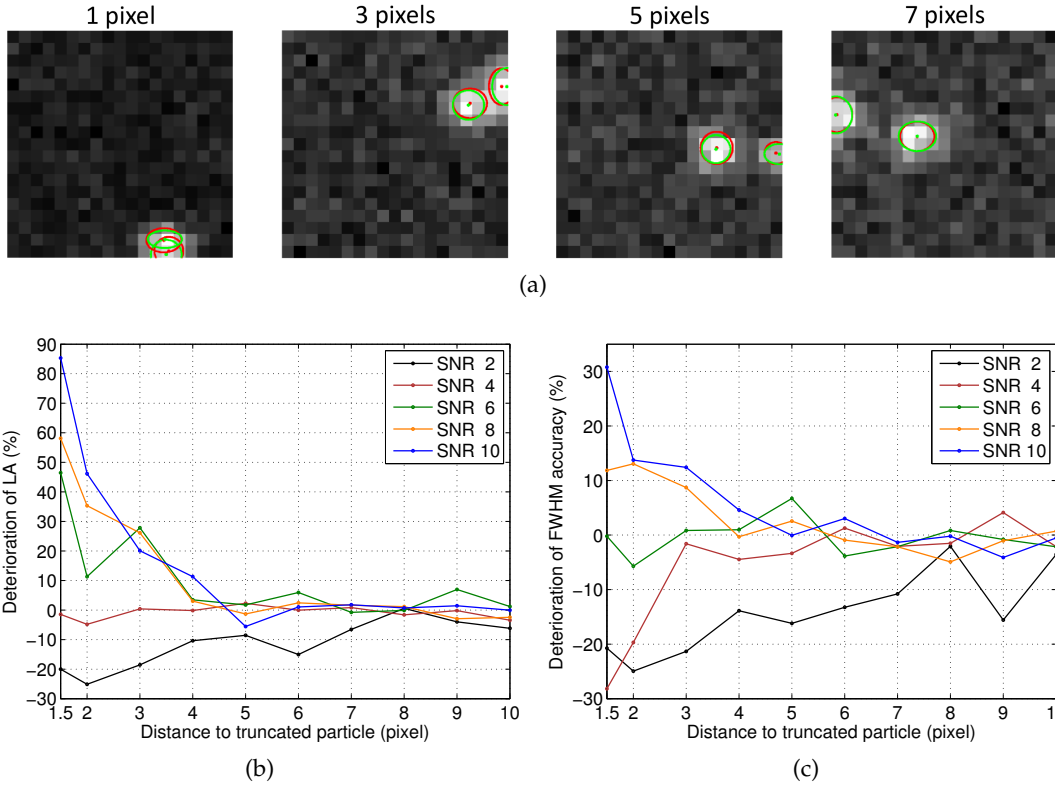
Figure 53: (a) Exemplary simulated images for different particle distances to a boundary particle at SNR = 6. The red shapes depict the GT and the green shapes the fitting result of the algorithm. (b)-(c) Relative deterioration of the LA respectively the FWHM accuracy as functions of the particle distance to a boundary particle and the SNR.

The distance to the boundary of the fitting sub-region should be $\geqslant$ 6 pixels. At these sub-region sizes, the fitting of the center particle is not biased by cutting out a sub-region, and determination of closed sets of superimposed particles can be avoided. However, the error may propagate even further for multiple concatenated particles, and error propagation should be analyzed in more detail for groups of particles.

4.10.1.4 *Simulation of SPT Images*

Since the aberrations induced by the RIM and the cylindrical lens leave the symmetric distribution along the lateral directions intact, the center coordinates are independent of the individual FWHMs. The axial LA can be analyzed in isolation from the lateral LA. The lateral position of simulated particles is kept constant, and the shape of a particle is only varied according to its relative axial position. The trajectory has therefore only an axial component.

The simulated axial trajectories are supposed to represent free diffusion of transmembrane molecules. Starting from the focal position, every next step of the trajectory is drawn from a normal distribution with zero mean (Qian et al. 1991). By choosing $D = 0.05 \ \mu m^2/s$ and $\Delta t \approx 0.0333$ s, the SD was set to $80 \ nm \approx \sqrt{MSD(\tau)} = \sqrt{2dD\tau}$. This was motivated by the determined diffusion of GPI-GFP in brain slices (see Fig. 35c)). The maximum step size was limited to three times the SD. The maximum axial range is limited to 300 nm away from the two individual focal planes. To simulate the axial tra-

jectories within this range, the direction of the next step is simply inverted if a particle would otherwise approach one of the two boundaries.

The axial sampling is set to 1 nm, and the length of each trajectory is 1000 frames. Since the trajectories of several particles can be concatenated for calibration, the actual length of the trajectory can become very large. The rather important variable is how often a particle actually crosses the focal planes during the acquisition because these are the important frames for the online calibration. The number of focal plane crossings was therefore forced to be 50 ± 10 for each focal plane. This range was chosen because it was typically obtained for randomly generated trajectories of length 1000. An exemplary simulated trajectory is displayed in Fig. 54.
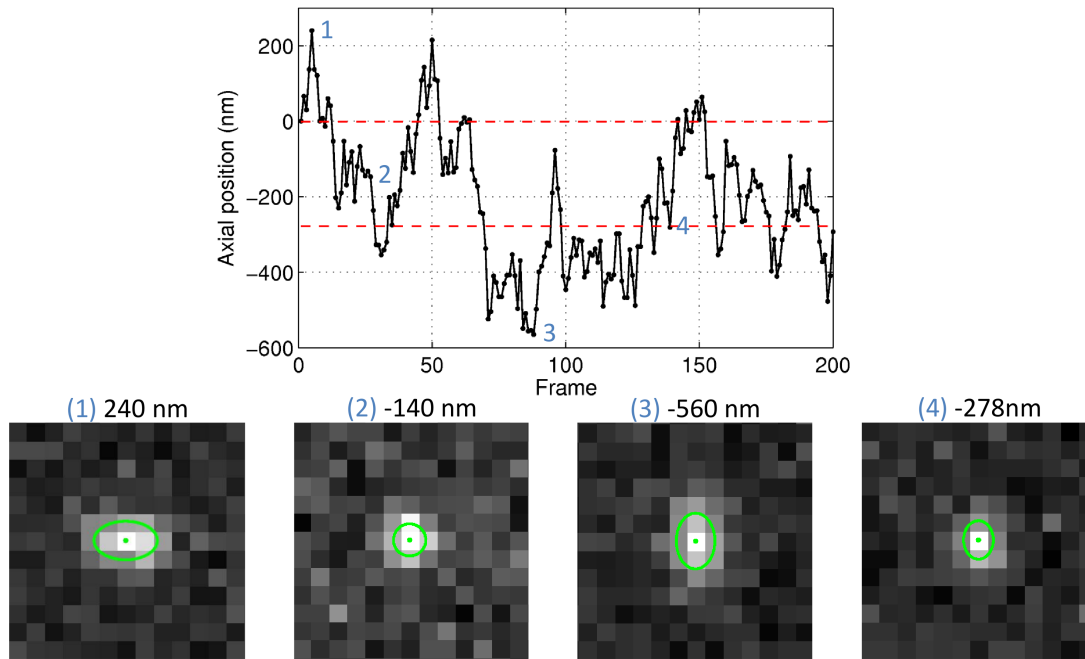
Figure 54: An exemplary axial trajectory and corresponding simulated images at different axial positions. The dashed red lines indicate the two focal planes.

The parametrization for the axial correlation functions at different depths is taken from the calibration measurements of beads in Mowiol (see Fig. 40a). The two correlation functions per depth get identical parametrization. The FWHM shift is ignored so that the model assumptions are perfectly met. According to the measurements in Sect. 4.9.1.2 the focal shift is set to $\Delta_f = 278$ nm.

In order to simulate realistic images, the number of photons for off-focus particles must decrease as a function of the axial distance to the center of the two focal planes. The decline of the peak intensity can be approximated by a Gaussian function (see Fig. 39b). The number of photons of a particle as a function of the preset SNR and the relative axial position are computed by multiplying N_p (see Equ. 64) with the value of the Gaussian function at the corresponding axial position. The FWHMs of the Gaussian functions at different depths are identical to the axial fitting ranges (see Fig. 41a). The declared SNR is consequently only valid for the center position between the focal planes and reduces at both sides.

In order to determine whether the algorithm works irrespectively of the noise, it is also always applied to images that do not contain noise. In such images the number

of photons per particle is similar to those with SNR = 66, but noise is not added. The corresponding results will be denoted by SNR = inf standing for infinite SNR. Fig. 54 also depicts exemplary simulated images at different axial positions.

The following evaluation configurations always comprise 50 realizations for each data point. To allow for comparable results at different depths, the simulated trajectories are identical across depths.

4.10.1.5 *Quantifying the Systematic Error and the Localization Accuracy*

In order to assess the capability of the online calibration method, the SE in combination with the LA are the crucial measures. For this thesis, the SE is of major importance. If the RIM is present, but only a calibration at zero depth is used - in the following denoted as prior calibration - then the SE increases as a function of the depth (see Fig. 40b) although it might be possible to keep the LA constant.

Systematic Error

The SE is the error in the axial position that exists independently of the actual SNR of the images. It is in principle solely defined by the deviation from the calibration curves and the true underlying axial correlation functions of the data. However, the estimation of the correlation functions depends on the SNR and therefore also the SE. As for simulated data the estimated and the true reference curves are available, the SE can be directly computed. For it, a particle that travels along the axial axis has to be considered. Its corresponding FWHM values can simply be taken from the reference curves at each position. Its measured position is obtained by plugging these values into the estimated calibration curves. The difference between the estimated and the true axial position then defines the SE.

Based on the high dimensionality of the data, Fig. 55a first of all presents the SE as a function of the relative axial position and the SNR. Since the fundamental course of the curves is similar for all depths, this is exemplary depicted for 10 μm depth, where the RIM has already a strong impact. The SE is plotted over an axial range that covers the center between the two focal planes ±300 nm. This corresponds to an axial range, where, from practical experiences with SDCM, the number of collected photons and the shape of the off-focus PSFs are suitable. Of course, this range is smaller than that achievable with WF microscopy (Huang et al. 2008b, Holtzer et al. 2007), which is owed to the axial sectioning capability of the CSU. Note also that the absolute differences are taken for averaging over many evaluation runs because the deviations could otherwise erroneously cancel out each other.

The SE deteriorates at both sides from the center. This is reasonable since the absolute deviation of the estimated and the true curves increases with distance to the center for any deviation in the determined coordinates. Furthermore, the SE decreases for higher SNRs indicating that the approximation of the correlation functions improves with the quality of the images.

To allow for representation of the SE as a function of the imaging depth and the SNR, the average of its values along the axial axis is computed. This is here denoted as the total SE. It is presented in Fig. 55b. Apparently, the total SE exhibits a tendency for deterioration towards higher imaging depths. This is most obvious for the first 10 μm, where the axial correlation function changes most in consequence of the RIM. This

deterioration is likely to result from the fact that the axial correlation curves become generally flatter with increasing depth, and therefore the FWHM differences between frames decrease for the same axial increment of a particle. This seems to impede the correct selection of vertex frames and is addressed in more detail in Sect. 4.10.1.8. The SE depends more notably on the SNR and is almost eliminated if noise is not present. The latter result proves that the online calibration is indeed functioning.

Since the outcome of the online calibration is primarily a function of the achievable SNR, and the deterioration over depth is only in the range of a few nanometer, it is fair to conclude that the online calibration procedure operates reasonably well independently of the actual parametrization of the underlying calibration curve. It may hence be applied to other imaging techniques that can penetrate the sample much deeper. For real acquisitions, the blurring of the PSF at larger depths further reduces the effective SNR and increases the SE. This is in fact a matter of the SNR and not of the parametrization at a certain depth.

Fig. 55b also presents the SE if the prior calibration would be applied. To facilitate the assessment of the difference between both methods, Fig. 55c depicts the corresponding reduction of the SE that the online calibration provides. As expected, the online calibration method results in worse SEs than the prior calibration at zero depth. The absolute values simply represent the actual SE of the online calibration since the prior calibration is correct at this depth. At zero depth the SE of the online calibration approaches that of the prior calibration only for very high SNRs. For any other depth, the SE is always substantially reduced by the online calibration method.

The reduction clearly increases constantly as a function of the depth. This is also apparent, for the relative reduction of the SE that is additionally provided in Fig. 55d. The proposed online calibration method can be considered particularly useful for imaging at large depths. In total, it can be concluded that the presented online calibration at least halves the SE at any depth and independently of the SNR. It is always useful to apply this technique even for low recording quality. For realistic SNRs such as 10, the reduction may even approach 70 %. This does not include acquisitions at zero depth, where the prior calibration must be more accurate.

Another useful perspective is enabled if the reduction is put in relation to the remaining SE of the online calibration method (see Fig. 55e). It becomes apparent that for any SNR the reduction in the SE is at least in the same range as the remaining SE, but can even be more than 300 % for SNR $\geqslant$ 10. Again, the relative reduction notably increases as a function of the imaging depth. It even overproportionally counteracts the grow of the SE as a function of the depth like it would be experienced by doing prior calibration. This makes application of the online calibration method very useful.

Axial Localization Accuracy

The LA cannot be directly computed like it was the case for the SE. Instead, 30 individual images were rendered for each realization and axial position. They were fit by the EM algorithm, and their axial positions were computed using the estimated calibration curves. The axial LA at each axial position then relates to the SD of the corresponding estimated positions.

Fig. 56a depicts the axial LA as a function of the relative axial position and the SNR. This is done again for the exemplary depth of 10 μm. As it is known from previous investigations (Badieirostami et al. 2010, Mlodzianoski et al. 2009), the axial LA varies
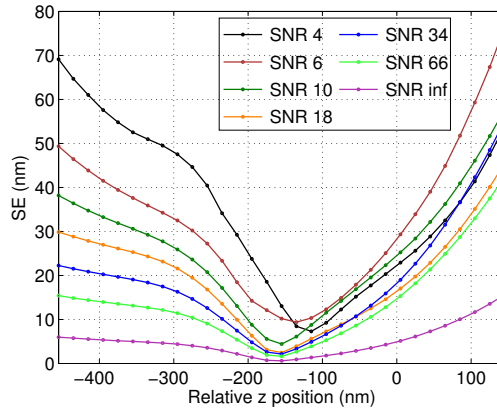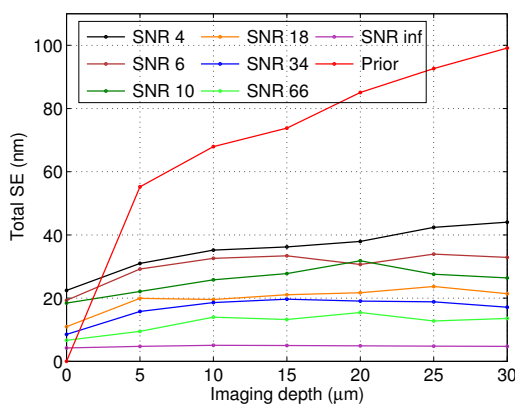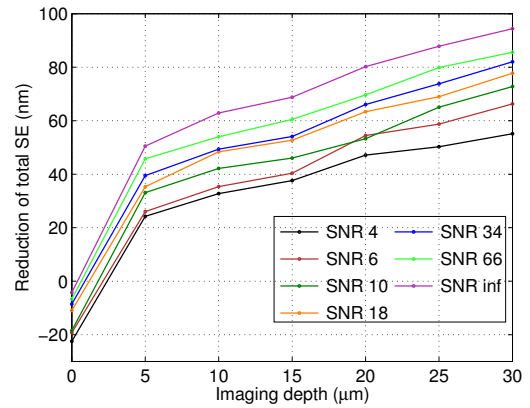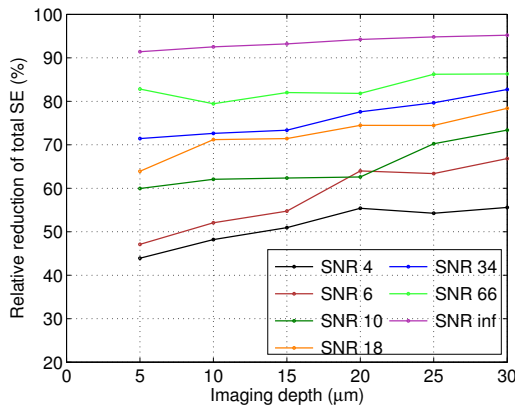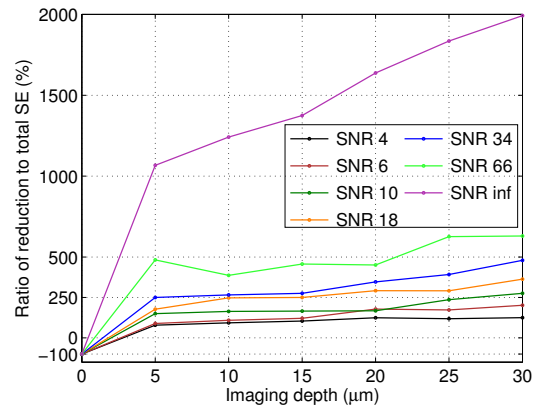
Figure 55: (a) The SE as a function of the relative axial position and the SNR. The (b) total SE, the (c) reduction of the total SE, the (d) relative reduction of the total SE, and the (e) ratio of reduction to the total SE as functions of the imaging depth and the SNR.

as a function of the SNR and the axial range. It is apparent that the axial LA improves from the left to the right beside the obvious improvement as a function of the SNR. The accuracy with that a particle can be measured is superior if it is located above the focal plane. Again, this can be explained by the course of the calibration curves. Their
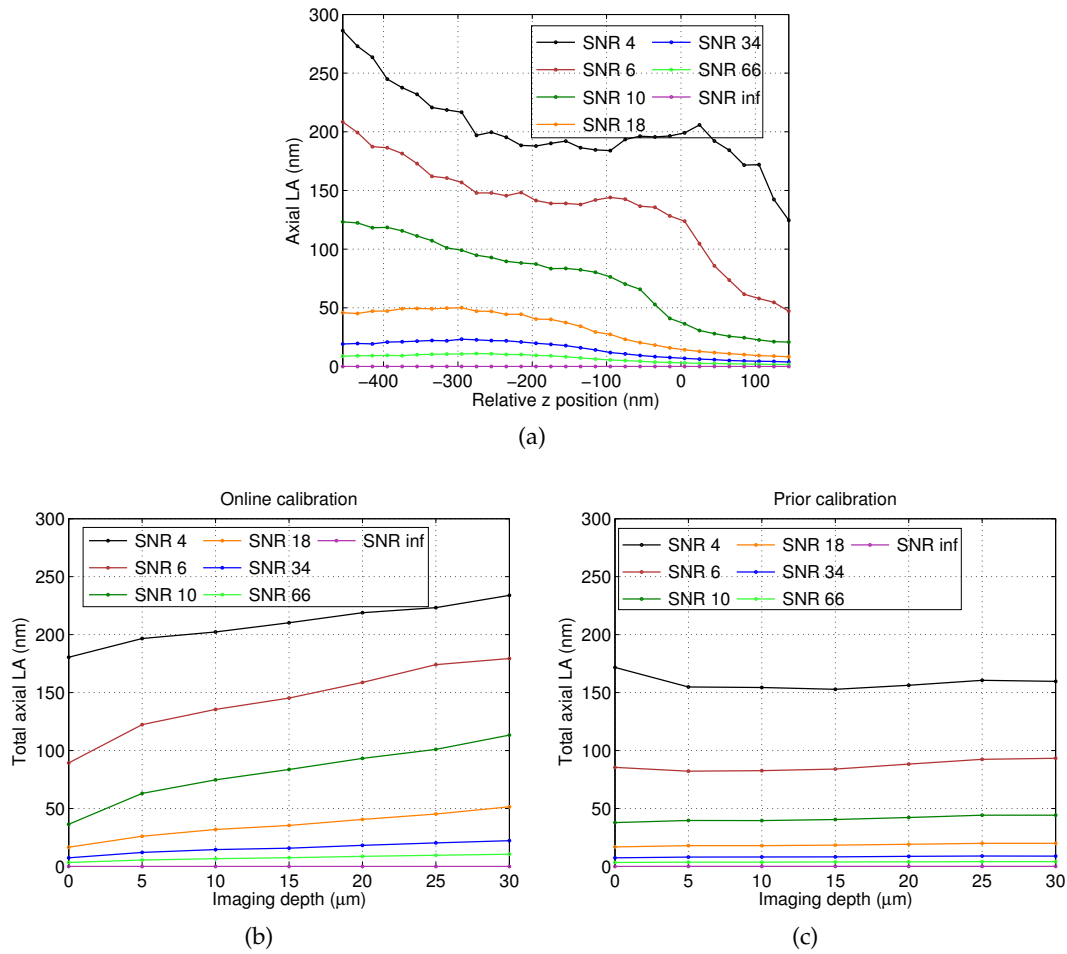
Figure 56: (a) The axial LA as a function of the relative axial position and the SNR. The total axial LA for the (b) online respectively the (c) prior calibration method as functions of the imaging depth and the SNR.

course is flatter if the particle resides below the focal plane. Already small deviations in the estimated FWHM result in substantial deviations in the axial position. This effect is consequently less pronounced for the steeper course of the curves on the other side of the focal plane.

Also the total axial LA, computed as the average value across the selected axial range, is presented in Fig. 56b. Similar to the SE, it improves for higher SNRs and also deteriorates as a function of the imaging depth. This is again owed to the generally flatter curves at larger depths leading to the similar effect as described for the position of a particle with respect to the focal plane. However, the axial LA appears to be more sensitive to the imaging depth than the SE, and also the absolute values are notably higher.

Fig. 56c presents the course of the axial LA if prior calibration is performed. At zero depth the axial LA is similar to that obtained with the online calibration method for any SNR. This was expected since the online calibration method aims at improving the SE. The axial LA should actually not be affected. Surprisingly, there is almost no deterioration towards larger imaging depths for the axial LA of the prior calibration.

This observation is best understood by looking at the measured axial trajectories and will be addressed in the following section.

4.10.1.6 *Visual Analysis of the Trajectories*

To obtain a visual impression of the performance of the online calibration method, exemplary measured and true axial trajectories at selected depths are plotted in Fig. 57a for SNR = 10.
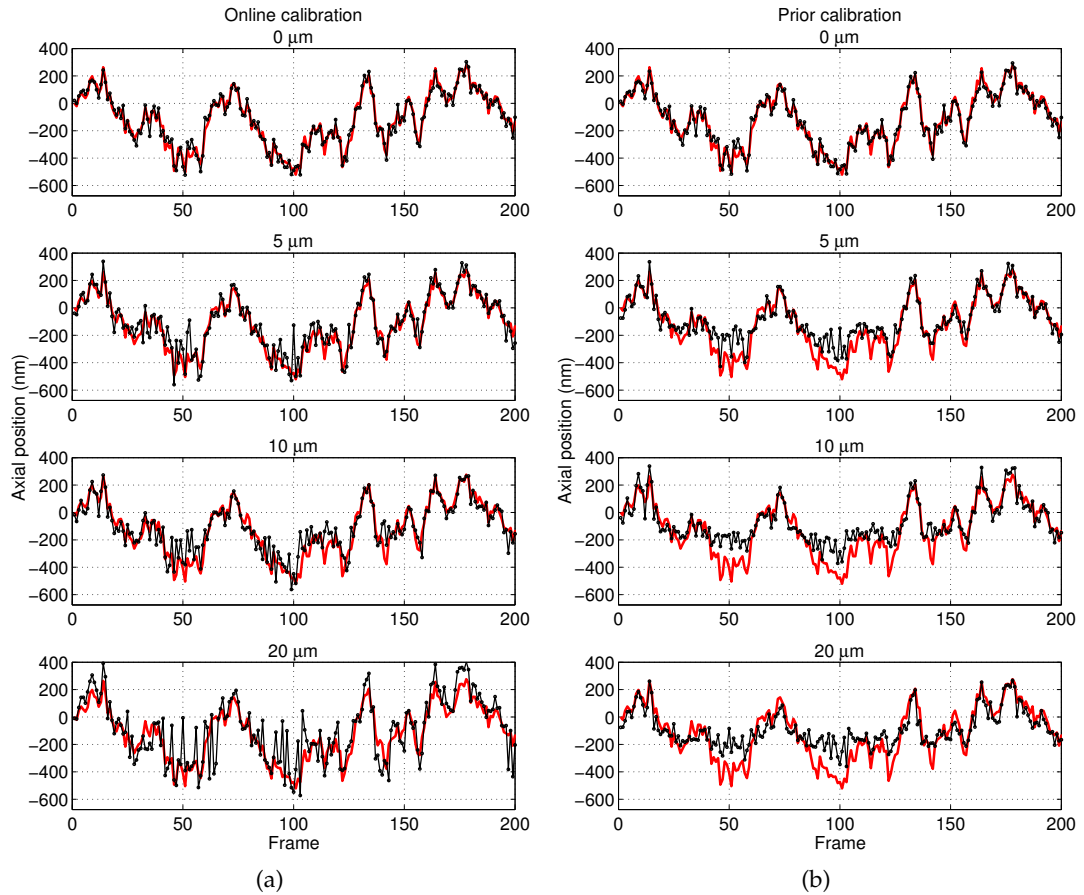

Figure 57: Measured trajectories determined by the (a) online and the (b) prior calibration method at selected depths. The red lines denote the true simulated trajectories.

Apparently, the measured trajectory approximates the true trajectory quite well at zero depth. The course of the particle movement is followed correctly and also the absolute positions are meet. The principal course is preserved also for larger depths proving that the online calibration indeed adjusts the axial correlation functions to the individual depths. It is also apparent that systematic deviations from the trajectory are more pronounced further away from the axial center between the two focal planes. This is in line with the results presented in Fig. 55a.

With increasing depth, the accuracy with that the absolute positions are met decreases significantly. This is owed to the axial LA and less to the SE. The correct fundamental course remains observable, but the measured positions scatter strongly around the true values. Moreover, it can be observed that the actual variation at any depth

even varies with respect to the relative axial position of the particle. The axial LA is worse if the particle is measured below the center of the focal planes (see Fig. 56a).

It must be concluded that the deteriorating axial LA is the primary limiting factor for application of 3D SPT deep in living tissue. Given that, why is it nevertheless reasonable to adjust the axial correlation function? This becomes apparent by looking at the measured trajectories if the prior calibration is applied (see Fig. 57b).

At zero depth, the measured trajectory reflects the true trajectory very well, and with increasing depth, the measured trajectories exhibit more and more systematic deviations from the true positions. This is most apparent for portions of the trajectory that are below the focal plane of the y curve. There, the shape of the axial correlation function changes most with respect to the imaging depth. If the influence of the RIM is ignored, particles should preferentially be imaged above the original focal plane. However, this reduces the available axial analysis range by more than its half.

In consequence of the strong SE, the measured trajectories hardly represent the true course of the trajectory. Instead, the particles are erroneously observed to move in a quite narrow axial range. This happens because owing to the influence of the RIM, large axial step sizes are only represented by small changes in the FWHM values. By computation of the axial position using the steep calibration curves from zero depth the axial increment is notably underestimated. This is particularly true below the center between the focal planes.

Another consequence is that the axial LA is erroneously measured to remain almost constant as a function of the depth. This is because also the estimation errors are downscaled using the steep calibration curves.

In the light of this, it must be concluded that the achieved axial LAs provided in the literature are clearly underestimated and should be reconsidered. Ignorance of the RIM does not only lead to biased absolute positions, it also leads experimenters to believe that their measurements are very accurate. As a final consequence, it can be expected that the diffusion properties are also notably underestimated. This is addressed in the following.

4.10.1.7 *Impact on the Calculated Diffusion Parameters*

Next to the absolute positions of molecules, particularly the determination of their diffusion properties is of crucial importance for neurobiologists. Fig. 58 summarizes the implications that the selection of either online or prior calibration has on the essential measures: MSD and D_l. Fig. 58a and 58c plot the observed MSD curves at selected depths for the online respectively the prior calibration method. Similarly, the dependency on the SNR is plotted in Fig. 58b and 58d. For varying depths, the SNR was fixed to 10, while for varying SNRs, a depth of 10 µm was chosen.

The MSD curves for the true trajectories, denoted as GT, are also always provided. They clearly exhibit confined motion and asymptotically approach a maximum value of ~ 0.1 µm^2. This corresponds to ~ 316 nm and is justified by the limitation of the simulated trajectories to the axial analysis range. The smallest MSD value is ~ 0.0064 µm^2. It corresponds exactly to the SD of 80 nm of the normal distribution with that the simulated trajectories were parameterized.

In addition to the MSD curves, Fig. 58e-58f plot the change of the corresponding D_l. The local diffusion coefficient was chosen since in real experiments the trajectories are usually quite short (see Fig. 35b). Differences have to be determined already by
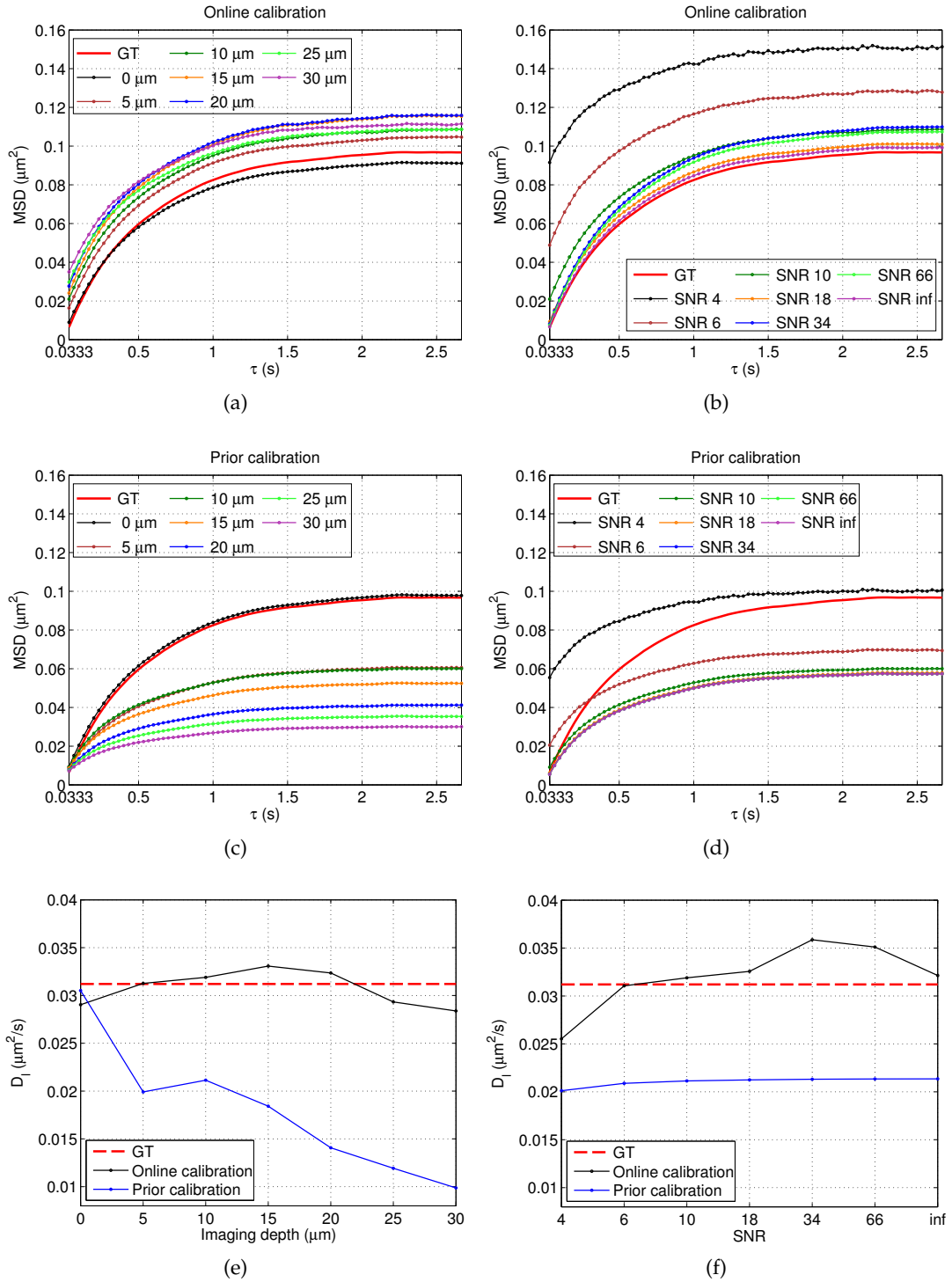
Figure 58: (a)-(b) Observed MSD curves for the online calibration method at selected imaging depths respectively SNRs. (c)-(d) Observed MSD curves for the prior calibration method at selected imaging depths respectively SNRs. (e)-(f) Observed courses of D_l as functions of the imaging depth respectively the SNR.

that measure. Again, the first 8 MSD points were used for computation of D_l (see

Sect. [4.5.2.2]). Note that the ground truth diffusion was determined to be $0.0312 \, \mu m^2/s$. This is smaller than the simulated $0.05 \, \mu m^2/s$ because the axial range was confined.

For varying imaging depths, the MSD curves determined using the online calibration method exhibit similar curvature, but have different absolute values that grow with depth. This is also observable in Fig. 58e, where D_l deviates not more than $\sim 10 \, \%$ from the GT. It can be concluded that the online calibration method approximates the true axial correlation functions reasonably well since large SEs should be reflected by incorrect diffusion results. The difference in the absolute values is attributed to the deteriorating axial LA since it artificially introduces larger step sizes between time points. As a result, the first MSD point, but also the maximum value are increased. The latter erroneously indicates a broader zone of confinement. For zero depth, where the axial LA is at its minimum, the absolute MSD values are approximated best.

These conclusions are supported by the results of the prior calibration method. As expected, the MSD curve and D_l are well approximated at zero depth and are superior to that of the online calibration. Owing to the larger deterioration of the SE as a function of the depth, the true D_l is significantly underestimated and deviates up to $\sim 70 \, \%$. This course is reasonable since the measured step size is erroneously decreased for prior calibration. This was already observed during visual analysis. The first MSD point is always correctly determined since the axial LA is almost independent of the imaging depth. Since this independence is an artifact of taking an inappropriate calibration curve, in addition, the true confinement is notably underestimated as a function of the depth. Application of the prior calibration method massively biases the short- and long-term diffusion results.

If just the SNR is varied, the fundamental shapes of the estimated MSD curves almost remain constant for both calibration methods. This is also clearly observable at the course of D_l. Here, the online calibration method exhibits a larger variance, but the maximum deviation from D_l is $\sim 18 \, \%$, which is significantly lower than that for the prior calibration that is $\sim 36 \, \%$. The online calibration achieves the best approximation of the true MSD curve at infinite SNR, but owing to the unavoidable SE when using prior calibration, the true curve is never correctly approximated no matter how well the SNR is. The SNR mainly affects the axial LA since the MSD curves vary in their absolute values, but less in their fundamental course. This is valid for both methods.

In summary, it must be concluded that there remains no linear relationship of the depth and the SNR with respect to D_l like it was experienced for the SE and the axial LA. Although the online calibration method cannot prevent that the measured absolute MSD values can deviate from the true values, it still allows to determine the correct diffusion coefficients almost independently of the depth and the SNR. This is of utmost practical importance for analysis of diffusion properties of different molecules in thick samples. It underlines the importance and ability of the online calibration method to make 3D SPT analyses readily available for the user.

4.10.1.8 *Evaluation of Intermediate Results*

The SE and the axial LA are the most direct measures for clarifying how the algorithm performs in the end. In this section, intermediate results will be analyzed in order to provide an inside about how the algorithm performs at different stages. Starting points for optimizing its functioning will be revealed. As a first intermediate result,

the accuracy with that the FWHM of the three required curve coordinates is estimated will be analyzed.

The Coordinate Estimation Procedure

Estimation of the three required coordinates is a crucial part of the algorithm because it already relies on all important model assumptions of the algorithm. Fig. 59a-59c present the average deviation B of the estimated coordinates from the reference coordinates as functions of the depth and the SNR. It is computed as $B = \langle \omega - \omega_r \rangle$, where ω_r denotes the known reference FWHM at each coordinate.
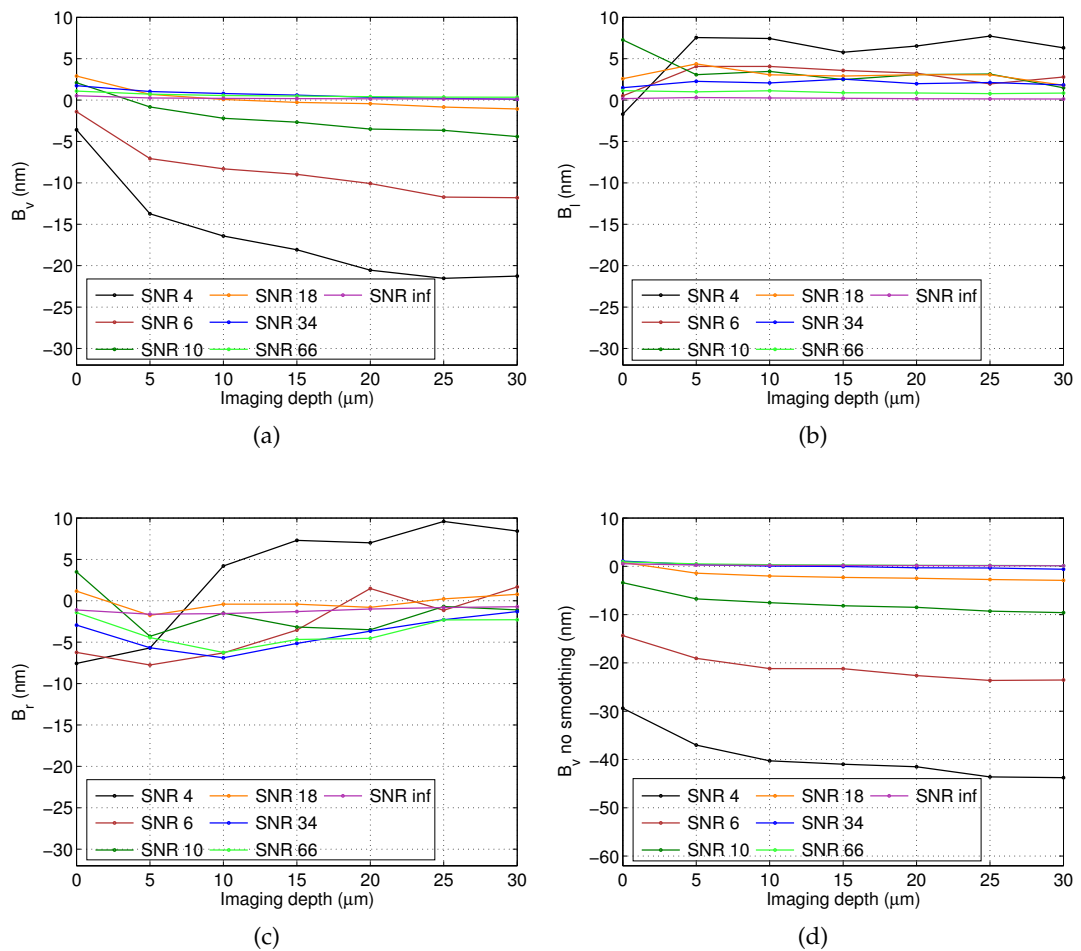

Figure 59: (a)-(c) Average deviation of the estimated from the reference coordinates as functions of the imaging depth and the SNR. (d) Average deviation of the estimated from the reference vertex as a function of the imaging depth and the SNR, but this time the image data was not smoothed for detection.

Apparently, B_v deteriorates as a function of the depth for SNR $\leqslant$ 10. This supports the assumption that the generally flatter calibration curves at higher depths make the correct selection of vertex frames more difficult. For higher SNRs, the FWHMs at the vertex are almost correctly determined. The quality of the vertex estimation depends mainly on the SNR.

Thereby the deviation is negative in most cases meaning that the FWHM at the vertex is underestimated. This issue was already addressed in Sect. 4.9.2.1. It was considered by smoothing the image just to support the correct selection of vertex frames. From Fig. 59d it is apparent that without additionally smoothing the data for vertex frame detection the course of the deviation is similar, but indeed much worse. However, the deviation could not be canceled out entirely. It must be accepted as an inherent problem of the estimation procedure with respect to noisy data. In fact, the error is effectively nullified for images with infinite SNR proving the functioning of the vertex selection.

The trend of the average deviations at the coordinates l and r is different from that at v. B_l and B_r appear to slightly improve as functions over depth. For the simulated images, where the SNR has not been decreased over depth, this may be reasoned by the axial blurring of the PSF as a function of the depth. Since Δ_f remains constant, the SNR at l and r is less decreased for larger depths allowing for more accurate FWHM estimations. In real samples, where the SNR decreases with depth, this advantage is likely to be compensated.

Note finally, that computation of B from the absolute deviations did lead to similar absolute errors for all coordinates. Their deviations did not cancel out over different trajectories.

In summary, it can be concluded that the coordinate estimation works reasonably well since the errors are in the low nanometer range also for relatively low SNRs. The dependency on the current configuration of the axial correlation function is observable.

The Curve Estimation Procedure

Estimation of the curve parametrization is the second major intermediate step. Based on the three defining coordinates, the wanted parametrization for the calibration curve is obtained by numerical approximation. Fig. 60a-60c present the course of the parameters m_r, ω_0, and d as functions of the depth and the SNR. They also include the true parametrization. Apparently, the principal courses of increasing m_r and ω_0 as well as a constant d are observable for almost all SNRs, but a reasonable approximation of the GT is only achieved for relatively high SNRs. For realistic SNRs, the concrete values deviate notably.

Substantial deviations are even obtained for very high SNRs. In order to investigate this finding the curve estimation was provided with the true coordinates. Then the estimated curves match the coordinates with residuals $< 10^{-3}$ nm for any depth proving that the parameter deviations cannot be solely attributed to the fitting procedure. It seems more likely that already small errors in the coordinate estimation, like they are remaining for any SNR (see Fig. 59), lead to noticeable changes in the curve parameters.

To substantiate this assumption, Fig. 61a illustrates the impact of individual coordinate estimation errors on the curve fitting procedure. Individual coordinate deviations were set to ± 10 nm, and an exemplary imaging depth of 10 μm was chosen. The variation of the fitting parameters and the residuals of the curve coordinates are plotted as functions of the coordinate estimation error in Fig. 61b and 61c, respectively.

The presented results reveal that, although by visual inspection the shape of the curve does not significantly change, small coordinate estimation errors can yield significant deviations in the respective curve parameters. It has to be stated that the parametrization is quite sensitive regarding the shape of the curve so that the pa-
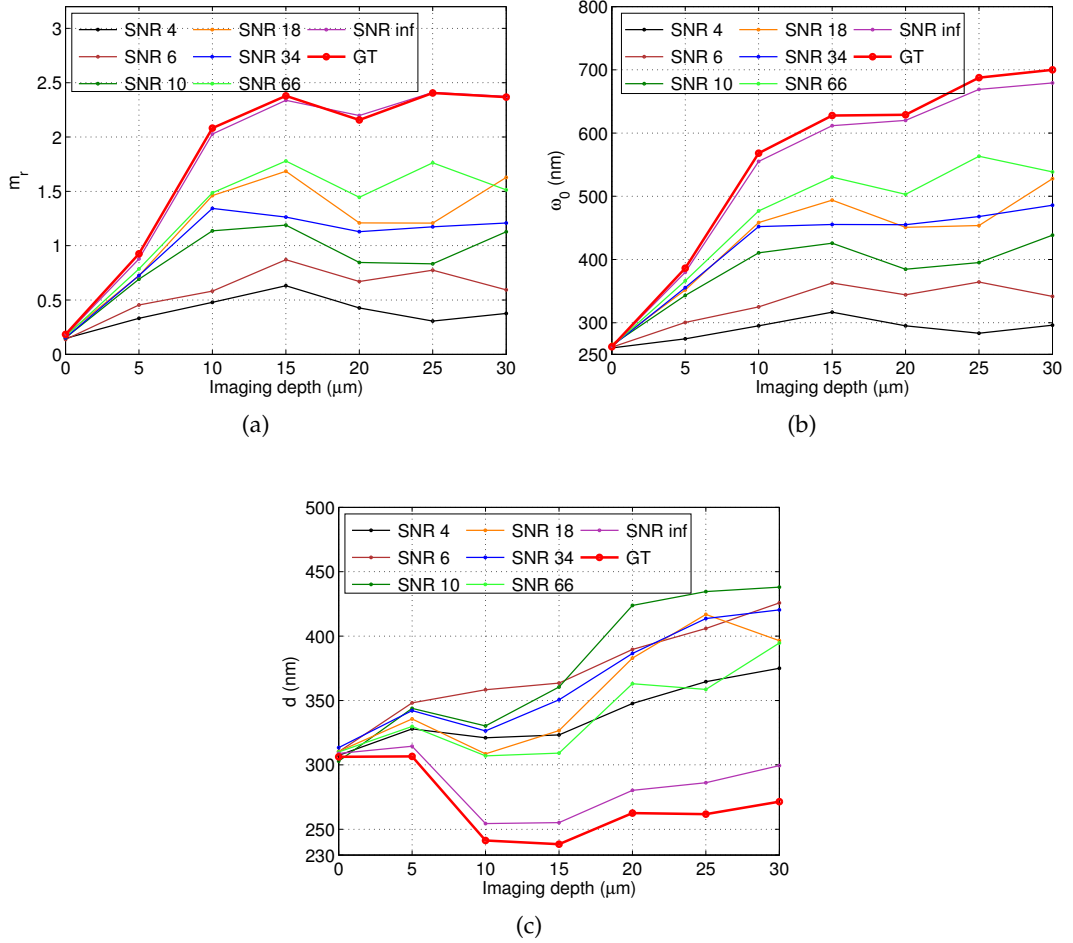
Figure 60: Course of the estimated curve parameters (a) m_r, (b) ω_0 and (c) d as functions of the imaging depth and the SNR. The corresponding GTs are provided in red.

rameters are an inappropriate measure to assess the present method. Although the parametrization indicates poor adjustment for the imaging depth, the resulting SE is nevertheless decreased by the online calibration (see Fig. 55b).

This discrepancy can be made plausible by the applied fitting bounds. They were involved to maintain realistic solutions in the presence of coordinate estimation errors. In Fig. 61b-61c it is apparent that in the moment when the fitting constraints take effect, the fitting residuals increase. The limits for the available parametrization have major effects for the residuals at the vertex and the left coordinate. This is clearly visible in Fig. 61a at the deviation of the estimated curve from the provided coordinates. The right coordinate is much less sensitive, which is justified by the steeper course of the curve below the particle.

In conclusion, the coordinate estimation is the most critical step of the online calibration since their course correlates with that of the total SE. The occurring coordinate estimation errors also explain the strong deviations in the obtained curve parametrization for realistic SNRs. However, the substantial deviations in the parametrization are
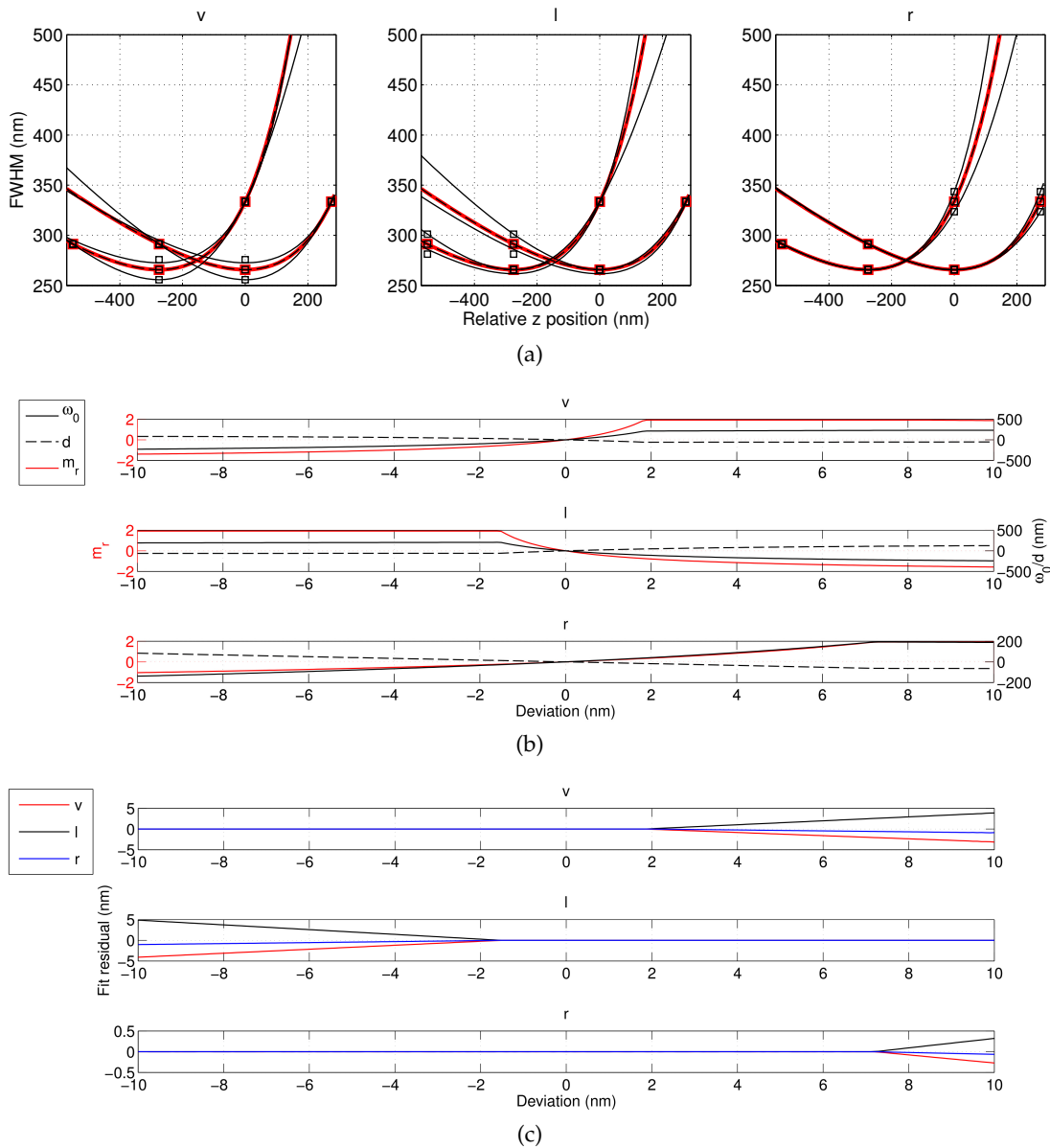
Figure 61: (a) Impact of individual coordinate estimation errors on the curve fitting procedure. The true curves are presented in red and the estimated ones in black. Variation of the (b) fitting parameters and the (c) residuals of the curve coordinates as functions of the coordinate estimation error.

not that directly reflected in the outcome of the online calibration since the total SE is significantly improved over that of the prior calibration for any SNR.

The vertex estimation procedure is consequently the most promising starting point for improvement of the online calibration. Besides the already implemented heuristic improvement of detecting vertex points in smoothed images, this may also include the involvement of a larger neighborhood of images in order to have a more restrictive vertex identification model. Also the number of photons can be an additional source of information. Since the vertex must be at a focal plane, only comparatively bright spots should be included. One could also think of filtering the selected vertices by removing outliers after analysis of their distribution.

This section assesses the dependency respectively the robustness of the algorithm to the experimental parameters. This includes the dependency on (1) the number of focal plane crossings during an acquisition and (2) the size of the focal shift that has to be configured manually. Furthermore, the robustness to the required parametrization is analyzed. This involves the accuracy with that the (3) focal and the (4) FWHM shift must be provided.

In these experiments, the total SE is evaluated since it is the determining criterion of interest for the online calibration method. The different experimental parameters will be tested in combination with varying depths and SNRs. If the SNR is varied, the depth will be fixed to 10 µm, whereas for varying depths the SNR will be set to 10. This reasonably high SNR was chosen to reduce the impact of errors induced by low SNRs. This way, the effects of the particular variables of interest are better isolated.

Number of Focal Plane Crossings

The number of focal plane crossings is a defining parameter for the online calibration. If more vertex frames are detected, then the coordinate estimation should be more accurate. It is also an indirect measure for an appropriate recording time. Although there is not necessarily a linear relationship, it is at least likely that longer recording times lead to higher number of focal plane crossings. The length of the trajectories had to be extended for simulation in order to increase the number of focal plane crossings.
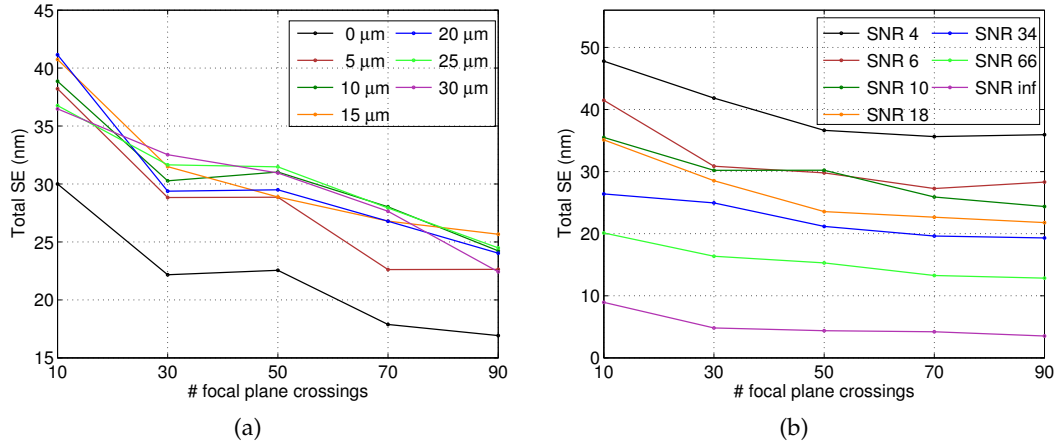

Figure 62: The total SE as a function of the number of focal plane crossings and the (a) imaging depth respectively the (b) SNR.

Fig. 62a and 62b present the total SE as a function of the number of focal plane crossings and the imaging depth respectively the SNR. As expected, the total SE improves with increasing number of focal plane crossings. It is advisable to include as many particles as possible or to extend the recording time. Since for the vertex frame selection only fast relative changes are analyzed, the independence of slow sample drifts, like they occur during most experiments, is an advantage of this method. In fact, it should

actually even be possible to manually refocus during the acquisition as long as the smeared images during refocusing are not analyzed.

Apart from that, the SNR is again the most influencing experimental parameter for the SE, while the current depth has minor impact. These findings are independent of how many focal plane crossings are actually detected. The prior calibration method leads to total SEs > 50 nm for imaging depths $\geqslant 5$ µm. Consequently, the online calibration provides more accurate results already for very low number of focal plane crossings.

Adjustment of the Focal Shift

Configuration of the focal shift for a given focal length of the cylindrical lens must be done manually by adjusting the distance of the lens to the camera. The configured focal shift is a measure for the degree of the introduced astigmatism and effects the operation of the online calibration.

Fig. 63a plots the total SE as a function of Δ_f and the imaging depth. As apparent from the course of the total SE, the adjustment of Δ_f represents a compromise between two opposing effects. For larger Δ_f, the three estimated coordinates distribute more preferable over the total axial analysis range. This improves the SE since for smaller Δ_f any deviation in the coordinates results in larger deviations from the true curves as a function of the distance to the focal planes.

On the opposite, the increasing degree of the astigmatism additionally blurs the PSF by spreading the photons over the axial range. This lowers the effective SNR at the vertex frames and increases the SE. This effect was indirectly simulated by keeping the decay of the SNR constant with respect to the distance to the center between the two focal planes. This was done irrespectively of the adjusted focal shift. The maximum degree of the astigmatism is physically limited by the axial sectioning of the CSU.

Apparently, there is almost no difference between the depths, and a single optimum at $\Delta_f \approx 280$ nm exists for the present parametrization. This was also used for adjustment of the setup.

Robustness to Calibration Errors of the Focal Shift

The robustness to calibration errors of Δ_f is of importance since it is the sole experimental parameter that the user must provide to the online calibration method. For the current experimental configuration, it was calibrated to be $\Delta_f = 278.40 \pm 45.37$ nm. In order to provide the experimenter with a guideline for the accuracy with that Δ_f should be determined, Fig. 63b-63c present the total SE as a function of the deviation from the true focal shift and the imaging depth respectively the SNR.

The SE deteriorates linearly for under- and overestimation of Δ_f. Since the SD of the presented Δ_f calibration was 45.37 nm, it must be concluded that calibration using just a single particle would be insufficient. The obtained total SE for any experiment could easily double. However, particularly for realistic SNRs, calibration errors of ± 20 nm appear to be tolerable. In order to maintain better results than with the prior calibration, the true Δ_f has to be determined with an error not larger than ± 60 nm for the present imaging configuration.

(a)

(b)   (c)
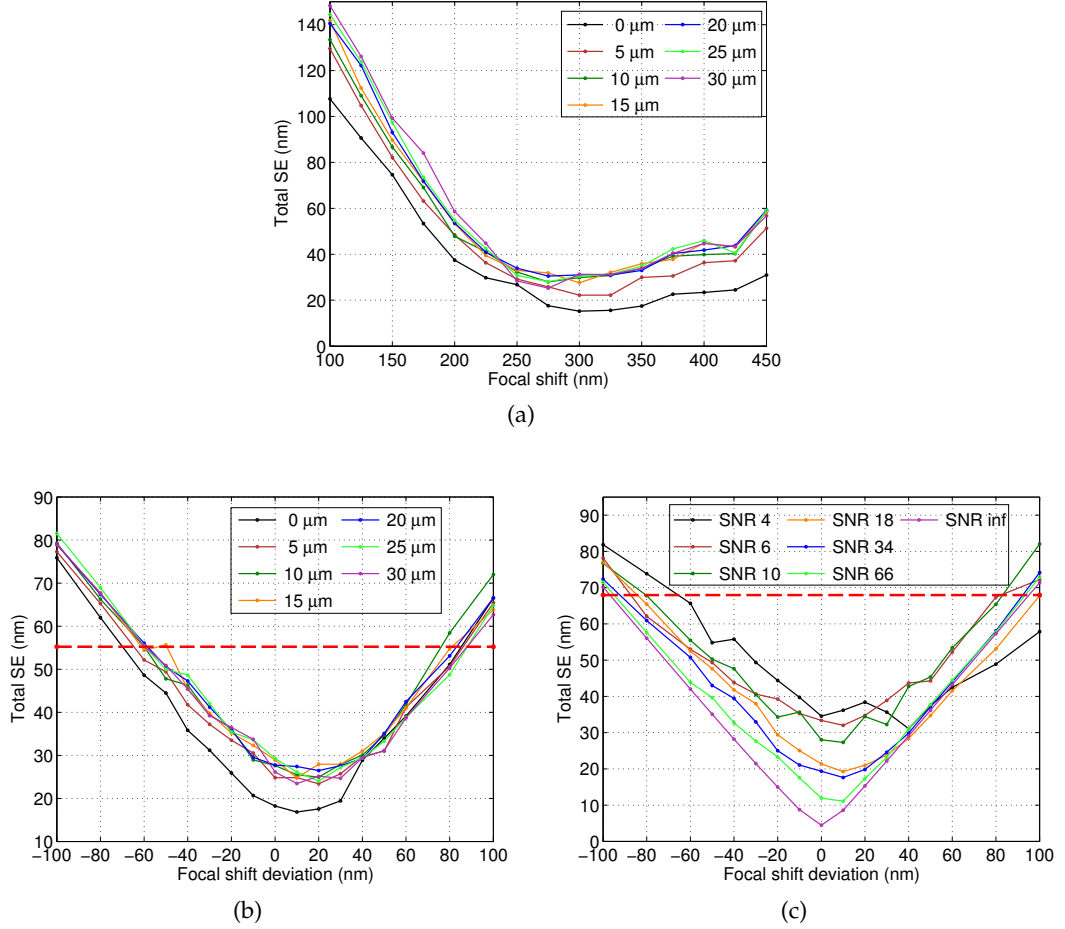
Figure 63: (a) The total SE as a function of Δ_f and the imaging depth. The total SE as a function of the deviation from the true focal shift and the (b) imaging depth respectively the (c) SNR. The dashed red lines represent the obtained total SE for the prior calibration at (b) 5 μm respectively (c) 10 μm imaging depth.

Robustness to Estimation Errors of the FWHM Shift

The robustness to estimation errors of Δ_ω is not of importance for the online calibration method itself, but a specific prerequisite for their application to confocal setups. In order to analyze the robustness, the images were now simulated with $\Delta_\omega = 60\,\mathrm{nm}$. In Fig. 64 the total SE is then presented as a function of the deviation from the true FWHM shift and the depth respectively the SNR.

The principal courses of the total SE are similar to those with respect to errors of the provided focal shift. The SE now also significantly deteriorates as a function of the imaging depth. This behavior is quite reasonable since for the flatter calibration curves at large imaging depths any additional error in the FWHM estimation must have an increased effect on the total SE.

Similar to Δ_f, Δ_ω should not be calibrated from a single particle since for the corresponding SD of 5.71 nm the total SE already deteriorates significantly. Lower deviations appear to be generally tolerable, but they should not be larger than 10 nm in order to maintain better results than the prior calibration.
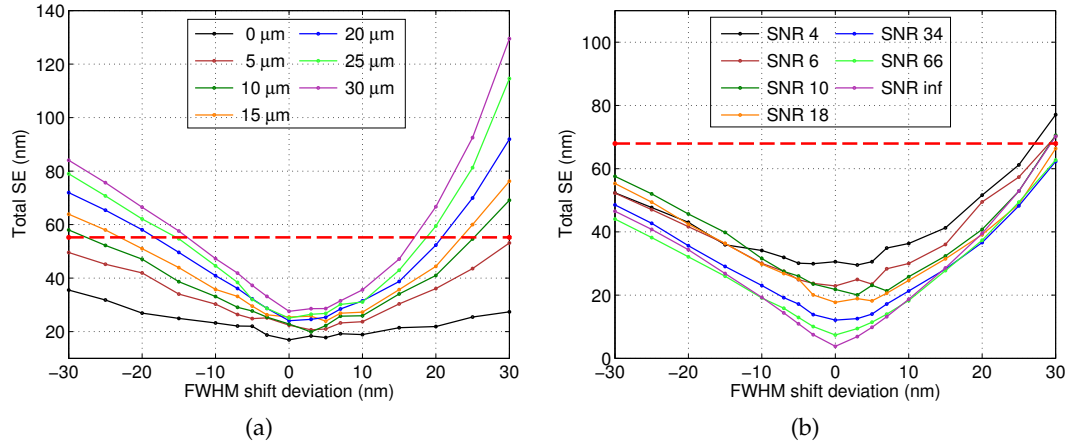
Figure 64: The total SE as a function of the deviation from the true FWHM shift and the (a) imaging depth respectively the (b) SNR. The dashed red lines represent the obtained total SE for the prior calibration at (a) 5 μm respectively (b) 10 μm imaging depth.

4.10.2 *Evaluation on Semi-synthetic Data*

Semi-synthetic 2D image streams were constructed on the basis of experimentally acquired z-scans of immobile particles. Then individual images were selected and aligned according to simulated axial trajectories. Such data also allows for evaluation of the calibration algorithm since the exact axial position of every image is known, and the calibration curves can be computed from the z-stacks. An important advantage is the fact that realistic artifacts of the image creation process are inherently considered. In detail, this includes the alignment of the setup, aberrations of the PSF owing to the cylindrical lens and the pinholes, as well as any deviation from the optimal model assumptions.

Particularly the revealed deviations between the axial calibration functions impede the evaluation (see Sect. 4.9.1.2). The required GT calibration can now either be created by individual fits to the axial correlation functions and would violate the model assumptions or identical curves can be enforced during the fitting, but would then exhibit substantial deviations from the true measurements. Consequently, semi-synthetic images cannot be evaluated against a known GT.

To still evaluate such images, individual fits to the axial curves of the two lateral directions are computed so that at least the values of the three required coordinates are available. Also the SE can be assessed. This is done by computation of the axial position of all images at each axial scan position. The measured axial position p is compared to the known axial scan position p_r of each image and the SE is computed as $\langle p - p_r \rangle$. This procedure avoids the evaluation against an incorrect GT calibration, but the result is dependent on the accuracy with that the vertex position of the y curve is calibrated from each z-stack.

The required parameters Δ_f and Δ_ω are taken from the calibrations in Sect. 4.9.1.2. The evaluation results are presented in the following.

The next sections first provide a detailed description of how the data is created and how the SNR can be estimated in real data. Then, similar evaluation procedures like in Sect. 4.10.1 are conducted and the results are discussed.

4.10.2.1 *Semi-synthetic Data Creation*

Semi-synthetic images are based on z-scans that were again acquired from 30 nm diameter fluorescent beads immobilized in Mowiol. Each bead was repeatedly scanned 50 times with an axial step size of 20 nm. The axial range was 1.6 µm and a temporal resolution of 20 Hz was set. This configuration was chosen as a compromise between the targeted temporal resolution, the possible number of images, and the drift of the piezo stage device during the scan. Within the depth range of 0-30 µm 5 particles were selected every 5 µm.

In order to maintain comparability, the axial trajectories were created using exactly the same parametrization as described in Sect. 4.10.1.4. To construct 2D image streams, the corresponding images for each computed axial position were selected from the acquired z-stack. The axial sampling of the obtained trajectories is now limited to 20 nm since the computed position must be rounded to the closest available axial scan position. Based on the limited number of repeated z-scans, at most 50 different images are available per position in a single stream. The length of the trajectory was limited to 1000 frames, which yielded about 50 focal plane crossings. At every penetration depth each of the 5 selected bead images was combined with 10 simulated trajectories so that the total data set comprised again 50 realizations per depth.

Inherent problems of this type of data sets are the uncontrollable drift of the nanometer focusing piezo stage device and the fact that the reference axial correlation functions are also only calibrations. Both issues introduce inevitable artifacts and inaccuracies in the evaluation. Given the relatively coarse axial sampling, it was found that the images at each position could still be combined for calibration. The occurring deviations during the total scanning procedure were still smaller.

In contrast to the evaluation of simulated data, the lateral particle positions per image were not initialized, and instead the full workflow of particle detection, fitting, and calibration was invoked. Images at off-focus positions with unreliable SNR were not included in the analysis like it was the case for real acquisitions. Since the dependency of the online calibration on the SNR was already analyzed for simulated data, the actual SNR is determined, but not varied again. The next section describes the corresponding procedure.

4.10.2.2 *SNR Estimation in Real Images*

The most critical part of the SNR estimation is the quantification of the noise. For real data, this can be accomplished experimentally by repetitive acquisition of particles and computation of the SD as a function of the peak intensity. This has to be done for the full dynamic range (Kubitscheck et al. 2000). In order to avoid these calibration efforts for varying experimental configurations, a method to estimate the SNR directly from the experimental data is proposed here.

The key idea is the employment of the fitting results. Based on the estimated intensity distribution of a particle, its peak intensity and the noise component can be easily derived. The peak intensity then corresponds to the maximum intensity of the discrete

surface of the estimated intensity distribution, and the noise component is obtained by subtraction of the estimated surface from the true data. In order to compute the noise values for the particle (σ_p) and the background (σ_b) separately, the SD is calculated for the corresponding pixels. Since the shape of a particle is subject to strong variation, all pixels covered by a rectangle, having edge lengths corresponding to the individual FWHMs, contribute to the noise of the particle.

The SNR of real images is then defined by:

$$SNR = \frac{\hat{N}}{\sqrt{\sigma_p^2 + \sigma_b^2}}. \tag{66}$$

This is similar to Equ. 63 except for the factor that considers δ_{mult}. It is left out because σ_p and σ_b are measured values and hence already include the multiplicative noise.

To evaluate the proposed procedure it is applied to synthetic images, where the true SNR is known. 1000 particles with varying individual FWHMs were rendered for a large range of SNRs. Fig. 65a plots the true and the estimated SNR. Apparently, the SNR estimation is correct for very low, but overestimates it for higher SNRs. This behavior was actually expected. The derivation of σ_p from several pixels of the intensity distribution must underestimate the noise because the shot noise scales with $\sqrt{N}$ and is hence largest at the peak pixel (Cheezum et al. 2001).
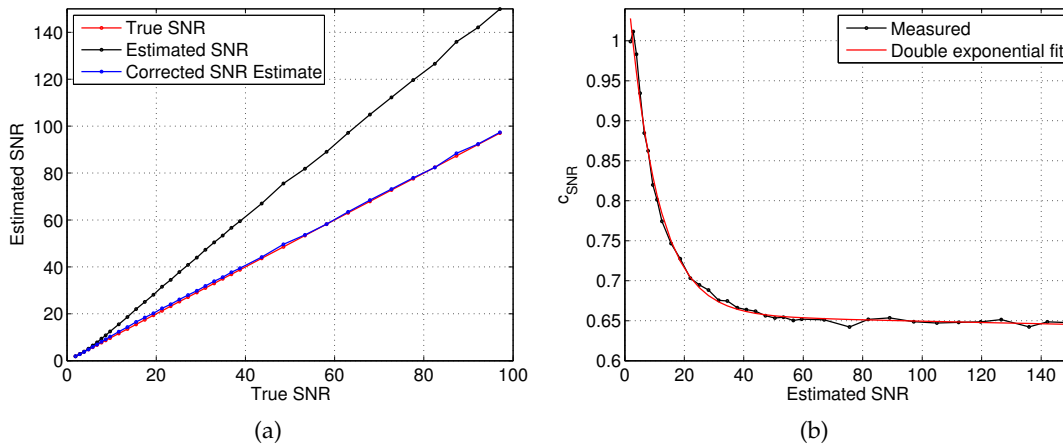

Figure 65: (a) Comparison of the true with the estimated SNR. (b) The SNR correction factor as a function of the estimated SNR.

For that reason, the estimated SNR needs to be corrected. This can be done using a correction factor c_{SNR} that is defined by the ratio of the true and the estimated SNR. Fig. 65b plots c_{SNR} as a function of the estimated SNR. It is well fit by a double exponential decay function and hence easily applicable.

The presented SNR estimation procedure can now be applied to the semi-synthetic data set. Fig. 66a presents the SNR of an exemplary particle at 10 μm depth as a function of the relative axial scan position and the scan iteration. The Gaussian profile along the axial axis is clearly visible. The missing values at the left side represent images where

the particle was not detected. In accordance with the results of Cheezum et al. 2001, missing detections start to occur at SNR < 4.
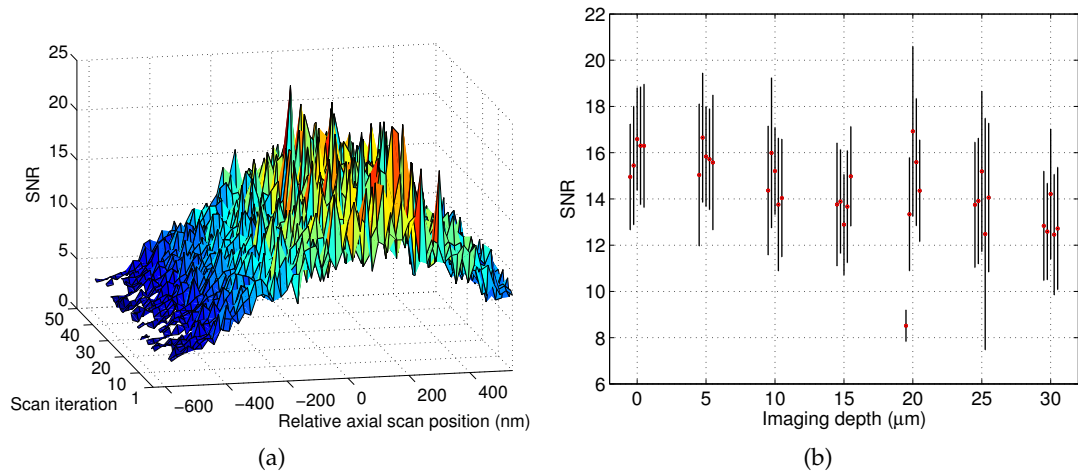

Figure 66: (a) The SNR of an exemplary particle at 10 μm depth as a function of the relative axial scan position and the scan iteration. (b) The average total SNR for each individual particle at its respective depth. The black bars represent the SD.

Fig. 66b finally presents the total SNR for each individual particle at its respective depth. It is computed as the average of all repeated iterations at the individual axial center position. Given that beads exhibit relatively bright and stable fluorescence, their average SNR is in the range 13-17. Owing to the transparent embedding medium and the subjective manual selection of the brightest particles at each depth, there is hardly a trend in the obtained SNR values towards larger imaging depths.

4.10.2.3 *Coordinate Estimation Procedure*

The error of the coordinate estimation as a function of the imaging depth is presented in Fig. 67. With the exception of zero depth, all three coordinates are reasonably well determined. The average deviations from the FWHM at the vertex are almost negligible, while for l and r they are in the low nanometer range. These results correspond very well to the expected values from the simulation at SNR = 18. The large errors at zero depth can be attributed to the deviations of Δ_f and Δ_ω at this depth. They were revealed in Sect. 4.9.1.2.

4.10.2.4 *Quantifying the Systematic Error and the Localization Accuracy*

Fig. 68 summarizes the performance of the online calibration method applied to the semi-synthetic data similarly to the simulated images. Fig. 68a and 68c present the SE respectively the axial LA as functions of the relative axial position and the depth. In accordance with the simulations, the fundamental course of the SE is similar for all depths and deteriorates in both directions away from the center between the focal planes. Again, the SE is significantly deteriorated at zero depth owing to the artifacts of Δ_f and Δ_ω at this depth. This effect will be observable in all provided measures for semi-synthetic data.
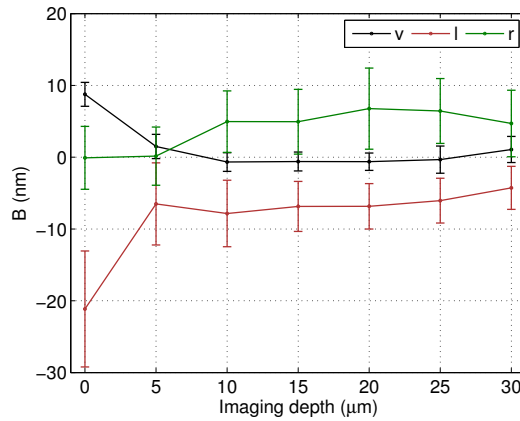
Figure 67: Average deviation of the estimated from the true curve coordinates as functions of the imaging depth.

The principal course of the axial LA is also consistent with the simulations. It deteriorates for particles measured below the focal plane and exhibits the expected strong dependency on the imaging depth.

Fig. 68b and 68d present the respective total measures as functions of the imaging depth, but also present the results if the prior calibration is applied. For the prior calibration, always the average configuration of all particles calibrated at zero depth was used.

The total SE deteriorates only slightly as a function of the depth, whereas the axial LA varies significantly. The total SE is only worse than the prior calibration at zero depth. The obtained deviations at zero depth correspond well to the results of the robustness measurements in Sect. 4.10.1.9. For any other depth, the online calibration reduces the error by at least half. The relative reduction increases as a function of the depth up to ∼ 70 %. The axial LA is again always superior and almost independent of the depth when using the prior calibration.

The principal courses of all measures are similar to that determined by simulation. The absolute values are deteriorated by ∼ 30 % for the SE, but almost 100 % for the LA with respect to the simulations at comparable SNR of 18. These degradations are reasonable since they can be attributed to the imperfections of the data set that particularly affect the accuracy. This includes the drift and positioning accuracy of the piezo stage device, the relatively low axial sampling, and the fact that the images contain deviations between the two axial correlation functions.

4.10.2.5 *Visual Analysis of the Trajectory*

For visual analysis, Fig. 69 presents exemplary axial trajectories at selected depths determined using the online respectively the prior calibration. It is apparent that for the online calibration the fundamental course of the true trajectories is followed for all depths. This is true with the exception of zero depth owing to the known deviations of Δ_f and Δ_ω. The systematic errors increase with depth, but the deteriorating axial LA has again more severe effect on the accuracy of the measured trajectories.

For prior calibration, the fundamental course is hardly followed at larger depths. The axial LA erroneously appears to be superior and is almost constant for all depths.
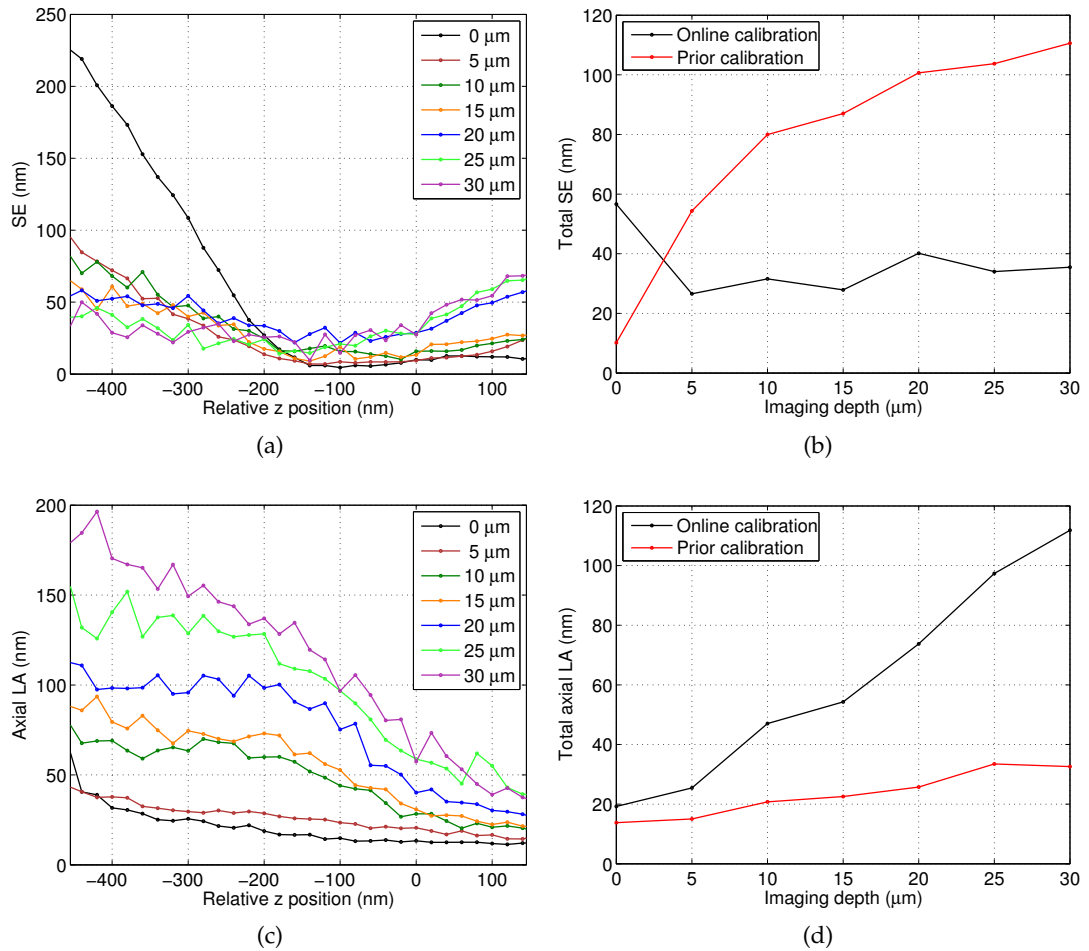
Figure 68: (a) The SE as a function of the relative axial position and the imaging depth. (b) The total SE as a function of the imaging depth for the online and the prior calibration method. (c) The axial LA as a function of the relative axial position and the imaging depth. (d) The total axial LA as a function of the imaging depth for the online and the prior calibration method.

Again, the principal findings are identical to that of the simulations proving that they are valid also for real acquisitions.

4.10.2.6 *Impact on the Calculated Diffusion Parameters*

For analysis of the resulting diffusion measures, Fig. 70a and 70b plot the MSD curves at different imaging depths for the online and the prior calibration method, respectively. The corresponding local diffusion coefficients are provided in Fig. 70c as functions of the imaging depth.

At zero depth both diffusion measures are well approximated using prior calibration, but deviate significantly for the online calibration method. For the other depths, it is apparent that the MSD curves almost preserve their principal shape, but the absolute values increase as a result of the deteriorating axial LA. The measured MSD curves exhibit significantly stronger confinement than the GT if the prior calibration is used. This is reasoned by the erroneously low axial LA as a result of the incorrect calibration curves.
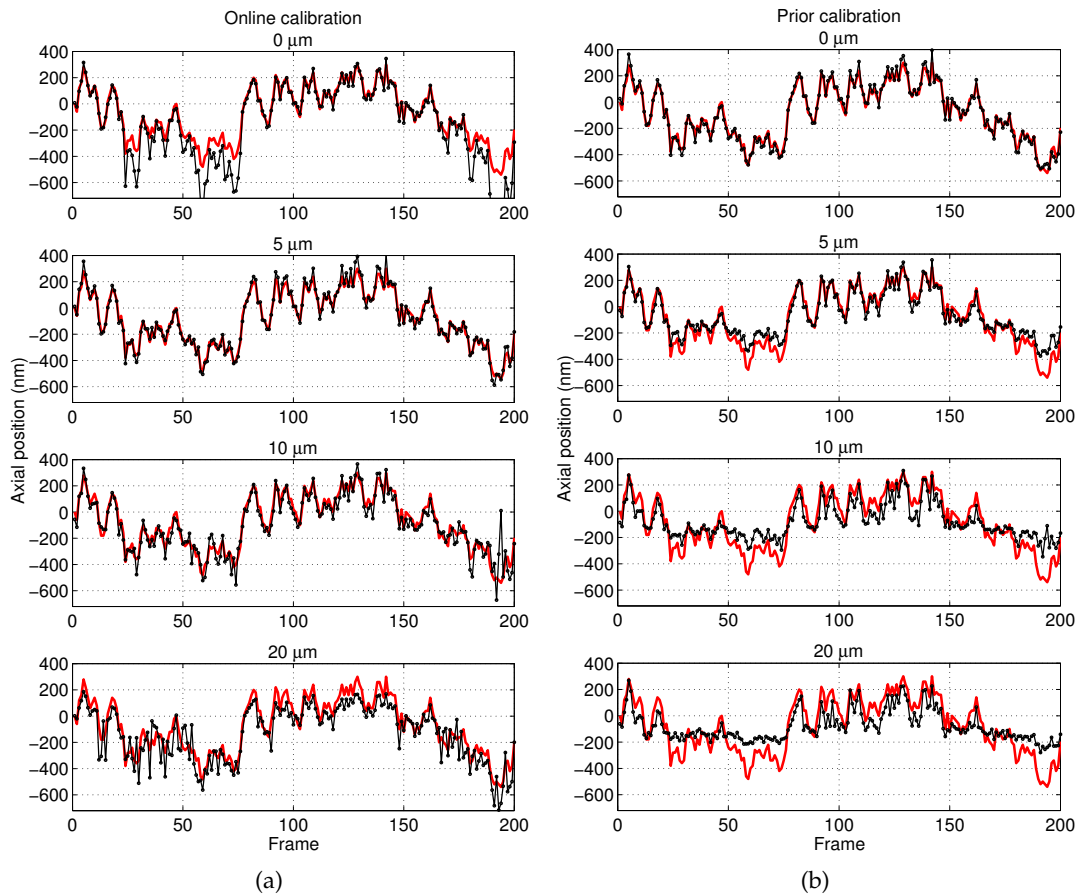
Figure 69: Measured trajectories determined by the (a) online and the (b) prior calibration method at selected depths. The red lines denote the true simulated trajectories.

These effects are also clearly visible by looking at the courses of D_l. Since the online calibration yields significantly lower deviations from the true D_l, it can be concluded that indeed more reasonable approximations to the true calibrations curves have been computed. In total, the results are similar to those of the simulation, but again the absolute errors are larger.

4.10.3 *Evaluation on Real Data*

By now the fundamental functioning of the online calibration method has been proven. Evaluation of their performance in real brain slice experiments is hardly possible as the GT is unknown, and the molecules cannot be immobilized without changing the optical properties of the sample. Only the plausibility of the output of the algorithm can be tested.

For it, brain slices were prepared as described earlier (Biermann et al. 2014) and transfected with GPI-GFP. Its mobility was monitored by labeling GPI-GFP with QDs (see Sect. 4.5.2). 2D image streams were acquired in brain slices at depths between 1 and 20 μm at an interval of 1 μm. Each image stream comprised 1000 frames and was acquired with a temporal resolution of 30 Hz. To increase the reliability of the
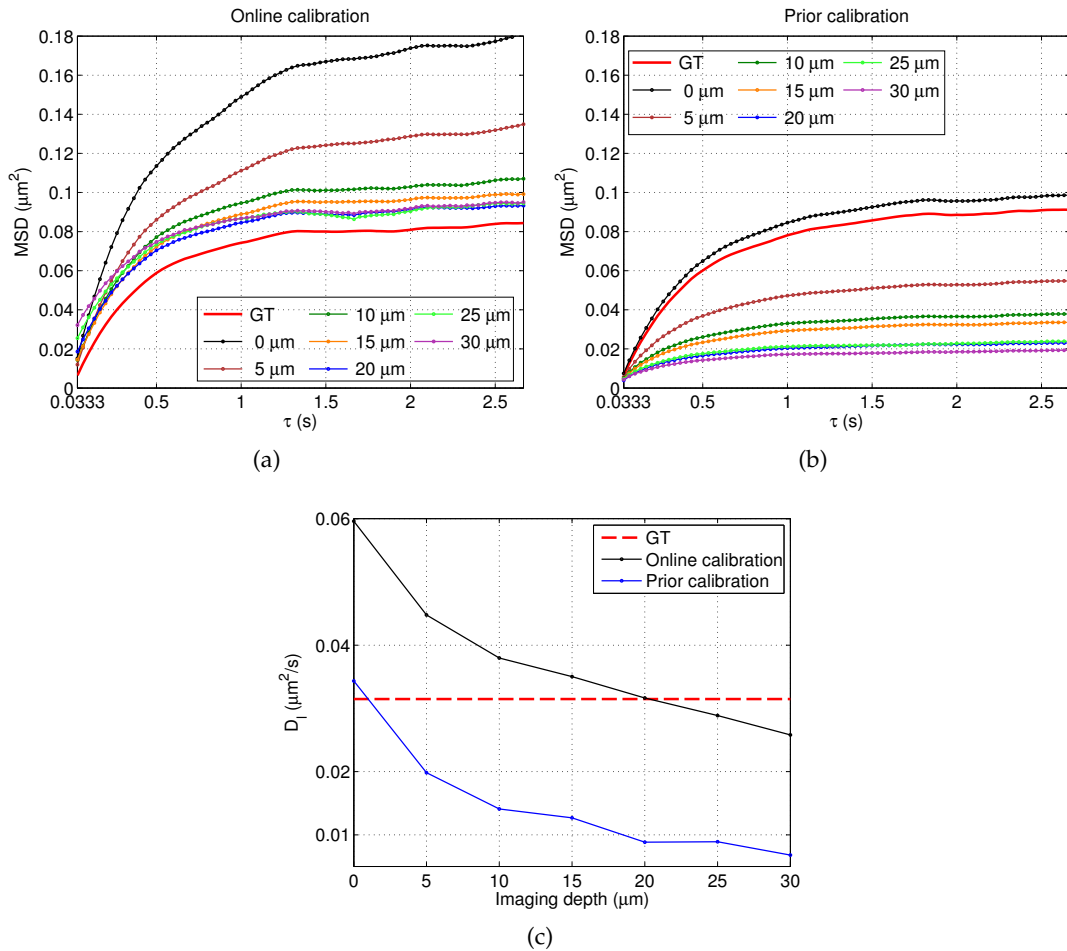
Figure 70: (a)-(b) Observed MSD curves at selected imaging depths for the online respectively the prior calibration method. (c) Observed courses of D_l as functions of the imaging depth.

results, only trajectories of length $\geqslant 20$ were considered for calibration and subsequent analysis.

4.10.3.1 *Visual Analysis*

To obtain a visual impression of the shape fitting capability of the workflow, the fitting results for exemplary acquisitions at different depths in the sample are provided in Fig. 71. Some situations that underline the functioning of the algorithm are also highlighted. It is apparent that nearby particles can be distinguished (mark 1), but if they are too close, they are rejected based on the allowed size (mark 2). Furthermore, varying elliptical shapes are observable (mark 3), and particles far off the focal plane that create non-uniform background are rejected (mark 4).

Fig. 72 additionally presents the measured 3D trajectories within the red regions indicated in Fig. 71. They illustrate the 3D capability of the developed SPT workflow.

The lateral extent of an axon is clearly recognizable in Fig. 72a and 72b. As expected from 3D measurements (Renner et al. 2011), the distribution of particles is highest at the axons lateral border. By encoding the axial position in the color, Fig. 72b also reveals

(a)   (b)   (c)

(d)   (e)   (f)
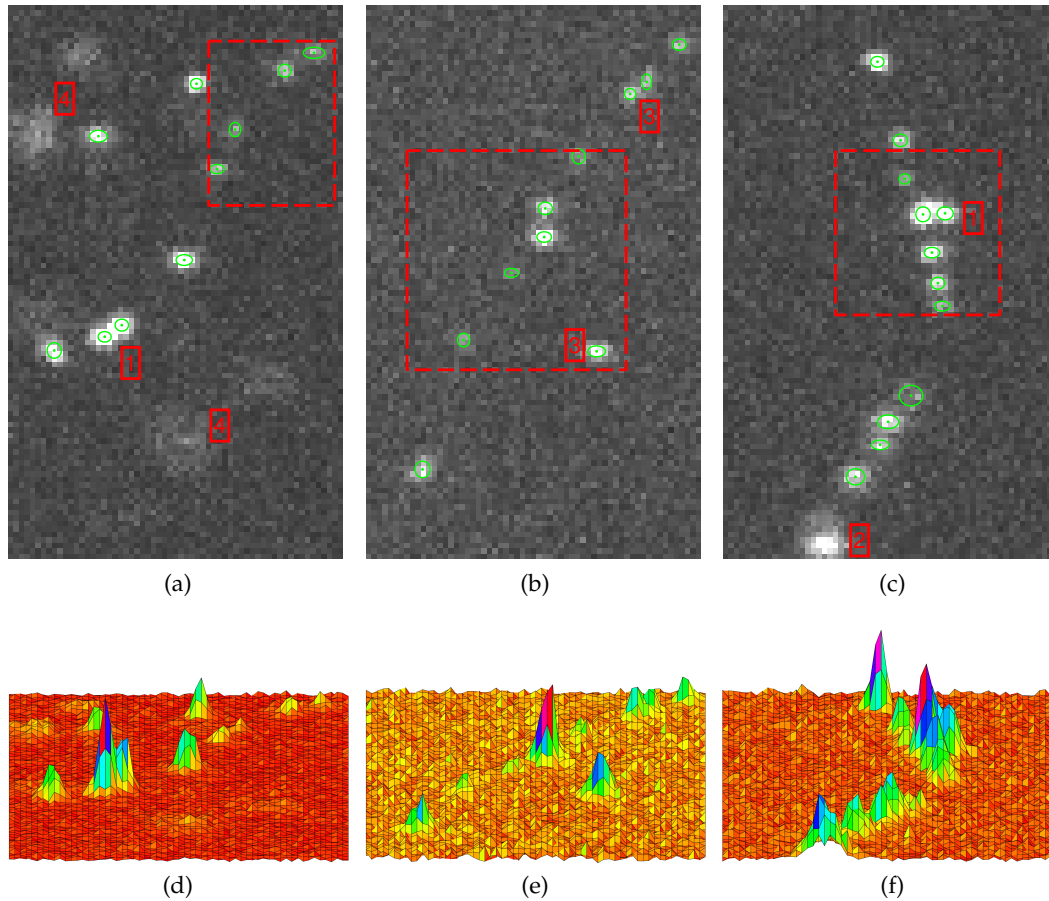
Figure 71: (a)-(c) Exemplary acquisitions in brain slices at varying depths (1, 3, and 6 µm). The green dots indicate the fitted sub-pixel positions, and the contour lines represent the individual FWHMs. The red dashed boxes depict the regions that are used for the 3D plots in Fig. 72, and the red marks denote situations that are described in the text. (d)-(f) Surface plots of the same acquisitions.

that the particles in the center of the image run on top of the axon, whereas those on the left are located below the axon. This conclusion is justified by the observation that in the center of the image the trajectories in the inner area of the axon have a higher axial position than those at the lateral border. The situation is vice versa on the left. In addition, the whole axon seems to follow the axial course of a bridge.

The second example (see Fig. 72c-72d) reveals that the algorithm allows to distinguish the axial course of two intersecting axons. The horizontal axon proceeds $\sim 400\,\text{nm}$ above the perpendicular axon.

Even the tubular structure of an axon can be determined. It is clearly observable in Fig. 72e-72f. It also becomes apparent that the axial LA considerably decreases if a particle moves below the center of the focal planes. This finding is in line with previous results (see Sect. 4.10.1.6).

The presented results reveal that meaningful axial information can be recovered by using the proposed online calibration method. If prior calibration is applied, Fig. 73 illustrates that the axial information is basically lost. Adjusting the correlation function to the imaging depth is indeed mandatory.
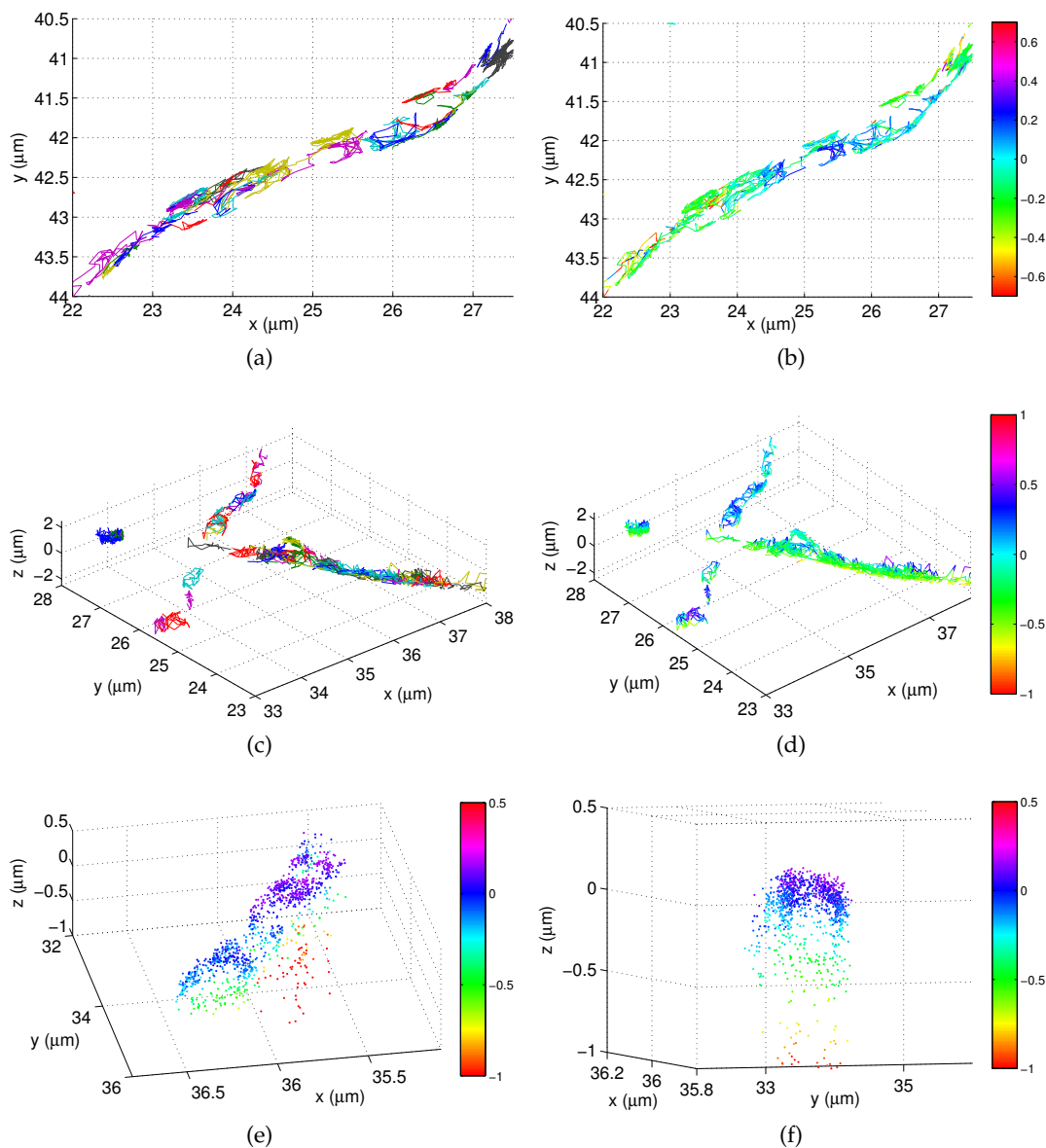
Figure 72: Exemplary measured 3D trajectories in brain slices. (a)-(b) 2D views of an axon illustrating that particles located on top and below the axon can be distinguished. In (a) the color distinguishes individual trajectories and in (b) it encodes the axial position. (c)-(d) 3D views of two intersecting axons that can now be axially separated. The meaning of the colors is the same like in the figures above. (e)-(f) 3D and front view of a part of an axon illustrating the tubular axon structure. In order to make the morphological structure more visually apparent, the trajectories are just presented with position markers, and the color encodes the axial position.

4.10.3.2 *Molecular Dynamics Analysis*

It is also apparent from the presented examples that the axial LAs with that the z coordinates are determined are very low. This is well observable by calculation of molecular dynamics parameters. Fig. 74a presents the MSD curves for the individual dimensions as well as their combinations at selected depths.
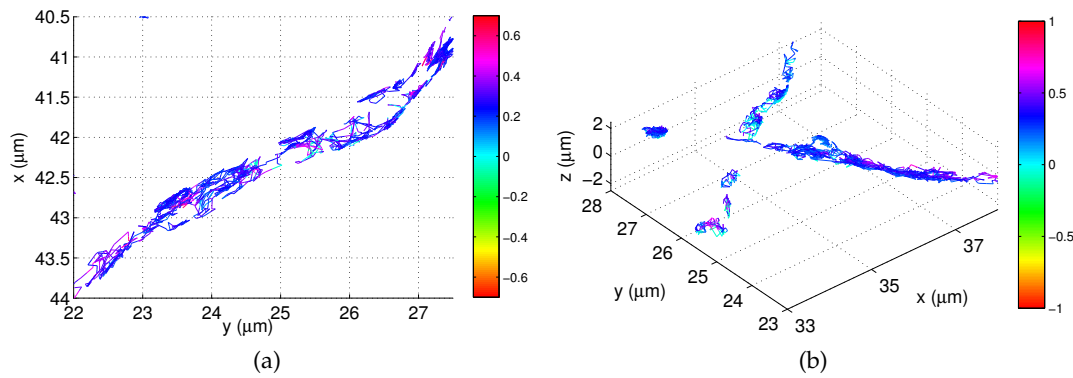
Figure 73: (a)-(b) The same views like in Fig. 72b and 72d, but calculated using prior calibration.

Apparently, the fundamental courses and correlations between the various MSD curves are similar. This is reasonable since it was already shown in Sect. 4.5 that the diffusion does not significantly change as a function of the depth in the sample. Only the correlations between the individual lateral dimensions vary because they depend on the underlying neuronal structure. If molecules are for instance measured at a single straight axon, the absolute MSD values are larger for the direction of the axon's expansion. If a true network is imaged, the two lateral directions are likely to exhibit almost identical MSD curves.

The absolute MSD values of the axial direction are significantly higher than those in the lateral directions. This is owed to the apparently much worse axial LA. Although the exact LAs can hardly be determined without additional calibration procedures, the average molecular step size can act as an indicator because the molecular motion should on average be similar in all directions. Consequently, deviations just stem from the individual LAs. The average step size can be computed from the first MSD point as $\sqrt{\mathrm{MSD}(\tau = 1\Delta t)}$. It is plotted in Fig. 74b as a function of the depth for the lateral and the axial directions.

The lateral step sizes are almost identical and much smaller than the axial step size. It can be concluded that the axial LA is indeed much worse than the lateral LA approximately ~ 5 times. Moreover, and in line with the simulated results, the axial step size deteriorates significantly as a function of the depth. If the prior calibration method is applied, the axial step size remains almost constant and appears to be much better.

To quantify the course of the MSD curves for the individual directions, the individual courses of D_l as functions of the imaging depth are provided in Fig. 74c. The absolute diffusion values are well compatible with the range observed for lateral diffusion (see Fig. 35c) and can hence be considered reasonable. Equally important are the findings that the axial diffusion is similar to the lateral diffusion and that a deterioration towards larger imaging depths cannot be observed for the first 10-15 µm. If prior calibration is applied, the axial diffusion is consistently underestimated and deteriorates as a function of the depth. The apparent breakdown of the performance of the online calibration for imaging depths $\geqslant 15$ µm is likely to be attributed to the limiting SNR that is achieved with the presented imaging configuration (see Fig. 74e). Further reasons may be the lower amount of detected particles and that the influence of the RIM is stronger in slices than in Mowiol. Since even the pure detection capability
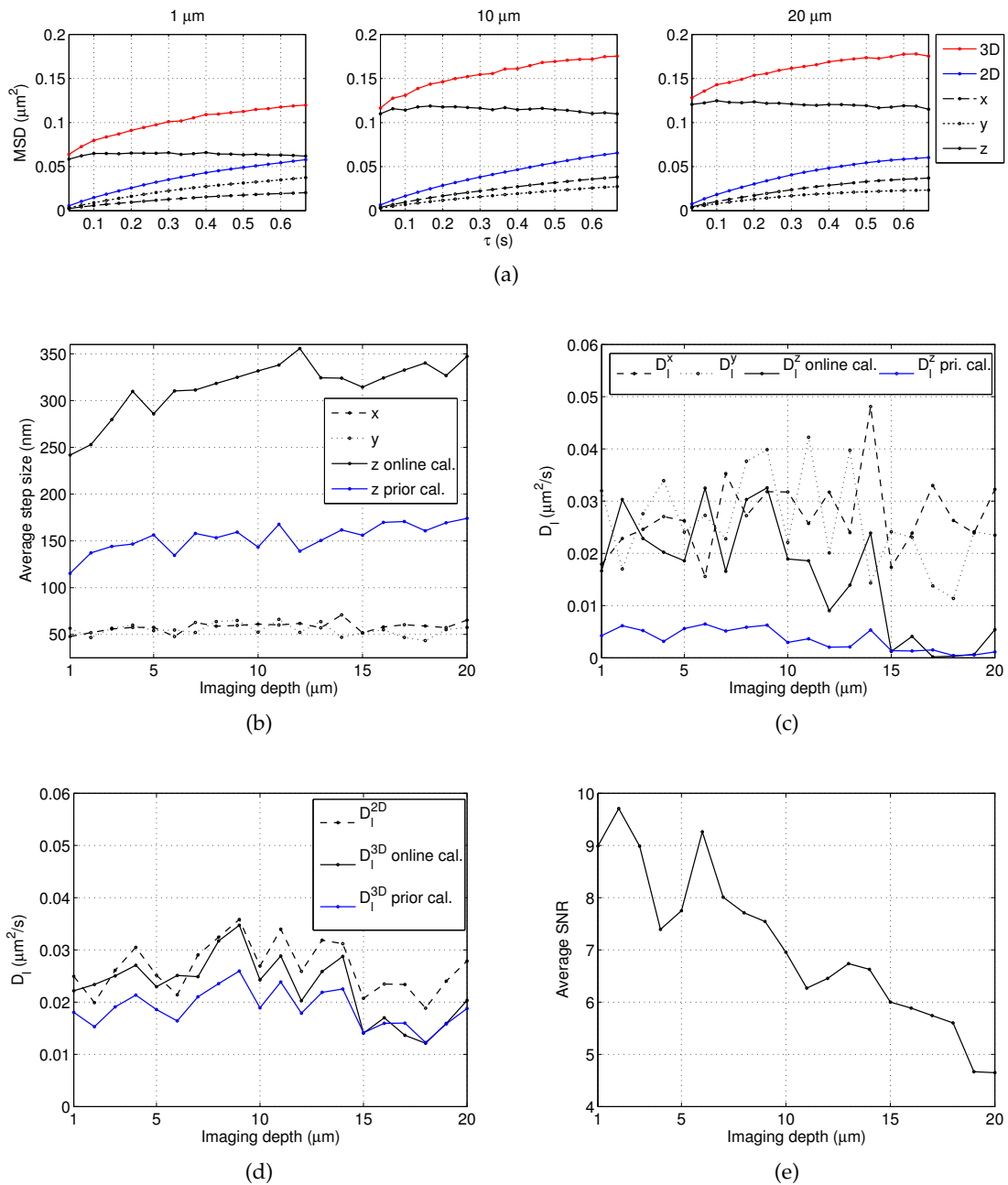
Figure 74: (a) MSD curves at selected depths in brain slices. (b) Individual average step sizes as functions of the imaging depth. (c) Individual and (d) combined diffusion results as functions of the depth. For comparison, also the axial diffusion coefficients when employing prior calibration are depicted. (e) Average estimated SNR as a function of the depth. (b)-(e) The presented data always includes in total 18098 trajectories with at least ∼ 300 trajectories per imaging depth. It was obtained from two slice cultures, five brain slices, and 125 acquisitions.

of using oil objective lenses in brain slices drops down to ∼ 20 % at these depths (see Fig. 34c), this is not an additional limitation.

Fig. 74d finally provides D_l for the combined diffusion as functions of the imaging depth. The 2D and 3D diffusion are similar for the online calibration method, but using prior calibration the 3D diffusion is significantly underestimated. These results indicate

that the proposed imaging configuration might not be sensitive enough to resolve the expected underestimation of 2D diffusion in relation to 3D diffusion. In primary cell cultures, similar results were obtained by Renner et al. 2011 who concluded that higher frame rates are required. It could be reasonable to extract the rough morphology first and then update the distance between two consecutive particle positions with respect to this information. By now, the analysis just takes the smallest distance between two measured positions and assumes an isotropic medium. However, when measuring surface dynamics, the morphology effectively enforces an anisotropic system. Taking the morphology into account may make the expected diffusion differences observable.

Conclusion

The presented experimental results indicate that the proposed online calibration is indeed able to adjust for the aberrations introduced by the RIM. This is justified by the result that the axial diffusion is in the same range as the lateral diffusion. Another important outcome is that although the axial LA deteriorates significantly over depth, D_l could nevertheless be correctly determined for the first 10-15 µm. D_l is clearly underestimated for prior calibration.

The most critical factor is the relatively poor SNR, which is especially limiting at imaging depths $\geqslant$ 15 µm. It must be concluded that the observed axial LA suffices for the extraction of morphological information, but is too poor for the interpretation of individual trajectories. The axial LA leads to uncertainties of almost half of the available axial analysis range. Improving the imaging quality is the major starting point to make such individual outcomes also available in brain slices.

4.10.4 *A Final Illustrative Example*

This section finally provides an illustrative 3D example. Realistic images that represent multiple particles diffusing at the surface of an axon or a spine neck are rendered. The simulation implements the algorithm described by Renner et al. 2011, which basically comprises the wrapping of 2D trajectories around a cylinder.

Fig. 75a-75b present different views of five exemplary surface trajectories at the surface of a single tube whose diameter was set to 400 nm. Each start point was randomized, and the trajectories had length 1000. The diffusion coefficient for each particle was drawn from an exponential distribution with mean 0.05 µm^2/s, and Δt was again 0.0333 s. The corresponding fluorescence images were rendered as described in Sect. 4.10.1.4 at imaging depth 10 µm and with SNR = 10.

For analysis, the complete SPT workflow was invoked. Fig. 75c-75f depict the measured trajectories at different perspectives for using the online as well as the prior calibration method. The higher number of different trajectory colors reveals that not all trajectories could be completely traced and were instead partitioned. Furthermore, the measured positions are subject to relatively strong noise, but the basic cylindrical surface is well recovered by the online calibration method. This supports the finding in real acquisitions (see Fig. 72f). Using prior calibration results in an oval deformation. The axial positions could not be correctly recovered and particularly the positions below the center of the focal planes constantly deviate more than 100 nm. The correct
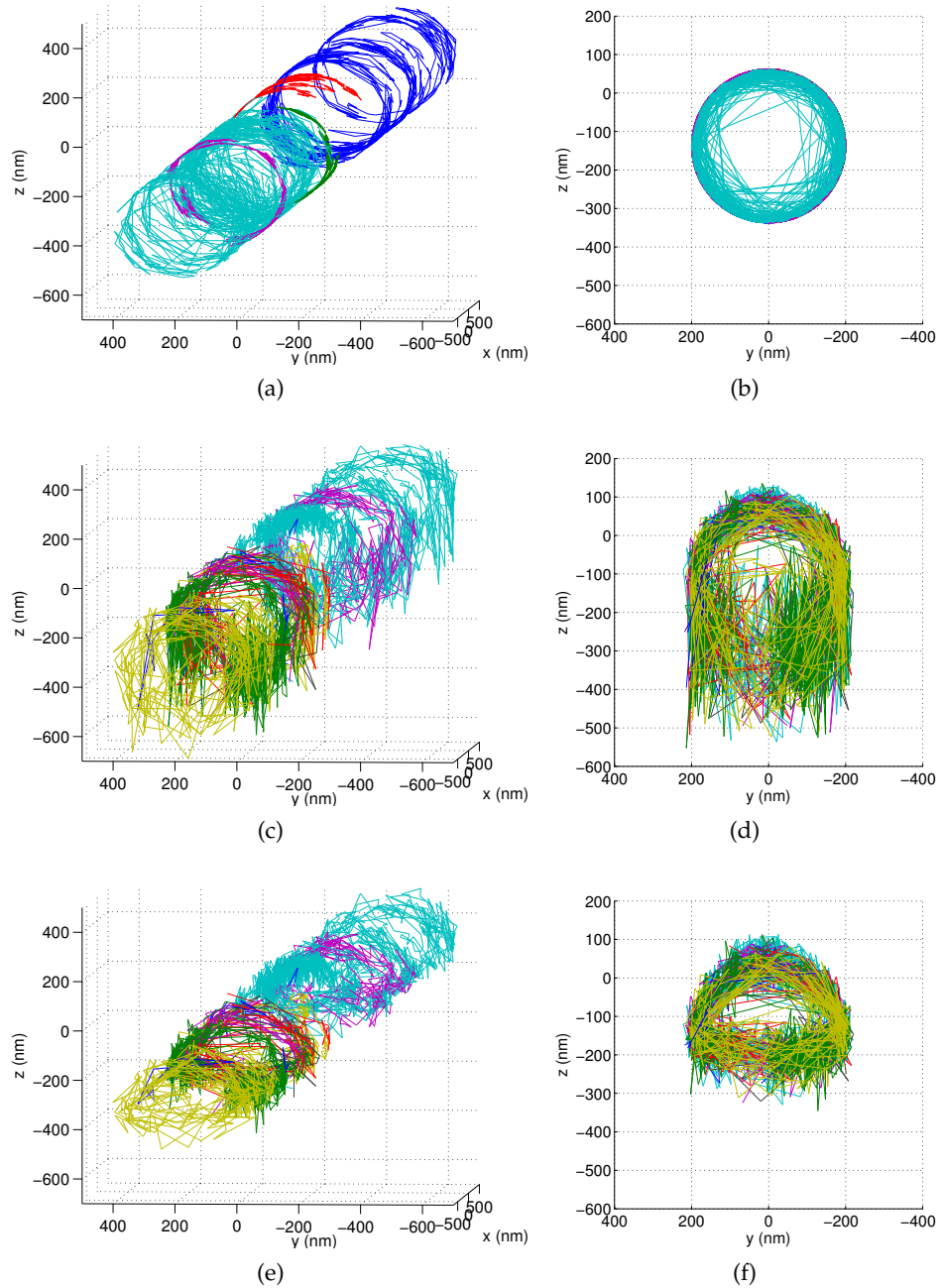
Figure 75: (a) 3D and (b) front view on the five simulated trajectories at the surface of a tube. (c) 3D and (d) front view on the measured trajectories recovered using the online calibration method. (e) 3D and (f) front view on the measured trajectories recovered with prior calibration.

recovery of the basic shape by the online calibration indicates that it is indeed capable of adjusting the correlation functions to the induced optical aberrations.

In Fig. 75c it is also apparent that the axial LA is worse than the lateral LA because the boundary representation is thinner at the sides of the tube. Again, the axial LA considerably decreases for particles that are located below the center of the focal planes. The axial LA appears to be constant for prior calibration, which is also in line with

previous findings (see Sect. 4.10.1.6). Again, it becomes obvious that the axial LA is the limiting factor for 3D SPT in brain slices.

The quality of the recovered trajectories is finally illustrated by plotting them with a color coding that represents the absolute 3D distance between the measured and the true positions. This is presented in Fig. 76 for SNR = 10 and 18. As expected, the absolute deviations are smaller for the image with higher SNR. The color coding also reveals that for SNR = 18 the circular shape is recovered with higher accuracy. Except for particle positions further below the center of the focal planes, the measured positions then deviate only by ~ 20 nm.

(a)   (b)
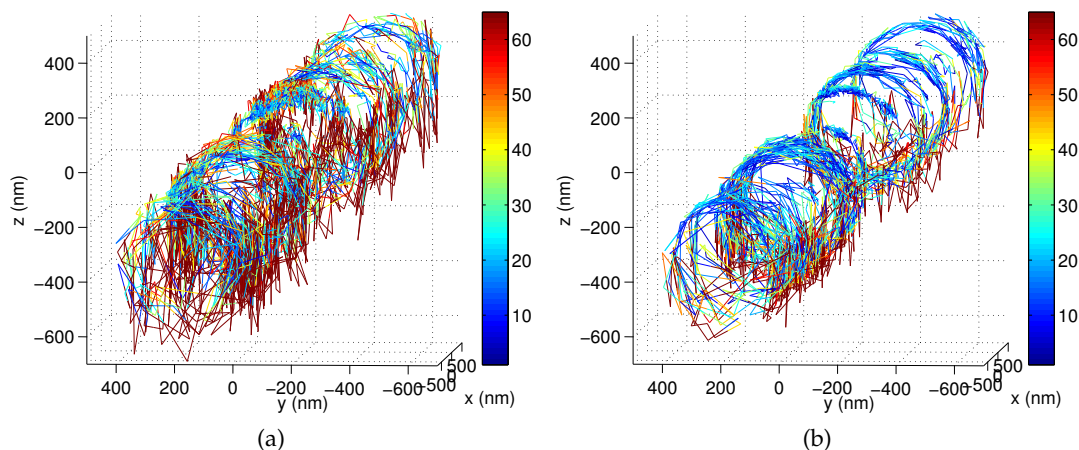
Figure 76: The measured trajectories for (a) SNR = 10 and (a) SNR = 18 recovered using the online calibration method. The color represents the deviation in nanometer and was clipped off after 64 nm in order to increase the resolution for smaller errors.

The presented results clearly illustrate the necessity for adjusting the axial correlation functions. Besides determination of less biased diffusion parameters, this also enables the recovery of the 3D morphology of neuronal structures below the resolution limit.

4.11 CONCLUSION AND FUTURE WORK

This chapter presented an imaging configuration and an algorithmic workflow to facilitate fast 3D SPT deep in living brain slices. The imaging configuration is based on a CSU. QDs were employed as fluorescent markers. It could be shown that this ensemble allows to assess parameters of molecular dynamics in complex living tissue at penetrations depths down to several tens of micrometers.

For analysis of the acquired images, a 3D SPT workflow was developed. The focus was set on the development of an axial online calibration method. It adjusts astigmatism-based 3D SPT techniques to the optical aberrations induced by the RIM, like they are unavoidable for the application of high NA objective lenses with living samples. Since it is an important prerequisite, this work also focused on the accurate estimation of the particle shapes and position. For the remaining aspects of particle detection and 2D linking, well-established techniques were implemented. A 3D particle linking procedure was considered optional and not implemented.

For shape estimation, an EM algorithm for binned and truncated data was applied to microscopy images. For axial localization deep within the sample, a formula that models the induced aberrations and an online calibration method that determines the current model directly from the 2D imaging stream, were developed. The key idea of the latter is the exploitation of the molecular particle motion and of the redundancy introduced by the astigmatism.

The performance of both methods was extensively evaluated on synthetic data and their functioning was proven. It turned out that the exact parametrization of the axial correlation function could not be consistently recovered. However, it was shown that the correct principal course of the underlying trajectories could nevertheless be detected at any depth. This is a result of the capability of the online calibration to at least halve the SE at any depth and SNR. In contrast, the axial LA was found to deteriorate more notably over depth and SNR, which in consequence yielded evident deviations from the absolute positions and MSD values. Nevertheless, and more importantly, it could be shown that correct diffusion coefficients can still be obtained almost independently of the imaging depth and SNR. Comparable results were also obtained for semi-synthetic data, where already the experimental artifacts of the setup were considered. Real experiments in brain slices were conducted and analyzed. The results indicated that the online calibration also works there because the axial diffusion was in the same range as the lateral diffusion, whereas for prior calibration D_l was clearly underestimated. From visual inspection, it became apparent that the 3D morphology can be extracted, but the axial LA is too poor for the interpretation of individual trajectories.

With respect to the stated objectives, it can be concluded that the proposed imaging configuration indeed allows to observe diffusion parameters that are similar to those known from primary cultures (Objective 1.1). The extracellular space seems to be permeable enough for the application of QDs, so that the observed 2D diffusion parameters were similar to those known from primary cultures and subpopulations could be differentiated. Limitations have only been observed for long-term diffusion, where the compartmentation impedes the mobility of QDs. As a major result it can be stated that the developed workflow is capable of making fast nanoscale 3D SPT experiments deep in living organotypic brain slices readily available (Objective 1.2). This is justified by the fact that the correct 3D morphology and diffusion parameters can be derived. Simulations showed that the SE can be reduced by more than 50 %. This is now possible with virtually no additional experimental efforts or compromises for the user and works for imaging depths up to ∼ 15 μm in real brain slices. Solely the focal shift has to be adjusted for the setup. A conceptually novel strategy to account for the effects of the RIM was developed. Instead of trying to counteract or measure the induced aberrations with additional experimental efforts, inherent properties of the experiment are exploited so that the analysis can be adapted to the aberrations. Users can search for transfected neurons in the sample and start imaging right away (Objective 1.6). This facilitates the generation of robust statistics from healthy samples. It could also be clarified how critical it is to neglect the influence of the RIM: the true axial motion and as a consequence also the axial LA are significantly underestimated.

Furthermore, the application of an EM algorithm for microscopy data was proposed. It allows for robust fitting of multiple neighboring particles in a standardized statistical fashion. In conjunction with the online calibration this enables assessment of 3D molec-

ular dynamics in nanoscale compartments with LAs below 100 nm and 30 Hz temporal resolution (Objectives 1.3 and 1.4). It must be admitted that in real brain slices, where the SNR drops below 10, the axial LA reduces to 200-300 nm. The obtained SNR is the major limiting factor.

The complete workflow, including a graphical user interface (GUI)[13], is available at http://sourceforge.net/projects/mdagui/. It can be run in the MATLAB environment and is published under the Creative Commons Attribution License.

In conjunction with the presented imaging configuration, which is commercially available and affordable, it should make the application of 3D SPT techniques in complex living tissue widely available (Objective 1.5). A final problem are the numerous artifacts that the imaging configuration introduces and that have been revealed in Sect. 4.9.1.2. They do not put the proposed method in question, but they reduce their accuracy and may impede the applicability in practice.

In the light of this, technical aspects of the imaging configuration are the most promising starting points for future improvements. Although the CSU-based setup was established for its axial sectioning capability and reasonable temporal resolution, it had shown during this work that the available SNR in packed brain slices is relatively low. This is due to the inefficient light transition through and the emerging stray light at the spinning disks.

Optical microscopy undergoes ongoing development. Just recently, Andor Borealis[14] has been released that utilizes conventional CSUs with multi-mode fibers in order to triple the light throughput. Another confocal technique that has been shown to improve the SNR several times, while maintaining video-rate temporal resolution, has been proposed by Lee et al. 2012. It combines line-scanning with WF detection and was particularly designed for single-molecule imaging in living samples.

Alternatively, the proposed online calibration method can also be applied to conceptionally different imaging configurations. LSFM seems to be the most promising technique (Rebollo et al. 2014, Ritter et al. 2010). It achieves the required axial sectioning by excitation of a thin layer within the sample using laser light that is projected perpendicular into the objective. Therefore, light efficient WF detection, that is compatible with the online calibration method, can be used. Another technique that achieves penetration depths up to several 100 µm and is well compatible with living cells is 2PM. Since Ragan et al. 2006 showed that optical aberrations can be introduced in order to obtain an astigmatism, the online calibration method should also be applicable to 2PM. Last but not least, it can be expected that application of the online calibration method is also reasonable for standard WF imaging in primary cultures. This assumption is justified by the results of Deng and Shaevitz 2009 and Huang et al. 2008a who illustrated that the influence of the RIM is already clearly recognizable at the very first micrometers when imaging into aqueous solutions.

Concerning the intentionally introduced astigmatism, AO should be employed (Izeddin et al. 2012a). This is likely to improve the performance of the online calibration since artifacts of the astigmatism, such as have been experienced with cylindrical lenses, can be avoided.

---

13 The GUI was designed and implemented by Magnus Hanses.
14 http://www.andor.com/microscopy-systems/revolution/borealis

From an algorithmic point of view, further improvements were already discussed in Sect. 4.10.1.8. The vertex estimation procedure has turned out to be the most promising starting point since the whole calibration procedure draws on the correct detection of vertex frames. Possible improvements are the involvement of a larger temporal neighborhood of images, inclusion of the peak intensity as a feature or statistical outlier detection.

The presented EM algorithm itself seems to have great potential for much broader application. Although evaluation of the EM implementation yielded promising results also for particle distances of just one pixel, the proposed workflow has not yet taken advantage of this capability. Instead, a few simplifications have been made. The most important simplification concerned the particle detection. In order to maintain the highest shape estimation accuracy for the subsequent online calibration method, it was limited to particles that are at least 3 pixels apart.

To allow for the extraction of large statistics (Sibarita 2014), advanced approaches like that of Huang et al. 2011, Holden et al. 2011 or Quan et al. 2011 should be included in the workflow. They try to iteratively estimate the correct number of neighboring particles. Although they still suffer from the risk of overfitting, such strategies should improve the final 3D linking procedure and simplify the determination of superimposed particles that may still be wanted to be removed for the sake of fitting accuracy.

The EM implementation could then be considered as an alternative fitting procedure for super-resolution techniques like PALM and STORM. Its ability to deal with truncated distributions is of particular advantage since the fitting becomes less sensitive to the selected region size, and determination of closed sets of superimposed particles can be avoided. Also its robustness to high number of particles is advantageous. Still, its performance in comparison to MLH algorithms, that use the Newton-Raphson method (Huang et al. 2011) or a rather proprietary optimization scheme (Babcock et al. 2012), remains to be assessed in detail.

In order to meet the runtime requirements of super-resolution techniques, the algorithm can be accelerated in the following ways: the number of iterations t_{iter} could be adjusted dynamically by terminating the EM algorithm once the improvement of the expected complete data log-likelihood per EM step falls below a certain threshold (Chen and Gupta 2010). Fewer iterations may be required by cascading of a standard with the presented more complex EM implementation that can deal with truncated distributions (Cadez et al. 2002). Convergence of the EM algorithm can be accelerated by implementing the new class of iterative schemes proposed by Varadhan and Roland 2008. The EM algorithms can also be parallelized for implementation on fast graphics processing units (GPUs) (Kumar et al. 2009).

Last but not least, it shall be stated that although the development of the proposed workflow was driven by the requirements in neurobiology, it is applicable to the more general field of cell biology.

DETECTION OF INDIVIDUAL SYNAPTIC ACTIVITY

This chapter covers the detection of individual synaptic signalling events. The detection of neuronal activity allows to quantify how the interaction of signalling molecules modulates synaptic transmission. This thesis focuses on the first half of the transmission process. Optical methods that translate the alteration of intracellular parameters into changes of optical signals are preferably employed. A pH-sensitive variant of GFP (pHluorin) is used as the optical reporter. It can be used to change its fluorescence in correlation to presynaptic vesicle fusion.

The major objective is the automatic detection of spontaneous individual synaptic activity. It should be noted that spontaneous activity is not to be confused with the spontaneous fusion of vesicles without signaling by an AP (Vardjan et al. 2007, Groemer and Klingauf 2007). Here, spontaneous activity is defined to comprise all individual vesicle fusion events whether triggered by an AP or not. The term spontaneous is used to distinguish these events from those artificially evoked.

Since the signals represent stochastic neuronal processes, the method cannot rely on a single pre-defined shape to detect such complex and variable signals. Moreover, it has to be robust to varying signal strengths and SNRs since all synapses in the field of view shall be analyzed. Strong variations in the intensity response are typical for this type of data owing to: off-focus synapses, non-planar light transmission of objective lenses, variations in the number of fused vesicles per AP, and different expression levels of pHluorin across transfected neurons.

The available readout from pHluorin data and the corresponding state-of-the-art methods are reviewed before the actual workflow is presented.

5.1 OPTICAL REPORTERS FOR STUDYING NEURONAL ACTIVITY

The standard methods for analysis of neuronal signaling stem from experimental electrophysiology. Here patch-clamp or multi-electrode array recordings rely on electrodes that directly measure the electrical signals during neuronal communication (Scanziani and Häusser 2009). Notwithstanding their extremely high SNR and temporal resolution, the major drawbacks of these techniques are the necessities to physically contact the samples and their low spatial resolution.

Owing to the nanometer-sized structures of chemical synapses, optical methods based on FM are therefore preferable for the analysis of individual synaptic activity. They employ optical reporters, which translate dynamic intracellular parameters into optical signals. They allow for specific determination of intracellular parameters at various sub-cellular compartments simultaneously, but do not interfere with the neuronal function (Scanziani and Häusser 2009).

Voltage-sensitive optical reporters are the direct equivalent to electrophysiology. They can be generally divided into fast- and slow-responding fluorophores, whereas only the fast-responding reporters are suitable for detecting short-term APs (Cox 2007). These fluorophores have to be incorporated into the neuronal membrane, where they

change their electronic structure and therewith also their fluorescence as a function of the reversing polarity of the membrane potential during neuronal signal transmission (Sjulson and Miesenböck 2007). Their major weakness are the low magnitude of voltage-dependent change in fluorescence ($\sim$ 10 % per 100 mV) (Cox 2007) and the spatial resolution limited to individual neurons (Sjulson and Miesenböck 2007).

A rather indirect reporter for neuronal activity are organic calcium-sensitive fluorophores (Grynkiewicz et al. 1985) since they determine changes in the Ca^{2+} concentration that are triggered by APs. They respond to varying Ca^{2+} concentrations not only with changes in fluorescence, but also in excitation or emission wavelength, which allows for ratiometric measurements and consequently high SNRs (Tsien et al. 2006). Since Ca^{2+}-sensitive fluorophores are usually employed to diffuse in the cytoplasm of the neuron, it is possible to simultaneously determine activity at individual neuronal compartments. However, identification of varying Ca^{2+} concentration does not necessarily mean that presynaptic neurotransmitter release did indeed occur.

Therefore, methods that directly report about presynaptic vesicle dynamics have been developed. Kraszewski et al. 1995 proposed monitoring neuronal activity by live staining of active synapses. The sample is incubated with fluorophores conjugated to antibodies that can attach to the inner domain of the vesicle protein synaptotagmin. Upon endocytosis these antibodies are uploaded into vesicles, and the amount of fluorescence per synapse is an indirect measure to quantify individual synaptic activity. The weaknesses of this approach are its low temporal resolution in the range of minutes and the difficulty to quantify absolute intensities owing to optical aberrations.

The most direct method uses a pH-sensitive variant of GFP (pHluorin) that is coupled to the inner domain of synaptic vesicle proteins by transfection (Miesenböck et al. 1998). This allows for monitoring of exocytosis and endocytosis since pHluorins change their fluorescence during vesicle cycling owing to the pH gradient between the inside of vesicles and the extracellular space (Miesenböck and Kevrekidis 2005). The resulting intensity signal characterizes the kinetics of the vesicle cycle during synaptic signal transmission. Fig. 77 illustrates the vesicle cycle, the principle of measuring presynaptic activity with pHluorins, and the resulting signal. Since this method features high temporal resolution and allows for identification of individual presynaptic activity with high sensitivity, it is employed in this thesis.

To date this method has primarily been used to characterize the vesicle cycle and to estimate biophysical parameters that modulate the presynaptic vesicle fusion efficiency. The next section highlights important findings with focus on their support for automatic activity detection.

5.2 CHARACTERIZING THE READOUT OF PHLUORIN-BASED MEASUREMENTS

The types of biological parameters that can be accessed via pHluorins are manifold and have been obtained using different vesicle proteins as reporters. Such optical measurements have already allowed to determine the necessary quantity of certain presynaptic molecules for successful vesicle fusion (Sinha et al. 2011) and preferred release sites at very active synapses have been observed (Gaffield et al. 2009, Tabares et al. 2007). It was determined that the sorting of proteins into vesicles is not random (Kim and Ryan 2009, Balaji and Ryan 2007), and that the absolute size of the vesicle pools is limited by the speed of endocytosis (Ariel and Ryan 2010, Granseth and Lagnado 2008). Also,
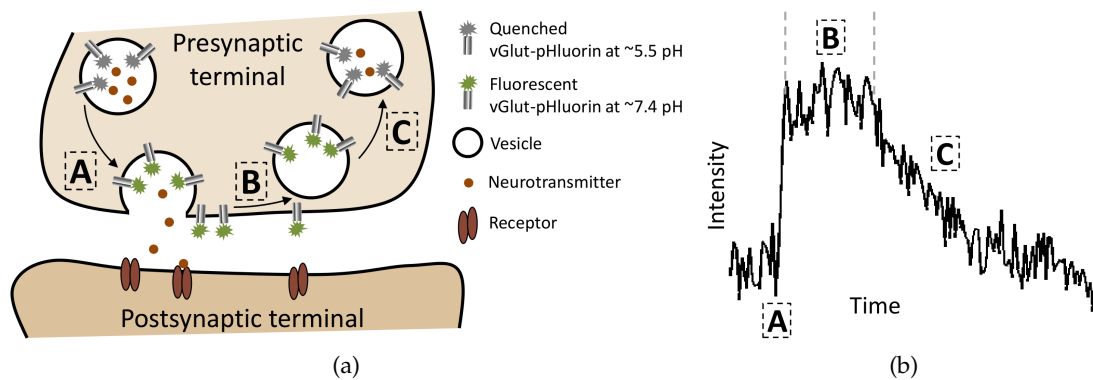
Figure 77: (a) The vesicle cycle at chemical synapses during synaptic signal transmission. At the low pH inside vesicles pHluorins are quenched and thus hardly fluorescent. Upon vesicle fusion with the presynaptic membrane pHluorins undergo a conformational change owing to the more alkaline pH of the extracellular space. Consequently, their fluorescence increases (A). At the onset of endocytosis vesicles get recycled (B) and reacidify (C), thus, pHluorins get quenched again. (b) The resulting intensity signal is characterized by an immediate increase of intensity (A), followed by a dwell time for endocytosis where it remains constant (B), and an intensity decay owing to vesicle reacidification (C).

pHluorin experiments are used for the ongoing discussion whether different modes of synaptic vesicle recycling exist (Granseth et al. 2009, Zhang et al. 2009, Gandhi and Stevens 2003).

In order to automate the derivation of these biological parameters, detailed knowledge about the time course of the intensity response to be detected is of utmost importance. In the remainder of this section the main features of the peak's shape are summarized.

To obtain the individual synaptic intensity signal, the mean intensity within a fixed region centered over each synapse is computed for each point in time. Independently of the chosen reporter protein, the kinetics of the vesicle cycle result in a signal of the general form exemplarily depicted and described in Fig. 77b.

The intensity difference between the fluorescent and the quenched state of pHluorin is $\sim$ 20-fold (Sankaranarayanan et al. 2000). As a result of the conformational change, it switches in an all-or-none fashion (Sankaranarayanan et al. 2000) with a switching time well below 10 ms (Ariel and Ryan 2010). Using video frame rates, exocytosis is characterized by an immediate increase of intensity between two consecutive images (see Fig. 77b). According to Granseth et al. 2006, the averaged signal decay is best described by two consecutive first-order kinetics (see Fig. 78a). These correspond to the particles dwell time for endocytosis at the surface and the time until reacidification of the vesicles. These processes have a mean lifetime of $\sim$ 14-15 s and $\sim$ 4-5 s, respectively. The results were independently verified by Balaji and Ryan 2007 and Atluri and Ryan 2006, whereby Balaji and Ryan 2007 even analyzed individual events. The maximum velocity of vesicle recycling is limited to one vesicle per second (Sankaranarayanan and Ryan 2000), and the average dwell time may vary across cells, but is kept constant for individual synapses (Armbruster and Ryan 2011). Some exemplary signals with individual dwell times and the histogram distribution of individual dwell times are

presented in Fig. 78b and 78c, respectively. Apparently, the intensity remains constant during the dwell time and decays rapidly during reacidification.
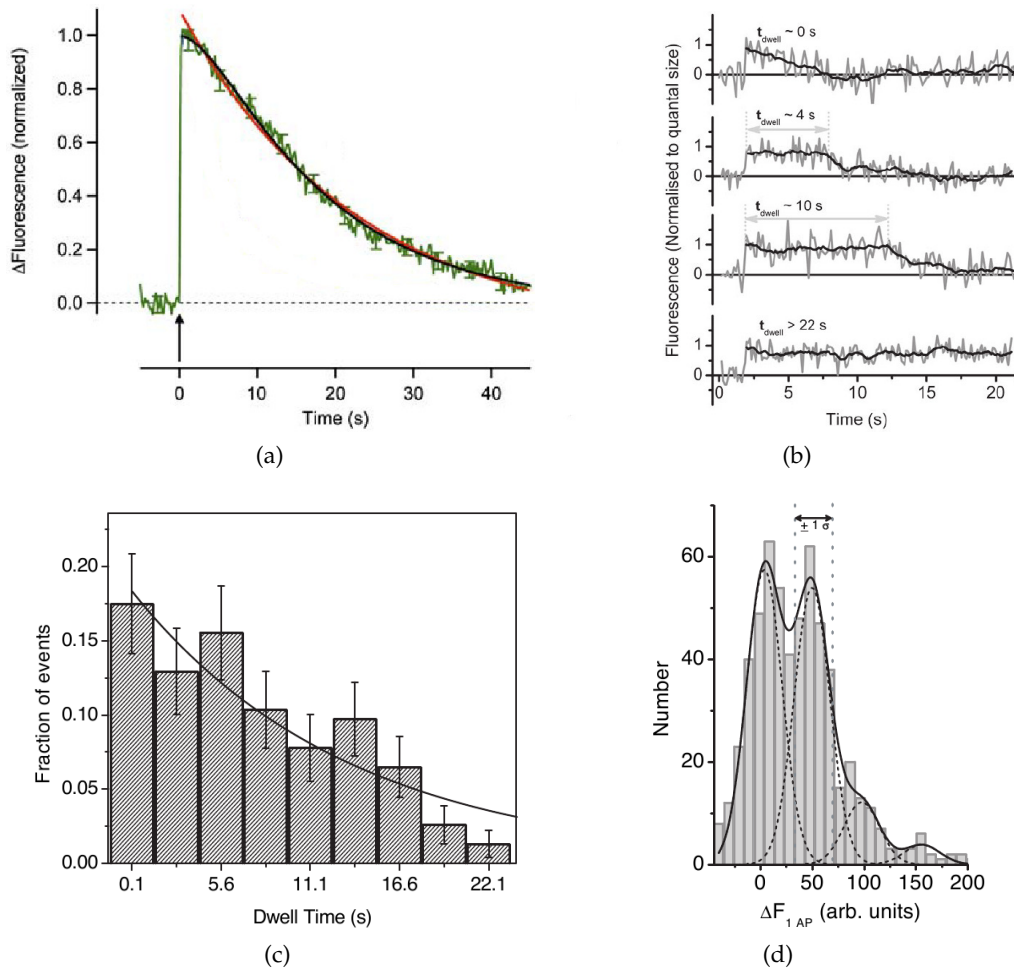

Figure 78: (a) The average signal decay can be described with a single (red) or, more exactly, with two consecutive first-order kinetics (black). (Adapted from Granseth et al. 2006, with permission from Elsevier.) (b) Individual measured signals with varying dwell times. (c) Distribution of individual dwell times. (d) Quantized intensity distribution of intensity responses. ((b)-(d) are reprinted from Balaji and Ryan 2007, copyright (2007) National Academy of Sciences, USA.)

The signal is transient and always decays to the baseline. This baseline is defined by a remaining surface population of diffusive vesicle proteins created most likely due to inefficiencies in the recycling process (Sankaranarayanan et al. 2000). Given the diffusive fluctuations of these surface proteins, they are an important factor for the available SNR. The intensity response to single APs must therefore be computed on exocytosis relative to the baseline. Analysis of intensity responses by Balaji and Ryan 2007 and Gandhi and Stevens 2003 revealed quantized intensity distributions (see Fig. 78d). The homogeneously distributed peaks correspond to the number of fused vesicles per AP, and it was shown that the number of proteins per vesicle is kept constant.

Since specific peak detection algorithms for the present data have not been developed yet, the next section generalizes the problem and provides a survey on peak detection algorithms in one-dimensional (1D) data.

5.3 RELATED WORK ON PEAK DETECTION IN 1D SIGNALS

In their majority, recent peak detection algorithms are specialized for some particular type of data. Considering pHluorin signals, the most closely related signal types, which have also received major attention, are electrophysiological recordings of APs and mass spectrometry data. The algorithms reviewed in this section were usually developed for either of these types of data.

Peak detection in 1D signals is challenging since measurements are subject to noise, distorted by unspecific background, and usually lack unique discriminating features owing to the low dimensionality as well as the spectral similarity of the signal and the background (Kim and Kim 2003).

5.3.1 *Threshold-based Methods*

The most basic, but still most widely used method is AT. Thresholds are either provided manually or using a factor for the expected noise yielding an adaptive threshold. For the latter, the automatic estimation of the noise component is the major concern. Noise estimates can be obtained using the SD (Pouzat et al. 2002) or, in order to reduce the dependency on the strength and the number of peaks in the data (Watkins et al. 2004), based on the median absolute deviation (Coombes et al. 2005, Quiroga et al. 2004). Thakur et al. 2007 also proposed fitting a Gaussian function to the central part of the histogram distribution in a so called "cap-fitting" procedure. To further improve robustness, these estimates can be computed using a running window (Biffi et al. 2010, Chan et al. 2008). However, regardless of how well the threshold is selected AT scales poorly towards low SNR (Shahid et al. 2010).

In order to consider that peaks usually distribute over several measurements, power detection methods have been developed. Bankman et al. 1993 apply a cumulative energy operator that computes the integral over the squared signal in a running window before thresholding. On this basis Mtetwa and Smith 2006 later proposed to use the normalized cumulative energy. By utilizing that at peak positions the power as well as the frequency increase, Kim and Kim 2000 employed a nonlinear energy operator that computes the product of the amplitude and frequency. Since these methods do not explicitly exclude noise, they also rapidly deteriorate for low SNR.

5.3.2 *Template Matching Methods*

Template matching methods yield better performance since they explicitly include knowledge about the expected shape of the peak, instead of just incorporating their length. They compute the similarity of a given shape with the signal at different positions (Jain et al. 2000). Reasonable similarity measures are for instance the sum of absolute (Jansen and Maat 1992) respectively squared differences (Mtetwa and Smith 2006) or cross-correlation (Kaneko et al. 1999). If the noise can be statistically described,

then probabilistic methods from the classical detection theory are another alternative (Kay 1993). They estimate whether a peak shape is present or not at a certain position using hypothesis testing on the assumption of an additive noise model. Although template matching methods are simple, but yet efficient, their major weaknesses are the necessity to have prior knowledge about the peak shape, and that the performance decreases if the peaks significantly vary in shape or size.

Since prior peak shape information may not always be available or obtainable without supervision, Shahid et al. 2010 proposed to estimate an optimal template directly from the acquired data in a blind equalization technique. For that reason, they employ the cepstrum of bispectrum, which is an higher order statistic technique to estimate an inverse filter. The obtained filter is subsequently used for deconvolution with the signal. A denoising and thresholding procedure is applied to detect the peaks. In order to reduce the weakness of extracting only an average filter that is usually suboptimal, Natora and Obermayer 2011 extended this approach by classifying the extracted filters and computation of individual filters for each class. This way, they are able to detect a larger variation of peak shapes.

5.3.3 Wavelet-based Methods

Assuming that at least basic peak shape features are preserved over all peaks, algorithms that employ the wavelet transform are another alternative to account for variation in the shape. The wavelet transform projects the signal $s(t)$ onto the wavelet basis $\psi_{a,b}(t)$ (Mallat 2008):

$$C(a, b) = \int_{\mathbb{R}} s(t)\psi_{a,b}(t)dt, \tag{67}$$

where $\psi_{a,b}(t)$ are shifted and scaled versions of a mother wavelet $\psi(t)$:

$$\psi_{a,b}(t) = \frac{1}{\sqrt{a}}\psi\left(\frac{t-b}{a}\right) \quad a, b \in \mathbb{R}, \ a > 0. \tag{68}$$

The wavelet coefficients C then determine the similarity between the signal and the mother wavelet at different scales a and translations b. A high value at $C(a, b)$ indicates a close match with the signal at the given scale and position. If a wavelet that resembles basic peak shape features is available, analysis of the wavelet coefficients can be considered as template matching with varying shape sizes.

Most wavelet-based algorithms implement a detection framework consisting of three subsequent steps: (1) decomposition of the signal using an appropriate mother wavelet selected by visual inspection, (2) separation of the signal from noise via thresholding the wavelet coefficients to increase the effective SNR, and (3) detection of peaks across multiple scales.

Recent algorithms mainly differ in the implementation of the last step. It is of utmost importance since significant signal structures propagate across scales (Mallat and Zhong 1992), and consideration of this effect is the key to further increase the effective SNR. Nakatani et al. 2001 only accept peak positions where the wavelet coefficient at a certain scale as well as the coefficients at the neighboring scales exceed a given threshold. The threshold for the neighboring scales may be 10 % lower. Kim and Kim 2003 extended this approach by computation of the point-wise product over three con-

secutive dyadic scales and thresholding in the combined coefficients. The selection of the three scales is driven by biophysical properties of the expected peak shape. Since this may limit the possible shape variation of the peaks, Du et al. 2006 employed every second scale until a maximum scale derived from the broadest expected peak shape. Their algorithm is motivated by visual inspection of the wavelet coeffcient image where peaks appear as so called ridge lines. These lines are detected by tracing local maxima in the coefficients across scales. A ridge line then indicates a peak if it fullfils a length and a SNR criterion.

Alternatively, probabilistic methods can be employed to detect peaks in the wavelet coefficients. Nenadic and Burdick 2005 perform statistical hypothesis testing for each coefficient to detect whether it belongs to noise or signal. They expect the noise to be Gaussian distributed, and an acceptance threshold has to be defined. Indications at multiple scales are finally combined to a single peak indication using a distance criterion. In so doing, they do not increase the likelihood for correct peak detection using multiple scales because peak indications at different scales are simply merged. Benitez and Nenadic 2008 rely only on two selected scales derived from biophysical properties of the signal. They analyzed the correlation between the two coefficients at each transition, and determined that noise coefficients can be described by a Gaussian mixture model in the 2D plot of the coefficients. If also signal is present, they propose a combination of the Gaussian mixture with an uniform distribution that describes the peak coefficients. Both models are fit using an EM algorithm that treats the assignment of the pairs of coefficients to the distributions as the missing observation. The model yielding the best fit is then selected to classify the coefficients as peak or noise, and several peak indications are again merged according to some distance criterion.

Evaluation

The presented peak detection approaches were mainly individually evaluated based on the specific data available to the authors. Therefore, the algorithms are highly specific, which prevents a general assessment of their performance. A comprehensive study is currently not available and would indeed be difficult given the very different types of data the algorithms are designed for. Still, there is a comparatively old review on spike detection in electrophysiology data (Wilson and Emerson 2002). The authors confine themselves to comparing algorithms according to the statements in the corresponding publications. A separate experimental evaluation is not conducted. Yang et al. 2009 apply recent algorithms to simulated and real mass spectrometry data. They conclude that wavelet-based peak detection methods are most appropriate owing to the consideration of multiple scales.

5.3.4   *Implications for the Thesis*

Vesicle fusion events appear with certain well defined shape features in the signal, but owing to the stochastic distribution of the fluorophores' dwell time at the presynaptic surface their time scale varies across events. This variability in scale, while preserving basic peak shape features, is well addressed by the wavelet transform. This renders it the preferred tool for the present peak detection task.

In order to reliably detect peaks in the signal, the mother wavelet must match the basic peak shape. Current methods are successful since adequate wavelets for electrophysiological or mass spectrometry data are available. However, the major wavelet families provide no wavelet that supports all shape features of synaptic vesicle fusion events in pHluorin data at the same time. Therefore, current approaches need to be extended for the present application.

A new method that employs multiple wavelets for combined matching of individual peak features will be presented in the following. Combination of multiple wavelets intends to make complex shapes detectable that are currently not addressable. At the same time it maintains the advantages of wavelet-based approaches to effectively separate signal from noise and to adjust to variation in the scale.

5.4 SYNAPTIC ACTIVITY DETECTION USING MULTIPLE WAVELETS

A wavelet transform-based detection method is proposed for the detection of synaptic vesicle fusion events in pHluorin intensity measurements since the peak shapes exhibit certain well defined features, but owing to the stochastic timing of the vesicle cycle they are subject to a large variability in scale.

As opposed to other peak detection algorithms that propose to use a single, but in the current case then suboptimal wavelet, the key idea of the present approach is the usage of multiple different wavelets that match individual peak features separately[1]. Their individual peak indications are then fused after processing the wavelet coefficients. This procedure may be interpreted as construction of more complex peak shapes from simple wavelets. The proposed method will be referred to as the multiple wavelet algorithm (MWA).

This section presents the entire detection procedure covering (1) the localization of synapses, (2) the computation of the intensity signals, and (3) the detailed description of the actual MWA. The presented workflow has originally been published in Sokoll et al. 2012b.

5.4.1 *Localization of Synapses*

The basis for synaptic activity detection are 2D time lapse images of pHluorins as well as of a red fluorescent protein attached to synapsin. The detection procedure is then as follows:

---

[1] This is not to be confused with multiwavelets (Keinert 2004), which are a generalization of the wavelet theory to gain mathematical properties that are otherwise mutually exclusive.

Data : Image streams of pHluorin and synapsin

Result : Synapse locations

Compute mean projection for the individual image streams;

for *both projections* **do**

> Convolve the image with a LoG filter;
> Segment image using a global threshold t_p;
> Compute watershed transformation;
> Use watershed lines to separate interconnected synaptic regions;
> Compute region centers from minimum values;
>
> **for** *each synapse candidate* **do**
>
> > Fit elliptical Gaussian function;
> > Validate fit results;
>
> **end**

end

Select synapses that are double positive for pHluorin and synapsin;

In order to locate individual synapses, all images are projected into a single image by computation of the mean intensity value at each pixel position. The mean projection is advantageous since it acts like a smoothing operation over time and reduces the likelihood for detection of non-synaptic locations, due to diffusive surface proteins. To further increase the likelihood of detecting true synapses, every culture is co-transfected with a red fluorescent protein attached to synapsin. Synapsin is a protein that accumulates in synapses and is commonly used as a synaptic marker (Evergren et al. 2007). Additional time lapse images of that fluorophore at exactly the same region are acquired, and only synapses that are double positive for pHluorin and synapsin are selected. Co-transfection increases the biological reliability of the detection and provides additional information about the ratio of active and silent synapses.

Synapses appear as elliptic spots in both images and have to be determined automatically. This is a classical spot detection task, and the corresponding algorithms were already discussed in Sect. 4.3.2. The proposed algorithm for particle detection is again employed. Since synapses are usually larger than the PSF of the microscope, the kernel size and the SD of the LoG filter would have to be adapted. Considering the present setup (see Sect. 5.5.1), the same parametrization can be used since the camera pixel size here corresponds to a larger range in the object space. The user-defined threshold factor k can again be set to 8, but owing to the temporal smoothing, estimation of the background noise using the median absolute deviation results in extremely low values δ_b. Therefore, δ_b must be estimated based on the original images before averaging.

In order to minimize the amount of unspecific detections or superimpositions of multiple synapses, the size of each detected spot is taken as an indirect argument (Kubitscheck et al. 2000). For it, 2D elliptical Gaussian functions of the form:

$$G(x,y) = o_b + h \cdot e^{-\left(a(x-x_c)^2 + 2b(x-x_c)(y-y_c) + c(y-y_c)^2\right)}, \tag{69}$$

where

$$a = \frac{\cos^2\theta}{2\sigma_x^2} + \frac{\sin^2\theta}{2\sigma_y^2}, \ b = \frac{\sin 2\theta}{4\sigma_x^2} + \frac{\sin 2\theta}{4\sigma_y^2}, \ c = \frac{\sin^2\theta}{2\sigma_x^2} + \frac{\cos^2\theta}{2\sigma_y^2} \tag{70}$$

are fitted to each synaptic candidate. Since synaptic shapes do not align with the image grid, θ is introduced to define the rotation angle of the Gaussian function. Equ. 69 is fitted using weighted LSQ. This is reasonable since a corresponding closed-form solution for the EM algorithm is not available, and owing to the temporal averaging the Poisson noise assumption is not valid anymore.

Because an approximate size estimate is sufficient, the fit is performed on a support region simply restricted by the watershed lines around each synaptic candidate. The individual FWHMs are subsequently used to constrain the size of detected synapses. Only synapses that have a size of 0.56-6 µm are selected for further analysis. The lower bound corresponds to the actual PSF measured using immobilized 30 nm diameter fluorescent beads that had the same emission wavelength than pHluorin. The upper bound was empirically established. Its relatively high value reflects the fact that synaptic spots may appear expanded owing to the diffusion of surface pHluorins and the averaging operation over a long time period.

5.4.2 *Computation of the Intensity Signals*

Based on the locations of synapses, their intensity responses for each point in time are then computed as follows:

> **Data** : Synapse locations and pHluorin image stream
> **Result** : Intensity signals
> **for** *each image* **do**
> **for** *each synapse* **do**
>   Take intersection of watershed and fixed region;
>   Compute mean intensity value;
> **end**
> **end**

The intensity responses for each point in time correspond to the mean intensities within individual regions. The fixed region for each synapse is computed from the intersection of the corresponding watershed region and a circular region centered over each synapse (see Fig. 79a). The center pixels are taken from the Gaussian fits. The region must be as small as possible to optimize the SNR of the signal, but large enough to contain the site of exocytosis and endocytosis so that the true kinetics of the vesicle cycle are detected (Royle et al. 2008). For the present experimental data (see Sect. 5.5.1) both requirements are robustly fulfilled by taking a diameter of three times the size of the PSF. This corresponds to ∼ 1.68 µm in the object space. This value was found empirically by analyzing the respective SNRs of the signal and corresponds well to the region sizes reported in the literature (Balaji and Ryan 2007, Granseth et al. 2006). In conjunction with the watershed region, this region selection then presents a compromise for small and large synapses since it also accounts for the actual size of each synapse. The intensity responses of neighboring synapses are well separated.

Alternative to taking static regions, the intensity signal could also be computed using the peak intensity of elliptical Gaussian fits at each individual point in time. This would have the advantage of maintaining the optimal center position at each time point and was also implemented. However, given the working memory-limited acquisition times

(a)

(b)
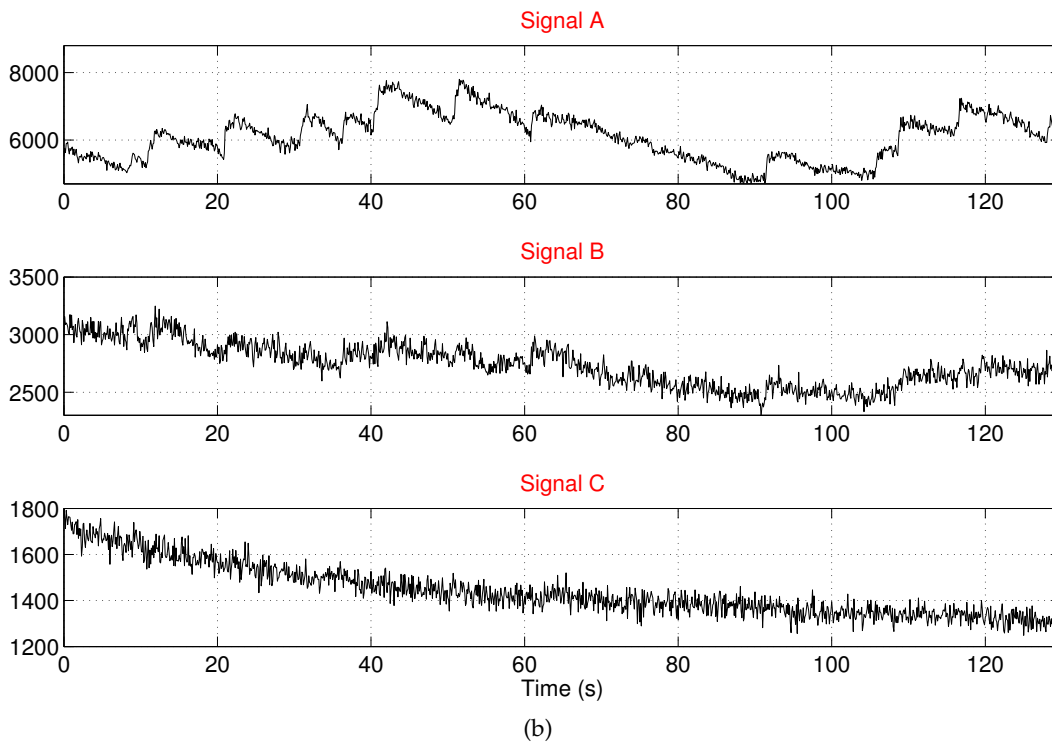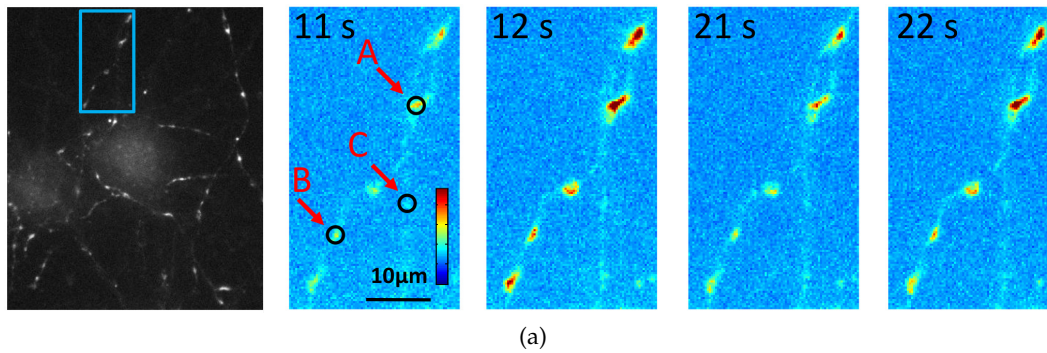
Figure 79: (a) Presentation of pHluorin image data by means of false color images. The circles indicate regions where the vesicle kinetics are analyzed. (b) Corresponding computed intensity signals that illustrate the variation in signal quality and peak shapes.

of only very few minutes, the sample drift was found to be negligible. In addition, the SNRs of the signals are lessened by $\sim$ 15 %. This considerable reduction probably stems from the mobility of vesicle proteins after exocytosis (Royle et al. 2008), which is why even the usage of the proposed most general Gaussian shape is not optimal.

Therefore, static regions are preferable, but it has to be kept in mind that particularly the maximum region size has to be adjusted according to the employed vesicle protein. As it was pointed out by Granseth et al. 2006, if selecting reporter proteins with high numbers per vesicle, the region size has to be enlarged in order to avoid measuring too fast decays owing to the lateral movement of the reporters out of the region.

Fig. 79b presents exemplary signals obtained using such static regions. As expected for imaging over a large field of view, the SNR and baseline intensity between individual synapses are subject to strong variation. It is already visually noticeable that signal A and B have their peaks at identical positions, but signal A has a higher SNR than

161

signal B. Also, the individual dwell times are highly variable. They depend on the rate of endocytosis, which in turn dependent on the activity of synapses and if more than one vesicle is fused (Gandhi and Stevens 2003, Sankaranarayanan and Ryan 2000). This is particularly noticeable for the clearly visible peaks in signal A. Signal C represents a silent synapse whose intensity just decreases as a result of photobleaching.

5.4.3 *The Multiple Wavelet Algorithm*

This section describes the core of the multiple wavelet peak detection algorithm. Recalling the peak description in Sect. 5.2, the immediate increase of signal intensity, the variation in the dwell time, and the subsequent intensity decay are found to be the characterizing peak shape features. However, there exists no single wavelet that closely resembles this peak shape.

In order to avoid the application of a single suboptimal wavelet, the peak shape is approximated by different wavelets that match separate features. By visual inspection it was found that a combination of the Haar and the Bior3.1 wavelet is capable of describing the major peak shape characteristics. This is illustrated in Fig. 80. The Haar wavelet detects the step response of the intensity in a small support region, and the Bior3.1 wavelet adjusts to the varying dwell time limited by the local discontinuities at the intensity increase and the onset of the decay.


(a)   (b)
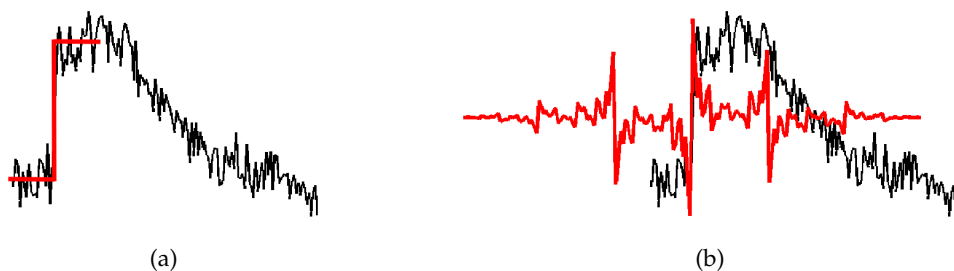
Figure 80: Illustration of the use of the (a) Haar and the (b) Bior3.1 wavelet. The decomposing wavelet functions ψ are presented in red and an almost ideal intensity response in black. The wavelets are mirrored at the x axis for illustration.

The actual peak detection method MWA comprises six steps:

Data : Intensity signals
Result : Peak positions
for *each signal* **do**
    for *each wavelet* **do**
        (I) Signal projection into the wavelet space;
        (II) Selection of relevant coefficients;
        (III) Combination of coefficients;
    end
    (IV) Fusion of multi wavelet information;
    (V) Bartlett window smoothing;
    (VI) Thresholding;
end

They are illustrated in Fig. 81 on the example of a section from signal B in Fig. 79b and are now explained in detail.
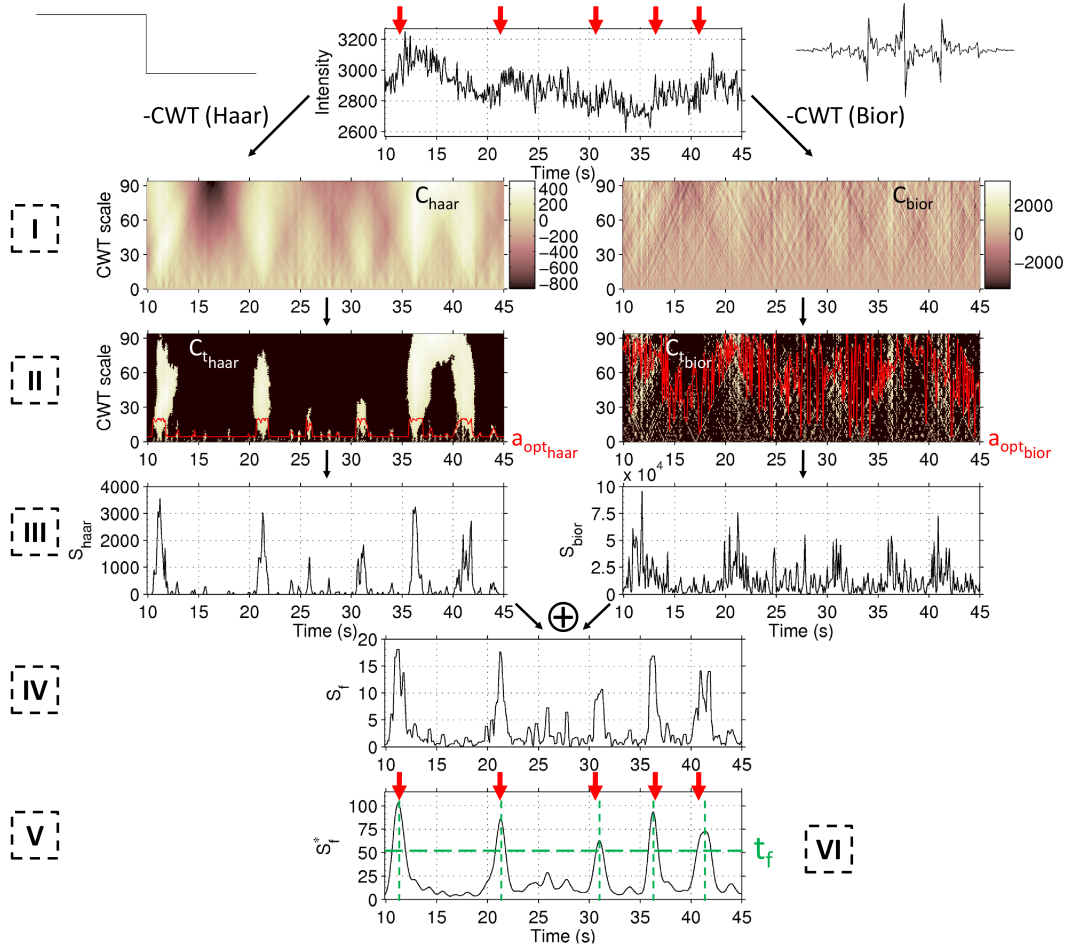

Figure 81: Illustration of the six steps of MWA. The true peak positions are indicated by the red arrows and were taken from the well observable peaks in signal A. The dashed green lines indicate the final threshold t_f as well as the found peak positions.

IN STEP I   the signal is projected onto two individual wavelet bases defined by the Haar and Bior3.1 mother wavelets. This results in the separate wavelet coefficients C_{haar} and C_{bior}. To avoid boundary artifacts, the signal is extrapolated at both sides using a preceding second-order polynomial fit.

The discrete wavelet transform (DWT) as well as the continuous wavelet transform (CWT) are available for transformation. The DWT operates on dyadic and the CWT on continuous scales and transitions. There are very efficient implementations for the DWT (Mallat 1989), but it has the undesirable property of being translational invariant. This means that even small shifts in the signal will lead to large changes in the wavelet coefficients (Mallat 2008), and this in turn will result in the fact that the detectability of a peak depends on its position in the signal (Benitez and Nenadic 2008). Since the CWT also allows to maintain the maximum resolution in scale and transition, it is the preferred transformation algorithm for the present application.

The individual transformations are directly applied to the raw signals without prior noise reduction or baseline removal. Although numerous preprocessing techniques exist and comprehensive reviews are provided by Komsta 2011 and Yang et al. 2009, they have been deliberately omitted in Sect. 5.3. This was due to the fact that state-of-the-art peak detection methods mainly consider them inherent and avoid explicit preceding procedures.

For the present application, the fitting of a double exponential decay function and its subsequent subtraction from the signal has been proposed by Royle et al. 2008. It was found here that this procedure is inadequate for synapses with high activity patterns. A practical alternative to computational baseline correction is intentional photobleaching of the initial surface population prior to the image acquisition. This is acceptable since pHluorins cannot be photobleached while being quenched (Gandhi and Stevens 2003). Such procedures are only necessary for the usage of reporter proteins with large surface populations. For the recently developed reporter employed in this study (Voglmaier et al. 2006), photobleaching was noticeable, but not very pronounced. It was also found that the existing photobleaching has no effect on the outcome of the algorithm, which is likely since its impact is minor over the peak support region. Consequently, baseline removal was omitted in order to avoid the introduction of additional parameters.

One of the major attractions of the wavelet transformation is the ability to separate a signal from noise by thresholding in the wavelet coefficients. It is an implicit part of the next step.

STEP II   selects the most significant coefficients. This is a crucial task since it mainly affects the effective SNR. The hard thresholding strategy proposed for wavelet denoising by Olivo-Marin 2002 is applied to all coefficients:

$$
C_t(a,b) = \begin{cases} C(a,b) & \text{if } C(a,b) \geqslant t_a \\ 0 & \text{otherwise} \end{cases}.
\tag{71}
$$

The individual threshold t_a for each scale a is derived from the noise coefficients at that scale. Since they are unknown and bias by true signal peaks must be avoided, a reasonably robust estimate is obtained from the median absolute deviation $\tilde{\sigma}_a$ yielding $t_a = \tilde{\sigma}_a/0.6745$.

Only coefficients at scales that fall within the variation in shape size are selected. This restriction is derived from biophysical properties and the support range of the individual mother wavelets. The lowest included scale for both wavelets was empirically set to $a_{min} = 4$. Because noise and distortions are usually high frequency components they are mainly present at lower scales and would otherwise indicate spurious peaks. The maximum scale $\hat{a}$ is independently defined. Since the Haar wavelet matches a narrow local discontinuity and the minimum time of vesicle recycling is one second (Sankaranarayanan and Ryan 2000), its maximum scale is set to $\hat{a}_{haar} = 20$. This corresponds to a time interval of 2 s for the present data with a sampling rate $f_s = 10$ Hz. The Bior3.1 wavelet covers larger parts of the peak shape corresponding to the dwell time. For an individual signal, the current dwell time is unknown, but follows an exponential distribution with a mean lifetime of $\tau \approx 14$ s (Balaji and Ryan 2007, Granseth et al. 2006). However, because the mean lifetime is defined as the arithmetic mean of

the exponentially decaying values, the majority of events has actually lower individual lifetimes. It is sufficient to set the maximum scale to $\hat{a}_{bior} = 94 \approx (2\tau f_s)/r_{bior}$, where r_{bior} is the support range of the Bior3.1 wavelet.

This selection then covers a relatively large possible time range for the peak shapes. In order to better account for the individual dwell times, the selection also exploits the property that significant signal structures, in contrast to uncorrelated noise, propagate across scales (Mallat and Zhong 1992). It was found that at the location of a peak wavelet coefficients continuously increase over scales until the match is optimal. Therefore, for any point in time all remaining coefficients from a_{min} up to the optimal scale $a_{opt}(b)$, which has the highest coefficient $\hat{c}(b)$, are continuously selected. Therewith the scale selection already aims at estimating from $\hat{c}(b)$ the scale $a_{opt}(b)$ that correlates to the current dwell time of a possible peak.

IN STEP III   the selected coefficients are combined to the individual signal $S(b)$ by summation:

$$S(b) = \sum_{a=1}^{a_{opt}(b)} C_t(a, b). \tag{72}$$

This is similar to computing the ridge lines in the wavelet coefficients (Du et al. 2006) since it also favors continuous scale combinations and tolerates gaps between scales. However, it is computationally much more efficient and requires no additional parameters to be set. In contrast to taking the commonly used product (Kim and Kim 2003, Olivo-Marin 2002), computing the continuous sum is more robust regarding outliers and the efficiency of the previous selection of coefficients. $S_{haar}(b)$ and $S_{bior}(b)$ represent then the individual peak indications of each wavelet.

STEP IV   addresses the fusion of the information from the two wavelets into combined peak indications. In a related application where multiple spectra are combined, Hsueh et al. 2008 proposed the integration of redundant signals by averaging the individual coefficients. Instead of being redundant representations, here, C_{haar} and C_{bior} contain complementary information. In addition, the underlying wavelets have non-identical support regions, and their coefficients cannot be merged. Therefore, information fusion is conducted after combination of the scales when individual peak indications are already available.

The complementary signals $S_{haar}(b)$ and $S_{bior}(b)$ are fused at the feature level by computation of their pointwise weighted sum ($\oplus$) yielding $S_f(b)$. The corresponding two weights are calculated as the inverse of the median of $S_{haar}(b)$ respectively $S_{bior}(b)$, but only non-zero values are included. The median computation selects the noisy baseline of each signal, and the weights normalize the signals so that the baseline is represented by the value one. The summation of the normalized signals can consequently be interpreted as a combined decision on whether there is a peak or not. The probability of a peak indication is increased with respect to its distance to the baseline noise.

A third-order local maximum filter is applied to each signal before fusion in order to account for the fact that the Haar and Bior3.1 wavelet may have a location shift at

the same peak. This also supports alignment of peak indications between the signals. The final data fusion hence becomes:

$$S_f(b) = \frac{S_{haar}}{\tilde{S}_{haar}} \oplus \frac{S_{bior}}{\tilde{S}_{bior}},$$ (73)

where

$$S_{haar} = \max_{b-1 \leqslant b^* \leqslant b+1} S_{haar}(b^*)$$ (74)

and

$$S_{bior} = \max_{b-1 \leqslant b^* \leqslant b+1} S_{bior}(b^*).$$ (75)

IN STEP V $S_f(b)$ is smoothed by convolution with a Bartlett window (Kim and Kim 2003) yielding $S_f^*(b)$. This removes spurious peaks in the vicinity of real peaks as well as plateaus of similar values in $S_f(b)$ that can occur due to the maximum filter operation. The window size was set to 15 and corresponds to the support region of the Bior3.1 wavelet at a_{min} since this wavelet was found to produce the majority of noise artifacts. The smoothed version of $S_f(b)$ can now be used to detect local maxima and compare them to a threshold.

IN STEP VI the threshold t_f is computed using robust statistics. Similar to t_a it computes as $t_f = \tilde{\mu}_{S_f^*} + k_f \tilde{\sigma}_{S_f^*}$, where $\tilde{\mu}$ is the median and $\tilde{\sigma}$ the median absolute deviation. Note that this computation only involves positions in the signal that contain non-zero values.

Provided that the experimental settings remain unchanged, the chosen adaptive thresholding scheme is applicable for all synapses without individual adjustment of k_f.

5.5 EXPERIMENTAL RESULTS

This section evaluates the proposed workflow for automatic detection of vesicle fusion events. This involves assessment of real and semi-synthetic data. For real data, the total workflow is invoked, while for semi-synthetic data only MWA is assessed in detail. First of all the experimental data and the SNR estimation routine are established.

5.5.1 *Experimental pHluorin Data*

For targeting pHluorin, currently about eight different vesicle proteins are accessible (see Fig. 5b). To date, synaptobrevin, synaptotagmin, synaptophysin, and the neurotransmitter transporter vGlut have been employed, and the corresponding surface expressions were summarized by Balaji and Ryan 2007. In order to allow for identification of single vesicle fusion events at individual presynaptic sites, low surface expression is preferred since this directly affects the available SNR and specificity. On these grounds, the construct developed by Voglmaier et al. 2006 that couples pHluorin to vGlut is employed in this work.

The downside of this choice is that the expression level of this construct seemed to be too low to be applicable in brain slices. The fluorescence was hardly detectable.

This is further explained by the low number of vGlut proteins per vesicle, and the fact that autofluorescence, which is much more prominent in packed brain slices, generally appears at the same wavelength as the employed green fluorescent pHluorin (Nienhaus and Nienhaus 2013, Schütz et al. 2000b). In order to establish the algorithm, all experiments have been done with cultured rat hippocampal neurons. Another consequence was that an inverted WF setup was employed because it allowed direct access for electrical stimulation. The constructed setup is presented in Fig. 82.
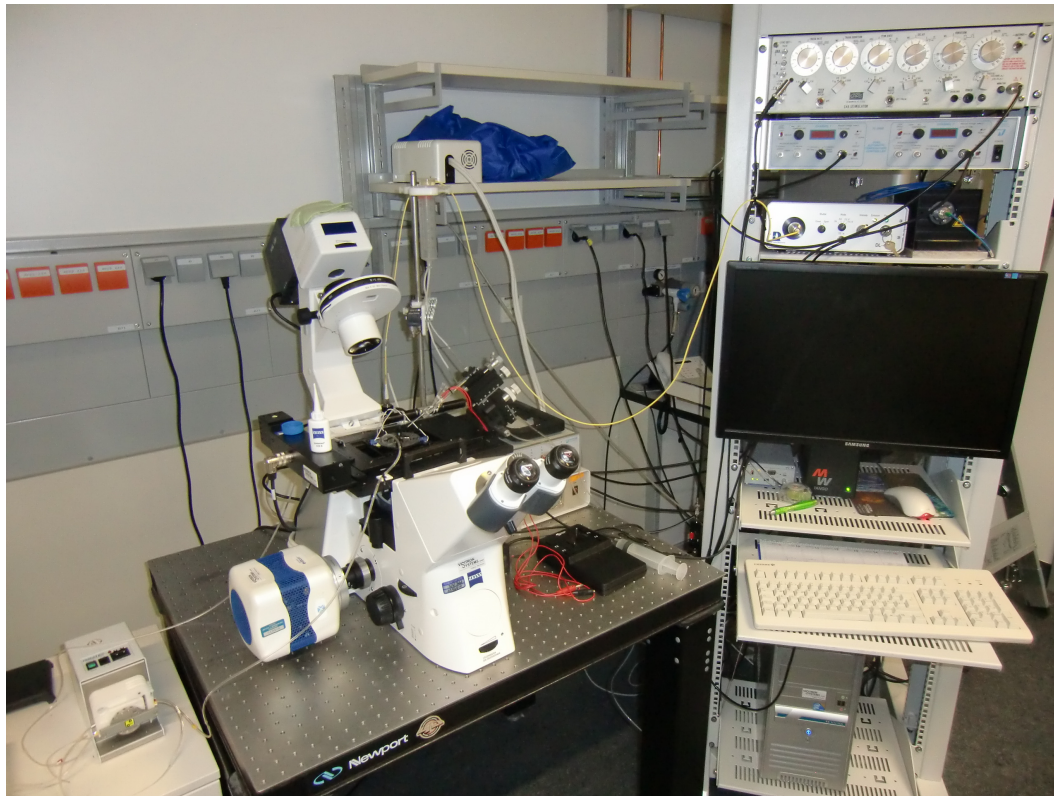
Figure 82: The WF setup that was established by the group Molecular Physiology. The major components are the inverted microscope Zeiss Axio Observer, the EMCCD camera Photometrics Evolve 512, and the light source Sutter Instrument Company LAMBDA DG-4. Electrical stimulation is provided by a manual micro-manipulator at the stage of the microscope in connection with the GRASS S48 stimulator on top of the rack on the right. Extracellular solution is provided by the ISMATEC perfusion device on the left.

Noteworthy is that the setup was equipped with a 63x oil immersion objective[2]. Based on the lower magnification and NA, each camera pixel now corresponds to 254 nm in the object space, and the FWHM of the PSF increased to 560 nm. Although this configuration reduced the available resolution, the SNR of the images appeared to be increased because more photons were now averaged on the same pixel. Since the expression level is quite low and the algorithm averages the intensity at a certain synapse anyway, this seemed to be a more reasonable choice than an objective with larger magnification.

---

2 Zeiss Plan-Apochromat oil immersion objective: 63x magnification, 1.49 NA

The actual recordings were performed with cultures after 14-18 days in vivo. During acquisition, they were perfused with normal extracellular solution and standard Ca^{2+} concentration[3]. The images were acquired at 10 Hz for 2-3 min.

To be able to distinguish between evoked and spontaneous activity, six APs have been evoked by single pulse electrical stimulation[4] at an interval of 10-13 s during each acquisition.

5.5.2 SNR Estimation in Real Data

Following Cheezum et al. 2001, the SNR of a peak in the present pHluorin data is defined by:

$$SNR = \frac{\Delta_i}{\sigma}. \tag{76}$$

Here, Δ_i represents the individual peak height computed as the difference between the average intensity of five frames before and five frames starting at the onset of a peak. σ denotes the noise and is also individually estimated for every peak. In order to remove the intensity decay after each peak, each intensity signal is highpass filtered before noise estimation. A 4th order Butterworth filter of cutoff frequency 0.05 Hz is applied using the *filtfilt* function of MATLAB's Signal Processing Toolbox. Subsequently, σ can be estimated by computing the SD of the intensities of 80 frames after the onset of the peak.
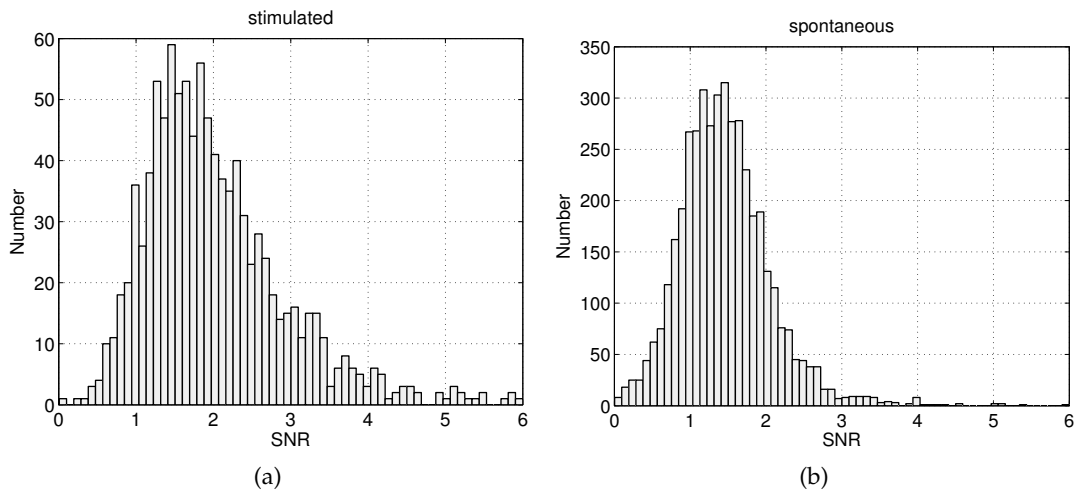

Figure 83: (a)-(b) Histograms of peak SNRs for stimulated respectively spontaneous activity.

To get an idea of the available SNR for the present experimental setup, Fig. 83 presents the SNR histograms for stimulated and spontaneous activity from 22 acquisitions. Here, k_f was set to 10, which is also the threshold factor used if not stated otherwise. The available SNR is between 1 and 4, and the SNR of spontaneous peaks appears to be on average slightly lower than that of stimulated ones. This is because incorrect detections are more likely for spontaneous activity since peaks are collected at any frame, whereas

---

3 The standard Ca^{2+} concentration contains 2mM $CaCl_2$ and 2mM $MgCl_2$.
4 Electrical stimulation included passing 1 ms pulses at 30 V via two electrodes at a distance of $\sim$ 5 mm. They were centered around the objective and put in the extracellular solution in close proximity to the neurons.

stimulated peaks are only accepted at defined positions. This bias will be noticeable in all of the following analyses.

5.5.3 *Evaluation on Real Data*

The evaluation on real data comprises (1) visual, (2) quantitative, and (3) plausibility analyses.

5.5.3.1 *Visual Analysis*

Fig. 84 illustrates the performance of MWA on the basis of signal A and B (see Fig. 79b) and indicates the time points of electrical stimulation. Signal A has a reasonably well SNR of 2.52, whereas signal B exhibits only a SNR of 1.71. Note that these SNRs have been estimated solely on the basis of stimulated peaks since it is more likely that these are indeed true peaks. By comparison it is apparent that stimulation does not always result in vesicle fusion at a synapse.

In order to get an impression of how well MWA separates peaks from noise, the corresponding signals S_f^*, where the thresholding finally takes place, are also provided. For comparison, these are also presented for AT since other automated detection algorithms for pHluorin data are not available yet.

A representative AT method was implemented as follows. Δ_i is computed at every position in the signal as described for SNR estimation in the preceding section. Then the adaptive thresholding scheme proposed by Quiroga et al. 2004 is applied. In order to compute a robust noise estimate, the corresponding intensity signal is highpass filtered using a more rigorous cutoff frequency of 1 Hz so that peak frequencies are largely eliminated.

Looking at S_f^* and the corresponding signal that would be available for AT, it is apparent that both algorithms manage to separate true peaks from noise quite well for the high SNR signal. Also a relatively broad range of threshold factors k_f is applicable without wrong peaks being included or true ones missed. This robustness is less pronounced for AT since possibly incorrect peaks are likely to be included in order to detect true peaks as indicated with mark 1.

The situation is different for the low SNR signal. So first of all it is already much more difficult to decide as an observer whether distortions in the signal are true peaks or just subject to noise. The effective SNR of the signals, where thresholding of the peaks is conducted, appears to be much smaller for both algorithms. However, MWA still provides reasonable freedom for selection of an optimal threshold that fits the requirements of the user without that the correct detection in signal A would be impeded. In comparison, threshold factors k_f that yield robust detection of true peaks in A using AT hardly detect any peak in signal B (see mark 2). If alternatively k_f is set to lower values, then false peaks are very likely to be included in A and B as for instance at mark 3.

It can be concluded that MWA is indeed capable of notably increasing the effective SNR for peak detection in contrast to standard adaptive AT. The selection of threshold factors k_f is much more robust with respect to varying SNRs of different synaptic signals.
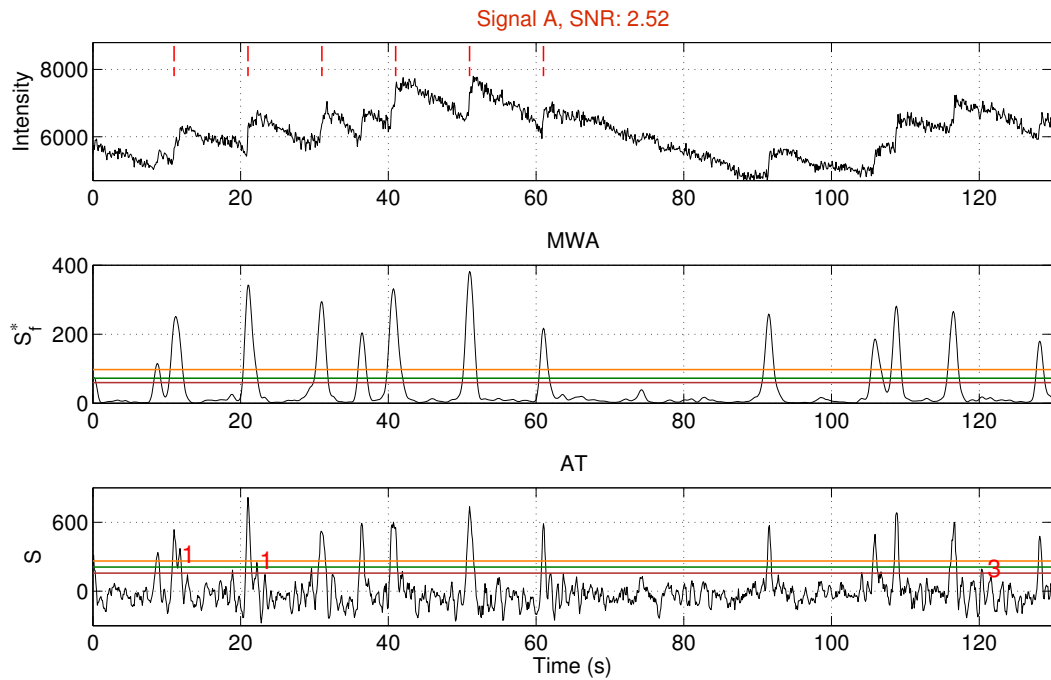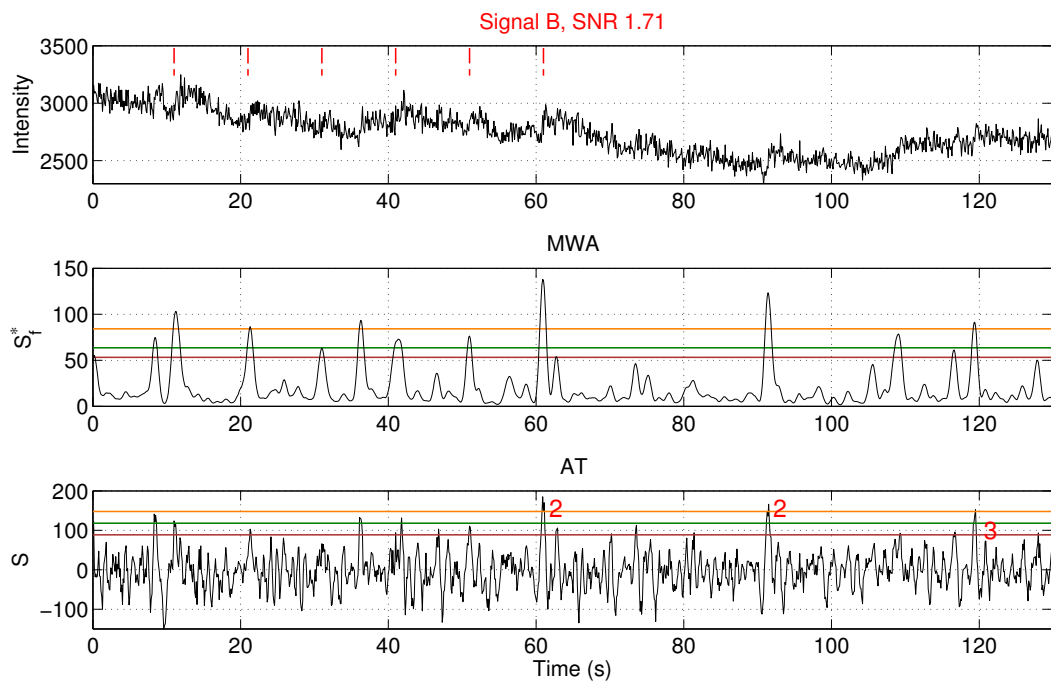
Figure 84: Visual comparison of the performance of MWA and AT using a (a) high and a (b) low SNR signal. The time points of electrical stimulation are indicated by the red dashed lines. The threshold lines correspond to $k_f = 8$, 10, and 14 for MWA and $k_f = 1.88$, 2.4, and 3 for AT.

5.5.3.2 *Quantitative Analysis*

In order to measure the detection performance of MWA quantitatively, a GT comprising the position of peaks in intensity signals must be available. Although the exact moment

Jaccard index	Expert 1	Expert 2	Expert 3	Expert 4	Expert 5
Expert 1	-	0.62/0.44	0.44/0.34	0.46/0.37	0.47/0.34
Expert 2	0.62/0.44	-	0.33/0.24	0.46/0.33	0.45/0.33
Expert 3	0.44/0.34	0.33/0.24	-	0.32/0.23	0.32/0.20
Expert 4	0.46/0.37	0.46/0.33	0.32/0.23	-	0.34/0.26
Expert 5	0.47/0.34	0.45/0.33	0.32/0.20	0.34/0.26	-

Table 2: Inter-rater reliability by means of the mutual Jaccard indices for stimulated (first number) and spontaneous (second number) peaks.

of stimulation is known, the GT is not even available for evoked APs because the release probability was experienced to be < 100 %. A GT must be constructed. For it, five neurobiologists from the LIN have individually been asked to manually select peaks in 123 synaptic intensity signals computed from four acquisitions. All neurobiologists were experts in the very related field of electrophysiology, where peak detection is a frequent task.

All acquisitions included the initial phase with six evoked APs, but of course the experts were not aware of this. Three of the four acquisitions underwent the standard single pulse stimulation, but the last acquisition actually saw four pulses per stimulus at 40 Hz. The release probability was increased, but still each stimulus just covered the time period of a single frame. Furthermore, two acquisitions dated from the same experiment. The required intensity signals have not been manually selected, instead the total workflow was invoked. Also, low SNR and empty signals from silent synapses were provided to the experts.

The outcome of the manual detections was fairly surprising. It turned out that 1D peak detection is a nontrivial task and highly subjective also for human experts since the inter-rater reliability was very low. It was measured by means of the Jaccard index J (Levandowsky and Winter 1971), which determines the similarity between two sets by:

$$J = \frac{|Set_1 \cap Set_2|}{|Set_1 \cup Set_2|}. \tag{77}$$

For the present application, it can be interpreted as the probability that a detected peak position by either human expert is actually detected by both experts. The mutual Jaccard indices for stimulated and spontaneous peaks are summarized in Table 2. The average mutual similarities are only 41.05 % respectively 30.80 %.

Given the low inter-rater reliability, a reliable GT could be constructed for neither of both types of activity. A quantitative evaluation against human experts could not be performed since the results would be hardly interpretable. Instead, MWA will be quantitatively analyzed on semi-synthetic data in Sect. 5.5.4, and in the following the output of MWA is at least made plausible on real experimental data. The outcome of the manual detections emphasized again how important an automated and reproducible activity detection algorithm is.

To obtain at least an indirect measure for the correctness of the detected peaks, it will now be tried to make plausible that the output of MWA yields biologically reasonable results. The quantized distribution of the peak heights Δ_i, individually demonstrated by Balaji and Ryan 2007 and Gandhi and Stevens 2003, is reproduced here, but now the computation is automatized and also covers spontaneous activity, which has not been shown yet.

In previous studies on biophysical properties, histograms of absolute peak intensities of stimulated activity at manually selected synapses have been calculated. The present algorithm scans the whole field of view and also includes off-focus synapses. Moreover, next to including different acquisitions into the analysis the test set combines acquisitions from cell preparations with different expression levels, which routinely happens if experiments are performed at different dates with fresh cell cultures. The distribution cannot be computed from absolute intensities since even peaks of different synapses in the same image may have different absolute intensity quanta.

Therefore, it is proposed here to transform absolute intensities into relative intensities that can be combined in a histogram. The key idea is that absolute peak intensities of a single synapse are quantitatively comparable as long as the sample drift during image acquisition is negligible. Then for each synapse the individual absolute quantal intensity can be estimated by use of hierarchical clustering if at least two peaks are available. The individual quantal intensity can then in turn be used to compute relative intensities by dividing the absolute peak intensities with the quanta.

In order to cluster the peak intensities of individual synapses, the *cluster* function of MATLAB's Statistics Toolbox was solely provided with a minimum quantal distance of 100 intensity counts empirically determined by examination of several acquisitions. Subsequently, the average peak intensity of each cluster was computed. The individual quantal intensity is then the smallest cluster distance or the smallest average cluster intensity, whichever is smaller.

The relative intensity histograms for evoked and spontaneous activity of three different data sets are summarized in Fig. 85. The first set comprises 22 acquisitions at standard Ca^{2+} concentration, and in the initial phase six peaks have been evoked by a single pulse. The second set comprises 19 acquisitions at high Ca^{2+} concentration[5]. The stimulation protocol was identical. The third set was again acquired at standard Ca^{2+} concentration and included nine acquisitions. However, the six stimulation events now included multiple pulses provided with 100 Hz during one sampling interval, and each event consisted of 10 instead of a single pulse.

Basically, there is only a single significant peak with Gaussian distribution in the stimulated and spontaneous relative intensity histograms of the first data set (see Fig. 85a-85b). This indicates that all peaks at a single synapse originated from the same number of fused vesicles. Since the Ca^{2+} concentration was low, it can be expected that actually only single vesicles did fuse.

In comparison, there are several evenly spaced peaks under high Ca^{2+} concentration (see Fig. 85c-85d). All figures also illustrate the best overall and individual fit to a set of Gaussians with identical SDs. The corresponding line fits to the fitted peak positions in Fig. 85f further visualize the integer multiples of the quantal distribution since all lines

---

5 The high Ca^{2+} concentration contains 5 mM $CaCl_2$ and 0.6 mM $MgCl_2$.
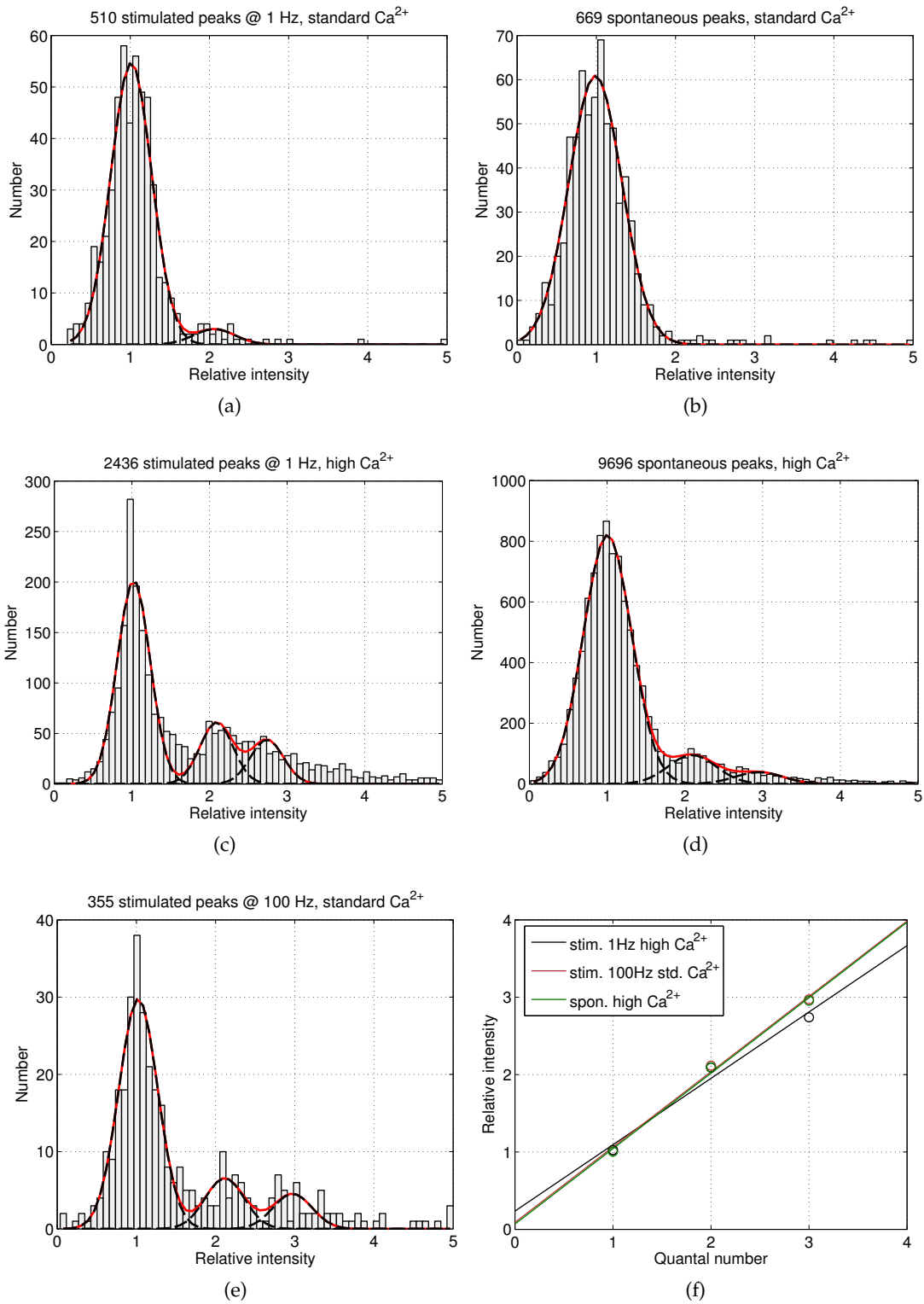
Figure 85: Relative intensity histograms for three different data sets: (a)-(b), (c)-(d), (e). The thick contour lines represents the best overall (red) and individual (black) fit to a set of Gaussians with identical SDs. (f) Line fits to the fitted peak positions of the individual data sets. They visualize the integer multiples of the quantal distributions.

almost approach the coordinate center. These results suggests that at single synapses peaks with different absolute intensities did occur, and hence the number of fused vesicles for a single AP varied. This is reasonable since it is well known that an increase in Ca^{2+} concentration increases the probability for larger numbers of fused vesicles per AP (Kandel et al. 2013). These findings were reproducible for both types of activity.

Similar results can be obtained by provision of multiple pulses with high frequency as was done for the third data set that remained with standard Ca^{2+} concentration. Again, the probability for multiple vesicle fusion increased since several evenly spaced peaks are identifiable in Fig. 85e.

The proposed clustering procedure is likely to result in an underestimation for the number of peaks with multiple quanta. They can only be detected if a single synapse indeed responded with different numbers of fused vesicles for different APs. Otherwise they were always only counted as single quanta. Nevertheless, it could be made plausible that the probability for multiple vesicle fusion can indeed be increased with higher Ca^{2+} concentration as well as bursts of APs.

Based on these findings, it can be concluded that the proposed workflow is capable of detecting relevant peaks irrespectively of whether they are manually evoked or result from the network activity itself. Biophysical parameters can reliably be derived using both types of activity.

5.5.4 Evaluation on Semi-synthetic Data

In order to evaluate the performance of MWA more rigorously, it was also applied to semi-synthetic synaptic intensity signals. The signals were created from 76 evoked and 91 spontaneous peaks that were clearly identifiable in the same data set that was provided to the human experts. Owing to the low inter-rater reliability the number of selected peaks turned out to be relatively low. To maintain a reliable GT, only peak shapes that showed no overlap with other peaks could be selected.

The peak shapes were repeatedly placed on signals of length 3 min until a total number of 500 peaks was reached for both types of activity. The individual positions were created by a homogeneous Poisson process with firing rate of 1 Hz, but overlapping peak shapes were prevented. The baseline signal had an offset of 2000 intensity units, and bleaching was simulated by an exponential decay with decay constant of 0.01.

To test how MWA performs as a function of the SNR, scaled noise from silent synapses was added to the signals. The noise between peaks was also adjusted to match the resulting SNR at the peaks. The semi-synthetic data consequently includes realistic peak shapes and noise instead of simulated approximations. A reliable GT is also available. Fig. 86 depicts an exemplary spontaneous activity signal at the four different SNRs adjusted in this study and indicates the underlying GT.

The performance of MWA, in comparison with AT, is assessed by plotting the true positive rate (TPR) versus the false discovery rate (FDR), where FDR is the number of falsely identified peaks divided by all identified peaks. This is similar to the commonly used receiver operating characteristic (ROC). Since the frequency of true peaks is relatively low in comparison to the sampling rate, evaluation of the ROC would not be very meaningful here. The performance curves for four different SNRs are presented in Fig. 87a-87b for stimulated respectively spontaneous activity. The threshold factor k_f was varied between $\sim$ 4-20.5 for MWA and $\sim$ 1.5-2.9 for AT.
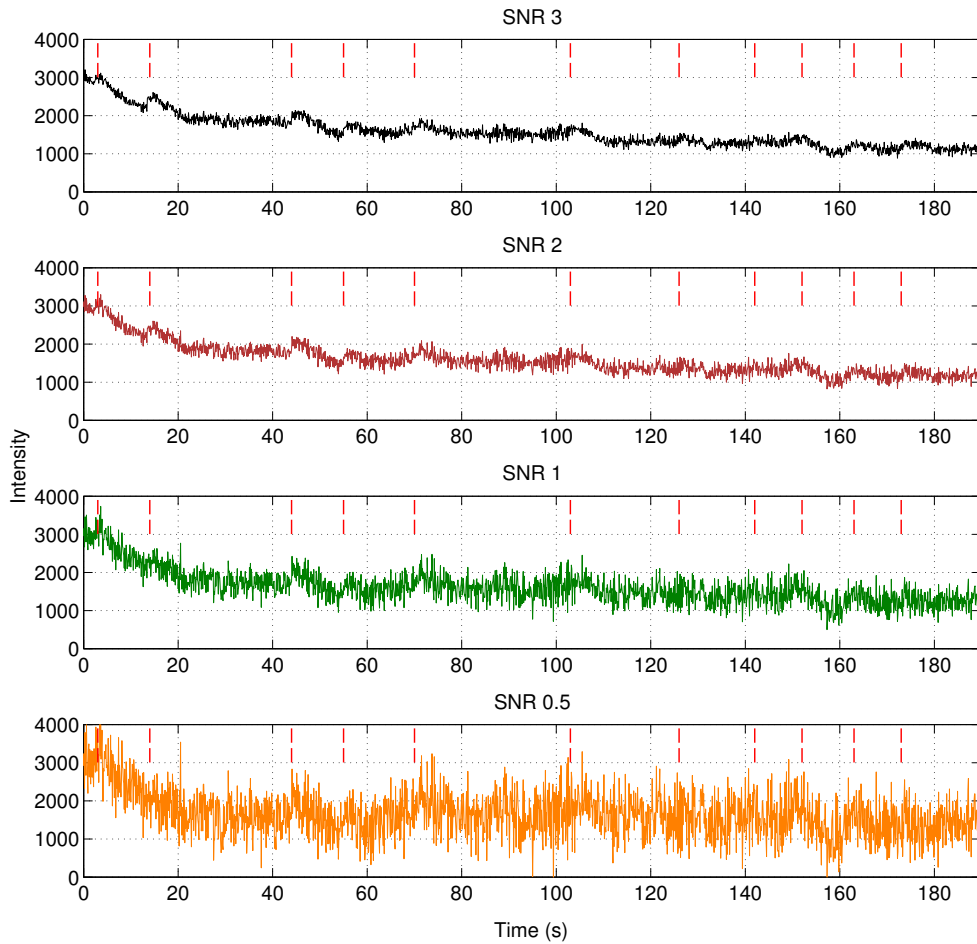
Figure 86: Exemplary semi-synthetic signal with spontaneous activity at four different SNRs. The red dashed lines indicate the GT.

Clearly, the detection capability of MWA is superior over AT at any SNR and type of activity. The results are worse for spontaneous activity, but it can be assumed that any ambiguous peak selection for creation of the semi-synthetic data did fall into this data set. The relative improvement even increases towards low SNR as is additionally depicted in Fig. 87c-87d. The overall performance of MWA is satisfactory only for SNR > 1, however, this is the SNR that most of the peaks have given the present experimental configuration. MWA can be reliably applied to such type of data.

5.6 GENERALIZATION OF THE MULTIPLE WAVELET CONCEPT

MWA introduces a new concept that employs multiple wavelets to match all relevant features of a peak. This stands opposed to other general peak detection algorithms that just use a single wavelet. For the present application, the number of wavelets was set to two, but more can be incorporated. In order to assess whether the fusion of multiple wavelets indeed improves the detection capability of MWA, Fig. 88 plots again the performance of MWA on semi-synthetic data, but also provides the curves if only the Haar or the Bior3.1 wavelet would be used for detection. The algorithm remained
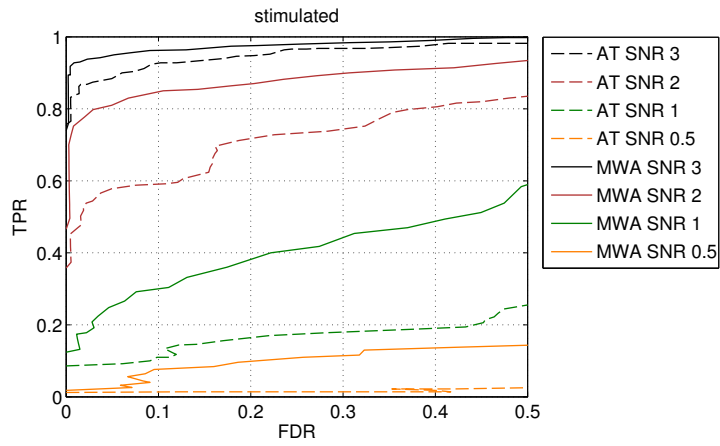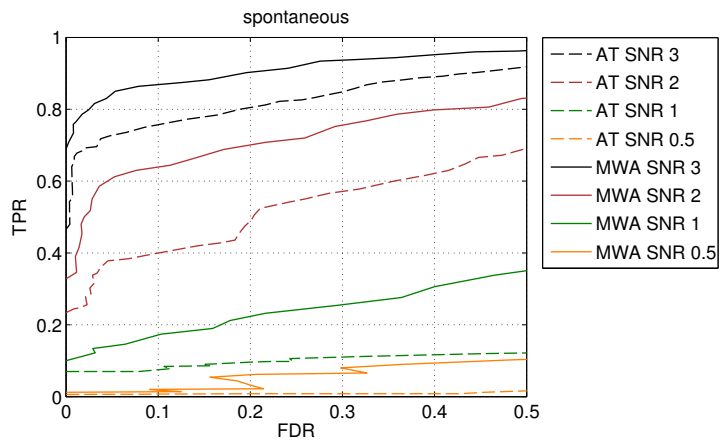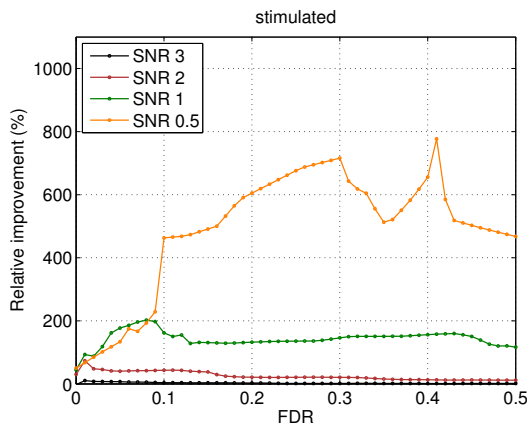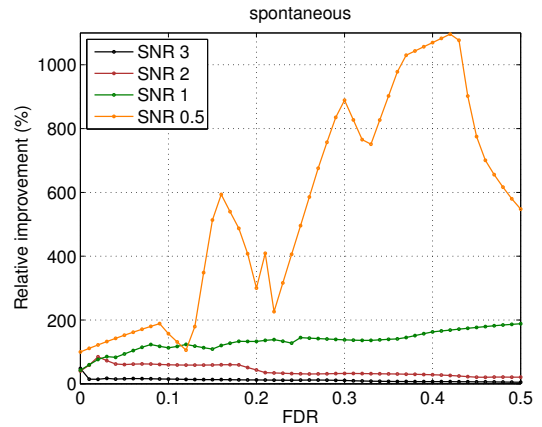
Figure 87: Performance analysis of MWA and AT. Both algorithms were applied to semi-synthetic data at different SNRs for (a) stimulated and (b) spontaneous activity. Relative improvement of MWA related to AT for (c) stimulated and (d) spontaneous activity at different SNRs. Since the performance curves for the two algorithms had different supporting points at the x axis, they were interpolated in order to be comparable.

unchanged except that in step IV the fusion defined by Equ. 73 is not conducted for the Haar or the Bior3.1 curves.


(a)

(b)
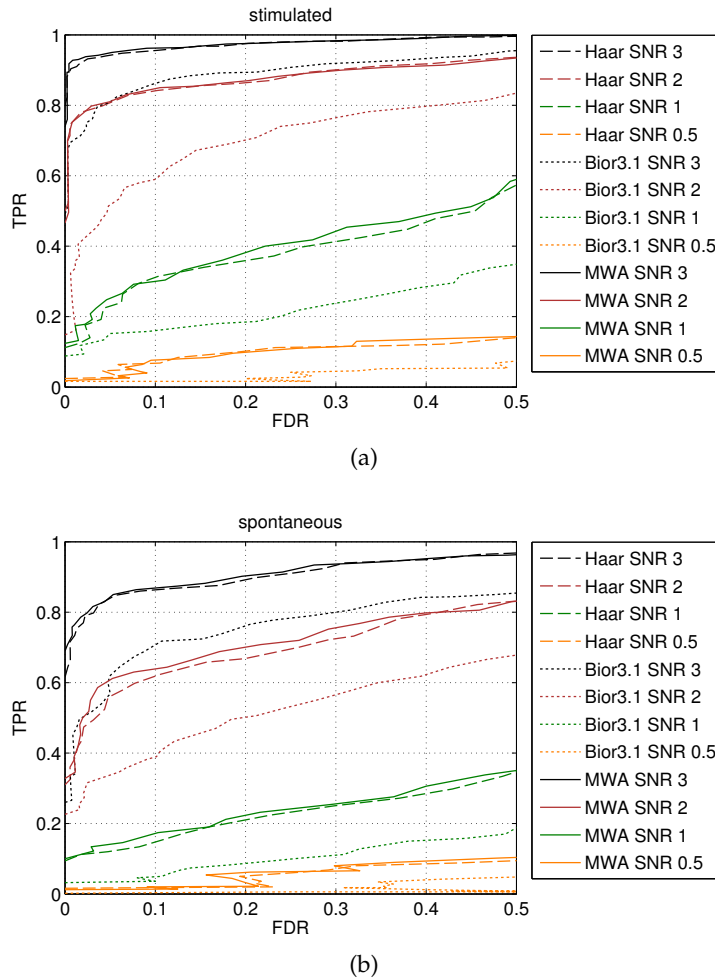
Figure 88: Performance analysis of the complete MWA and if just the individual wavelets are used. Both algorithms are applied to semi-synthetic data at different SNRs for (a) stimulated and (b) spontaneous activity.

It appears that the performance of using just the Haar wavelet is a lot better than solely relying on the Bior3.1 wavelet. This was expected since the Bior3.1 wavelet results in a much noisier signal S_{bior}, which is clearly recognizable in the example of Fig. 81. The discrimination between noise and signal is much more unreliable than in S_{haar}.

Although their results are considerably different, fusion of both wavelet decisions, as performed by MWA, manages to increase the performance. It has to be admitted that the improvement is relatively small, but this is justified by the following circumstances. First, the individual performance of the Bior3.1 wavelet is indeed very weak, and hence its ability to contribute reasonably to the weighted result can be considered low. Second, it is likely that the created semi-synthetic data set is biased to some degree. It must be considered that humans tend to select peaks mainly based on a clear immediate increase of the intensity. The semi-synthetic data consequently favors the feature that is mainly addressed by the Haar wavelet, and the corresponding performance is overly good.

In spite of it all, MWA exhibits some minor improvement, which proves that the key idea is working. It is also fair to expect that if the data set would be less biased or if a more powerful wavelet than Bior3.1 could be found the resulting improvement would be more pronounced.

Besides these considerations with respect to the present specific data, the key concept of MWA should be generalizable to other applications since varying or complex shapes are a typical challenge in signal and image processing. This is particularly true for electrophysiology, where in fact the true peak shape and not just its scaling varies significantly. Several wavelets have their justification, but always only a single one was chosen (Benitez and Nenadic 2008, Nenadic and Burdick 2005, Kim and Kim 2003). It would be of great interest if their combined application can yield higher robustness.

More complex shapes that can be disassembled into several clear features should be addressed with multiple wavelets. This may for instance be advantageous for advanced driver assistance or geo-information systems. It must be stated that for the present application two wavelets that match the signal at the same position have been employed, which was shown to facilitate the fusion strategy. In order to achieve more general applicability and to support compounded shapes, an improved fusion strategy that can deal with fixed or even varying distances between different wavelet decisions must be developed. If this is developed further it can also be advisable to conduct the fusion at another level. Here, the feature level was chosen, but for multiple wavelets (> 2) the fusion could also take place at the decision level (Hall and Llinas 1997).

5.7 CONCLUSION AND FUTURE WORK

This chapter presented a workflow for automated detection of individual synaptic activity in pHluorin images. It includes the detection of synaptic spots, computation of their intensity signals and subsequent determination of activity by means of 1D peak detection. Activity detection was the main matter of interest and a wavelet-based algorithm that employs multiple wavelets was proposed.

Instead of choosing a single suboptimal wavelet for peak detection, individual features of the shape of interest are addressed by different wavelets. The resulting signals in the wavelet space are subsequently fused so that the final thresholding is facilitated and more robust. This could be made plausible by visual analysis of real data and was more rigorously assessed by means of the detection performance on semi-synthetic data. In either way the proposed MWA was clearly superior to standard AT, which is currently the only algorithm available for pHluorin measurements. For real acquisitions it was also shown that detected peaks reveal the quantal nature of vesicle fusion indicating the reliability of the outcome of MWA. A ground truth evaluation against human experts failed owing to the poor inter-rater reliability.

It is particularly the latter result that emphasizes the difficulty to interpret pHluorin signals. It underlines the stated objective for robust automatic approaches. It can be concluded that the proposed procedure is capable of fulfilling this demand, since the complete workflow is automatized and its performance is clearly superior to AT (Objective 2.1). It is advantageous that only the two thresholds for synapse and peak detection remain as free parameters because all other variables could be well defined with respect to the application. Since all analyses have been conducted for evoked and

spontaneous activity and similar results were achieved, MWA can be reliably used for analysis of spontaneous activity that has not been investigated yet (Objective 2.2).

The incorporation of two different wavelets to detect complex peak shapes that are subject to strong variation can be considered as a novel concept. It enables the MWA to perform more than twice as good as AT, particularly at low SNRs (Objective 2.3). The fundamental functioning of this multiple wavelet concept could be proven, but for the present application the improvement was shown to be marginal. However, since the method is not limited to only two wavelets as employed here, it can be expected that it yields great potential for the detection of more complex peak shapes in other applications. Finally, MWA makes the analysis of synaptic activity less subjective by incorporating all synapses and their varying signal quality into the analysis (Objective 2.4). It was possible to reveal the quantal nature of vesicle fusion without manual selection of clearly identifiable activity.

In order to make this workflow widely available, MWA, including a GUI, can be downloaded at `http://sourceforge.net/projects/isad/`. It is implemented in MATLAB and published under the Creative Commons Attribution License.

MWA could not be applied to acquisitions in brain slices since the fluorescence of pHluorin was barely distinguishable from the autofluorescence in the compact tissue. To fulfill this demand it must be referred to the promising imaging configurations stated in Sect. 4.11.

There are two major directions for future work that would make the fundamental idea more generally applicable. First, closely overlapping peaks have so far not been considered in this work. For the present application, occurrence of overlapping peaks have found to be rare. For instance in electrophysiology this appears to happen more frequently. So called bursts are an exception where all pHluorins are released with high frequency. This typically happens when cultures die. Detection of such events would be of interest from a biological point of view. It allows to draw conclusions on the viability of the cells and if recorded data should be used or not. Consequently, the impact of nearby peaks on the detection performance should be analyzed in detail. It is particularly the relatively large support range of the Bior3.1 wavelet that can cause problems if peaks are too close.

On the other hand, the fusion strategy should gain more attention. In order to address more complex shapes it is required to handle wavelets that match features at different positions in the signal or image. To fuse their information, a strategy that can deal with variable distances between the peak correlation of the individual wavelets is necessary. For the present application, this situation would arise if for instance a wavelet that matches the intensity decay shall also be included. Since the dwell times vary significantly, the individual signals S cannot be combined by simple arithmetic treatment. It might be advisable to conduct the fusion at the decision level after individual thresholding.

From a biological point of view, the presented workflow can now also be applied to investigate spontaneous activity of neurons. Such analyses could now be combined with measurements of multi-electrode arrays. This would allow to bridge the gap between single synaptic analysis and the network level because multi-electrode arrays only have a low spatial resolution, but can record signals over a large area (Scanziani and Häusser 2009).

An algorithm for neuronal network skeletonization, that just relies on optical activity reporters, has also been developed during the work for this thesis. The major difficulty was that exclusively active synapses are labeled while the neuronal structure is only visible by autofluorescence. It was applied to images containing live staining of active synapses using fluorescent labelled anti-synaptotagmin antibody uptake and was published in Sokoll et al. 2012a. Synaptotagmin uptake and pHluorin images have similar properties with respect to the stationary network structure and hence the algorithm should also be applicable to pHluorin recordings. In combination, these techniques have the potential to analyze the process of signal transmission at the neuronal network level.

A final application of interest that shall be addressed here is the determination of the exact vesicle fusion site at the presynaptic terminal. The existence of preferred vesicle fusion sites has been postulated by Freche et al. 2011 on the basis of simulations and was experimentally investigated by Gaffield et al. 2009 and Zenisek et al. 2000. However, both used types of cells with very large synaptic terminals that simplified the analysis.

In order to determine the fusion sites of neurons using pHluorins, the very first idea could be to apply localization algorithms. Although the likelihood for only single vesicle fusions is high, each vesicle contains several pHluorins and the density is too high even for multiple particle finding algorithms. Pilot experiments have been conducted where the weighted Gaussian fitting procedure described in Sect. 5.4.1 was applied to synaptic locations in the pHluorin images at any time point. The underlying assumption is that at least at the moment of vesicle fusion the pHluorins are so closely located that they can be considered as a single fluorophore until they diffuse apart.
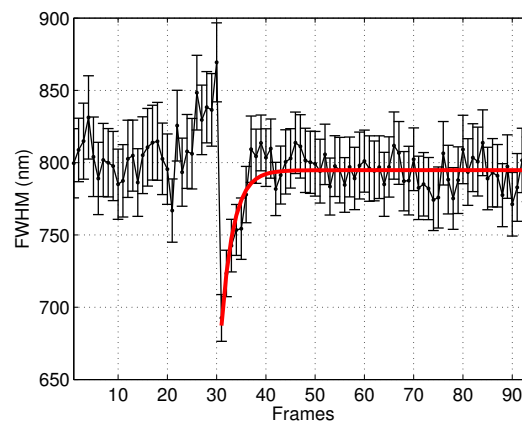

Figure 89: Course of the average FWHM over the support range of stimulated peaks. The red line represents a single exponential recovery fit to the course after vesicle fusion.

As a first result, Fig. 89 plots the course of the average FWHM over the support range of stimulated peaks. The FWHM decreases immediately at the onset of the peak and recovers exponentially. The course of the obtained curve is similar to that experienced in FRAP experiments and is likely to describe the assumed pHluorin diffusion. If it turns out that this is indeed the case, the fitted location at the onset of each peak could be an indicator for the fusion site at the active zone. This remains to be investigated in more detail. As a side effect, the FWHM signal could also be used in combination with the intensity signal so that the peak detection can be further improved.

SUMMARY AND FUTURE WORK

This thesis aimed at developing tools that support neurobiologists in investigating the functioning of neurons at the molecular level. The focus was on two subjects: the measurement of fast 3D molecular dynamics in complex living samples and the detection of individual synaptic activity.

Both topics are interrelated since the highly dynamic arrangement, mobility and interaction of molecules modulate synaptic transmission efficacy. This variability in neuronal signalling must be detectable and is in turn considered fundamental for higher brain functions.

These underlying biological principles were the topic of Chapter 2. Since the corresponding investigations have to be conducted in nanoscale compartments of living samples, FM is used as the basic analysis technique. It was introduced in detail in Chapter 3.

Chapter 4 addressed the observation of 3D molecular dynamics inside complex living samples. For it, a suitable imaging configuration was established. As a first contribution, it could be proven that at least the derivation of 2D mobility parameters is possible at depths of several tens of micrometers in organotypic brain slices. Owing to the optical aberrations introduced by the RIM, such analyses are not directly extendable to 3D. The major contribution is the development of an online calibration procedure that adjust astigmatism-based 3D SPT techniques to the induced aberrations. It requires virtually no additional experimental efforts or compromises for the experimenter and is conceptually novel by estimating the aberrations directly from the acquired image stream. Improved 3D diffusion parameters and the correct 3D morphology of neuronal structures can now be observed below the resolution limit. The systematic positioning error is at least halved. As a final contribution, also the application of an EM algorithm for shape estimation of multiple particles at distances below the resolution limit was proposed.

In Sect. 4.11 the evaluation results and the achieved objectives were in detail discussed. In summary, it can be concluded that the observation of fast 3D molecular dynamics in nanoscale compartments is now readily available in complex living samples. The experimenter can start imaging right away. The spatial and temporal resolutions are basically only limited by the available SNR. Increasing the imaging quality remains the biggest challenge. The presented imaging configuration does not suffice to reach the intended goal of having axial LAs $\leqslant 100\,\mathrm{nm}$ in brain slices. However, the fundamental functioning of the algorithm in combination with the setup could be proven. Its simplicity makes it easy for others to further improve the presented method.

A method for the detection of individual presynaptic neurotransmitter release was presented in Chapter 5. It employs pHluorins as fluorescent markers and detects intensity changes that correspond to vesicle fusion events at individual synapses using a

wavelet-based algorithm. The analysis procedure is fully automatized and allows to detect spontaneous activity. The major scientific contribution is the incorporation of two different wavelets to match individual features of the shape of interest. Taking multiple wavelets is conceptionally novel and allows to address more complex shapes than with just a single suboptimal wavelet. Particularly for low SNRs, the detection capability is increased by more than 100 % with respect to that of standard AT approaches.

Again, the evaluation results and the achieved objectives were already in detail discussed in Sect. 5.7. It can be stated that the proposed workflow allows for robust automated detection of individual synaptic activity in pHluorin images. By incorporating all observable synapses into the analysis, subjectivity has been largely eliminated. It is now possible to derive biologically relevant parameters also for spontaneous activity, which has not been investigated yet.

The two major subjects have mainly been considered separately in this thesis. The directions for future work were individually described in Sect. 4.11 and Sect. 5.7, respectively. Their combined application requires two prerequisites: first, both must be available for the same biological system and second, multiple wavelengths have to be detected in parallel.

The first issue could not be fully accomplished during this work. The application to brain slices could only be shown for the analysis of molecular dynamics, but it was found that the determined pHluorin signals are too weak for the reliable extraction of neuronal activity. It can be assumed that activity detection is likely to be accomplished in brain slices using the proposed alternative imaging configurations (see Sect. 4.11). The combined application is rather a matter of improvements in microscopy hardware than of algorithmic difficulties.

The detection of multiple wavelengths can be easily accomplished by introduction of a beam splitter between the CSU and the detector. It transmits a certain wavelength, but reflects another (see Sect. 3.1.4.2). This creates two light paths that can either be detected by individual cameras or projected on either halve of the sensor of a single camera. The fluorescence of QDs and pHluorins can be detected in parallel, since the Stokes shift of QDs can be quite large so that even a single excitation wavelength can be used. Such a configuration would already provide the ability to observe interactions of different types of molecules. They simply have to be labeled with QDs of varying emission wavelengths.

The combined application of both methods would finally allow to address various biological questions. The direct readout of the probability of neurotransmitter release is of utmost importance. It allows to determine variations in short-term plasticity. The facilitation or depression of the release probability, that may last from milliseconds to seconds, is now directly observable at the single synaptic level where the stochastic variability cannot be neglected anymore (see Sect. 2.4.2). It can now be investigated whether facilitation or depression correlate with the presence of certain molecules and their interplay. Furthermore, do they need to maintain fixed positions or is it indeed their random behavior that facilitates synaptic plasticity. What happens if certain subpopulations are coupled via antibodies and hence their mobility is decreased. What is the result with respect to over- or underexpression of subpopulations. Finally, also the patterns of activation and their timings have an influence on synaptic plasticity (Abbott and Regehr 2004) and can now be investigated for each individual synapse.

As an ultimate goal, analyses at the molecular and the network level should be combined (Scanziani and Häusser 2009). Then, it can be investigated how local changes in synaptic transmission modulate the organization of cells to local circuits. For instance, what happens if Ca^{2+} channels are overexpressed and hence the synaptic transmission probability is globally increased. Does this lead to certain synchronization patterns at the network level, or does it become more static so that fast and reliable reactions are favored over adaptability.

All in all, it can be concluded that the techniques for investigating the functioning of the brain have been tremendously improved until today. Employing image and signal processing algorithms, the present thesis supports this direction by making current techniques widely and readily available in less artificial systems. This fosters and encourages further investigations on how the brain fulfills our complex daily tasks.

E. Abbe. Beiträge zur theorie des mikroskops und der mikroskopischen wahrnehmung. *Archiv für mikroskopische Anatomie*, 9(1):413–68, 1873. (Cited on page 28.)

E.A. Abbondanzieri, W.J. Greenleaf, J.W. Shaevitz, R. Landick, and S.M. Block. Direct observation of base-pair stepping by rna polymerase. *Nature*, 438:460–5, 2005. (Cited on page 38.)

L.F. Abbott and W.G. Regehr. Synaptic computation. *Nature*, 431:796–803, 2004. (Cited on pages 13 and 182.)

A.V. Abraham, S. Ram, J. Chao, E.S. Ward, and R.J. Ober. Quantitative study of single molecule location estimation techniques. *Optics Express*, 17(26):23352–73, 2009. (Cited on pages 38, 53, and 84.)

F. Aguet, D.V.D. Ville, and M. Unser. A maximum-likelihood formalism for sub-resolution axial localization of fluorescent nanoparticles. *Optics Express*, 13(26):10503–22, 2005. (Cited on pages 56, 62, and 66.)

P.L. Ainsleigh. A tutorial on em-based density estimation with histogram intensity data. Nuwc-npt technical report 11,807, Sensors and Sonar Systems Department, NAVSEA, Newport, Rhode Island, 2009. (Cited on pages 86 and 87.)

G.B. Airy. On the diffraction of an object-glass with circular aperture. *Transactions of the Cambridge Philosophical Society*, 5:283–91, 1835. (Cited on page 29.)

C.M. Anderson, G.N. Georgiou, I.E. Morrison, G.V. Stevenson, and R.J. Cherry. Tracking of cell surface receptors by fluorescence digital imaging microscopy using a charge-coupled device camera. low-density lipoprotein and influenza virus receptor mobility at 4 degrees c. *Journal of Cell Science*, 101:415–25, 1992. (Cited on pages 44, 52, and 68.)

D. Aquino, A. Schönle, C. Geisler, C. Middendorff, C.A. Wurm, Y. Okamura, T. Lang, S.W. Hell, and A. Egner. Two-color nanoscopy of three-dimensional volumes by 4pi detection of stochastically switched fluorophores. *Nature Methods*, 8(4):353–9, 2011. (Cited on page 61.)

P. Ariel and T.A. Ryan. Optical mapping of release properties in synapses. *Frontiers in Neural Circuits*, 4(18):1–10, 2010. (Cited on pages 152 and 153.)

M. Armbruster and T.A. Ryan. Synaptic vesicle retrieval time is a cell-wide rather than individual-synapse property. *Nature Neuroscience*, 14(7):824–6, 2011. (Cited on page 153.)

J. Art. Photon detectors for confocal microscopy. In *Handbook of Biological Confocal Microscopy*, pages 251–64. Springer, 3th edition, 2006. (Cited on page 24.)

P.P. Atluri and T.A. Ryan. The kinetics of synaptic vesicle reacidification at hippocampal nerve terminals. *The Journal of Neuroscience*, 26(8):2313–20, 2006. (Cited on page 153.)

D. Axelrod. Total internal reflection fluorescence microscopy in cell biology. *Traffic*, 2 (11):764–74, 2001. (Cited on page 35.)

D. Axelrod, D.E. Koppel, J. Schlessinger, E. Elson, and W.W. Webb. Mobility measurement by analysis of fluorescence photobleaching recovery kinetics. *Biophysical Journal*, 16(9):1055–69, 1976. (Cited on page 41.)

M. Axmann, J. Madl, and G.J. Schütz. Single-molecule microscopy in the life sciences. In *Fluorescence Microscopy - From Principles to Biological Applications*, pages 293–343. Wiley-Blackwell, 1th edition, 2013. (Cited on pages 22, 25, and 85.)

O. Azucena, J. Crest, J. Cao, W. Sullivan, P. Kner, D. Gavel, D. Dillon, S. Olivier, and J. Kubby. Wavefront aberration measurements and corrections through thick tissue using fluorescent microsphere reference beacons. *Optics Express*, 18(16):17521–32, 2010. (Cited on page 65.)

H. Babcock, Y.M. Sigal, and X. Zhuang. A high-density 3d localization algorithm for stochastic optical reconstruction microscopy. *Optical Nanoscopy*, pages 1–6, 2012. (Cited on pages 59, 63, 71, 85, 113, and 150.)

R. Bacallao, S. Sohrab, and C. Phillips. Guiding principles of specimen preservation for confocal fluorescence microscopy. In *Handbook of Biological Confocal Microscopy*, pages 368–80. Springer, 3th edition, 2006. (Cited on page 65.)

D. Baddeley, I.D. Jayasinghe, C. Cremer, M.B. Cannell, and C. Soeller. Light-induced dark states of organic fluochromes enable 30 nm resolution imaging in standard media. *Biophysical Journal*, 96(2):L22–4, 2009. (Cited on page 53.)

M. Badieirostami, M.D. Lew, M.A. Thompson, and W.E. Moerner. Three-dimensional localization precision of the double-helix point spread function versus astigmatism and biplane. *Applied Physics Letters*, 97:161103, 2010. (Cited on pages 61, 111, and 119.)

J. Balaji and T.A. Ryan. Single-vesicle imaging reveals that synaptic vesicle exocytosis and endocytosis are coupled by a single stochastic mode. *Proceedings of the National Academy of Sciences*, 104(51):20576–81, 2007. (Cited on pages 152, 153, 154, 160, 164, 166, and 172.)

M.L. Bang and L. Owczarek. A matter of balance: Role of neurexin and neuroligin at the synapse. *Neurochemical Research*, 38(6):1174–89, 2013. (Cited on page 77.)

I.N. Bankman, K.O. Johnson, and W. Schneider. Optimal detection, classification, and superposition resolution in neural waveform recordings. *IEEE Transactions on Biomedical Engineering*, 40(8):836–41, 1993. (Cited on page 155.)

M.O. Baradez, C.P. McGuckin, N. Forraz, R. Pettengell, and A. Hoppe. Robust and automated unimodal histogram thresholding and potential applications. *Pattern Recognition*, 37(6):21131–48, 2004. (Cited on page 49.)

A.P. Bartko and R.M. Dickson. Imaging three-dimensional single molecule orientations. *The Journal of Physical Chemistry B*, 103:11237–41, 1999. (Cited on page 53.)

P.I.H. Bastiaens and A. Squire. Fluorescence lifetime imaging microscopy: spatial resolution of biochemical processes in the cell. *Trends in Cell Biology*, 9(2):48–52, 1999. (Cited on page 42.)

R. Benitez and Z. Nenadic. Robust unsupervised detection of action potentials with probabilistic models. *IEEE Transactions on Biomedical Engineering*, 55(4):1344–54, 2008. (Cited on pages 157, 163, and 178.)

M.R. Bennett, L. Farnell, and W.G. Gibson. The probability of quantal secretion near a single calcium channel of an active zone. *Biophysical Journal*, 78(5):2201–21, 2000. (Cited on page 13.)

A.J. Berglund, M.D. McMahon, J.J. McClelland, and J.A. Liddle. Fast, bias-free algorithm for tracking single particles with variable size and shape. *Optics Express*, 16 (18):14064–75, 2008. (Cited on page 51.)

S. Berning, K.I. Willig, H. Steffens, P. Dibaj, and S.W. Hell. Nanoscopy in a living mouse brain. *Science*, 335(6068):551, 2012. (Cited on page 73.)

G. Best, R Amberger, and C. Cremer. Super-resolution microscopy: Interference and pattern techniques. In *Fluorescence Microscopy - From Principles to Biological Applications*, pages 345–74. Wiley-Blackwell, 1th edition, 2013. (Cited on page 30.)

E. Betzig. Proposed method for molecular optical imaging. *Optics Letters*, 20(3):237–9, 1995. (Cited on pages 35 and 37.)

E. Betzig, G.H. Patterson, R. Sougrat, W. Lindwasser, S. Olenych, J.S. Bonifacino, M.W. Davidson, J. Lippincott-Schwartz, and H.F. Hess. Imaging intracellular fluorescent proteins at nanometer resolution. *Science*, 313(5793):1642–5, 2006. (Cited on pages 38, 39, 40, and 49.)

B. Biermann, S. Sokoll, J. Klueva, M. Missler, J.S. Wiegert, J.B. Sibarita, and M. Heine. Imaging of molecular surface dynamics in brain slices using single-particle tracking. *Nature Communications*, 5(3024):1–10, 2014. (Cited on pages 72, 76, 82, and 139.)

E. Biffi, D. Ghezzi, A. Pedrocchi, and G. Ferrigno. Development and validation of a spike detection and classification algorithm aimed at implementation on hardware devices. *Computational Intelligence and Neuroscience*, 2010(8):1–15, 2010. (Cited on page 155.)

J. Binding, J.B. Arous, J.F. Léger, S. Gigan, C. Boccara, and L. Bourdieu. Brain refractive index measured in vivo with high-na defocus-corrected full-field oct and consequences for two-photon microscopy. *Optics Express*, 19(6):4833–47, 2011. (Cited on page 93.)

P. Bingen, M. Reuss, J. Engelhardt, and S.W. Hell. Parallelized sted fluorescence nanoscopy. *Optics Express*, 19(24):2316–26, 2011. (Cited on page 37.)

S.S. Blackman. Multiple hypothesis tracking for multiple target tracking. *IEEE Aerospace and Electronic Systems Magazine*, 19(1):5–18, 2004. (Cited on page 67.)

S. Bonneau, M. Dahan, and L.D. Cohen. Single quantum dot tracking based in perceptual grouping using minimal paths in a spatiotemporal volume. *IEEE Transactions on Image Processing*, 14(9):1384–95, 2005. (Cited on page 68.)

M.J. Booth. Adaptive optics in microscopy. *Philosophical Transactions of the Royal Society A*, 365(1861):2829–43, 2007. (Cited on page 65.)

H. Bornfleth, P. Edelmann, D. Zink, T. Cremer, and C. Cremer. Quantitative motion analysis of subchromosomal foci in living cells using four-dimensional microscopy. *Biophysical Journal*, 77(5):2871–86, 1999. (Cited on page 48.)

J Boulanger, C. Kervrann, J. Salamero, J.B. Sibarita, and P. Bouthemy. Non-parametric regression for patch-based fluorescence microscopy image sequence denoising. In *5th IEEE International Symposium on Biomedical Imaging: From Nano to Macro*, pages 748–51, 2008. (Cited on page 48.)

E.J. Breen, G.H. Joss, and K.L. Williams. Locating objects of interest within biological images: The top hat box filter. *Journal of Computer-Assisted Microscopy*, 3(2):97–102, 1991. (Cited on page 49.)

D.S. Bright and E.B. Steel. Two-dimensional top hat filter for extracting spots and spheres from digital images. *Journal of Microscopy*, 146(2):191–200, 1987. (Cited on page 49.)

R.E. Burkard and E. Çela. Linear assignment problems and extensions. In *Handbook of Combinatorial Optimization*, pages 75–149. Springer US, 1th edition, 1999. (Cited on page 69.)

N. Burnashev and A. Rozov. Presynaptic ca_{2+} dynamics, ca_{2+} buffers and synaptic efficacy. *Cell Calcium*, 37(5):489–95, 2005. (Cited on page 14.)

D.T. Burnette, P. Sengupta, Y. Dai, J. Lippincott-Schwartz, and B. Kachar. Bleaching/blinking assisted localization microscopy for superresolution imaging using standard fluorescent molecules. *Proceedings of the National Academy of Sciences*, 108 (52):21081–6, 2011. (Cited on page 39.)

I.V. Cadez, P. Smyth, G.J. McLachlan, and C.E. McLaren. Maximum likelihood estimation of mixture densities for binned and truncated multivariate data. *Machine Learning*, 47(1):7–34, 2002. (Cited on pages 86, 90, and 150.)

E.J. Càndes. Compressive sampling. In *Proceedings of the International Congress of Mathematicians*, pages 1433–52, 2006. (Cited on page 56.)

H.L. Chan, M.A. Lin, T. Wu, S.T. Lee, Y.T. Tsai, and P.K. Chao. Detection of neuronal spikes using an adaptive threshold based on the max–min spread sorting method. *Journal of Neuroscience Methods*, 172(1):112–21, 2008. (Cited on page 155.)

P.Y. Chan, M.B. Lawrence, M.L. Dustin, L.M. Ferguson, D.E. Golan, and T.A. Springer. Influence of receptor lateral mobility on adhesion strengthening between membranes containing lfa-3 and cd2. *The Journal of Cell Biology*, 115(1):245–55, 1991. (Cited on page 3.)

J. Chao, S. Ram, A.V. Abraham, E.S. Ward, and R.J. Ober. A resolution measure for three-dimensional microscopy. *Optics Communications*, 282(9):1751–61, 2009. (Cited on page 54.)

M.K. Cheezum, W.F. Walker, and W.H. Guilford. Quantitative comparison of algorithms for tracking single fluorescent particles. *Biophysical Journal*, 81:2378–88, 2001. (Cited on pages 51, 53, 75, 135, 136, and 168.)

Y. Chen and M.R. Gupta. Em demystified: An expectation-maximization tutorial. Technical report number uweetr-2010-0002, Department of Electrical Engineering, University of Washington, 2010. (Cited on pages 85, 90, and 150.)

N. Chenouard, I. Bloch, and J.C. Olivo-Marin. Multiple hypothesis tracking in microscopy images. In *IEEE International Symposium on Biomedical Imaging: From Nano to Macro*, pages 1346–9, 2009. (Cited on page 70.)

N. Chenouard, T. Smal, F. de Chaumont, M. Maška, I.F. Sbalzarini, Y. Gong, J. Cardinale, C. Carthel, S. Coraluppi, M. Winter, A.R. Cohen, W.J. Godinez, K. Rohr, Y. Kalaidzidis, L. Liang, J. Duncan, H. Shen, Y. Xu, K.E.G. Magnusson, J. Jaldén, H.M. Blau, P. Paul-Gilloteaux, P. Roudot, C. Kervrann, F. Waharte, J.Y. Tinevez, S.L. Shorte, J. Willemse, K. Celler, G.P. van Wezel, H.W. Dan, Y.S. Tsai, C.O. de Solörzano, J.C. Olivo-Marin, and E. Meijering. Objective comparison of particle tracking methods. *Nature Methods*, 11:281–9, 2014. (Cited on page 70.)

A. Chmyrov, J. Keller, T. Grotjohann, M. Ratz, E. d'Este, S. Jakobs, C. Eggeling, and S.W. Hell. Nanoscopy with more than 100,000 'doughnuts'. *Nature Methods*, 10(8): 737–42, 2013. (Cited on page 37.)

N.B. Cole, C.L. Smith, N. Sciaky, M. Terasaki, M. Edidin, and J. Lippincott-Schwartz. Diffusional mobility of golgi proteins in membranes of living cells. *Science*, 273(5276): 797–801, 1996. (Cited on page 41.)

T.F. Coleman and Y. Li. An interior, trust region approach for nonlinear minimization subject to bounds. *SIAM Journal on Optimization*, 6:418–45, 1996. (Cited on page 104.)

S. Coombes, K.R. Tsavachidis, J.S. Morris, K.A. Baggerly, M.C. Hung, and H.M. Kuerer. Improved peak detection and quantification of mass spectrometry data acquired from surface-enhanced laser desorption and ionization by denoising spectra with the undecimated discrete wavelet transform. *PROTEOMICS*, 5(16):4107–17, 2005. (Cited on page 155.)

N. Coudray, J.L. Buessler, and J.P. Urban. Robust threshold estimation for images with unimodal histograms. *Pattern Recognition Letters*, 31(9):1010–9, 2010. (Cited on page 49.)

G. Cox. *Optical Imaging Techniques in Cell Biology*. Taylor & Francis Group, 1th edition, 2007. (Cited on pages 15, 18, 22, 24, 27, 28, 34, 151, and 152.)

G. Cox and C.J.R. Sheppard. Practical limits of resolution in confocal and non-linear microscopy. *Microscopy Research and Technique*, 63(1):18–22, 2004. (Cited on page 34.)

S. Cox, E. Rosten, J. Monypenny, T. Jovanovic-Talisman, D.T. Burnette, J. Lippincott-Schwartz, G.E. Jones, and R Heintzmann. Bayesian localization microscopy reveals nanoscale podosome dynamics. *Nature Methods*, 9(2):195–200, 2012. (Cited on page 55.)

J.C. Crocker and D.G. Grier. Methods of digital video microscopy for colloidal studies. *Journal of Colloid and Interface Science*, 179(1):298–310, 1996. (Cited on pages 44, 47, 50, and 102.)

P.A. Dalgarno, H.I.C. Dalgarno, A. Putoud, R. Lambert, L. Paterson, D.C. Logan, D.P. Towers, R.J. Warburton, and A.H. Greenaway. Multiplane imaging and three dimensional nanoscale particle tracking in biological microscopy. *Optics Express*, 18(2): 877–84, 2010. (Cited on page 60.)

S.B. Dalziel. Decay of rotating turbulence: some particle tracking experiments. In *Flow Visualization and Image Analysis*, pages 27–54. Springer Netherlands, 1th edition, 1993. (Cited on page 69.)

M.W. Davidson. Microscope objective specifications, 2013. URL http://www.microscopyu.com/articles/optics/objectivespecs.html. (Cited on page 24.)

R.N. Day and F. Schaufele. Fluorescent protein tools for studying protein dynamics in living cells: a review. *Journal of Biomedical Optics*, 13(3):031202–6, 2008. (Cited on page 42.)

A.P. Dempster, N.M. Laird, and D.B. Rubin. Maximum likelihood from incomplete data via the em algorithm. *Journal of the Royal Statistical Society. Series B (Methodological)*, 39(1):1–38, 1977. (Cited on pages 85 and 90.)

Y. Deng and J.W. Shaevitz. Effect of aberration on height calibration in three-dimensional localization-based microscopy and particle tracking. *Applied Optics*, 48 (10):1886–90, 2009. (Cited on pages 63, 99, and 149.)

W. Denk, J.H. Strickler, and W.W. Webb. Two-photon laser scanning fluorescence microscopy. *Science*, 248(4951):73–6, 1990. (Cited on page 34.)

H. Deschout, K. Neyts, and K. Braeckmans. The influence of movement on the localization precision of sub-resolution particles in fluorescence microscopy. *Journal of Biophotonics*, 5(1):97–109, 2012. (Cited on page 54.)

H. Deschout, F.C. Zanacchi, M. Mlodzianoski, A. Diaspro, J. Bewersdorf, S.T. Hess, and K. Braeckmans. Precisely and accurately localizing single emitters in fluorescence microscopy. *Nature Methods*, 11(3):253–66, 2014. (Cited on pages 46, 54, and 71.)

A. Diaspro, F. Federici, and M. Robello. Influence of refractive-index mismatch in high-resolution three-dimensional confocal microscopy. *Applied Optics*, 41(4):685–90, 2002. (Cited on page 62.)

A. Diaspro, G. Chirico, C. Usai, P. Ramoino, and J.W. Dobrucki. Photobleaching. In *Handbook of Biological Confocal Microscopy*, pages 690–702. Springer, 3th edition, 2006. (Cited on page 19.)

J. Dittman and T.A. Ryan. Molecular circuitry of endocytosis at nerve terminals. *Annual Review of Cell and Developmental Biology*, 25:133–60, 2009. (Cited on page 12.)

J.W. Dobrucki. Fluorescence microscopy. In *Fluorescence Microscopy - From Principles to Biological Applications*, pages 97–142. Wiley-Blackwell, 1th edition, 2013. (Cited on pages 18, 21, 22, 24, and 25.)

P. Du, W.A. Kibbe, and S.M. Lin. Improved peak detection in mass spectrum by incorporating continuous wavelet transform-based pattern matching. *BIOINFORMATICS*, 22:2059–65, 2006. (Cited on pages 157 and 165.)

G.A. Dunn, I.M. Dobbie, J. Monypenny, M.R. Holt, and D. Zicha. Fluorescence localization after photobleaching (flap): a new method for studying protein dynamics in living cells. *Journal of Microscopy*, 205(1):109–12, 2002. (Cited on page 41.)

M.L. Dustin and D. Depoil. New insights into the t cell synapse from single molecule techniques. *Nature Reviews Immunology*, 11:672–84, 2011. (Cited on page 3.)

M. Dyba, J. Keller, and S.W. Hell. Phase filter enhanced sted-4pi fluorescence microscopy: theory and experiment. *New Journal of Physics*, 7(134):1–21, 2005. (Cited on page 37.)

C. Eggeling, C. Ringemann, R. Medda, G. Schwarzmann, K. Sandhoff, S. Polyakova, V.N. Belov, B. Hein, V. Middendorff, A. Schönle, and S.W. Hell. Direct observation of the nanoscale dynamics of membrane lipids in a living cell. *Nature*, 457:1159–62, 2009. (Cited on page 77.)

M.D. Egger and M. Petran. New reflected-light microscope for viewing unstained brain and ganglion cells. *Science*, 157(3786):305–7, 1967. (Cited on page 34.)

A. Egner and S.W. Hell. Aberrations in confocal and multi-photon fluorescence microscopy induced by refractive index mismatch. In *Handbook of Biological Confocal Microscopy*, pages 404–13. Springer, 3th edition, 2006. (Cited on page 65.)

J. Enderlein, E. Toprak, and P.R. Selvin. Polarization effect on position accuracy of fluorophore localization. *Optics Express*, 14(18):8111–20, 2006. (Cited on page 53.)

E. Evergren, F. Benfenati, and O. Shupliakov. The synapsin cycle: A view from the synaptic endocytic zone. *Journal of Neuroscience Research*, 85(12):2648–56, 2007. (Cited on page 159.)

T.J. Feder, I. Brust-Mascher, J.P. Slattery, B. Baird, and W.W. Webb. Constrained diffusion or immobile fraction on cell surfaces: a new interpretation. *Biophysical Journal*, 70(6):2767–73, 1996. (Cited on page 44.)

M. Fernández-Suárez and A.Y. Ting. Fluorescent probes for super-resolution imaging in living cells. *Nature Reviews Molecular Cell Biology*, 9:929–43, 2008. (Cited on page 37.)

M.A.T. Figueiredo and R.D. Nowak. Wavelet-based image estimation: an empirical bayes approach using jeffrey's noninformative prior. *IEEE Transactions on Image Processing*, 10(9):1322–31, 2001. (Cited on page 50.)

J. Fölling, V. Belov, D. Riedel, A. Schönle, A. Egner, C. Eggeling, M. Bossi, and S.W. Hell. Fluorescence nanoscopy with optical sectioning by two-photon induced molecular switching using continuous-wave lasers. *Chemical Physics and Physical Chemistry*, 9 (2):321–6, 2008. (Cited on page 73.)

D. Freche, U. Pannasch, N. Rouach, and D. Holcman. Synapse geometry and receptor dynamics modulate synaptic strength. *PLOS ONE*, 6(10):e25122, 2011. (Cited on pages 13 and 180.)

M. Friedrich, Q. Gan, V. Ermolayev, and G.S. Harms. Sted-spim: Stimulated emission depletion improves sheet illumination microscopy resolution. *Biophysical Journal*, 100 (8):43–5, 2011. (Cited on page 37.)

M.A. Gaffield, L. Tabares, and W.J. Betz. Preferred sites of exocytosis and endocytosis colocalize during high- but not lower-frequency stimulation in mouse motor nerve terminals. *The Journal of Neuroscience*, 29(48):15308–16, 2009. (Cited on pages 152 and 180.)

C.G. Galizia and P.M. Lledo. *Neurosciences, From Molecule to Behavior: A University Textbook*. Springer Spektrum, 1th edition, 2013. (Cited on page 8.)

S.P. Gandhi and C.F. Stevens. Three modes of synaptic vesicular recycling revealed by single-vesicle imaging. *Nature*, 423:607–13, 2003. (Cited on pages 153, 154, 162, 164, and 172.)

J. Gelles, B.J. Schnapp, and M.P. Sheetz. Tracking kinesin-driven movements with nanometre-scale precision. *Letters to Nature*, 331:450–3, 1988. (Cited on page 51.)

A. Genovesio, T. Liedl, V. Emiliani, W.J. Parak, M. Coppey-Moisan, and J.C. Olivo-Marin. Multiple particle tracking in 3-d+t microscopy: method and application to the tracking of endocytosed quantum dots. *IEEE Transactions on Image Processing*, 15 (5):1062–70, 2006. (Cited on pages 50 and 70.)

K. Gerrow and A. Triller. Synaptic stability and plasticity in a floating world. *Current Opinion in Neurobiology*, 20(5):631–9, 2010. (Cited on page 14.)

R.N. Ghosh and W.W. Webb. Automated detection and tracking of individual and clustered cell surface low density lipoprotein receptor molecules. *IEEE Transactions on Image Processing*, 66(5):1301–18, 1994. (Cited on page 51.)

S.F. Gibson and F. Lanni. Experimental test of an analytical model of aberration in an oil-immersion objective lens used in three-dimensional light microscopy. *Journal of the Optical Society of America A*, 8(10):1601–13, 1991. (Cited on page 66.)

W.J. Godinez. *Probabilistic Tracking and Behavior Identification of Fluorescent Particles*. PhD thesis, PhD thesis, Ruperto-Carola University of Heidelberg, 2013. (Cited on pages 69 and 70.)

W.J. Godinez, M. Lampe, S. Wörz, B. Müller, R. Eils, and K. Rohr. Deterministic and probabilistic approaches for tracking virus particles in time-lapse fluorescence microscopy image sequences. *Medical Image Analysis*, 13(2):325–342, 2009. (Cited on page 70.)

M.P. Gordon, T. Ha, and P.R. Selvin. Single-molecule high-resolutionwith photobleaching imaging. *Proceedings of the National Academy of Sciences*, 101(17):6462–5, 2004. (Cited on page 39.)

T.J. Gould, D. Burke, J. Bewersdorf, and M.J. Booth. Adaptive optics enables 3d sted microscopy in aberrating specimens. *Optics Express*, 20(19):20998–1009, 2012. (Cited on pages 65 and 71.)

M. Goulian and S.M. Simon. Tracking single proteins within cells. *Biophysical Journal*, 79(4):2188–98, 2000. (Cited on pages 47 and 67.)

B. Granseth and L. Lagnado. The role of endocytosis in regulating the strength of hippocampal synapses. *The Journal of Physiology*, 586(24):5969–82, 2008. (Cited on page 152.)

B. Granseth, B. Odermatt, S.J. Royle, and L. Lagnado. Clathrin-mediated endocytosis is the dominant mechanism of vesicle retrieval at hippocampal synapses. *Neuron*, 51: 773–86, 2006. (Cited on pages 153, 154, 160, 161, and 164.)

B. Granseth, B. Odermatt, S.J. Royle, and L. Lagnado. Comment on "the dynamic control of kiss-and-run and vesicular reuse probed with single nanoparticles". *Science*, 325(5947):1499, 2009. (Cited on page 153.)

E. Gratton and M.J. vandeVen. Laser sources for confocal microscopy. In *Handbook of Biological Confocal Microscopy*, pages 80–125. Springer, 3th edition, 2006. (Cited on page 22.)

T.W. Groemer and J. Klingauf. Synaptic vesicles recycling spontaneously and during activity belong to the same vesicle pool. *Nature Neuroscience*, 10(2):145–7, 2007. (Cited on page 151.)

T. Grotjohann, I. Testa, M. Reuss, T. Brakemann, C. Eggeling, S.W. Hell, and S. Jakobs. rsegfp2 enables fast resolft nanoscopy of living cells. *eLife*, 00248:1–14, 2012. (Cited on page 37.)

G. Grynkiewicz, M. Poenie, and R.Y. Tsien. A new generation of ca2+ indicators with greatly improved fluorescence properties. *The Journal of Biological Chemistry*, 260(6): 3440–50, 1985. (Cited on page 152.)

D.L. Hall and J. Llinas. An introduction to multisensor data fusion. *Proceedings of the IEEE*, 85(1):6–23, 1997. (Cited on page 178.)

B. Harke, C.K. Ullal, J. Keller, and S.W. Hell. Three-dimensional nanoscopy of colloidal crystals. *Nano Letters*, 8(5):1309–13, 2008. (Cited on page 37.)

E. Hecht. *Optik*. Oldenbourg, 5th edition, 2009. (Cited on pages 15, 16, 21, 22, 24, and 28.)

M. Heilemann, S. van de Linde, M. Schüttpelz, R. Kasper, B. Seefeldt, A. Mukherjee, P. Tinnefeld, and M. Sauer. Subdiffraction-resolution fluorescence imaging with conventional fluorescent probes. *Angewandte Chemie*, 47(33):6172–6, 2008. (Cited on page 40.)

M. Heine, L. Groc, R. Frischknecht, B. Béïque, J.C. Lounis, G. Rumbaugh, R.L. Huganir, L. Cognet, and D. Choquet. Surface mobility of postsynaptic ampars tunes synaptic transmission. *Science*, 320(5873):201–5, 2008. (Cited on page 14.)

R. Heintzmann. Introduction to optics and photophysics. In *Fluorescence Microscopy - From Principles to Biological Applications*, pages 1–31. Wiley-Blackwell, 1th edition, 2013. (Cited on pages 18 and 19.)

R. Heintzmann and G. Ficz. Breaking the resolution limit in light microscopy. *Briefings in Functional Genomics*, 5(4):289–301, 2006. (Cited on pages 32 and 35.)

S. Hell, G. Reiner, C. Cremer, and E.H.K. Stelzer. Aberrations in confocal fluorescence microscopy induced by mismatches in refractive index. *Journal of Microscopy*, 169(3): 391–405, 1993. (Cited on pages 62, 63, 64, and 66.)

S.W. Hell. Far-field optical nanoscopy. *Science*, 316:1153–8, 2007. (Cited on pages 36 and 37.)

S.W. Hell and M. Kroug. Ground-state-depletion fluorscence microscopy: a concept for breaking the diffraction resolution limit. *Applied Physics B*, 60(5):495–7, 1995. (Cited on page 36.)

S.W. Hell and J. Wichmann. Breaking the diffraction resolution limit by stimulated emission: stimulated-emission-depletion fluorescence microscopy. *Optics Letters*, 19 (11):780–2, 1994. (Cited on page 36.)

J.A. Helmuth, C.J. Burckhardt, P. Koumoutsakos, U.F. Greber, and I.F. Sbalzarini. A novel supervised trajectory segmentation algorithm identifies distinct types of human adenovirus motion in host cells. *Journal of Structural Biology*, 159(3):347–58, 2007. (Cited on page 45.)

S.T. Hess, T.P.K Girirajan, and M.D. Mason. Ultra-high resolution imaging by fluorescence photoactivation localization microscopy. *Biophysical Journal*, 91(11):4258–72, 2006. (Cited on pages 39 and 40.)

S.T. Hess, T.J. Gould, M.V. Gudheti, S.A. Maas, K.D. Mills, and J. Zimmerberg. Dynamic clustered distribution of hemagglutinin resolved at 40 nm in living cell membranes discriminates between raft theories. *Proceedings of the National Academy of Sciences*, 104(44):17370–5, 2007. (Cited on pages 40 and 53.)

A.R. Hibbs, G. MacDonald, and K. Garsha. Practical confocal microscopy. In *Handbook of Biological Confocal Microscopy*, pages 650–71. Springer, 3th edition, 2006. (Cited on page 93.)

S. Hiware, P. Porwal, R. Velmurugan, and S. Chaudhuri. Modeling of psf for refractive index variation in fluorescence microscopy. In *18th IEEE International Conference on Image Processing (ICIP)*, pages 2037–40, 2011. (Cited on page 66.)

M. Hofmann, C. Eggeling, S. Jakobs, and S.W. Hell. Breaking the diffraction barrier in fluorescence microscopy at low light intensities by using reversibly photoswitchable proteins. *Proceedings of the National Academy of Sciences*, 102(49):17565–9, 2005. (Cited on pages 36 and 37.)

S.J. Holden, S. Uphoff, and A.N. Kapanidis. Daostorm: an algorithm for high- density super-resolution microscopy. *Nature Methods*, 8(4):279–80, 2011. (Cited on pages 55, 59, 91, 109, 112, 113, and 150.)

L. Holtzer, T. Meckel, and T. Schmidt. Nanometric three-dimensional tracking of individual quantum dots in cells. *Applied Physics Letters*, 90(5):53902–5, 2007. (Cited on pages 59, 61, 105, 106, and 118.)

E. Hoogendoorn, K.C. Crosby, D. Leyton-Puig, R.M.P Breedijk, K. Jalink, T.W.J. Gadella, and M. Postma. The fidelity of stochastic single-molecule super-resolution reconstructions critically depends upon robust background estimation. *Scientific Reports*, 4(3854):1–10, 2014. (Cited on page 53.)

H. Hsueh, H. Kuo, and C. Tsai. Multispectra cwt-based algorithm (mcwt) in mass spectra for peak extraction. *Journal of Biopharmaceutical Statistics*, 18(5):869–82, 2008. (Cited on page 165.)

B. Huang, S.A. Jones, B. Brandenburg, and X. Zhuang. Whole-cell 3d storm reveals interactions between cellular structures with nanometer-scale resolution. *Nature Methods*, 5(12):1047–52, 2008a. (Cited on pages 59, 62, 65, 73, 94, and 149.)

B. Huang, W. Wang, M. Bates, and X. Zhuang. Three-dimensional super-resolution imaging by stochastic optical reconstruction microscopy. *Science*, 319(5864):810–3, 2008b. (Cited on pages 59, 61, 63, 105, 106, and 118.)

B. Huang, M. Bates, and X. Zhuang. Super-resolution fluorescence microscopy. *Annual Review of Biochemistry*, 78:993–1016, 2009. (Cited on pages 30, 32, 35, and 40.)

B. Huang, H. Babcock, and X Zhuang. Breaking the diffraction barrier: Super-resolution imaging of cells. *Cell*, 143:1047–58, 2010. (Cited on page 32.)

F. Huang, S.L. Schwartz, J.M. Byars, and K.A. Lidke. Simultaneous multiple-emitter fitting for single molecule super-resolution imaging. *Biomedical Optics Express*, 2(5): 1377–93, 2011. (Cited on pages 55, 71, 85, 91, 106, 109, 112, 113, and 150.)

S. Huet, E. Karatekin, V.S. Tran, I. Fanget, S. Cribier, and J.P. Henry. Analysis of transient behavior in complex trajectories: Application to secretory vesicle dynamics. *Biophysical Journal*, 91(9):3542–59, 2006. (Cited on page 45.)

S. Inoué. Foundations of confocal scanned imaging in light microscopy. In *Handbook of Biological Confocal Microscopy*, pages 1–16. Springer, 3th edition, 2006. (Cited on pages 28, 30, 33, and 56.)

M. Isard and A. Blake. Condensation - conditional density propagation for visual tracking. *International Journal of Computer Vision*, 29(1):5–28, 1998. (Cited on page 70.)

I. Izeddin, M.E. Beheiry, J. Andilla, D. Ciepielewski, X. Darzacq, and M. Dahan. Psf shaping using adaptive optics for three-dimensional single-molecule super-resolution imaging and tracking. *Optics Express*, 20(5):4957–67, 2012a. (Cited on pages 59, 62, 65, 100, 105, and 149.)

I. Izeddin, J. Boulanger, V. Racine, C.G. Specht, A. Kechkar, D. Nair, A. Triller, D. Choquet, M. Dahan, and J.B. Sibarita. Wavelet analysis for single molecule localization microscopy. *Optics Express*, 20(3):2081–95, 2012b. (Cited on pages 50, 51, 55, 80, and 95.)

A. Jabłoński. Efficiency of anti-stokes fluorescence in dyes. *Nature*, 131:839–40, 1931. (Cited on page 18.)

A.K. Jain, R.P.W. Duin, and J. Mao. Statistical pattern recognition: A review. *IEEE Transactions on Pattern Analysis and Machine Intelligence*, 22(1):4–37, 2000. (Cited on page 155.)

R.F. Jansen and A.T. Maat. Automatic wave form classification of extracellular multi-neuron recordings. *Journal of Neuroscience Methods*, 41(2):123–32, 1992. (Cited on page 155.)

K. Jaqaman, D. Loerke, M. Mettlen, H. Kuwata, S. Grinstein, S.L. Schmid, and G. Danuser. Robust single-particle tracking in live-cell time-lapse sequences. *Nature Methods*, 5(8):695–702, 2008. (Cited on pages 43, 67, and 69.)

S. Jiang, X. Zhou, T. Kirchhausen, and S.T.C. Wong. Detection of molecular particles in live cells via machine learning. *Cytometry Part A*, 71A(8):563–75, 2007. (Cited on page 50.)

I.D. Johnson. Practical considerations in the selection and amplification of fluorescent probes. In *Handbook of Biological Confocal Microscopy*, pages 353–67. Springer, 3th edition, 2006. (Cited on page 26.)

M.F. Juette and J. Bewersdorf. Three-dimensional tracking of single fluorescent particles with submillisecond temporal resolution. *Nano Letters*, 10(11):4657–63, 2010. (Cited on page 61.)

M.F. Juette, T.J. Gould, M.D. Lessard, M.J. Mlodzianoski, B.S. Nagpure, B.T. Bennett, S.T. Hess, and J. Bewersdorf. Three-dimensional sub–100 nm resolution fluorescence microscopy of thick samples. *Nature Methods*, 5(6):527–9, 2010. (Cited on pages 60, 61, and 73.)

E.R. Kandel, J.H. Schwartz, T.M. Jessell, S.A. Siegelbaum, and A.J. Hudspeth. *Principles of Neural Science*. McGraw-Hill, 5th edition, 2013. (Cited on pages 7, 8, 13, and 174.)

H. Kaneko, S.S. Suzuki, J. Okada, and M. Akamatsu. Multineuronal spike classification based on multisite electrode recording, whole-waveform analysis, and hierarchical clustering. *IEEE Transactions on Biomedical Engineering*, 46(3):280–90, 1999. (Cited on page 155.)

H.P. Kao and A.S. Verkman. Tracking of single fluorescent particles in three dimensions: Use of cylindrical optics to encode particle position. *Biophysical Journal*, 67:1291–1300, 1994. (Cited on page 59.)

Y. Katayama, O. Burkacky, M. Meyer, C. Bräuchle, E. Gratton, and D.C. Lamb. Real-time nanomicroscopy via three-dimensional single-particle tracking. *Chemical Physics and Physical Chemistry*, 10(14):2458–64, 2009. (Cited on page 57.)

S.M Kay. *Fundamentals of Statistical Signal Processing: Estimation Theory.* Prentice Hall, 1th edition, 1993. (Cited on pages 52 and 156.)

F. Keinert. *Wavelets and Multiwavelets.* Chapman & Hall/CRC, 1th edition, 2004. (Cited on page 158.)

H.E. Keller. Objective lenses for confocal microscopy. In *Handbook of Biological Confocal Microscopy*, pages 145–61. Springer, 3th edition, 2006. (Cited on pages 20, 23, 24, and 65.)

J. Keller, A. Schönle, and S.W. Hell. Efficient fluorescence inhibition patterns for resolft microscopy. *Optics Express*, 15(6):3361–71, 2007. (Cited on page 36.)

K.H. Kim and S.J. Kim. Neural spike sorting under nearly 0-db signal-to-noise ratio using nonlinear energy operator and artificial neural-network classifier. *IEEE Transactions on Biomedical Engineering*, 47(10):1406–11, 2000. (Cited on page 155.)

K.H. Kim and S.J. Kim. A wavelet-based method for action potential detection from extracellular neural signal recording with low signal-to-noise ratio. *IEEE Transactions on Biomedical Engineering*, 50(8):999–1011, 2003. (Cited on pages 155, 156, 165, 166, and 178.)

S.H. Kim and T.A. Ryan. Synaptic vesicle recycling at cns synapses without ap-2. *The Journal of Neuroscience*, 29(12):3865–74, 2009. (Cited on page 152.)

H. Kirshner, F. Aguet, D. Sage, and M. Unser. 3-d psf fitting for fluorescence microscopy: implementation and localization application. *Journal of Microscopy*, 249(1): 13–25, 2013. (Cited on page 66.)

T.A. Klar and S.W. Hell. Subdiffraction resolution in far-field fluorescence microscopy. *Optics Letters*, 24(14):954–6, 1999. (Cited on page 36.)

T.A. Klar, S. Jakobs, M. Dyba, A. Egner, and S.W. Hell. Fluorescence microscopy with diffraction resolution barrier broken by stimulated emission. *Proceedings of the National Academy of Sciences*, 97(15):8206–10, 2000. (Cited on page 37.)

L. Komsta. Comparison of several methods of chromatographic baseline removal with a new approach based on quantile regression. *Chromatographia*, 73(7–8):721–31, 2011. (Cited on page 164.)

K. Kraszewski, O. Mundigl, L. Daniell, C. Verderio, M. Matteoli, and P. De Camilli. Synaptic vesicle dynamics in living cultured hippocampal neurons visualized with cy3-conjugated antibodies directed against the lumenal domain of synaptotagmin. *The Journal of Neuroscience*, 15(6):4328–42, 1995. (Cited on page 152.)

U. Kubitscheck. Principles of light microscopy. In *Fluorescence Microscopy - From Principles to Biological Applications*, pages 33–96. Wiley-Blackwell, 1th edition, 2013a. (Cited on pages 18, 20, 23, 29, 30, and 31.)

U. Kubitscheck, editor. *Fluorescence Microscopy - From Principles to Biological Applications*. Wiley-Blackwell, 1th edition, 2013b. (Cited on page 15.)

U. Kubitscheck, O. Kückmanna, T. Kuesa, and R. Peters. Imaging and tracking of single gfp molecules in solution. *Biophysical Journal*, 78:2170–9, 2000. (Cited on pages 39, 42, 46, 52, 75, 111, 134, and 159.)

H.W. Kuhn. The hungarian method for the assignment problem. *Naval Research Logistics*, 2(1):83–97, 1955. (Cited on page 91.)

N. Kumar, S. Satoor, and I. Buck. Fast parallel expectation maximization for gaussian mixture models on gpus using cuda. In *11th IEEE International Conference on High Performance Computing and Communications*, pages 103–9, 2009. (Cited on page 150.)

A. Kusumi, Y. Sako, and M. Yamamoto. Confined lateral diffusion of membrane receptors as studied by single particle tracking (nanovid microscopy). effects of calcium-induced differentiation in cultured epithelial cells. *Biophysical Journal*, 65(5):2021–40, 1993. (Cited on pages 44 and 45.)

A. Kusumi, T.K. Fujiwara, N. Morone, K.J. Yoshida, R. Chadda, M. Xie, R.S. Kasai, and K.G.N. Suzuki. Membrane mechanisms for signal transduction: The coupling of the meso-scale raft domains to membrane-skeleton-induced compartments and dynamic protein complexes. *Seminars in Cell & Developmental Biology*, 23(2):126–44, 2012. (Cited on pages 14, 45, and 77.)

B.C. Lagerholm, L. Averett, G.E. Weinreb, K. Jacobson, and N.L. Thompson. Analysis method for measuring submicroscopic distances with blinking quantum dots. *Biophysical Journal*, 91(8):3050–60, 2006. (Cited on page 39.)

J.R. Lakowicz. *Principles of Fluorescence Spectroscopy*. Springer, 3th edition, 2006. (Cited on pages 15, 18, and 42.)

G.M. Lee, A. Ishihara, and K.A. Jacobson. Direct observation of brownian motion of lipids in a membrane. *Proceedings of the National Academy of Sciences*, 88(14):6274–8, 1991. (Cited on page 51.)

J. Lee, K. Miyanaga, S. Ueda, and N. Hohng. Video-rate confocal microscopy for single-molecule imaging in live cells and superresolution fluorescence imaging. *Biophysical Journal*, 103(8):1691–7, 2012. (Cited on page 149.)

G.A. Lessard, P.M. Goodwin, and J.H. Werner. Three-dimensional tracking of individual quantum dots. *Applied Physics Letters*, 91:2241061–3, 2007. (Cited on page 57.)

M. Levandowsky and D. Winter. Distance between sets. *Letters to nature*, 234:34–5, 1971. (Cited on page 171.)

V. Levi, Q. Ruan, and E. Gratton. 3-d particle tracking in a two-photon microscope: application to the study of molecular dynamics in cells. *Biophysical Journal*, 88(4):2919–28, 2005. (Cited on page 57.)

M.D. Lew, S.F. Lee, M. Badieirostami, and W.E. Moerner. Corkscrew point spread function for far-field three-dimensional nanoscale localization of pointlike objects. *Optics Letters*, 36(2):202–4, 2011. (Cited on page 60.)

K.A. Lidke, T.M. Rieger, B. andJovin, and R. Heintzmann. Superresolution by localization of quantum dots using blinking statistics. *Optics Express*, 13(18):7052–62, 2005. (Cited on pages 39 and 54.)

J. Lippincott-Schwartz, E. Snapp, and A. Kenworthy. Studying protein dynamics in living cells. *Nature Reviews Molecular Cell Biology*, 2:444–56, 2001. (Cited on page 42.)

X. Lou, F. Fan, M. Messa, A. Raimondi, Y. Wu, L.L. Looger, S.M. Ferguson, and P.D. Camilli. Reduced release probability prevents vesicle depletion and transmission failure at dynamin mutant synapses. *Proceedings of the National Academy of Sciences*, 109(8):515–23, 2012. (Cited on page 12.)

S. Mallat, editor. *A Wavelet Tour of Signal Processing: The Sparse Way*. Academic Press, 3th edition, 2008. (Cited on pages 156 and 163.)

S. Mallat and S. Zhong. Characterization of signals from multiscale edges. *IEEE Transactions on Pattern Analysis and Machine Intelligence*, 14(7):710–32, 1992. (Cited on pages 156 and 165.)

S.G. Mallat. A theory for multiresolution signal decomposition: the wavelet representation. *IEEE Transactions on Pattern Analysis and Machine Intelligence*, 11(7):674–93, 1989. (Cited on page 163.)

S. Manley, J.M. Gillette, G.H. Patterson, H. Shroff, H.F. Hess, E. Betzig, and J. Lippincott-Schwartz. High-density mapping of single-molecule trajectories with photoactivated localization microscopy. *Nature Methods*, 5(2):155–7, 2008. (Cited on pages 40 and 43.)

P.N. Marsh, D. Burns, and J.M. Girkin. Practical implementation of adaptive optics in multiphoton microscopy. *Optics Express*, 11(10):1123–30, 2003. (Cited on page 65.)

S.B. Marston, I.D.C. Fraser, W. Bing, and G. Roper. A simple method for automatic tracking of actin filaments in the motility assay. *Journal of Muscle Research and Cell Motility*, 17(4):497–506, 1996. (Cited on page 67.)

D.S. Martin, M.B. Forstner, and J.A. Käs. Apparent subdiffusion inherent to single particle tracking. *Biophysical Journal*, 83(4):2109–17, 2002. (Cited on page 46.)

R.J. Martin-Palma, M. Manso, and V. Torres-Costa. Optical biosensors based on semiconductor nanostructures. *Sensors*, 9(7):5149–72, 2009. (Cited on page 27.)

M. Maus, M. Cotlet, J. Hofkens, T. Gensch, and F.C. De Schryver. An experimental comparison of the maximum likelihood estimation and nonlinear least-squares fluorescence lifetime analysis of single molecules. *Analytical Chemistry*, 73(9):2078–86, 2001. (Cited on page 90.)

A.K. McAllister and C.F. Stevens. Nonsaturation of ampa and nmda receptors at hippocampal synapses. *Proceedings of the National Academy of Sciences*, 97(11):6173–8, 2000. (Cited on page 14.)

R. McGorty, J. Schnitzbauer, W. Zhang, and B. Huang. Correction of depth-dependent aberrations in 3d single-molecule localization and super-resolution microscopy. *Optics Letters*, 39(2):275–278, 2014. (Cited on page 66.)

G.J. McLachlan and P.N. Jones. Fitting mixture models to grouped and truncated data via the em algorithm. *Biometrics*, 44(2):571–8, 1988. (Cited on page 86.)

E. Meijering, I. Smal, and G. Danuser. Tracking in molecular bioimaging. *IEEE Signal Processing Magazine*, 23(3):46–53, 2006. (Cited on page 47.)

E. Meijering, O. Dzyubachyk, I. Smal, and W.A. van Cappellen. Tracking in cell and developmental biology. *Seminars in Cell and Developmental Biology*, 20(8):894–902, 2009. (Cited on page 69.)

E. Meijering, O. Dzyubachyk, and I. Smal. Methods for cell and particle tracking. *Methods in Enzymology*, 504:183–200, 2012. (Cited on pages 43, 67, 72, and 110.)

X. Michalet. Mean square displacement analysis of single-particle trajectories with localization error: Brownian motion in an isotropic medium. *Physical Review E*, 82(4): 041914, 2010. (Cited on pages 43, 45, and 46.)

X. Michalet, F.F. Pinaud, L.A. Bentolila, J.M. Tsay, S. Doose, J.J. Li, G. Sundaresan, A.M. Wu, S.S. Gambhir, and S. Weiss. Quantum dots for live cells, in vivo imaging, and diagnostics. *Science*, 307(5709):538–44, 2005. (Cited on page 73.)

G. Miesenböck and I.G. Kevrekidis. Optical imaging and control of genetically designated neurons in functioning circuits. *Annual Review of Neuroscience*, 28:533–63, 2005. (Cited on page 152.)

G. Miesenböck, D.A. De Angelis, and J.E. Rothman. Visualizing secretion and synaptic transmission with ph-sensitive green fluorescent proteins. *Letters to Nature*, 394:192–5, 1998. (Cited on page 152.)

M. Minsky. Microscopy apparatus. *US patent*, 3,013,467, 1961. (Cited on page 33.)

M.J. Mlodzianoski, M-F. Juette, G.L. Beane, and J. Bewersdorf. Experimental characterization of 3d localization techniques for particle-tracking and super-resolution microscopy. *Optics Express*, 17(10):8264–77, 2009. (Cited on pages 61, 111, and 119.)

M. Monici. Cell and tissue autofluorescence research and diagnostic applications. *Biotechnology Annual Review*, 11:227–56, 2005. (Cited on page 19.)

D. Montiel, H. Cang, and H. Yang. Quantitative characterization of changes in dynamical behavior for single-particle tracking studies. *The Journal of Physical Chemistry B*, 110(40):19763–70, 2006. (Cited on page 45.)

K.I. Mortensen, L.S. Churchman, J.A. Spudich, and H. Flyvbjerg. Optimized localization analysis for single-molecule tracking and super-resolution microscopy. *Nature Methods*, 7(5):377–81, 2010. (Cited on pages 38, 52, 53, 55, and 84.)

N. Mtetwa and L.S. Smith. Smoothing and thresholding in neuronal spike detection. *Neurocomputing*, 69(10–12):1366–70, 2006. (Cited on page 155.)

E.A. Mukamel, H. Babcock, and X. Zhuang. Statistical deconvolution for superresolution fluorescence microscopy. *Biophysical Journal*, 102(10):2391–400, 2012. (Cited on page 56.)

U.V. Nägerl, K.I. Willig, B. Hein, S.W. Hell, and T. Bonhoeffer. Live-cell imaging of dendritic spines by sted microscopy. *Proceedings of the National Academy of Sciences*, 105(48):18982–7, 2008. (Cited on pages 37 and 65.)

D Nair, E. Hosy, J.D. Petersen, A. Constals, G. Giannone, D. Choquet, and J.B. Sibarita. Super-resolution imaging reveals that ampa receptors inside synapses are dynamically organized in nanodomains regulated by psd95. *The Journal of Neuroscience*, 33 (32):13204–24, 2013. (Cited on pages 40 and 43.)

H. Nakatani, T. Watanabe, and N. Hoshimiya. Detection of nerve action potentials under low signal-to-noise ratio condition. *IEEE Transactions on Biomedical Engineering*, 48(8):845–9, 2001. (Cited on page 156.)

N. Naredi-Rainer, J. Prescher, A. Hartschuh, and D.C. Lamb. Confocal microscopy. In *Fluorescence Microscopy - From Principles to Biological Applications*, pages 175–213. Wiley-Blackwell, 1th edition, 2013. (Cited on pages 33 and 34.)

M. Natora and K. Obermayer. Research article an unsupervised and drift-adaptive spike detection algorithm based on hybrid blind beamforming. *EURASIP Journal on Advances in Signal Processing*, 696741:1–13, 2011. (Cited on page 156.)

Z. Nenadic and J.W. Burdick. Spikedetection using the continuous wavelet transform. *IEEE Transactions on Biomedical Engineering*, 52(1):74–87, 2005. (Cited on pages 157 and 178.)

K.C. Neuman, E.A. Abbondanzieri, and S.M. Block. Measurement of the effective focal shift in an optical trap. *Optics Letters*, 30(11):1318–20, 2005. (Cited on page 62.)

H. Niedrig, editor. *Lehrbuch der Experimentalphysik*. Walter de Gruyter, 9th edition, 1993. (Cited on page 56.)

G.U. Nienhaus and K. Nienhaus. Fluorescence labeling. In *Fluorescence Microscopy - From Principles to Biological Applications*, pages 143–73. Wiley-Blackwell, 1th edition, 2013. (Cited on pages 19, 26, 27, 28, 42, 75, and 167.)

P. Nipkow. Elektrisches teleskop. *German Patent*, 30,105, 1884. (Cited on page 34.)

A. Nolte, J.B. Pawley, and L. Höring. Non-laser light sources for three-dimensional microscopy. In *Handbook of Biological Confocal Microscopy*, pages 126–44. Springer, 3th edition, 2006. (Cited on page 21.)

H. Nyquist. Certain topics in telegraph transmission theory. *Transactions AIEE*, 47: 38–42, 1928. (Cited on page 31.)

R.J. Ober, S. Ram, and E.S. Ward. Localization accuracy in single-molecule microscopy. *Optics Express*, 86(2):1185–200, 2004. (Cited on pages 38, 52, and 53.)

A.M. van Oijen, J. Köhler, J. Schmidt, M. Müller, and G.J. Brakenhoff. 3-dimensional super-resolution by spectrally selective imaging. *Chemical Physics Letters*, 292:183–7, 1998. (Cited on pages 39, 56, and 57.)

J.C. Olivo-Marin. Extraction of spots in biological images using multiscale products. *Pattern Recognition*, 35(9):1989–96, 2002. (Cited on pages 48, 49, 50, 164, and 165.)

N. Otsu. A threshold selection method from gray-level histograms. *Automatica*, 20(1): 62–6, 1975. (Cited on page 49.)

R. Parthasarathy. Rapid, accurate particle tracking by calculation of radial symmetry centers. *Nature Methods*, 9(7):724–8, 2012. (Cited on page 51.)

A. Patwardhan. Subpixel position and measurement using 1d, 2d and 3d centroid algorithms with emphasis on applications in confocal microscopy. *Journal of Microscopy*, 186(3):246–57, 1997. (Cited on page 51.)

S.R.P. Pavani, M.A. Thompson, J.S. Biteen, S.J. Lord, N. Liu, R.J. Twieg, R. Piestun, and W.E. Moerner. Three-dimensional, single-molecule fluorescence imaging beyond the diffraction limit by using a double-helix point spread function. *Proceedings of the National Academy of Sciences*, 106(9):2995–9, 2009. (Cited on pages 60 and 61.)

J.B. Pawley. Fundamental limits in confocal microscopy. In *Handbook of Biological Confocal Microscopy*, pages 20–42. Springer, 3th edition, 2006a. (Cited on pages 24, 25, 31, and 47.)

J.B. Pawley. Points, pixels, and gray levels: Digitizing image data. In *Handbook of Biological Confocal Microscopy*, pages 59–79. Springer, 3th edition, 2006b. (Cited on pages 26, 31, and 32.)

J.B. Pawley, editor. *Handbook of Biological Confocal Microscopy*. Springer, 3th edition, 2006c. (Cited on page 15.)

R. Peters, J. Peters, K.H. Tews, and W. Bähr. A microfluorimetric study of translational diffusion in erythrocyte membranes. *Biochimica et Biophysica Acta*, 367(3):282–94, 1974. (Cited on page 41.)

R. Peters, A. Brünger, and K. Schulten. Continuous fluorescence microphotolysis: A sensitive method for study of diffusion processes in single cells. *Proceedings of the National Academy of Sciences*, 78(2):962–6, 1981. (Cited on page 41.)

M. Piccardi. Background subtraction techniques: a review. In *2004 IEEE International Conference on Systems, Man and Cybernetics*, pages 3099–104, 2004. (Cited on page 53.)

C. Pouzat, O. Mazor, and G. Laurent. Using noise signature to optimize spike-sorting and to assess neuronal classification quality. *Journal of Neuroscience Methods*, 122(1): 43–57, 2002. (Cited on page 155.)

P. Prabhat, S. Ram, E.S. Ward, and R.J. Ober. Simultaneous imaging of different focal planes in fluorescence microscopy for the study of cellular dynamics in three dimensions. *IEEE Transactions on NanoBioscience*, 3(4):237–42, 2004. (Cited on page 60.)

A. Punge, S.O. Rizzoli, R. Jahn, J.D. Wildanger, L. Meyer, A. Schönle, L. Kastrup, and S.W. Hell. 3d reconstruction of high-resolution sted microscope images. *Microscopy Research and Technique*, 71(9):644–50, 2008. (Cited on page 37.)

H. Qian, M.P. Sheetz, and E.L. Elson. Single particle tracking. analysis of diffusion and flow in two-dimensional systems. *Biophysical Journal*, 60(4):910–21, 1991. (Cited on pages 43, 45, 46, and 116.)

X. Qu, D. Wu, L. Mets, and N.F. Scherer. Nanometer-localized multiplefluorescence microscopy single-molecule. *Proceedings of the National Academy of Sciences*, 101(31): 11298–303, 2004. (Cited on page 39.)

T. Quan, H. Zhu, X. Liu, Y. Liu, J. Ding, S. Zeng, and Z.L. Huang. High-density localization of active molecules using structured sparse model and bayesian information criterion. *Optics Express*, 19(18):16963–74, 2011. (Cited on pages 55 and 150.)

S. Quirin, S.R.P. Pavani, and R. Piestun. Optimal 3d single-molecule localization for superresolution microscopy with aberrations and engineered point spread functions. *Proceedings of the National Academy of Sciences*, 109(3):675–9, 2012. (Cited on page 65.)

R. Quiroga, Z. Nadasdy, and Y. Ben-Shaul. Unsupervised spike detection and sorting with wavelets and superparamagnetic clustering. *Neural Computation*, 16(8):1661–87, 2004. (Cited on pages 155 and 169.)

V. Racine, A. Hertzog, J. Jouanneau, J. Salamero, C. Kervrann, and J.-B. Sibarita. Multiple-target tracking of 3d fluorescent objects based on simulated annealing. In *3rd IEEE International Symposium on Biomedical Imaging: Nano to Macro*, pages 1020–3, 2006. (Cited on page 80.)

T. Ragan, H. Huang, P. So, and E. Gratton. 3d particle tracking on a two-photon microscope. *Journal of Fluorescence*, 16(3):325–36, 2006. (Cited on pages 59, 73, and 149.)

S. Ram, E.S. Ward, and R.J. Ober. Beyond rayleigh's criterion: A resolution measure with application to single-molecule microscopy. *Proceedings of the National Academy of Sciences*, 103(12):4457–62, 2006. (Cited on pages 54 and 55.)

S. Ram, P. Prabhat, J. Chao, E.S. Ward, and R.J. Ober. High accuracy 3d quantum dot tracking with multifocal plane microscopy for the study of fast intracellular dynamics in live cells. *Biophysical Journal*, 95:6025–43, 2008. (Cited on page 60.)

L. Rayleigh. Investigations in optics with special reference to the spectroscope. *Philosophical Magazine*, 8:261–74, 1879. (Cited on page 30.)

E. Rebollo, K. Karkali, F. Mangione, and E. Martín-Blanco. Live imaging in drosophila: The optical and genetic toolkits. *Methods*, 68(1):48–59, 2014. (Cited on page 149.)

D.B. Reid. An algorithm for tracking multiple targets. *IEEE Transactions on Automatic Control*, 24(6):843–54, 1979. (Cited on page 67.)

M. Renner, D. Choquet, and A. Triller. Control of the postsynaptic membrane viscosity. *The Journal of Neuroscience*, 29(9):2926–37, 2009. (Cited on pages 77 and 82.)

M. Renner, Y. Domanov, F. Sandrin, I. Izeddin, P. Bassereau, and A. Triller. Lateral diffusion on tubular membranes: Quantification of measurements bias. *PLOS ONE*, 6(9):e25731, 2011. (Cited on pages 3, 82, 140, and 145.)

C. Ribrault, K. Sekimoto, and A. Triller. From the stochasticity of molecular processes to the variability of synaptic transmission. *Nature Reviews Neuroscience*, 12:375–87, 2011. (Cited on pages 13 and 14.)

J.G. Ritter, R. Veith, J.P. Siebrasse, and U. Kubitscheck. High-contrast single-particle tracking by selective focal plane illumination microscopy. *Optics Express*, 16(10):7142–52, 2008. (Cited on page 73.)

J.G. Ritter, R. Veith, A. Veenendaal, J.P. Siebrasse, and U. Kubitscheck. Light sheet microscopy for single molecule tracking in living tissue. *PLOS ONE*, 5(7):e11639, 2010. (Cited on pages 59 and 149.)

E. Rittweger, K.Y. Han, S.E. Irvine, C. Eggeling, and S.W. Hell. Sted microscopy reveals crystal colour centres with nanometric resolution. *Nature Photonics*, 3:144–7, 2009. (Cited on page 36.)

M.S. Robbins and B.J. Hadwen. The noise performance of electron multiplying charge-coupled devices. *IEEE Transactions on Electron Devices*, 50(5):1227–32, 2003. (Cited on page 26.)

H. Robenek. *Mikroskopie in Forschung und Praxis*. GIT VERLAG, 1th edition, 1995. (Cited on pages 15, 19, 22, and 23.)

S.S. Rogers, T.A. Waigh, X. Zhao, and J.R. Lu. Precise particle tracking against a complicated background: polynomial fitting with gaussian weight. *Physical Biology*, 4: 220–7, 2007. (Cited on pages 52, 53, and 54.)

P.L. Rosin. Unimodal thresholding. *Pattern Recognition*, 34(11):2083–96, 2001. (Cited on page 49.)

S.J. Royle, B. Granseth, B. Odermatt, A. Derevier, and L. Lagnado. Imaging phluorin-based probes at hippocampal synapses. In *Membrane Trafficking*, volume 457, pages 293–303. Humana Press, 2008. (Cited on pages 160, 161, and 164.)

J. Rudnick and G. Gaspari. The shapes of random walks. *Science*, 237(4813):384–9, 1987. (Cited on page 45.)

M.J. Rust, M. Bates, and X. Zhuang. Stochastic optical reconstruction microscopy (storm) provides sub-diffraction-limit image resolution. *Nature Methods*, 3(10):793–5, 2006. (Cited on pages 39 and 40.)

D. Sage, F.R. Neumann, F. Hediger, S.M. Gasser, and M. Unser. Automatic tracking of individual fluorescence particles: Application to the study of chromosome dynamics. *IEEE Transactions on Image Processing*, 14(9):1372–83, 2005. (Cited on pages 47, 49, 68, and 83.)

S.J. Sahl and W.E. Moerner. Super-resolution fluorescence imaging with single molecules. *Current Opinion in Structural Biology*, 23(5):778–87, 2013. (Cited on pages 38 and 58.)

S. Sankaranarayanan and T.A. Ryan. Real-time measurements of vesicle-snare recycling in synapses of the central nervous system. *Nature Cell Biology*, 2:197–204, 2000. (Cited on pages 153, 162, and 164.)

S. Sankaranarayanan, D. De Angelis, J.E. Rothman, and T.A. Ryan. The use of phluorins for optical measurements of presynaptic activity. *Biophysical Journal*, 79(4):2199–208, 2000. (Cited on pages 153 and 154.)

P.A. Santi. Light sheet fluorescence microscopy a review. *Journal of Histochemistry & Cytochemistry*, 59(2):129–38, 2011. (Cited on page 73.)

S. Saurabh, S. Maji, and M.P. Bruchez. Evaluation of scmos cameras for detection and localization of single cy5 molecules. *Optics Express*, 20(7):7338–49, 2012. (Cited on page 24.)

M.J. Saxton. Lateral diffusion in an archipelago. single-particle diffusion. *Biophysical Journal*, 64(6):1766–80, 1993. (Cited on pages 44, 45, and 46.)

M.J. Saxton. Single-particle tracking: connecting the dots. *Nature Methods*, 5(8):671–2, 2008. (Cited on page 70.)

M.J. Saxton and K. Jacobson. Single-particle tracking: Applications to membrane dynamics. *Annual Review of Biophysics and Biomolecular Structure*, 26:373–99, 1997. (Cited on pages 42, 43, 44, 45, 46, and 80.)

I.F. Sbalzarini and P. Koumoutsakos. Feature point tracking and trajectory analysis for video imaging in cell biology. *Journal of Structural Biology*, 151(2):182–95, 2005. (Cited on pages 43 and 69.)

M. Scanziani and M. Häusser. Electrophysiology in the age of light. *Nature*, 461:930–9, 2009. (Cited on pages 151, 179, and 183.)

L. Schermelleh, R. Heintzmann, and H. Leonhardt. A guide to super-resolution fluorescence microscopy. *Journal of General Physiology*, 190(2):165–75, 2010. (Cited on pages 2, 32, 40, and 73.)

T.H. Schmidt, G.J. Schütz, W. Baumgartner, H.J. Gruber, and H. Schindler. Imaging of single molecule diffusion. *Proceedings of the National Academy of Sciences*, 93(7):2926–9, 1996. (Cited on pages 39 and 68.)

R. Schneggenburger and E. Neher. Presynaptic calcium and control of vesicle fusion. *Current Opinion in Neurobiology*, 15(3):266–74, 2005. (Cited on page 14.)

G.J. Schütz, W. Trabesinger, and T. Schmidt. Direct observation of ligand colocalization on individual receptor molecules. *Biophysical Journal*, 74(5):2223–6, 1998. (Cited on page 39.)

G.J. Schütz, G. Kada, V.P. Pastushenko, and H. Schindler. Properties of lipid microdomains in a muscle cell membrane visualized by single molecule microscopy. *The EMBO Journal*, 19(5):892–901, 2000a. (Cited on pages 42 and 46.)

G.J. Schütz, V.P. Pastushenko, H.J. Gruber, H.G. Knaus, B. Pragl, and H. Schindler. 3d imaging of individual ion channels in live cells at 40 nm resolution. *Single Molecules*, 1:25–31, 2000b. (Cited on pages 56, 75, and 167.)

M. Schwertner, M.J. Booth, and T. Wilson. Characterizing specimen induced aberrations for high na adaptive optical microscopy. *Optics Express*, 12(26):6540–52, 2004. (Cited on page 65.)

A. Sergé, N. Bertaux, H. Rigneault, and D. Marguet. Dynamic multiple-target tracing to probe spatiotemporal cartography of cell membranes. *Nature Methods*, 5(8):687–94, 2008. (Cited on pages 55 and 68.)

S. Shahid, J. Walker, and L.S. Smith. A new spike detection algorithm for extracellular neural recordings. *IEEE Transactions on Biomedical Engineering*, 57(4):853–66, 2010. (Cited on pages 155 and 156.)

C.E. Shannon. Communication in the presence of noise. *Proceedings of the IRE*, 37:10–21, 1949. (Cited on page 31.)

G.M. Shepherd. *Neurobiology*. Oxford University Press, 3th edition, 1994. (Cited on pages 7 and 8.)

C.J.R. Sheppard and M. Gu. Aberration compensation in confocal microscopy. *Applied Optics*, 30(25):3563–8, 1991. (Cited on page 65.)

C.J.R. Sheppard and P. Török. Effects of specimen refractive index on confocal imaging. *Journal of Microscopy*, 185(3):366–74, 1997. (Cited on pages 62 and 64.)

L. Sherman, J.Y. Ye, O. Albert, and T.B. Norris. Adaptive correction of depth-induced aberrations in multiphoton scanning microscopy using a deformable mirror. *Journal of Microscopy*, 206(1):65–71, 2002. (Cited on page 65.)

O. Shimomura, F.H. Johnson, and Y. Saiga. Extraction, purification and properties of aequorin, a bioluminescent protein from the luminous hydromedusan, aequorea. *Journal of Cellular and Comparative Physiology*, 59(3):223–39, 1962. (Cited on page 26.)

T. Shimozawa, K. Yamagata, T. Kondo, S. Hayashi, A. Shitamukai, D. Konno, F. Matsuzaki, J. Takayama, S. Onami, H. Nakayama, Y. Kosugi, T.M. Watanabe, K. Fujita, and Y. Mimori-Kiyosue. Improving spinning disk confocal microscopy by preventing pinhole cross-talk for intravital imaging. *Proceedings of the National Academy of Sciences*, 110(9):3399–404, 2013. (Cited on pages 65 and 73.)

H. Shroff, C.G. Galbraith, J.A. Galbraith, and E. Betzig. Live-cell photoactivated localization microscopy of nanoscale adhesion dynamics. *Nature Methods*, 5(5):417–23, 2008. (Cited on page 40.)

G. Shtengel, J.A. Galbraith, C.G. Galbraith, J. Lippincott-Schwartz, J.M. Gillette, S. Manley, R. Sougrat, C.M. Waterman, P. Kanchanawong, M.W. Davidson, R.D. Fettera, and H.F. Hess. Interferometric fluorescent super-resolution microscopy resolves 3d cellular ultrastructure. *Proceedings of the National Academy of Sciences*, 106(9):3125–30, 2008. (Cited on page 61.)

J.B. Sibarita. Deconvolution microscopy. *Microscopy Techniques*, 95:201–43, 2005. (Cited on page 47.)

J.B. Sibarita. High-density single-particle tracking: quantifying molecule organization and dynamics at the nanoscale. *Histochemistry and Cell Biology*, 141(6):587–95, 2014. (Cited on pages 3 and 150.)

P.D. Simonson, E. Rothenberg, and P.R. Selvin. Single-molecule-based super-resolution images in the presence of multiple fluorophores. *Nano Letters*, 11:5090–6, 2011. (Cited on page 39.)

R. Simson, E.D. Sheets, and K. Jacobson. Detection of temporary lateral confinement of membrane proteins using single-particle tracking analysis. *Biophysical Journal*, 69(3):989–93, 1995. (Cited on page 45.)

R. Sinha, S. Ahmed, R. Jahn, and J. Klingauf. Two synaptobrevin molecules are sufficient for vesicle fusion in central nervous system synapses. *Proceedings of the National Academy of Sciences*, 108(34):14318–23, 2011. (Cited on page 152.)

L. Sjulson and G. Miesenböck. Optical recording of action potentials and other discrete physiological events: A perspective from signal detection theory. *Physiology*, 22:47–55, 2007. (Cited on page 152.)

I. Smal, W. Niessen, and E. Meijering. Advanced particle filtering for multiple object tracking in dynamic fluorescence microscopy images. In *4th IEEE International Symposium on Biomedical Imaging: From Nano to Macro*, pages 1048–51, 2007. (Cited on pages 67 and 70.)

I. Smal, E. Meijering, K. Draegestein, N. Galjart, I. Grigoriev, A. Akhmanova, M.E. van Royen, A.B. Houtsmuller, and W. Niessen. Multiple object tracking in molecular bioimaging by rao-blackwellized marginal particle filtering. *Medical Image Analysis*, 12(6):764–77, 2008a. (Cited on page 70.)

I. Smal, W. Niessen, and E. Meijering. A new detection scheme for multiple object tracking in fluorescence microscopy by joint probabilistic data association filtering. In *5th IEEE International Symposium on Biomedical Imaging: From Nano to Macro*, pages 264–7, 2008b. (Cited on page 50.)

I. Smal, M. Loog, W. Niessen, and E. Meijering. Quantitative comparison of spot detection methods in fluorescence microscopy. *IEEE Transactions on Medical Imaging*, 29(2):282–301, 2010. (Cited on pages 50, 83, and 109.)

A. Small and S. Stahlheber. Fluorophore localization algorithms for super-resolution microscopy. *Nature Methods*, 11(3):267–79, 2014. (Cited on pages 53 and 54.)

A.R. Small. Theoretical limits on errors and acquisition rates in localizing switchable fluorophores. *Biophysical Journal*, 96(2):16–8, 2009. (Cited on page 54.)

S. Sokoll, K. Tönnies, and M. Heine. Towards fast 3d nanoparticle localization for studying molecular dynamics in living cells. In *BIOINFORMATICS: International Conference on Bioinformatics Models, Methods and Algorithms*, pages 210–5, 2011. (Cited on pages 63, 92, and 98.)

S. Sokoll, H. Beelitz, M. Heine, and K. Tönnies. Towards automatic reconstruction of axonal structures in volumetric microscopy images depicting only active synapses. In *3rd International Conference on Image Processing Theory, Tools and Applications (IPTA)*, pages 426–31, 2012a. (Cited on page 180.)

S. Sokoll, K. Tönnies, and M. Heine. Detection of spontaneous vesicle release at individual synapses using multiple wavelets in a cwt-based algorithm. In *Medical Image Computing and Computer-Assisted Intervention (MICCAI)*, pages 165–72, 2012b. (Cited on page 158.)

S. Sokoll, K. Tönnies, and M. Heine. An online calibration method for astigmatism-based 3d particle tracking in complex living tissue. In *10th IEEE International Symposium on Biomedical Imaging: From Nano to Macro*, pages 181–4, 2013. (Cited on pages 92 and 96.)

C.G. Specht, I. Izeddin, P.C. Rodriguez, M.E. Beheiry, P. Rostaing, X. Darzacq, M. Dahan, and A. Triller. Quantitative nanoscopy of inhibitory synapses: Counting gephyrin molecules and receptor binding sites. *Neuron*, 79(2):308–21, 2013. (Cited on page 71.)

M. Speidel, A. Jonáš, and E.L. Florin. Three-dimensional tracking of fluorescent nanoparticles with subnanometer precision by use of off-focus imaging. *Optics Letters*, 28:69–71, 2003. (Cited on pages 57 and 58.)

J.H. Spille, T. Kaminski, H.P. Königshoven, and U. Kubitscheck. Dynamic three-dimensional tracking of single fluorescent nanoparticles deep inside living tissue. *Optics Express*, 20(18):19697–707, 2012. (Cited on pages 59, 62, 73, and 105.)

S. Stallinga and B. Rieger. Accuracy of the gaussian point spread function model in 2d localization microscopy. *Optics Express*, 18(24):24461–76, 2010. (Cited on page 53.)

J.L. Starck, J. Fadili, and F. Murtagh. The undecimated wavelet decomposition and its reconstruction. *IEEE Transactions on Image Processing*, 16(2):297–309, 2007. (Cited on page 48.)

D.J. Stephens and V.J. Allan. Light microscopy techniques for live cell imaging. *Science*, 300(5616):82–6, 2003. (Cited on pages 32, 33, and 35.)

Y. Sun, J.D. McKenna, J.M. Murray, E.M. Ostap, and Y.E. Goldman. Parallax: High accuracy three-dimensional single molecule tracking using split images. *Nano Letters*, 9(7):2676–82, 2009. (Cited on page 60.)

E. Syková and C. Nicholson. Diffusion in brain extracellular space. *Physiological Reviews*, 88:1277–340, 2008. (Cited on pages 27 and 78.)

L. Tabares, R. Ruiz, P. Linares-Clemente, M.A. Gaffield, G.A. de Toledo, R. Fernandez-Chacón, and W.J. Betz. Monitoring synaptic function at the neuromuscular junction of a mouse expressing synaptophluorin. *The Journal of Neuroscience*, 27(20):5422–30, 2007. (Cited on page 152.)

J. Tang, J. Akerboom, A. Vaziri, L.L. Looger, and C.V. Shank. Near-isotropic 3d optical nanoscopy with photon-limited chromophores. *Proceedings of the National Academy of Sciences*, 107(22):10068–73, 2010. (Cited on page 61.)

I. Testa, N.T. Urban, S. Jakobs, C. Eggeling, K.I. Willig, and S.W. Hell. Nanoscopy of living brain slices with low light levels. *Neuron*, 75(6):992–1000, 2012. (Cited on pages 37 and 73.)

P.H. Thakur, H. Lu, S.S. Hsiao, and K.O. Johnson. Automated optimal detection and classification of neural action potentials in extra-cellular recordings. *Journal of Neuroscience Methods*, 162(1–2):364–76, 2007. (Cited on page 155.)

D. Thomann, D.R. Rines, P.K. Sorger, and G. Danuser. Automatic fluorescent tag detection in 3d with super-resolution: application to the analysis of chromosome movement. *Journal of Microscopy*, 208(1):49–64, 2002. (Cited on pages 50 and 68.)

M.A. Thompson, M.D. Lew, M. Badieirostami, and W.E. Moerner. Localizing and tracking single nanoscale emitters in three dimensions with high spatio-temporal resolution using a double-helix point spread function. *Nano Letters*, 10(1):211–8, 2010. (Cited on page 60.)

R.E. Thompson, D.R. Larson, and W.W. Webb. Precise nanometer localization analysis for individual fluorescent probes. *Biophysical Journal*, 82:2775–83, 2002. (Cited on pages 37, 49, 51, 53, 75, and 76.)

R.G. Thorne and C. Nicholson. In vivo diffusion analysis with quantum dots and dextrans predicts the width of brain extracellular space. *Proceedings of the National Academy of Sciences*, 103(14):5567–72, 2006. (Cited on page 78.)

D. Toomre and J.B. Pawley. Disk-scanning confocal microscopy. In *Handbook of Biological Confocal Microscopy*, pages 221–38. Springer, 3th edition, 2006. (Cited on pages 34 and 74.)

E. Toprak, H. Balci, B.H. Blehm, and P.R. Selvin. Three-dimensional particle tracking via bifocal imaging. *Nano Letters*, 7(7):2043–5, 2007. (Cited on page 60.)

P. Török, P. Varga, Z. Laczik, and G.R. Booker. Electromagnetic diffraction of light focused through a planar interface between materials of mismatched refractive indices: an integral representation. *Journal of the Optical Society of America A*, 12(2):325–32, 1995. (Cited on page 66.)

S.F. Traynelisa and F. Jaramillo. Getting the most out of noise in the central nervous system. *Trends in Neurosciences*, 21(4):137–45, 1998. (Cited on page 14.)

A. Triller and D. Choquet. New concepts in synaptic biology derived from single-molecule imaging. *Neuron*, 59:359–74, 2008. (Cited on pages 3 and 73.)

R.Y. Tsien. The green fluorescent protein. *Annual Review of Biochemistry*, 67(1):509–44, 1998. (Cited on page 27.)

R.Y. Tsien, L. Ernst, and A. Waggoner. Fluorophores for confocal microscopy: Photophysics and photochemistry. In *Handbook of Biological Confocal Microscopy*, pages 338–52. Springer, 3th edition, 2006. (Cited on pages 26 and 152.)

W. Tvaruskó, M. Bentele, T. Misteli, R. Rudolf, C.K. Aether, D.L. Spector, H.H. Gerdes, and R. Eils. Time-resolved analysis and visualization of dynamic processes in living cells. *Proceedings of the National Academy of Sciences*, 96(14):7950–5, 1999. (Cited on pages 48 and 68.)

N.T. Urban, K.I. Willig, S.W. Hell, and U.V. Nägerl. Sted nanoscopy of actin dynamics in synapses deep inside living brain slices. *Biophysical Journal*, 101(5):1277–84, 2011. (Cited on page 65.)

D. Uttenweiler, C. Weber, B. Jähne, R.H.A. Fink, and H. Scharr. Spatiotemporal anisotropic diffusion filtering to improve signal-to-noise ratios and object restoration in fluorescence microscopic image sequences. *Journal of Biomedical Optics*, 8(1): 40–7, 2003. (Cited on page 48.)

P. Vallotton, A. Ponti, C.M. Waterman-Storer, E.D. Salmon, and G. Danuser. Recovery, visualization, and analysis of actin and tubulin polymer flow in live cells: A fluorescent speckle microscopy study. *Biophysical Journal*, 85(2):1289–306, 2003. (Cited on page 68.)

A. Van Harreveld, J. Crowell, and S.K. Malhotra. A study of extracellular space in central nervous tissue by freeze-substitution. *The Journal of Cell Biology*, 25(1):117–37, 1965. (Cited on page 78.)

R. Varadhan and C. Roland. Simple and globally convergent methods for accelerating the convergence of any em algorithm. *Scandinavian Journal of Statistics*, 35(2):335–53, 2008. (Cited on page 150.)

N. Vardjan, M. Stenovec, J. Jorgačevski, M. Kreft, and R. Zorec. Subnanometer fusion pores in spontaneous exocytosis of peptidergic vesicles. *The Journal of Neuroscience*, 27(17):4737–46, 2007. (Cited on page 151.)

A. Vaziri, J. Tang, H. Shroff, and C.V. Shank. Multilayer three-dimensional super resolution imaging of thick biological samples. *Proceedings of the National Academy of Sciences*, 105(51):20221–6, 2008. (Cited on page 73.)

L. Vincent. Morphological grayscale reconstruction in image analysis: applications and efficient algorithms. *IEEE Transactions on Image Processing*, 2(2):176–201, 1993. (Cited on page 50.)

S.M. Voglmaier, K. Kam, H. Yang, D.L. Fortin, Z. Hua, R.A. Nicoll, and R.H. Edwards. Distinct endocytic pathways control the rate and extent of synaptic vesicle protein recycling. *Neuron*, 51(1):71–84, 2006. (Cited on pages 164 and 166.)

Y. Wang, T. Quan, S. Zeng, and Z.L. Huang. Palmer: a method capable of parallel localization of multiple emitters for high-density localization microscopy. *Optics Express*, 20(14):16039–49, 2012. (Cited on page 55.)

Y. Wang, G. Fruhwirth, E. Cai, T. Ng, and P.R. Selvin. 3d super-resolution imaging with blinking quantum dots. *Nano Letters*, 13(11):5233–41, 2013. (Cited on page 63.)

T.M. Watanabe, T. Sato, K. Gonda, and H. Higuchi. Three-dimensional nanometry of vesicle transport in living cells using dual-focus imaging optics. *Biochemical and Biophysical Research Communications*, 359(1):1–7, 2007. (Cited on pages 60 and 61.)

P.T. Watkins, G. Santhanam, K.V. Shenoy, and R.R. Harrison. Validation of adaptive threshold spike detector for neural recording. In *26th Annual International Conference of the IEEE Engineering in Medicine and Biology Society*, pages 4079–82, 2004. (Cited on page 155.)

R.H. Webb. Confocal optical microscopy. *Reports on Progress in Physics*, 59(3):427–71, 1996. (Cited on page 34.)

K. Weisshart, T. Dertinger, T. Kalkbrenner, I. Kleppe, and M. Kempe. Super-resolution microscopy heads towards 3d dynamics. *Advanced Optical Technologies*, 2(3):211–31, 2013. (Cited on pages 32, 35, and 40.)

V. Westphal, S.O. Rizzoli, M.A. Lauterbach, D. Kamin, R. Jahn, and S.W. Hell. Video-rate far-field optical nanoscopy dissects synaptic vesicle movement. *Science*, 320 (5873):246–9, 2008. (Cited on page 37.)

S. Wieser and G.J. Schütz. Tracking single molecules in the live cell plasma membrane - do's and don't's. *New Methods in Membrane Protein Research*, 46(2):131–40, 2008. (Cited on page 68.)

D. Wildanger, R. Medda, L. Kastrup, and A.W. Hell. A compact sted microscope providing 3d nanoscale resolution. *Journal of Microscopy*, 236(1):35–43, 2009. (Cited on page 37.)

K.M. Wilson, I.E. Morrison, P.R. Smith, N. Fernandez, and R.J. Cherry. Single particle tracking of cell-surface hla-dr molecules using r-phycoerythrin labeled monoclonal antibodies and fluorescence digital imaging. *Journal of Cell Science*, 109:2101–9, 1996. (Cited on page 44.)

S.B. Wilson and R. Emerson. Spike detection: a review and comparison of algorithms. *Clinical Neurophysiology*, 113:1873–81, 2002. (Cited on page 157.)

S. Wolter, U. Endesfelder, S. van de Linde, M. Heilemann, and M. Sauer. Measuring localization performance of super-resolution algorithms on very active samples. *Optics Express*, 19(8):7020–33, 2011. (Cited on page 54.)

M. Wu, J.W. Roberts, and M. Buckley. Three-dimensional fluorescent particle tracking at micron-scale using a single camera. *Experiments in Fluids*, 38(4):461–5, 2005. (Cited on page 58.)

Q. Wu, F. Merchant, and K.R. Castleman. *Microscope Image Processing*. Elsevier, 1th edition, 2008. (Cited on pages 29, 31, 46, 47, 49, 50, 67, and 69.)

K. Xu, H.P. Babcock, and X. Zhuang. Dual-objective storm reveals three-dimensional filament organization in the actin cytoskeleton. *Nature Methods*, 9(2):185–8, 2012. (Cited on page 59.)

J. Yajima1, K. Mizutani1, and T. Nishizaka. A torque component present in mitotic kinesin eg5 revealed by three-dimensional tracking. *Nature Structural & Molecular Biology*, 15(10):1119–21, 2008. (Cited on page 60.)

C. Yang, Z. He, and W. Yu. Comparison of public peak detection algorithms for maldi mass spectrometry data analysis. *BMC Bioinformatics*, 10(4):1–13, 2009. (Cited on pages 157 and 164.)

A. Yildiz, J.N. Forkey, S.A. McKinney, T. Ha, Y.E. Goldman, and P.R. Selvin. Myosin v walks hand-over-hand: Single fluorophore imaging with 1.5-nm localization. *Science*, 300(5628):2061–5, 2003. (Cited on page 39.)

A.G. York, A. Ghitani, A. Vaziri, M.W. Davidson, and H. Shroff. Confined activation and subdiffractive localization enables whole-cell palm with genetically expressed probes. *Nature Methods*, 8(4):327–33, 2011. (Cited on pages 33, 56, and 65.)

G.W. Zack, W.E. Rogers, and S.A. Latt. Automatic measurement of sister chromatid exchange frequency. *Journal of Histochemistry & Cytochemistry*, 25(7):741–53, 1977. (Cited on page 49.)

F.C. Zanacchi, Z. Lavagnino, M.P. Donnorso, A.D. Bue, L. Furia, M. Faretta, and A. Diaspro. Live-cell 3d super-resolution imaging in thick biological samples. *Nature Methods*, 8(12):1047–9, 2011. (Cited on page 73.)

D. Zenisek, J.A. Steyer, and W. Almers. Transport, capture and exocytosis of single synaptic vesicles at active zones. *Nature*, 406:849–54, 2000. (Cited on page 180.)

B. Zhang, M.J. Fadili, J.L. Starck, and J.C. Olivo-Marin. Multiscale variance-stabilizing transform for mixed-poisson-gaussian processes and its applications in bioimaging. In *IEEE International Conference on Image Processing*, pages 233–6, 2007a. (Cited on page 50.)

B. Zhang, J. Zerubia, and J.C. Olivo-Marin. Gaussian approximations of fluorescence microscope point-spread function models. *Applied Optics*, 46(10):1819–29, 2007b. (Cited on page 30.)

Q. Zhang, Y. Li, and R.W. Tsien. The dynamic control of kiss-and-run and vesicular reuse probed with single nanoparticles. *Science*, 323(5920):1448–53, 2009. (Cited on page 153.)

R. Zhang, E. Rothenberg, G. Fruhwirth, P.D. Simonson, F. Ye, I. Golding, T. Ng, W. Lopes, and P.R. Selvin. Two-photon 3d fiona of individual quantum dots in an aqueous environment. *Nano Letters*, 11(10):4074–8, 2011. (Cited on page 56.)

L. Zhu, W. Zhang, D. Elnatan, and B. Huang. Faster storm using compressed sensing. *Nature Methods*, 9(7):721–3, 2012. (Cited on pages 56, 109, and 112.)

ABBREVIATIONS

SYMBOLS

a Wavelet scale

$a_{min}, \hat{a}$ Min/max wavelet scale parameters for MWA

$\hat{a}_{haar}, \hat{a}_{bior}$ Max scale parameter for the Haar respectively the Bior3.1 wavelet

$a_{opt}(b)$ Optimal scale for fitting a certain peak shape at transition b

a_1, a_2 Positive constants that relate to the geometry of a confined region

α Half of the angular aperture; Anomaly parameter for anomalous diffusion

b Wavelet translation

B Generally for bias

c Speed of light in vacuum

$\hat{c}(b)$ Highest employed wavelet coefficient at transition b

c_n Speed of light in material with RI n

c_{SNR} Correction factor for the estimated SNR

C Wavelet coefficients

C_{haar}, C_{bior} Wavelet coefficients for the Haar respectively the Bior3.1 wavelet

$\mathcal{C}$ General component mixture model

d Focal depth; Spatial dimension

δ Overall noise of EMCCD cameras

δ_b Background noise of EMCCD cameras

δ_{dark} Dark noise of EMCCD cameras

δ_{mult} Multiplicative noise of EMCCD cameras

δ_{photon} Photon noise of EMCCD cameras

δ_{read} Read noise of EMCCD cameras

d_p Pixel size of the camera

d_{po} Pixel size in the object space

d_R Rayleigh distance

d_{SML} Distance for SML resolution

d_{STED} Distance for STED resolution

d_u Distance between center coordinates and each gradient line

d_z Distance for axial resolution

Δ_f Focal shift intentionally introduced by a cylindrical lens

Δ_i Peak intensity in pHluorin data

Δs Generally for LA

Δ_σ FWHM shift inherently introduced by a cylindrical lens for confocal setups

Δs_r Reduced localization error

Δt Discrete sampling interval

D Diffusion coefficient

D_c Combined distance between the measured widths and the axial calibration curve

D_l Local diffusion coefficient

E Energy of a photon; Expectation operator

E_j Expectation within a single pixel

f Frequency of light; Focal length in geometrical optics

f_s Sampling rate

f_v Vertex frames

F Generally for some function

g Number of components in a mixture model

G Generally for Gaussian function

G_{EM} Gain factor of the electron multiplication register of EMCCD camera's

h Planck's constant; Height of a Gaussian function

i Intensity of light

i_b Amount of background intensity at a pixel

$i_{x,y}$ Pixel intensity

I Generally for image

I_{Airy} Image of the Airy pattern

I, I_{Airy}, I_{fit} Image that is fitted to a particle's intensity distribution

J Jaccard index

k Threshold factor for particle detection in microscopy data

k_f Threshold factor for peak detection in pHluorin data

κ_i Number of photons per mixture component i

K_p Number of particles

l Coordinate at axial distance $-\Delta_f$ from v of the axial correlation function

L Joint likelihood in maximum likelihood estimation

λ Wavelength of light

λ_{pois} Mean of a Poisson distribution

μ Generally for expected value

m Generally for running index

m_j Expected intensity at the j-th pixel

m_u Generally for the slope of a line

m_r Slope of the line that adjust the axial correlation function to the RIM

m_{min} Optimal number of included MSD data points

M Magnification; Number of measurements of a trajectory

n Refractive index

N Generally for number of photons

N_b Number of background photons

N_p Total number of photons per particle

$N_{x,y}$ Number of particle photons at a pixel

$\hat{N}$ Number of particle photons at the center pixel

N_j Number of particle photons at the j-th pixel

$\mathcal{N}$ Gaussian mixture model

$\mathcal{N}_i$ i-th multivariate normal distribution

o_b Offset for a Gaussian function; Number of observed pixels for the EM algorithm

ω Generally for FWHM

p Generally for position

p_{pois} Realization of a Poisson random variable

φ Phase of light

P Generally for probabilities

P_{pois} Poisson distribution

$\vec{P}$ Polarization of light

Φ_j Unconditional probability that a photon is detected at a certain pixel j

Φ_i, Φ_l, Φ_r Angle of the incoming, the reflected and the refracted light ray

π Vector of component mixing proportions

$\psi(t)$ Wavelet

O Real objects

r Random variable for the sub-pixel position of photon measurements on a camera chip; Coordinate at axial distance $+\Delta_f$ from v of the axial correlation function

r_{bior} Support range of the Bior3.1 wavelet

$\mathcal{R}$ Sample space of R

R_c Size of a confined region

σ Generally for SD

σ_p, σ_b Signal and background noise of the intensity distribution of a particle

Σ_i Covariance matrix

$\tilde{\sigma}$ Generally for median absolute deviation

$S(b)$ Signal containing the combined wavelet coefficients across scales

$S_{haar}(b)$, $S_{bior}(b)$ Signals containing the combined coefficients across scales for the Haar respectively the Bior3.1 wavelet

S_{CCD} Sensitivity of a CCD camera's analog-to-digital converter

$S_f(b)$ Signal containing the fused information of multiple wavelets

$S_f^*(b)$ Fused signal after convolution with the Bartlett window

$s(t)$ Generally for a 1D signal over time

S_x Fundamental electronic states

t Generally for time; Current iteration number for EM algorithm

t_a Scale dependent threshold in the wavelet space

t_f Threshold for final peak detection in $S_f^*(b)$

t_{init} Number of random starts for the EM algorithm

t_{iter} Maximum number of iterations for the EM algorithm

t_p Intensity threshold for particles during spot detection

t_s Threshold for the skewness of $S_{bior}(b)$

T Transpose operation

τ Generally for time interval; Mean lifetime; Relative weight of each mixture component with respect to an individual photon measurement

θ Rotation angle of general Gaussian function; Parameter vector for Gaussian mixture model

Θ Parameter vector for general component mixture model

u Generally for running index

v Generally for running index; Vertex coordinate of the axial correlation function; Total number of pixels for EM algorithm

w Generally for some weight

V Velocity

x, y Lateral x and y coordinates

x_c, y_c Lateral x and y center coordinates

z Relative axial position

z_s Parameter that shifts the axial correlation function along the axial axis

EHRENERKLÄRUNG

Ich versichere hiermit, dass ich die vorliegende Arbeit ohne unzulässige Hilfe Dritter und ohne Benutzung anderer als der angegebenen Hilfsmittel angefertigt habe; verwendete fremde und eigene Quellen sind als solche kenntlich gemacht. Insbesondere habe ich nicht die Hilfe eines kommerziellen Promotionsberaters in Anspruch genommen. Dritte haben von mir weder unmittelbar noch mittelbar geldwerte Leistungen für Arbeiten erhalten, die im Zusammenhang mit dem Inhalt der vorgelegten Dissertation stehen. Ich habe insbesondere nicht wissentlich:

- Ergebnisse erfunden oder widersprüchliche Ergebnisse verschwiegen,

- statistische Verfahren absichtlich missbraucht, um Daten in ungerechtfertigter Weise zu interpretieren,

- fremde Ergebnisse oder Veröffentlichungen plagiiert,

- fremde Forschungsergebnisse verzerrt wiedergegeben.

Mir ist bekannt, dass Verstöße gegen das Urheberrecht Unterlassungs- und Schadensersatzansprüche des Urhebers sowie eine strafrechtliche Ahndung durch die Strafverfolgungsbehörden begründen kann. Die Arbeit wurde bisher weder im Inland noch im Ausland in gleicher oder ähnlicher Form als Dissertation eingereicht und ist als Ganzes auch noch nicht veröffentlicht.

Magdeburg, 30.10.2015

Stefan Sokoll